Galactic Cosmic Ray Exposure of Humans in Space

Influence of galactic cosmic ray models and shielding on dose calculations for low-Earth orbit and near-Earth interplanetary space

Dissertation
in fulfillment of the requirements for the degree "Dr. rer. nat."
of the Faculty of Mathematics and Natural Sciences
at Kiel University

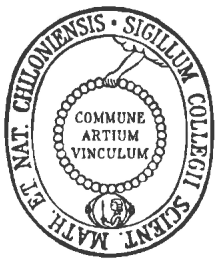

submitted by
Alankrita Isha Mrigakshi

Kiel, 2013

First referee:	Prof. Dr. Robert Wimmer-Schweingruber
Second referee:	Prof. Dr. Lembit Sihver
Date of the oral examination:	05.09.2013
Approved for publication:	05.09.2013

Signed: _____

Prof. Dr. Wolfgang J. Duschl, Dean

To My Family

" Nothing in life is to be feared, it is only to be understood "

*–Marie Sklodowska Curie**

(* As quoted in - Ham D., Marie Sklodowska Curie: The woman who opened the nuclear age. 21st Century Science & Technology 15(4), 2002, pp 30-68)

Abstract

The radiation environment in space is one of the primary concerns for human spaceflight as it poses potential risk to astronauts' health. Galactic Cosmic Rays (GCR), consisting of high-energy nuclei, are a major source of radiation exposure in space. As the number of people visiting space in low-Earth orbit is increasing and mankind prepares to go beyond, the issue of radiation protection against GCR thus becomes vitally important.

The pre-flight assessment of radiation-related health risks is achieved by performing numerical simulations of the mission scenario to estimate the necessary radiation-dose quantities. This technique requires models describing the radiation spectra, the target and shield configurations, and additionally transport codes to simulate the passage of radiation through matter. The reliability of the calculated dose therefore depends on the accuracy of all these models.

During the course of this PhD work, commonly used models describing the GCR spectra are evaluated for their accuracy for various time periods. The model spectra of nuclei, most relevant for space dosimetry, are compared with measurements from high-altitude balloon flights and space missions. The GCR models included in this work are CREME96, CREME2009, Burger-Usoskin, Badhwar-O'Neill2010, Badhwar-O'Neill2011, Matthiä-ACE/OULU and SPENVIS/ISO15390. The influence of using these different GCR models on the dose calculations is studied for a time period ranging over the last four decades. This is achieved by calculating the absorbed dose and dose equivalent rates in a spherical water phantom using the GEANT4 Monte-Carlo framework. Additionally, the influence of aluminium shielding of varying thicknesses (0.3 g/cm^2, 10 g/cm^2 and 40 g/cm^2) on the dose is investigated for a time period ranging from 1997 to 2012. All these investigations are performed for near-Earth interplanetary space and the orbit of the International Space Station (ISS).

Apart from examining these parameters the effective dose, being the baseline quantity for radiation-risk assessment, is estimated. The quantity is calculated for the end of the year 2009 when the highest GCR intensity since the dawn of human spaceflight era was observed. Further studies presented in the thesis include the relative contribution of particles with different energies to the total exposure and the comparison of calculated dose with the measurements conducted inside the ISS and in-transit to Mars by the MSL/RAD instrument.

Zusammenfassung

Die Strahlungsumgebung im Weltraum ist eine der großen Herausforderungen der bemannten Raumfahrt, da sie ein potenzielles Gesundheitsrisiko für Astronauten darstellt. Galaktisch kosmische Strahlung (GCR), hauptsächlich bestehend aus hochenergetischen Atomkernen, ist dabei eine der Hauptquellen der Strahlenexposition. Da die Anzahl der Menschen, die sich im erdnahen Orbit aufhalten, stetig wächst und die Menschheit sich auf Reisen zu weiter entfernten Zielen vorbereitet, erlangt der Strahlenschutz hinsichtlich der GCR besondere Bedeutung.

Um das Gesundheitsrisiko durch die Strahlenexposition im Vorhinein abschätzen zu können, werden numerische Simulationen der Missionsszenarien dazu genutzt, die notwendigen Strahlendosisgrößen zu bestimmen. Hierfür werden Computermodelle benötigt, die das Energiespektrum der Strahlungsumgebung, Zielobjekt und Abschirmung, sowie den Transport von Strahlung durch Materie beschreiben. Die Zuverlässigkeit der berechneten Dosisgrößen hängt dementsprechend von der Genauigkeit all dieser Modelle ab.

In der vorliegenden Arbeit werden die Spektren gängiger GCR Modelle auf ihre Genauigkeit innerhalb ausgewählter Zeiträume untersucht und für die dosimetrisch wichtigsten Ionen mit Messungen aus Ballon- und Weltraumexperimenten verglichen. Die dabei verwendeten GCR Modelle sind CREME96, CREME2009, Burger-Usoskin, Badhwar-O'Neill2010, Badhwar-O'Neill2011, Matthiä-ACE/OULU und SPENVIS/ISO15390. Der Einfluss, den die Anwendung dieser verschiedenen Modelle auf Dosisberechnungen hat, wird für den Zeitraum der letzten vier Jahrzehnte analysiert, indem die absorbierte Dosis sowie Äquivalentdosisraten in einem sphärischen Wasserphantom mit Hilfe von GEANT4 Monte-Carlo Simulationen berechnet werden. Zusätzlich wird für den Zeitraum von 1997 bis 2012 der Einfluss unterschiedlicher Abschirmungsdicken ($0.3\,\mathrm{g/cm^2}$, $10\,\mathrm{g/cm^2}$ and $40\,\mathrm{g/cm^2}$ Aluminium) auf die Dosis untersucht. Alle Analysen werden für den erdnahen interplanetaren Raum sowie für den Orbit der Internationalen Raumstation (ISS) durchgeführt.

Außerdem wird die effektive Dosis als Basisgröße zur Strahlenrisikoeinschätzung berechnet. Diese Größe wird für das Ende des Jahres 2009 abgeschätzt, da zu diesem Zeitpunkt die höchste GCR Intensität seit Anbeginn der bemannten Raumfahrt beobachtet wurde. Weitere Studien in der vorliegenden Arbeit beinhalten den relativen Beitrag von Teilchen verschiedener Energien zur Gesamtexposition und Vergleiche von berechneten Dosiswerten mit Messungen, die innerhalb der ISS und auf dem Weg zum Mars mit dem MSL/RAD Instrument vorgenommen wurden.

Preface

This is a cumulative doctoral thesis containing research work accomplished between July 2009 and June 2013 within the framework of the SpaceLife Program at the Helmholtz Space Life Science Research School. The program was initiated and implemented by the German Aerospace Centre (DLR) in Cologne, Germany. With this program, DLR together with partner universities in Germany and abroad aims to deepen the understanding of various issues associated with the interaction of living systems with the extreme environment of space by conducting research in relevant scientific disciplines such as Radiation Biology, Astrobiology, Gravitational Biology and Space Physiology.

As a participant of the Helmholtz Space Life Science Research School, I received the SpaceLife scholarship which is funded in equal parts by the Initiative and Networking Fund of the Helmholtz Association, and the DLR.

The study presented in this dissertation focuses on the numerical estimation of radiation exposure from Galactic Cosmic Rays (GCR) in space outside and inside the Earth's magnetosphere. This topic falls under a branch of science called Radiation Protection in Space which deals with the development of methods and concepts to mitigate the radiation related health risks for humans in space.

The work was performed at the Institute of Aerospace Medicine, DLR-Cologne, Germany under the supervision of Dr. Thomas Berger leading the Biophysics group at the Department of Radiation Biology in DLR-Colgone and Prof. Dr. Robert Wimmer-Schweingruber leading the Extraterrestrial Physics group at the Institute of Experimental and Applied Physics, Christian-Albrechts-University Kiel, Germany.

This dissertation includes four scientific papers published in peer-reviewed scientific journals relevant to the field of study. All publications are co-authored by several scientists, however I am the primary author of three. Additional results from further investigations performed during the research work are added in the thesis as well.

Publications presented in this thesis

Mrigakshi, A. I., D. Matthiä, T. Berger, G. Reitz and R. F. Wimmer-Schweingruber, Assessment of galactic cosmic ray models, J. Geophys. Res., 117, A08109, 2012. doi:10.1029/2012JA017611

Mrigakshi, A. I., D. Matthiä, T. Berger, G. Reitz and R. F. Wimmer-Schweingruber, How Galactic Cosmic Ray models affect the estimation of radiation exposure in space, Adv. Space Res., 51, p. 825-834, 2013a. doi:10.1016/j.asr.2012.10.017

Matthiä, D., T. Berger, A. I. Mrigakshi and G. Reitz, A Ready - to - Use Galactic Cosmic Ray Model, Adv. Space Res., 51, p. 329-338, 2013a. doi:10.1016/j.asr.2012.09.022

Mrigakshi, A. I., D. Matthiä, T. Berger, G. Reitz and R. F. Wimmer-Schweingruber, Estimation of Galactic Comic Ray exposure inside and outside the Earth's magnetosphere during the recent solar minimum between solar cycles 23 and 24, Adv. Space Res., 52, p. 979-987, 2013b. doi:10.1016/j.asr.2013.05.007

Cologne, 10^{th} July 2013 Alankrita Isha Mrigakshi

Contents

Abstract i

Zusammenfassung iv

Preface vi

Page

1 Introduction 1

2 Radiation Protection in Space 3
- 2.1 Galactic Cosmic Rays . . . 6
  - 2.1.1 GCR Energy Spectra . . . 6
  - 2.1.2 Solar Modulation . . . 8
  - 2.1.3 Geomagnetic Modulation . . . 13
- 2.2 Radiation-Matter Interaction . . . 18
  - 2.2.1 Electromagnetic Interactions . . . 18
  - 2.2.2 Nuclear Interactions . . . 21
- 2.3 Dosimetric Concepts . . . 24
  - 2.3.1 Dose quantities . . . 24
  - 2.3.2 GCR Hazard in Space . . . 27

3 Numerical Dose Assessment 31
- 3.1 Methodology of GCR dose estimation . . . 32
- 3.2 GCR Model Spectra . . . 33
  - 3.2.1 Outside magnetosphere near-Earth . . . 33
  - 3.2.2 Inside magnetosphere at ISS orbit . . . 36
- 3.3 GEANT4 Simulation . . . 38
  - 3.3.1 GEANT4 Monte-Carlo Method . . . 39
  - 3.3.2 Simulation Setup . . . 40
  - 3.3.3 Simulation Processing and Output . . . 44
- 3.4 GCR Dose Estimation . . . 47

4 Publications 51
- 4.1 An Overview of the papers . . . 51

4.2 Paper I - Mrigakshi et al. 2012 55
4.3 Paper II - Mrigakshi et al. 2013a 69
4.4 Paper III - Matthiä et al. 2013 81
4.5 Paper IV - Mrigakshi et al. 2013b 93

5 Additional Results 105
5.1 Badhwar-O'Neill2011 model 105
5.1.1 Model vs measured energy spectra 105
5.1.2 Influence on the dose calculations 110
5.2 Variation of dose with particle energy 112
5.3 Estimation of effective dose rate 115
5.4 Comparison with experimental data 120

6 Summary and Conclusions 125

7 Outlook 133

Bibliography 137

Appendix A GCR Model Data Retrieval 147
A.1 CREME96 and CREME2009 147
A.2 Badhwar-O'Neill 2010 and 2011 models 150
A.3 Burger-Usoskin and Matthiä et al. 2013a 152

Appendix B Primary Particle Generation 155
B.1 Input spectra: particle number over energy 155
B.2 Quality of statistics 157
B.3 Example GPS macro file 158

Appendix C SPENVIS GCR Model 159
C.1 The ISO15390 GCR model in SPENVIS 159
C.2 Model assessment 159
C.3 Dose Assessment 161

List of Abbreviations 163

List of Figures 165

List of Tables 167

Acknowledgment 169

Statutory Declaration 171

1 Introduction

Curiosity has always stimulated mankind to question and understand the world we live in, its origin and what lies beyond. Together with determination it has led us to innovate and develop technologies to reach for space. Soon after the launch of the first artificial spacecraft, *Sputnik-1*, in 1957, Yuri Gagarin was the first man to voyage into space in 1961 marking the beginning of the human spaceflight era. Since then there have been over 500[1] astronauts (Sandoval et al., 2010) to space, spending extended periods of time lasting from a few days to several months. In fact, the number of people from across the globe visiting space is increasing and is projected to rise at a faster rate with private companies now investing in human spaceflight.

The extreme environmental conditions in space, contrary to those on Earth where life as we know has evolved, have long been regarded as a limiting factor for manned missions in terms of duration and destinations. The negative effects of reduced gravity, the enhanced level of radiation and psychological issues arising from prolonged confinement and isolation can affect astronaut's performance and can be dangerous to their health (White and Averner 2001; Horneck et al. 2003; Setlow 2003).

Much effort and research has been undertaken since the conception of manned missions to counteract these effects. However, our understanding of the interaction between the human body and the space environment is still incomplete due to several reasons, e.g., the inadequate knowledge of fundamental concepts of human body systems and technical complexity to simulate the space environment on Earth. Nevertheless, advancements in this field of study have been made over the years and through detailed assessment of missions, with the existing and continuously growing knowledge, appropriate steps are being taken to improve the safety and mitigate the negative effects of space travel on humans.

The assessment of the health risk arising from radiation requires the determination of the radiation exposure of astronauts. This is achieved by performing measurements of the radiation dose which is required for monitoring the crew exposure and by making numerical estimations using radiation transport codes to simulate the passage of radiation through matter. The latter approach is essential for the prediction of the radiation exposure for future missions to space and for locations where measurements are not feasible, e.g., inside human body or where they have not yet been made e.g. during future space missions. The reliability of this approach is, unquestionably,

[1] http://www.nasa.gov/worldbook/astronaut_worldbook.html

dependent on the accuracy of the models used for the numerical calculations.

The work presented in this thesis is an effort to further improve methods essential for the numerical estimation of the radiation-related health risks in space. It focusses on the radiation exposure from Galactic Cosmic Rays (GCR) in space and shows how the application of different models describing the GCR radiation field affects the dose quantities required for the estimation of the health risks. This was achieved by testing the GCR spectra described by frequently used models against the measurements. The differences produced in the estimated dose quantities using these models were then quantified for the last four decades. Furthermore, the influence of different amounts of shielding on the dose quantities was studied as well.

Structure of the thesis

This thesis begins with an introduction into the field of Radiation Protection in Space in Chapter 2. The chapter includes scientific background on GCR and the variability in its intensity over time inside and outside the magnetosphere close to Earth. Additionally, a brief overview of the relevant physical processes involved in radiation-matter interactions, an introduction to dosimetric concepts required for the quantification of radiation exposure, and a brief overview of the relevance of GCR for radiation protection in space is provided. Chapter 3 describes the tools, methods and algorithm used in this work for the numerical estimation of the radiation exposure from GCR. The following Chapter 4 consists of scientific papers which present the results of the different investigations performed during the course of the research work. They include an assessment of models describing the GCR spectra, calculation of the radiation exposure from GCR over the past four decades with a special emphasis on the GCR exposure during the 2009 solar minimum, and the effect of using different GCR models and shielding on the dose values. The publications are arranged in an order to logically follow and understand how the consequence of each study impacted the development of the research work. The next Chapter 5 contains additional results that have not been published in the papers. The findings of the work and associated conclusions are summarised in Chapter 6. The thesis ends with an outlook in Chapter 7 wherein topics for possible future studies related with this work are discussed.

2 Radiation Protection in Space

Soon after the discovery of X-rays and radioactivity in 1895 and 1896, their inadvertent use for various applications, e.g., in the field of medicine and physics, resulted in numerous injuries and prompted the immediate need for establishing guidelines for people working with radiation (Lindell, 1996). In the 1920s several advisory bodies (Lindell, 1996) like the International Commission on Radiation Units and Measurements (ICRU), the International Commission on Radiological Protection (ICRP), the National Council on Radiation Protection and Measurements (NCRP) of the United States were founded to formulate methods and develop recommendations for protection against radiation. These committees have been since providing the guidelines which are constantly updated with the increasing knowledge in the field of radiation protection with time. In fact, several countries across the world including the European Member States (Council Directive 96/29/Euratom, 1996)[1] have adopted many of the recommendations especially from ICRP into their legislation to develop safety standards for radiation workers [2] for various types of occupations and general public against ionizing radiation.

Space contains both ionizing and non-ionizing radiation which can be distinguished by their energy. In comparison with non-ionizing radiation such as near UV and infrared, ionizing radiation has greater energy and is able to penetrate deeper into the medium. When interacting with living cells, it can cause greater biological damage. The damage process starts with the absorption of energy that is transferred from the incident ionizing radiation through mechanisms explained later in Section 2.2. A series of biochemical transformations of water and biological molecules are triggered which eventually may result in observable biological effects. The radiation can affect the cells or tissues directly or indirectly through reactive free radicals produced on interaction with water (Goodhead, 1994). The DNA (deoxyribonucleic acid) within the cell nucleus is the most critical target as it contains the genetic information. Genotoxic stress like DNA damage caused by irradiation can lead to cell death, mutations and abnormal biological functioning depending on the kind of DNA-damage

[1] http://eur-lex.europa.eu/LexUriServ/LexUriServ.do?uri=OJ:L:1996:159:0001:0114:EN:PDF

[2] Astronauts are not listed under radiation workers in the current Directive 96/29/Euratom, however in May 2012 the European Commission adopted the proposal for a council directive laying down basic safety standards for protection against dangers from exposure to ionizing radiation which includes space crew as radiation workers as well and is foreseen to be included in the national laws in the coming years. See http://ec.europa.eu/energy/nuclear/radiation_protection/radiation_protection_en.htm

repair response (Koch 2013 and references therein).

Ionizing radiation includes far ultraviolet (UV) light, X-rays, gamma rays and energetic atomic nuclei. Earth is constantly bombarded with such radiation from space, however, due to the Lorentz force the Earth's magnetosphere deflects charged particles away that have energies below a certain threshold. Particles having enough energy to penetrate through the Earth's magnetic field to lower altitudes suffer from continuous energy losses via interactions with the atoms and molecules comprising the atmosphere and cause the production of secondary particles. As a consequence, the composition and the energy spectrum of the space radiation changes dramatically with increasing atmospheric depth. On ground, this secondary radiation field constitutes part of the background radiation contributing to such a low level of exposure that it is not considered a health risk.

In space, however, the radiation exposure is significantly larger. It depends on the intensity, composition and energy distribution of the radiation field which varies both spatially and temporally. It is for this reason that the assessment of the risks related to radiation in space is conducted separately for each mission scenario. Such assessments lead to certain guidelines which facilitate the space agencies to develop methods to control the amount of radiation received by the astronauts. The increased radiation dose in space has been recognized as a concern by ICRP (1991, 2007) and NCRP (1989, 2000, 2002, 2006). While NCRP provides the guidelines for radiation protection specifically in space, the ICRP has not published any such guidelines yet although a report concerning this issue is currently in preparation and its draft can be found on their website[3].

Clearly, the assessment of radiation exposure requires the identification of the radiation source, the description of the radiation field and the physics of the radiation-matter interaction. Furthermore, it requires the understanding of the biological effects radiation can have on the exposed human tissue to evaluate the potential health risks. In this chapter, many of these aspects are briefly discussed starting with the description of the Galactic Cosmic Rays (GCR) and their characteristics, the particle interactions leading to major energy losses inside a medium and the dosimetric concepts required to quantify the extent of radiation exposure.

It should be noted that besides the GCR, there exist other important sources of radiation exposure in space mainly the Sun and for destinations close to Earth additional sources including trapped particles in the Van-Allen radiation belts (van Allen et al.,

[3]http://www.icrp.org/page.asp?id=163

1959) and albedo particles like neutrons and protons produced by scattering of primary particles (NCRP 1989, 2000, 2002, 2006; Reitz 2008; Cucinotta and Durante 2006). However, these are not discussed in this dissertation because this work is focused on the importance and the consequences of GCR on humans in space only.

2.1 Galactic Cosmic Rays

Over a century ago in the year 1912, Victor Franz Hess discovered a type of radiation (Hess, 1912) originating from extra-terrestrial sources. He called it "*Höhenstrahlung*" (can be translated to as 'high-altitude radiation' in English) and was awarded the Nobel Prize for its discovery in 1936.
Since the 1920s, this type of radiation has been denoted as Cosmic Rays (CR). Its sources include the Sun (often called Solar Cosmic Radiation) and sources present outside the solar system such as supernova remnants (Ackermann et al., 2013). CRs from outside the solar system are termed Galactic Cosmic Rays (GCR).

In this section, the characteristics and the dynamics of GCR in Near-Earth space, i.e., within a distance of 1 AU from the sun (Section 2.1.2) and inside the Earth's magnetic field (Section 2.1.3) are briefly discussed. For a recent review on GCR in the heliosphere see Heber (2011) and Potgieter (2011) and for a detailed description on Heliospheric Physics see Kallenrode (2004) and Wimmer-Schweingruber (2005).

2.1.1 GCR Energy Spectra

Galactic cosmic rays arriving at Earth consist of about 98% fully ionized atoms and about 2% of electrons and photons as measured by various balloon and space missions. GCR nuclei range from hydrogen to iron and beyond, with energies extending up to 10^{21} eV. Hydrogen nuclei are the most abundant, constituting around 87% of the total nucleon component, followed by helium nuclei, 12%, and heavy nuclei, 1% (Simpson, 1983).

Figure 2.1 shows the differential energy spectra of GCR hydrogen, helium, oxygen and iron nuclei measured by various space missions as given in Table 2.1. The differential energy spectrum or the particle flux J, is the number of particles dN observed by a detector in the energy band from E to $E + dE$ passing through a unit surface area dA and arriving from direction Ω within a solid angle $d\Omega$ during time interval dt:

$$J = \frac{dN}{dA \cdot dt \cdot d\Omega \cdot dE} \tag{2.1}$$

Throughout this document J is expressed in the units $m^{-2}s^{-1}sr^{-1}(MeV/nuc)^{-1}$ where nuc is nucleon.

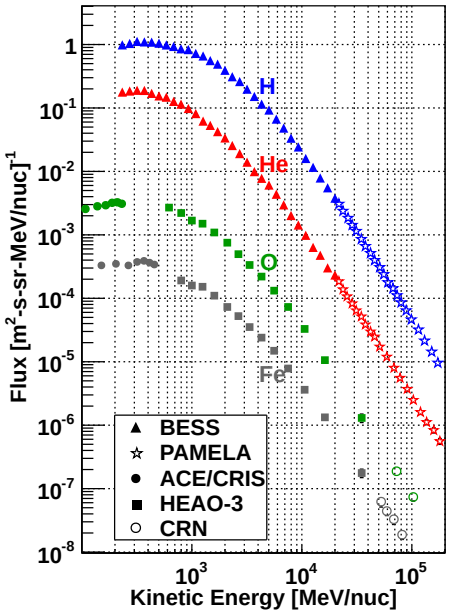

Figure 2.1: Measured GCR spectra of different ions. See Table 2.1 for the details of the GCR measurements plotted in the figure.

At high energies around some tens of GeV/nuc, as can also be seen in Figure 2.1, the GCR spectral shape can be described by a power law

$$J_i \propto E^{-\gamma_i} \tag{2.2}$$

where J_i is the differential flux of particle type i with kinetic energy E per nucleon and γ_i is the differential spectral index. This part of the GCR represents the spectrum outside the heliosphere and is called the Local Interstellar Spectrum (LIS). On encountering the heliosphere the lower energetic nuclei experience solar modulation and thus the spectrum deviates from the power law and becomes flatter. At about a distance of 1 AU from the Sun, the modulated GCR particle spectrum peaks at energies around a few hundreds of MeV/nuc.

Table 2.1: Details of the GCR data shown in Figure 2.1.

Nuclei	Experiment	Energy Range (MeV/nuc)	Time of measurement
H, He	BESS (Shikaze et al., 2007)	$210 - 21.5 \cdot 10^3$	August 1999
	PAMELA (Adriani et al., 2011)	$21.7 \cdot 10^3 - 183 \cdot 10^3$	July 2006 – March 2008
O, Fe	ACE/CRIS (Stone et al., 1998)	$70.4 - 470$	December 1999 – January 2000
	HEAO-3 (Engelmann et al., 1990)	$620 - 35 \cdot 10^3$	October 1979 – June 1980
	CRN (Mueller et al., 1991)	$52.6 \cdot 10^3 - 103 \cdot 10^3$	July – August 1985

2.1.2 Solar Modulation

The variation of GCR over time caused by the solar activity is called solar modulation which was first observed and investigated by Forbush (1954). Figure 2.2 shows energy spectra of GCR hydrogen and helium ions measured by the BESS experiment (Shikaze et al., 2007) during extreme solar activity periods of the 23^{rd} solar cycle. The difference in the particle fluxes during solar activity minimum (July 1997) and maximum (August 2000) periods can be clearly seen for energies below about 10 GeV/nuc. The intensity of the particles is highest during solar activity minimum and lowest during solar activity maximum conditions. Additionally, the shift in the peak of the spectrum to higher energies during solar maximum can also be observed.
Note that in the text hereafter the solar activity minimum is referred to as simply "solar minimum" and solar activity maximum as "solar maximum".
The solar modulation can be explained by understanding the propagation of GCR inside the heliospheric magnetic field (HMF). The heliosphere can be imagined as a big magnetic bubble in the interstellar medium filled with solar wind which moves outward from the sun carrying along with it the frozen-in HMF towards its outer boundaries. Since GCR are ionized particles they experience the Lorentz force exerted by the HMF which varies in space and time with the changing solar activity.

A charged particle in a homogeneous magnetic field gyrates in helical trajectories around a guiding centre with constant radius of gyration (gyroradius) along the magnetic field lines. The angle between the particles direction of flight and the magnetic field lines is called the pitch angle α with

$$\tan\alpha = \frac{v_\perp}{v_\parallel} \tag{2.3}$$

where, $v_\perp$ = velocity component of the particle perpendicular to $\vec{B}$ such that it is $v\sin\alpha$
$v_\parallel$ = velocity component of the particle parallel to $\vec{B}$ such that it is $v\cos\alpha$

The gyroradius r_g is defined as the ratio between the magnetic rigidity R and the magnetic field strength $|\vec{B}|$ where magnetic rigidity describes the resistance of a charged particle q to change its direction due to the magnetic field (Kallenrode, 2004). The gyroradius is determined from the following equation:

$$r_g = \frac{m_0\gamma v_\perp}{|q||\vec{B}|} = \frac{m_0\gamma v\sin\alpha}{|q||\vec{B}|} = \frac{p\sin\alpha}{|q||\vec{B}|} = \frac{R\sin\alpha}{|\vec{B}|} \tag{2.4}$$

with

$$\gamma = \frac{1}{\sqrt{1-\beta^2}} \quad \text{and} \quad \beta = \frac{v}{c} \tag{2.5}$$

where

m_0	=	rest mass of the particle
c	=	speed of light
v	=	velocity of the particle
q	=	charge of the particle
$\vec{B}$	=	uniform magnetic field
R	=	p/q is the magnetic rigidity of the particle
p	=	particle momentum

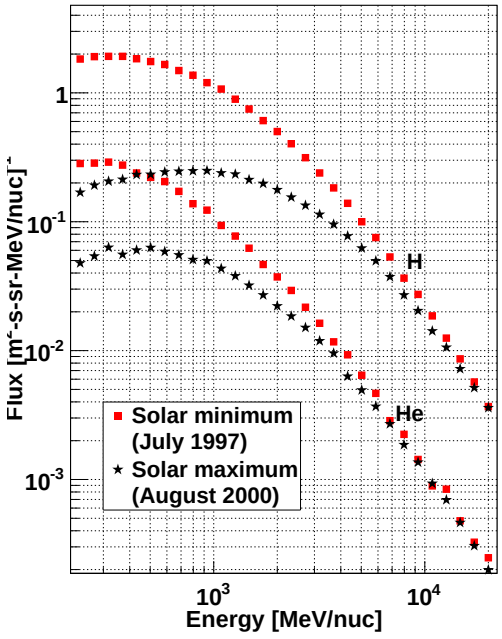

Figure 2.2: Galactic cosmic ray spectra of hydrogen and helium nuclei measured by BESS during different solar activity periods (Shikaze et al., 2007).

The magnetic field inside the heliosphere is inhomogeneous. Thus the motion of the particle has to be characterized by the curvature of its path (also called as the local gyration radius) imposed by the local magnetic field which varies along the trajectory of the particle. The same formula (equation 2.4) can be applied for this magnetic configuration as well.

With the magnetic rigidity in the numerator of equation 2.4 it is evident that low-energy particles follow trajectories of stronger curvature (smaller gyroradius) than high-energy particles and are therefore more easily deflected than the latter. E.g., for 1 GeV, 10 GeV and 220 GeV protons the gyroradius in near-Earth space is 178 Earth-radii, 1140 Earth-radii and 23,450 Earth radii (1 AU) respectively when $|\vec{B}| = 5$ nT during typical solar minimum periods (Caballero-Lopez et al., 2004b).

As the solar activity increases, the sun floods the heliosphere with larger quantities of magnetic plasma bubbles causing a higher number of irregularities and therefore localized inhomogeneity in the magnetic field strength. In regions of strong HMF the local radius of particle trajectories becomes small (equation 2.4). The GCR particles are more deviated and scattered, and do not penetrate as easily in the inner regions of the heliosphere.

The temporal variability of GCR intensity has been extensively studied since 1951 using ground-based instruments called Neutron Monitors (see Simpson (2000)). Neutron monitors (NM) measure the secondary by-products, mainly neutrons and protons (Clem and Dorman, 2000), of the interactions between primary GCR and the particles constituting the Earth's atmosphere. Therefore, NM counts give information regarding the GCR intensity. Figure 2.3 shows monthly sunspot numbers over time, indicating the quasi-periodic change in solar activity, and the NM data collected at various ground stations over the same time period. The figure clearly shows an anti-correlation of the GCR intensity with the 11-year sunspot cycle (discovered by Schwabe 1844) and the 22-year solar magnetic cycle or the Hale cycle first discovered by Hale et al. (1919). The alternating peak-plateau shaped GCR maxima is caused by the change in solar magnetic polarity which affects the drift directions of positively charged GCR nuclei in the heliosphere (Jokipii and Kota 1983).

Elevated GCR intensity during the last solar minimum between the solar cycles 23 and 24 (2009-2010) in comparison with the previous minima can be seen in the NM data by the Oulu and Mc Murdo stations in Figure 2.3b. The cause of this is associated with the prolonged low solar activity leading to reduced HMF strength and the level of turbulence (Heber et al. 2009; Mewaldt et al. 2010; Bazilevskaya et al. 2013). Unlike the data from these two NM station, the data from the Kiel NM shows no exceptional increase during this time period which is associated with the so-called vertical cut-off rigidity R_c at its geographical location and is explained in Section 2.1.3.

Note: During the PhD work, the radiation exposure from GCR over the last four

decades was calculated and the period from 2009-2010 was especially investigated to see the impact of increased GCR particle fluxes on the radiation exposure in comparison with the previous solar minima (Mrigakshi et al. 2013b, Section 4.5). The results indeed show an increase in the dose rates during the end of 2009 relative to the peak exposure in the 1997 solar minimum period.

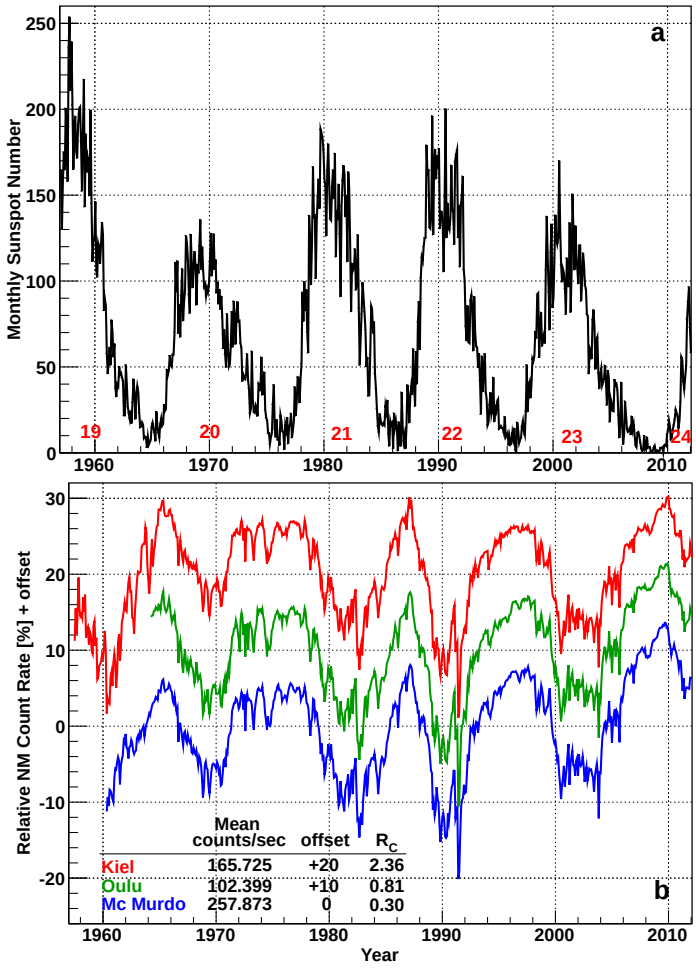

Figure 2.3: Variation of sunspot numbers[4] shown in Figure 2.3a with the solar cycle numbers indicated in red. Figure 2.3b shows the neutron monitor count rates (10-day averages) relative to the mean values over time. The mean count rate (counts/second) and the vertical cut-off rigidity R_c (explained in Section 2.1.3) for each NM station are also indicated. The offset values are added to the relative NM count rates to clearly distinguish the separate graphs. The neutron monitor data collected by Kiel and Mc Murdo stations are from the Neutron Monitor Database (NMBD)[5]. The data from the Oulu station was acquired from their website[6].

[4]http://sidc.oma.be/sunspot-data/
[5]http://previ.obspm.fr/hidden3/search.php
[6]http://cosmicrays.oulu.fi/

Description of GCR energy spectra

The spatial and temporal evolution of the GCR distribution function can be described by the transport theory introduced by Parker (1965) via the transport equation, also known as the Parker equation. It considers the underlying physical processes affecting the transport of GCR inside the heliosphere such as diffusion of the particles in the irregular magnetic fields, convection with solar wind, adiabatic energy changes related to the solar wind expansion in the heliosphere and drifts that depend on the polarity of the magnetic field (see Potgieter 2011 for detailed description of the transport equation).

The transport equation is usually approximated for practical applications due to the fact that solving the complete equation is complex (Kota and Jokipii, 1991). Gleeson and Axford (1968) suggested a simplification of the transport equation known as the Force-Field approximation with assumptions such as spherical symmetry and steady state of the heliosphere, negligible adiabatic energy loss and no drifts(see Caballero-Lopez and Moraal 2004a). The analytical solution of this approximation gives the differential energy spectrum, J_i of GCR particle type i at 1 AU, as a function of its kinetic energy and the so-called solar modulation parameter Φ for a certain point. It is given by

$$J_i(T,\varphi) = J_{LIS,i}(T+\Phi)\frac{(T)(T+2T_R)}{(T+\Phi)(T+\Phi+2T_R)} \tag{2.6}$$

where,

Φ	=	$\lvert\frac{Ze}{A}\cdot\varphi\rvert$ is the modulation function
Z	=	atomic number
A	=	mass number
e	=	elementary charge
φ	=	modulation parameter
T	=	particle's kinetic energy
T_R	=	rest energy of proton
J_{LIS}	=	Local Interstellar Spectrum of the particle flux

The modulation parameter φ is the only time-variable factor in the formula and indicates the strength of the solar modulation. The value of the modulation parameter φ lies generally between 300 MV during solar minimum when the solar modulation of the GCR is well above 1000 MV during solar maximum periods when the modulation is the strongest. Equation 2.6 also indicates that the calculation of the GCR fluxes at 1 AU need the description of the flux of the LIS, J_{LIS}, and therefore is an

important parameter for the description of GCR modulation. However, the current knowledge of the J_{LIS} is rather poor due to the lack of direct measurements and thus also needs to be modelled. The use of various models of the J_{LIS} induce slight differences in the calculated values of the modulation parameter as shown by Usoskin et al. (2005), Herbst et al. (2010) and Herbst et al. (2012). These differences are subsequently carried forward into the calculation of the GCR spectra close to Earth. Even though the Force-Field approximation models an incomplete modulation scenario in the heliosphere by neglecting important physical processes, it is still able to describe the energy spectrum of GCR particles close to the Earth with reasonable precision for particle energies above ∼100 MeV/nuc (Caballero-Lopez and Moraal 2004a; Usoskin, 2005; Fisk, 1971). The model is, therefore, often used for various applications including numerical estimation of GCR exposure in space close to Earth which requires the description of the GCR particle fluxes over an energy range from 10 MeV/nuc to 100 GeV/nuc. It has been shown in Section 5.2 that nearly the entire GCR exposure (>98% of the total dose) is caused by particles with energies between 100 MeV/nuc to 100 GeV/nuc for locations both inside and outside the Earth's magnetosphere (∼1 AU from the Sun), thus making it an appropriate choice for GCR dose calculations. Widely used GCR models for this purpose including some that are based on the Force-Field approximation have been inter-compared and tested against GCR measurements in Mrigakshi et al. (2012) (see Section 4.2). It is nevertheless stressed that due to the assumptions made in the Force-Field model, it has limitations for theoretical applications such as to understand the role of drifts in modulation of GCR and the effect on GCR propagation during high solar activity periods.

2.1.3 Geomagnetic Modulation

Similar to the heliosphere, the Earth's magnetosphere is a region around our planet formed by the Earth's magnetic field. It is continuously reshaped by the interaction of the Earth's magnetic field with the solar wind. Close to the surface of the Earth, the magnetic field can be approximated as a dipole with the dipole axis inclined by 11.3° with respect to the Earth's rotation axis. At higher altitudes the dipole-like field gets distorted due to electric currents created by the ionospheric plasma and the energetic particles from the Sun and GCR trapped in the Earth's magnetic field (Van-Allen radiation belts). The outer structure is strongly modified by the solar wind.

The motion of charged particles in proximity to Earth is influenced by the Lorentz

force exerted by the Earth's magnetic field. As shown in equation 2.4, charged particles in a magnetic field can be characterized by their magnetic rigidity for their motion (gyroradius). From this equation it follows that CR particles with high rigidity (or energy) above a certain threshold penetrate into the magnetosphere with nearly straight trajectories, particles with intermediate rigidity will penetrate through with a curved path and the low-rigidity particles will get strongly deflected such that they may even bounce back towards their original incoming direction. This is an important reason why not all GCR particles which penetrate deep inside the heliosphere reach the top of the Earth's atmosphere. The intensity of GCR particles below certain energies, corresponding to the particle rigidity is reduced.

The level of geomagnetic shielding for a given location inside the magnetosphere is often quantified by the so-called effective vertical cut-off rigidity R_c (Cooke et al., 1991). In the text hereafter, it is referred to simply as cut-off rigidity. The cut-off rigidity lies in the rigidity interval between the value below which (lower threshold) no particle arrives from the vertical direction at the location of interest, and the highest rigidity value above which (upper threshold) all particles arrive in vertical direction. This quantity is often used to calculate the lower energy threshold for a particle, independent of the particle type, to reach the top of the atmosphere. Thereby the cut-off rigidity strongly depends on the geomagnetic latitudes as the magnetic field strength varies from equator to the poles, the altitude of the observation point and the geomagnetic conditions at the observation time.

Figure 2.4 shows the cut-off rigidity contours on the geographical latitude-longitude grid calculated for an altitude of 20 km in January 2005 (intermediate solar activity period) by Matthiä (2009). The lowest R_c values ($R_c \approx 0\ GV$) correspond to the region around the geomagnetic poles and the highest values ($R_c \approx 17\ GV$) seen around southern Asia correspond to the region around the geomagnetic equator. The minimum energy that a CR particle must have in order to reach an altitude of 20 km over this region, based on the cut-off rigidity, can be calculated and is ∼16 GeV for H nuclei and ∼7.6 GeV/nuc for He nuclei. The differences in the cut-off rigidity contours at the same latitudes especially around the geographical equator is due to the tilt in the magnetic dipole axis relative to the rotation axis of the Earth.

When studying the transmission of the charged particles and interpreting their measurements, it is important to carefully consider the rigidity interval between the

[7] http://visibleearth.nasa.gov

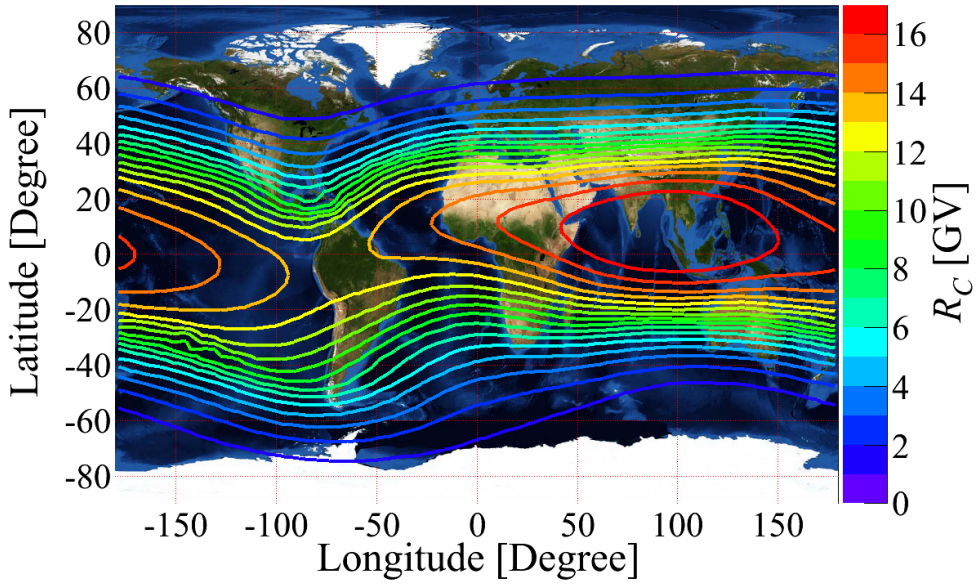

Figure 2.4: World map of the vertical cut-off rigidities R_c at an altitude of 20 km for epoch 2005 calculated and provided by Dr. Daniel Matthiä (Matthiä, 2009) using the PLANETOCOSMICS code (Desorgher et al., 2005). World map credit: NASA Goddard Space Flight Center[7].

upper and lower rigidity thresholds (mentioned above) for a given location and time (Störmer, 1930). The trajectories of particles are not only dependent on the rigidity and location but are also dependent on their angle of arrival with respect to the magnetic field lines i.e. the pitch angle α defined in equation 2.3. From equations 2.3 and 2.4 (defining gyroradius), it can be deduced that as the Lorentz force reduces with decreasing pitch angle α, the gyroradius of a particle also becomes smaller and the particle is less deflected by the magnetic field. Therefore, particles with rigidities between the lower cut-off and upper cut-off rigidity interval may experience large and frequent variation of pitch angle in the magnetic field of the Earth. This can result in complex trajectories when these particles encounter the magnetic field which changes spatially with latitude and longitude. As a consequence, the particles travel to completely different locations in comparison to their original point of incidence inside the magnetosphere. Some particles may eventually even reach the atmosphere at higher latitudes and some may get trapped in the magnetic cavities such as the Van Allen belts. The low-rigidity (or low-energy) particles arriving parallel to the magnetic field can easily enter the atmosphere at magnetic poles, where the field lines

are vertical.

Another factor influencing the GCR fluxes near-Earth is the altitude dependent factor accounting for the obstruction of the GCR particles caused by the presence of the solid Earth (Vallarta, 1948). For an altitude of the International Space Station (ISS) at 350 km, the solid angle occulted by the Earth (solid angle of a cone) is about $0.34 * 4\pi$.

In Figure 2.3 (Section 2.1.2), the difference in the relative NM count rates measured by various NM stations can be observed e.g. in the years between 2009 and 2010. Unlike the Mc Murdo and the Oulu NM, the NM at Kiel did not record any unusual increase in the NM count rates during this time period. The observation can be explained by the greater geomagnetic shielding effect on GCR particles arriving above Kiel. As indicated in Figure 2.3, the cut-off rigidity for Kiel (54.3°N, 10.1°E) is $R_c = 2.36\ GV$ which is less than for Mc Murdo (77.9°S, 166.6°E), $R_c = 0.3\ GV$ and for Oulu NM stations (65.05°N, 25.47°E), $R_c = 0.81\ GV$. Due to the higher R_c at Kiel, particles with energies below a certain threshold are unable to penetrate into the atmosphere above it. Thus, in contrast to Mc Murdo and Oulu NM, there is no contribution of these low-energy particles to the NM count rate measured at Kiel.

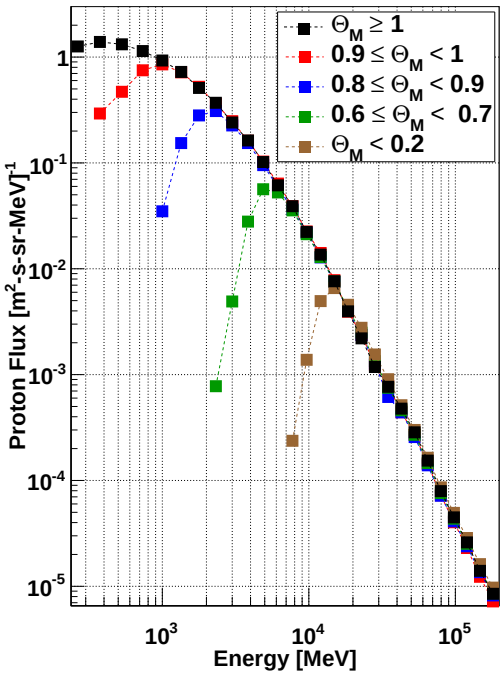

Figure 2.5: Downward primary GCR H spectra at different geomagnetic latitudes Θ_M (radians) measured by the AMS-01 experiment in June 1998 during the STS-91 flight with an orbital inclination of 51.7° and an altitude between 320 and 390 km (Aguilar et al., 2002).

Measurements from various space missions e.g. PAMELA (see Figure 5 in Casolino et al. 2009) and AMS-01 (see Figure 4.9 a-c in Aguilar et al. 2002) also reveal the geomagnetic modulation of the GCR particle fluxes wherein the decrease in the GCR intensity from higher geomagnetic latitudes towards the geomagnetic equator can be seen. This effect is illustrated in Figure 2.5, showing the results of the AMS-01 measurements provided in Aguilar et al. (2002). The figure shows primary spectra of the proton flux directed towards nadir at various geomagnetic latitude intervals measured by the AMS-01 instrument on-board the space-shuttle (STS-91) orbiting at an altitude between 320 and 390 km with an inclination of 51.7°. The geomagnetic modulation leads to reduced particle intensities below 10 GeV/nuc and the drop in the proton fluxes with decreasing latitude can be seen. Particles with energies above 10 GeV/nuc are not affected by the Earth's magnetic field and the spectra are similar to the proton spectra at 1 AU outside the Earth's magnetosphere.

The GCR flux variation caused by the geomagnetic shielding also affects the radiation exposure. The measurements made by the DOSIS experiment (Burmeister et al., 2012) on-board the Columbus module show that the exposure from GCR in terms of absorbed dose (defined in Section 2.3.1) ranges from about 2 μGy/h - 17 μGy/h (Labrenz, 2013).

From the topics discussed in this section, it is clear that the GCR particle fluxes vary significantly with time and location inside the heliosphere. The GCR particles entering the heliosphere are modulated by the sun resulting in the reduction of their total fluxes and energy spectra over time. Additionally, fluxes are further reduced when particles travel from outside to inside of the Earth's magnetosphere.
Particles that are able to penetrate through the magnetosphere reach the atmosphere and interact with its constituting atoms and molecules. As a result secondary particles are produced which in fact are a source of radiation exposure at aviation altitudes (ICRU, 2010). As mentioned above, these particles can be detected by instruments (Grieder, 2001) such as the Neutron Monitors and are used as an index for the GCR intensity as shown in Figure 2.3.

During the PhD work, the influence on the radiation exposure by the varying GCR fluxes at location outside the Earth's magnetosphere at 1 AU and inside the magnetosphere at ISS orbit was studied. Additionally, the temporal change associated with the quasi-periodic GCR intensity was also investigated. The results can be found in Mrigakshi et al. 2013a (see Section 4.3), Mrigakshi et al. 2013b (see Section 4.5) and Chapter 5.

2.2 Radiation-Matter Interaction

An understanding of the interaction processes between radiation and the traversed medium is necessary for radiation detection, measurement, shielding studies, radiation transport calculations and the assessment of the radiation-related health risks.
When GCRs traverse through matter, they interact with the constituting atoms and molecules through electromagnetic and nuclear forces. The interactions between GCR and a target, e.g. spacecraft, produces a large variety of secondary particles (e.g. gamma radiation, electrons, muons, neutrons, pions and secondary protons and heavy ions). Neutrons and secondary ions are especially crucial for space applications since they can deposit large energies into the medium. Other secondary particles like electrons and photons contribute only a small fraction to the total exposure; however, since these can travel to greater distances than heavier particles and deposit energy there, they can be of importance in radiation protection in space.
In this section some of the relevant radiation-matter interaction processes for space radiation studies are discussed. For further reading see, e.g., Zeitlin (2012), NCRP (2006) and Cucinotta et al. (1996).

2.2.1 Electromagnetic Interactions

While traversing through matter charged particles exert long-range Coulomb forces on the electrons of the target atoms along their path and undergo inelastic scattering thereby suffering energy loss as they penetrate deeper inside. The energy lost is transferred to the orbital electrons, causing ionization or excitation of the target atoms. The laws of conservation of both energy and momentum are important for the formulation of the energy losses of radiation in matter. By following these laws, the maximum energy transfer, T_{max}, that occurs during a single head-on collision between the heavy ion projectile of mass M with velocity v and the orbital electrons of mass m_e at rest can be deduced. The relativistic expression for maximum energy transfer is (Turner, 2007)

$$T_{max} = \frac{2\gamma^2 m_e v^2}{1 + 2\gamma m_e/M + m_e^2/M^2} \tag{2.7}$$

with

$$\gamma = \frac{1}{\sqrt{1-\beta^2}} \quad \text{and} \quad \beta = \frac{v}{c} \tag{2.8}$$

If $M >> m_e$ then equation 2.7 reduces to

$$T_{max} \approx 2\gamma^2 m_e v^2 \approx 2\gamma^2 m_e c^2 \beta^2 \tag{2.9}$$

From equation 2.9 it can be deduced that when the projectile protons or heavy ions i interact with atomic electrons, they lose a very small fraction of their energy during a head-on single collision and are only slightly deflected. This kind of scattering is also known as Coulomb scattering. Thus they travel mostly in nearly straight lines continuously transferring a small fraction of their energy during each collision (cross section $\sigma_{i,coulomb} \approx 10^{-16}$ cm^2, NCRP 2002) with the electrons on their path. Occasionally these ions can get large-angle deflections when undergoing elastic collisions with atomic nuclei ($\sigma_{i,elastic} \approx 10^{-19}$ cm^2, NCRP 2002) and transfer energy to them leading them to recoil.
Furthermore, sometimes the orbital electrons may gain sufficient energy from the projectile so that they may leave the atom and induce secondary ionization of neighbouring atoms. Such electrons are often called δ-electrons or δ-rays. The range of δ-rays is small compared to the charged ions so that ionizations occur close to the primary ion track. However, sometimes they can be long-ranged and deposit energy at considerable distance from the primary ion track (see Kobetich and Katz 1968 for details).

Stopping Power

A quantity described as the stopping power of a medium for a charged particle is used to determine the average energy loss per unit length in the medium and is of fundamental importance in radiation dosimetry (Leo, 1994). It is calculated as a product of the probability per unit path length, usually expressed in cm^{-1} of a charged particle to have an interaction and the average energy loss per collision usually expressed in MeV (Turner, 2007). The stopping power is thus usually given in $MeVcm^{-1}$. There are different kinds of stopping powers depending on the type of energy loss such as the collision stopping power (also known as electronic stopping power) and radiation stopping power. The former is associated with the inelastic collisions of the projectile ions with electrons which can lead to, e.g., ionization and excitation of target atoms and molecules. The latter is associated with the emission of bremsstrahlung photons when typically electrons, e.g., δ-rays are decelerated by sharp deflections caused by their interaction with atomic nuclei of the medium. Another type of stopping power is called the nuclear stopping power which is associated with the elastic collisions between the projectile ion and nuclei of the medium. It is only important for low energy

heavy particles. When the projectile energy becomes higher, nuclear stopping is not important, and can be neglected in the calculations (Schiavi, 2003). The description of the collision stopping power is particularly important for the transport of ions in matter as they suffer energy losses mainly due to ionization as stated above. The expression for the collision stopping power of a uniform medium for relativistic heavy charged particles, $-dE/dx$, was derived from the work of Bohr (1913) and (1915), Bethe (1932), Bloch (1933) and is given by (Leo, 1994)

$$-\frac{dE}{dx} = 2\pi N_{\mathrm{a}} r_{\mathrm{e}}^2 m_{\mathrm{e}} c^2 \rho \frac{Z}{A} \frac{z^2}{\beta^2} \left[\ln\left(\frac{2m_{\mathrm{e}}\gamma^2 v^2 T_{\max}}{I^2} \right) - 2\beta^2 \right] \tag{2.10}$$

where

N_{a}	Avogadro's number	r_{e}	classical radius of electron
z	charge of incoming particle	m_{e}	mass of electron
Z	charge number of medium	A	mass number of medium
ρ	density of medium	I	mean excitation potential of medium

$T_{\max}$, γ, β, v and c are the same as in equation 2.7

This formula is called the Bethe-Bloch formula (Leo, 1994) and is the basic expression for the energy loss calculations. For a complete description, certain correction factors associated with other processes that contribute to the energy loss of heavy charged particles have to be added in the equation 2.10. For example, the equation presented above has to be modified for energetic particles (energies in the GeV region and above). Other important corrections include the so-called shell and density corrections. The shell correction accounts for the non-participation of the inner-shell electrons during ionization and excitation processes caused by low energy projectiles. The density correction considers the polarization of the atoms along the path of energetic projectiles wherein the distant electrons are shielded from the electric field resulting in lower contribution of the distant electrons to the total energy loss. See Leo (1994) for details regarding these correction factors and others that are not introduced here.

From the formula it is clear that the stopping power is dependent on certain properties of both the incident ion type, its energy and also on the target material. When particles have non-relativistic energy, their energy loss is dominated by $1/\beta^2$ term in equation 2.10. It follows from the equation that with decreasing velocity and energy of the projectile the energy loss increases. As a result, a characteristic maximum in the energy deposition with depth curve is observed at the end of their path in the

medium and is called Bragg-peak. Another factor to note is that the energy loss of a particle is proportional to the square of their charge z^2. This means that heavier ions lose energy in a given medium at a faster rate than the lighter ones which further indicates that they have shorter range (penetration depth) as well. The equation also indicates the influence of the medium traversed on the energy loss of heavy ions. The energy loss is proportional to Z/A which means that materials having high charge-to-mass ratio, e.g. hydrogen in comparison with aluminium, will lead to greater energy loss of the projectiles.

Other processes leading to energy loss due to electromagnetic interactions are pair-production when high-energy particles on traversing through the Coulomb field of the target nucleus produce electron-positron pairs, and interaction of secondary photons with nuclei such as photoelectric effect and Compton scattering. In this chapter the interactions of photons with matter are not discussed. However, it has to be noted that photons, produced as secondaries by the incident heavy ions as in the case of GCRs, can be highly penetrating in a medium and can lead to energy deposition at a distance from their original locations. Thus, photons were also treated in the radiation transport calculations performed in this work.

2.2.2 Nuclear Interactions

Unlike the quasi-continuous energy loss through electromagnetic interactions of a charged particle along its track, the energy loss via strong interactions occur rather less frequently. This can be explained by the lower cross section of the strong interaction , i.e., $\sigma_{i,nuclear} \approx 10^{-24}$ cm^2, related to the size of the nucleus (radius $\approx 10^{-15}$ m) in comparison with the cross section for Coulomb scattering, $\sigma_{i,coulomb} \approx 10^{-16}$ cm^2 (radius of an atom $\approx 10^{-10}$ m). Additionally, the charged particles feel the repulsion from the nucleus thereby also leading to reduced probability for such interactions to occur. But when the energy of the ions are greater than what is required to overcome this repulsion, which is called Coulomb barrier, then these interactions can take place.

Nuclear interactions such as inelastic nucleus-nucleus or nucleon-nucleus interactions are dominant for heavy ions with energies above 100 MeV/nuc (Hüfner, 1985). These processes therefore are highly relevant for GCR nuclei interactions with the spacecraft

and tissue. An important process at high energies called fragmentation can occur which leads to the production of secondary particles which further interact with the medium and lose energy. In such a process either the projectile or the target nucleus fragments (or disintegrates) into smaller nuclei and some nucleons (Hüfner, 1985). While the projectile fragments mostly preserve the velocity of the incident particle, the target fragments emitted are slow relative to the incident particle (Zeitlin 2012, NCRP 2006, Hüfner 1985).

The secondary neutrons are of great importance as they, being electrically neutral particles, are extremely penetrating and deposit large amounts of energy indirectly through the production of secondary charged particles due to nuclear interactions.
If neutrons are produced with energies below ∼20 MeV, they may get absorbed by the nucleus leading to reactions such as the production of deuterium when a neutron is captured by a hydrogen atom ($^1_1$H(n,γ)$^2_1$H reaction). This process, called radiative neutron capture, is accompanied by the emission of gamma rays which can in turn be absorbed by an atomic nucleus to knock out a nucleon. Other neutron capture processes can occur which may result in the emission of charged particles such as protons and alpha particles or induce nuclear fission (Turner, 2007).
Another process that is associated with neutrons is evaporation which occurs when target nucleus may fragment due to high-energy neutrons (>100 MeV) which can lead them or the fragment nuclei to be in an excited state and subsequently decay while emitting nucleons including neutrons (Zeitlin, 2012).

The fragmentation process during GCR interactions leads to a large production of pions. Some of these may decay or travel further to interact with target atoms and produce more pions, secondary nucleons, and photons. Thus pions also contribute to a significant amount of radiation exposure (Aghara et al., 2009).

The nuclear interactions of nuclei, especially heavy ions, are not yet described by any fundamental theory as these are not fully understood and the cross-sections are calculated using semi-empirical models in the transport codes (Zeitlin, 2012).
NCRP (2006) and Zeitlin (2012) give a detailed description of nuclear interactions especially important to space radiation studies. For fragmentation process in particular, see Hüfner (1985).

Hadronic and Electromagnetic Showers

The cascade of secondary particle production as a result of interactions between high-energy particles with dense matter is often termed a shower. Thus, the inter-

action of GCR particles with spacecraft shielding and Earth's atmosphere mostly results in such showers. Hadronic showers are usually produced by high-energy nuclei, pions or atomic nuclei and can lead to electromagnetic showers due to the production of charged particles in the process. Electromagnetic showers are triggered by high-energy electrons via bremsstrahlung, or photons via pair-production which produce an electron-positron pair. Positrons may again recombine with electrons to emit more photons. This process continues to produce low energy photons and electrons which are ultimately absorbed by the atoms.

The transport calculations concerning GCR interactions with matter are thus required to treat the propagation of these showers by including all physical processes as described above in Section 2.2.1 and 2.2.2.

2.3 Dosimetric Concepts

The health risk arising from exposure to ionizing radiation is quantified by determining dose quantities that are related to the biological effects of the radiation. As mentioned earlier, the ICRP, ICRU and NCRP work towards developing and recommending the dose quantities and units relevant for radiation protection. These quantities are defined below in Section 2.3.1 and are based on ICRP reports 60 (ICRP, 1991) and 103 (ICRP, 2007), ICRU report 85 (ICRU, 2011), and NCRP reports 132 (NCRP, 2000) and 142 (NCRP, 2002). Additionally, the problem of GCR for manned missions to space is also discussed in Section 2.3.2.

2.3.1 Dose quantities

Absorbed Dose

The absorbed dose D is a fundamental dose quantity in radiation protection which gives a measure of the mean energy $d\bar{\epsilon}$ imparted by ionizing radiation in a mass element dm of the target material:

$$D = \frac{d\bar{\epsilon}}{dm} \tag{2.11}$$

The unit of absorbed dose is J/kg but is expressed with a special name gray (Gy) where 1 Gy is equal to 1 J/kg. For the purpose of radiation protection it is required to calculate the **mean absorbed dose**, D_T, in an organ or tissue which is defined as the total energy imparted divided by the mass of the tissue or organ.

The level of biological damage varies with several factors, mainly the radiation type, amount and energy. The biological response to charged particles, especially, mainly depends on their charge z and velocity v. This can be explained, to an extent, by understanding the cluster-damage wherein a population of cells can experience high density damage. Cluster-damage is particularly crucial when it occurs in DNA as explained in the introduction of this chapter. δ-rays (or secondary electrons, explained in section 2.2.1) are a primary cause of clustering of energy deposition (NCRP, 2006). The number of δ-rays produced per unit of charged particle track depends on the stopping power $-dE/dx \propto z^2/\beta^2$ (equation 2.10). Higher z particles produce a larger number of ionization events which yield a large number of electrons. These electrons may posses enough energy to in fact produce even more secondary

electrons. The range of the electrons and their energy depends on the velocity of the primary particle. Most of the δ-rays however deposit energies within a short distance from the primary particle track leading to small clusters along the track on the micrometer or smaller scale (NCRP, 2006).
In addition to the charge and velocity of the primary particle, the level of biological damage also depends on the sensitivity of the biological material to the radiation it is exposed to, and the duration of irradiation.

Linear Energy Transfer and Quality Factor

As mentioned above, the amount of energy deposited (given by absorbed dose), the biological effectiveness of the radiation, or the extent of damage it causes depends on how densely ionizing the radiation is along its track through an organ or tissue (NCRP 2006, ICRP 2007, Cucinotta and Durante 2009). The ionizing density as mentioned above depends on the stopping power, therefore a quantity closely related to it called **unrestricted Linear Energy Transfer** (LET) is additionally used for the dose assessment. It is given as the amount of energy deposited by charged particles, dE, divided by the distance, dl, traversed.

$$LET = \frac{dE}{dl} \tag{2.12}$$

LET is equivalent to the collision stopping power (Section 2.2.1). Low-LET radiation results in diffusely distributed damages in a cell which can easily be repaired in contrast to clustered or localized multiple DNA damage caused by high-LET radiation with densely ionizing tracks (Cucinotta and Durante 2009 and see Figure 4-3 therein for a visual illustration). An example of clustered DNA damage is a double strand break wherein both strands in the double helix are damaged which is difficult or sometimes impossible to repair.

LET is thus a physical quantity which can be related with the biological effectiveness of radiation of different types and energy (NCRP 2000, NCRP 2002) . The absorbed dose can be weighted with an LET dependent factor to quantitatively reflect the extent of biological damage.

The **quality factor**, Q, is specified for a point in the tissue and is given as a function of LET of charged particles in water given in $keV\mu\mathrm{m}^{-1}$ as shown below. It is a dimensionless quantity defined by ICRP (2007):

$$Q(LET) = \begin{cases} 1 & , \quad LET < 10\ keV\mu\mathrm{m}^{-1} \\ 0.32 \cdot LET - 2.2 & , \quad 10\ keV\mu\mathrm{m}^{-1} \leq LET \leq 100\ keV\mu\mathrm{m}^{-1} \\ 300/\sqrt{LET} & , \quad LET > 100\ keV\mu\mathrm{m}^{-1} \end{cases} \tag{2.13}$$

The equation illustrates how the biological effectiveness (for a given absorbed dose) changes with LET and is based on available experimental data for cancer induction on various biological targets. It can be seen that the biological effectiveness of the radiaion increases with increasing LET from 10 keV/μm up to 100 keV/μm after which it falls depicting cell-death. As a result there is a reduced probability of mutations in the DNA that can eventually lead to cancer.

Dose Equivalent

The mean absorbed dose in a tissue or an organ can be weighted with the quality factor to get a measure of the biological damage and the resulting quantity is called dose equivalent H (NCRP, 2000). It is thus given by

$$H = D \cdot Q \tag{2.14}$$

The unit of dose equivalent is J/kg as well, however to differentiate between the two dose quantities a special name for the unit called sievert (Sv) is used.

Effective Dose

For individual radiation protection monitoring of a person, a quantity called effective dose is used. As recommended by the NCRP (2000) and NCRP (2002), this quantity E can be calculated as the sum of dose equivalent (called organ dose equivalent) H_T in the tissues and organs, considered sensitive to the induction of stochastic effects, multiplied by the corresponding tissue weighting factors w_T. It is given by

$$E = \sum_T w_T \cdot H_T \tag{2.15}$$

The effective dose is also given in the unit sievert (Sv) as the tissue weighting factors are dimensionless. These factors represent the relative contribution of individual tissues or organs to the total health detriment (stochastic) when the whole body is irradiated uniformly. Stochastic effect implies the statistical nature of the manifestation of biological effects such as cancer which do not show existence of an exposure threshold for these types of effects to occur. Deterministic effects on the other hand are associated with high doses in a short period of time resulting in the death of a

population of cells. Examples of such an effect include cataract or infertility. The accumulated effective dose received by an astronaut during the time spent in space currently used for the estimation of the cancer risk, but it is emphasized that the risk also depends on gender, age, genetic predisposition as well as smoking habits etc. See NCRP (2000) and NCRP (2000) for more details about these quantities and dose limits.
In this work, all these dose quantities to estimate the exposure from GCR have been estimated and are presented in Mrigakshi et al. 2013a (see Chapter 4.3), Mrigakshi et al. 2013b (see Chapter 4.5), Chapter 5 and Appendix C.

2.3.2 GCR Hazard in Space

By looking at the composition of the GCR (Section 2.1.1 or black line in Figure 2.6), it may appear that the consideration of hydrogen and helium nuclei alone might be sufficient for the GCR dose assessment as these particles comprise ∼98% of the total nucleonic component of GCR. However, heavy ions contribute significantly to the radiation exposure as the extent of the biological damage is related to a particle's energy loss, which in turn is proportional to the square of charge of the particle (equation 2.10) within a material. By accounting for these facts, the assessment of the radiation exposure from GCR heavy nuclei becomes important for radiation protection in space.

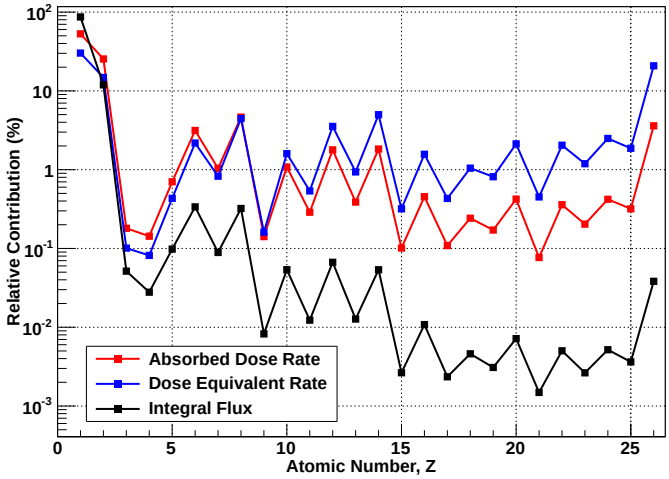

Figure 2.6: Relative contribution of GCR nuclei to total absorbed dose rate (in red), dose equivalent rates (in blue) and flux integrated over energy (in black).

Figure 2.6 shows the relative contribution of GCR particles between 1≤z≤26 with

energies ranging from 10 MeV/nuc and 100 GeV/nuc to total particle fluxes integrated over energy (in black), absorbed dose rates (dD/dt, in red) and dose equivalent rates (dH/dt, in blue). GCR nuclei with z>26 are usually ignored as they are much less abundant and contribute insignificant doses to the total exposure. The values have been estimated by computer simulations (see Section 3 for the calculation method) for an unshielded water phantom exposed to GCR at ISS orbit during November 2009. The GCR particle spectra were calculated from the model by Matthiä et al. (2013a). The figure illustrates how many of the less abundant nuclei with z>2 such as C, O, Mg, Si and Fe contribute a large fraction to the total GCR exposure after weighting with the absorbed dose and their biological effectiveness quantified by the dose equivalent rate.

Effect of shielding on GCR exposure

There exist are several datasets with measurements of GCR dose rates in Low Earth Orbits (LEO) and show that GCR, in addition to the particles trapped in the radiation belts, are the major source of radiation exposure at LEO. Between July 2009 and July 2012, measurements taken by the DOSIS and DOSIS-3D experiment (Burmeister et al., 2012) in the Columbus module of the International Space Station (ISS) showed a GCR contribution of about 60-70% (150-157 μGy/d) to the total absorbed dose rate and about 70-80% (496 - 517 μSv/d) to the total dose equivalent rate.

When GCR interact with the material constituting the spacecraft, the composition and the energy spectra of the radiation field inside the spacecraft changes which in turn influences the exposure resulting from GCR. The dose rates measured at different location inside the ISS show strong dependence on the amount of shielding. The absorbed dose rates measured inside the Russian Module, Zvezda, between May-December 2009 ranged from 100 μGy/d to 125 μGy/d (Lishnevskii et al. 2012, Semones 2009). However, higher absorbed dose rates of about 158 μGy/d were measured inside the Columbus module between August-September 2009 (Semones, 2009). The mean shielding has been estimated to be about 32 g/cm^2 - 47 g/cm^2 around the detectors considering the entire mass distribution around them in the Zvezda module (Jadrníčková et al., 2009) while in the Columbus module the estimated median shielding was about 100 g/cm^2 (Stoffle et al., 2012).
Besides the measurements on-board the ISS, there have been several measurement campaigns on STS-shuttle missions at similar altitude as that of the ISS. During the STS-89 flight in the solar minimum period of January 1998, variable behaviour

in dose rates with an increase in shielding was observed (Badhwar and Cucinotta, 2000). The measured absorbed dose rates were 175.6, 167.2, 148.5 and 170.5 μGy/d and dose equivalent rates 614.4, 487.6, 617.2 and 540.5 μSv/d behind a shielding of 0, 17.145, 24.003 and 30.861 g/cm^2.

These data sets clearly indicate the complexity of the issue of shielding in radiation protection from GCR in space and show that it is not trivial to predict the variation of the GCR exposure with shielding. See Mrigakshi et al. (2013b) and Matthiä et al. (2013b) for numerically estimated dose values changing with increasing aluminium shielding. Additionally, Figure 5.7 in Chapter 5 shows the variation of calculated absorbed dose rate and dose equivalent rate with different amount of aluminium shielding thicknesses for near-Earth interplanetary space and the ISS orbit.

The effect of shielding on dose can be explained by understanding the interaction processes of GCR with matter and their energy deposition characteristics. Due to their greater LET or stopping power which is proportional to z^2, the heavy ions lose energy faster and are stopped in smaller shielding depths in comparison with lighter ions. This is true for energies below which the nuclear interactions are less likely to occur and the ionization process dominates. However, when the energies are higher, as in the case of GCR, such that nuclear interactions do occur, then there is a production of lighter nuclei which may penetrate deeper inside the shielding. In fact the main mechanism of energy loss of the GCR heavy nuclei is through fragmentation (Zeitlin 2012, 2006) . These fragment nuclei are lighter and have lower LET. Thus even though they are more penetrating and may yield higher absorbed doses, they have lower biological effectiveness yielding lower dose equivalent in comparison with the incident nuclei. On the other hand, if the incident nuclei with high-LET above 100 $keV\mu m^{-1}$ (Section 2.13) interacts with the shielding then the production of lighter nuclei with higher quality factor may result in higher dose equivalent (Zeitlin et al., 2006).

GCR cannot be shielded completely in space but by selecting appropriate materials the shielding can nevertheless be optimized to minimize their contribution to dose. It has been found that materials which increase the probability of nuclear interactions resulting in fragmentation of the heavy GCR nuclei into smaller nuclei can be efficient per unit mass of material in slowing down heavy ions. This suggests that an efficient shielding material should have low mean atomic mass, with as few neutrons as possible (Sihver, 2008) which would in turn also reduce the production of neutrons. Hy-

drogenous materials such as Polyethylene are therefore expected to be more effective in shielding (Sihver, 2008) GCR than the aluminium conventionally used in spacecraft.

3 Numerical Dose Assessment

The determination of the dose quantities (Section 2.3.1) necessary to quantify the radiation related health risks is achieved by performing either measurements utilizing various detector techniques or numerical calculations using computer simulation.

Measurements of radiation exposure in space can be made with passive and active dosimeters. Passive dosimeters measure dose accumulated over a period of time and can only be evaluated on ground. An example of a passive dosimeter is the European Crew Personal Dosimeter (EuCPD) (Straube et al., 2010) which uses thermoluminescence detectors (TLDs) and plastic nuclear track detectors (PNTDs) for the assessment of absorbed dose and LET spectra. Active dosimeters, on the other hand, give a possibility to measure these dose quantities and acquire data over comparatively shorter periods of time, but require a power supply to function. Examples of active dosimeters include DOSTEL (Beaujean et al., 1999) and MDT (Ritter, 2013) which use silicon detectors arranged in a telescope configuration. For a review on dosimetry on-board the ISS see Berger (2008), and Caffrey and Hamby (2011).
In computer simulations, the real scenario is modelled by software. It is a powerful method for understanding complex physical systems to study the influence of various parameters and the behaviour of a system in a short period of time. For space applications, simulations are essential especially for making estimations of the radiation doses that are likely to be received by astronauts during future missions to space and in the case when measurements are not feasible or have not yet been made. They also play an important role in understanding the effect of shielding on the radiation exposure.
However, since the models used in numerical calculations are approximations of the real scenario, uncertainties are introduced in the system and the models must therefore be validated by measurements and carefully selected to produce reliable results for any application. Experimental data are thus extremely important for the validation of the models used in computer simulation.

In this work, numerical calculations were performed to estimate the radiation exposure from GCR. An introduction to the GCR dose calculation methodology, giving an overview of the experimental scenario and the workflow illustrating the various steps at different stages of the calculation process, is presented below in Section 3.1.

3.1 Methodology of GCR dose estimation

In general, simulation of radiation exposure requires a description of the radiation field, material and geometries of the target and its surrounding volumes, the physics of particle interactions and methods to transport the radiation in the target volumes. Therefore to estimate the radiation GCR exposure of humans in space, models describing the GCR energy spectra, the human body, the surrounding shielding and a radiation transport code which simulates the transport and interactions of GCR particles through the simulated targets are required.

The transport code GEANT4 was selected for this purpose and will briefly introduced in Section 3.3. Since the software does not provide GCR spectra, external models were used for their description (see Section 3.2). Several models widely used for space applications were investigated. The procedure developed for the data analysis of the simulation output and for calculating the dose quantities to estimate the GCR exposure is explained in Section 3.4. An overview of the applied methodology is illustrated in Figure 3.1 below.

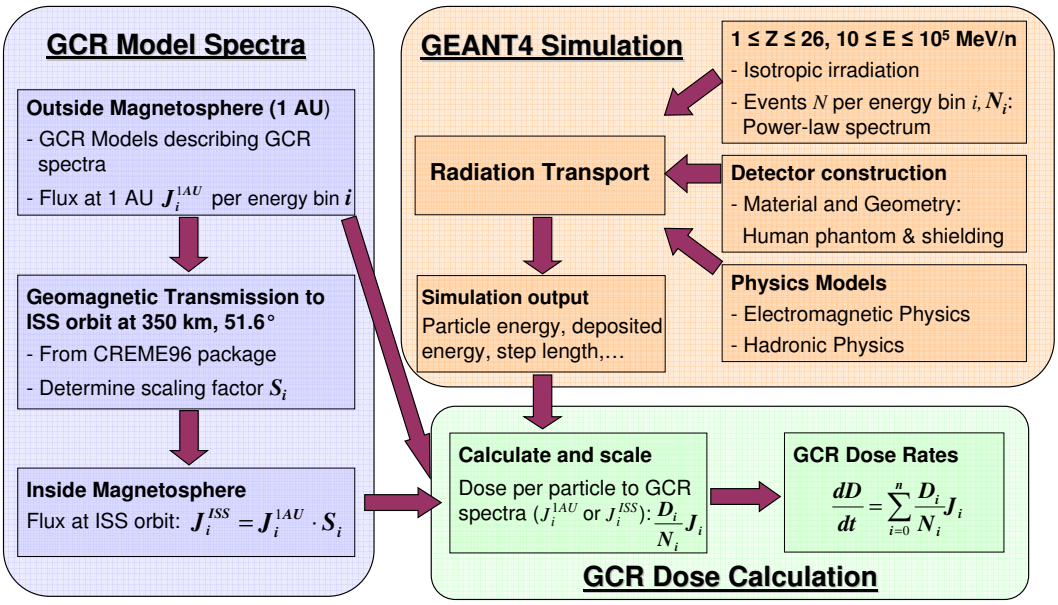

Figure 3.1: Schematic diagram illustrating the procedure applied to estimate the GCR exposure. Note that the absorbed dose, D, shown in the diagram is exemplary of the procedure which was also applied for the dose equivalent H.

The three boxes show the separate stages of the calculation process. The box in yellow shows the simulation stage (see Section 3.3) wherein the isotropic irradiation of the human body by the relevant (for radiation exposure assessment from GCR) particles and energies were simulated. The box in purple shows the stage wherein the GCR energy spectra of all the relevant particles was calculated using GCR models for a location outside the magnetosphere (1 AU) and the ISS orbit after applying a scaling procedure to the spectra at 1 AU (see Section 3.2). The box in green shows the data analysis stage wherein the radiation exposure from GCR was calculated (see Section 3.4) by scaling the dose per particle per energy bin (output of the simulation stage) with the desired GCR energy spectrum (output of the GCR spectra calculation stage).
Each of these stages are explained in detail in the sections below.

3.2 GCR Model Spectra

The assessment of radiation exposure from GCR requires the energy spectra of GCR particles between $1 \leq z \leq 26$ (the relevance of these particles is discussed in Section 2.3.2) with energies from $10 - 10^5$ MeV/nuc. Calculations probing the relevant energy range for GCR dose assessment in Mrigakshi et al. (2013a) (see Section 4.3) have shown that from the entire energy range investigated ($10 - 10^5$ MeV/nuc), particles with $100 - 10^5$ MeV/nuc energy contribute over 98% of the total GCR exposure. Since measurements of the GCR energy spectra are only available over limited energy ranges, particle types, time periods and locations, numerical models are used to derive GCR spectra.

In this work, the GCR exposure was investigated for near-Earth locations outside the magnetosphere as well as for the ISS orbit. The GCR model spectra were thus required for these locations.

3.2.1 Outside magnetosphere near-Earth

Widely used GCR models were investigated in order to find the most accurate model for the GCR dose assessment. These models are Badhwar-O'Neill2010 (O'Neill, 2010), Burger-Usoskin (Usoskin et al., 2005), CREME96 (Tylka et al., 1997), CREME2009

(https://creme.isde.vanderbilt.edu/), SPENVIS/ISO15390 (ISO-15390, 2004) and a new model developed at the German Aerospace Centre (Matthiä et al., 2013a) and the Badhwar-O'Neill2011 model which is an update of the Badhwar-O'Neill2010 model. These models describe the GCR spectra for a location outside the Earth's magnetosphere at a distance of 1 AU from the sun. A brief overview of the properties and capabilities of these GCR models used is shown in Table 3.1.

Most of the models were evaluated for a time period covering the last four decades as presented in Mrigakshi et al. 2012 (see Section 4.2) except for the Badhwar-O'Neill2011 which was tested for a time period between 1997 and 2011 (see Section 5.1). Additionally, the SPENVIS/ISO15390 (ISO-15390, 2004) was examined only for two epochs, i.e., at GCR intensity minimum and maximum periods in 2000 (solar maximum) and 2009 (solar minimum) respectively (see Appendix C). All these models were evaluated by inter-comparing and testing the model spectra of light and heavy nuclei described by each of the models against measurements taken from various high-altitude balloon experiments and space missions (Mrigakshi et al. 2012, Section 5.1, Appendix C).

The models, as they are provided, can generate energy spectra for only one point in time for each run and therefore to get spectra for a large number of points in time, individual batch retrieval scripts for each model needed to be written. These scripts are described in Appendix A.

Table 3.1: An overview of the models describing GCR spectra outside the Earth's magnetosphere at a distance of 1 AU from the sun.

Model	Model type	Modulation function based on	Energy (MeV/nuc)	Particle type (z)	Validity period	Mode of access
CREME96	Semi-empirical based on Nymmik et al. 1992	Monthly-averaged Wolf numbers	$10 - 10^5$	1 - 28	1950-1997	Web interface CREME website†
CREME2009	Semi-empirical based on ISO-15390	Smoothed Wolf numbers	$10 - 10^5$	1 - 28	1760 onwards	Web interface CREME website†
Badhwar-O'Neill2010 (BON2010) and Badhwar-O'Neill2011 (BON2011)	Force-Field approximation	Monthly-averaged sunspot numbers	$1 - 10^6$	1 - 94	1955 onwards	Fortran Source code and DOS binary upon request
Burger-Usoskin	Force-Field approximation	NM count rates	$10 - 10^6$	1, 2	1951 onwards	User-implemented‡
Matthiä/ACE	Semi-empirical based on ISO-15390	ACE/CRIS carbon data	$10 - 10^6$	1 - 28	1997 onwards	JAVA binary‡ upon request
Matthiä/Oulu	Semi-empirical based on ISO-15390	NM count rates	$10 - 10^6$	1 - 28	1964 onwards	JAVA binary‡ upon request
SPENVIS/ISO15390	based on ISO-15390	Smoothed Wolf numbers	$1 - 20 \times 10^3$	1 - 92	1950 onwards	Web interface SPENVIS website*

† https://creme.isde.vanderbilt.edu/ ; ‡ Source code provided by Dr. Daniel Matthiä for this work; * http://www.spenvis.oma.be

3.2.2 Inside magnetosphere at ISS orbit

The GCR particle fluxes inside the Earth's magnetosphere are attenuated as a result of the shielding provided by the Earth's magnetic field as explained in Section 2.1.3. The GCR models therefore have to account for this geomagnetic shielding effect and transport the GCR particles accordingly to a specific orbit. Except for CREME96 and CREME2009, the models introduced in Section 3.2.1 do not provide GCR spectra for LEO. Therefore, a model calculating the attenuation factor based on the cut-off rigidity and accounting for the solid Earth obstruction was required.

For this purpose, the so-called geomagnetic transmission function calculated by the GTRN (Geomagnetic TRaNsmission) routine in the CREME package was used. The function describes the fraction of particles reaching the ISS orbit (350 km altitude, 51.6° inclination) as a function of the particle's magnetic rigidity. The geomagnetic transmission function is calculated from 0 to 20 GV in 0.2 GV steps and is shown in Figure 3.2a.

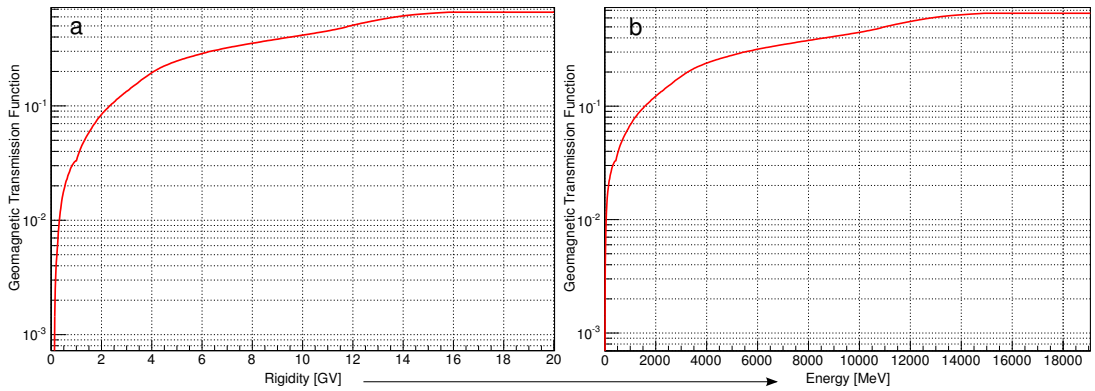

Figure 3.2: Figure a shows the geomagnetic transmission function calculated by the CREME96 package for the ISS orbit at 350 km altitude and 51.6° inclination and Figure b shows the same function plotted against the kinetic energy of H nuclei.

To calculate the GCR spectra at ISS orbit, the particle fluxes derived for a location outside the magnetosphere were scaled by the geomagnetic transmission function. However, the rigidity was first converted to energy per nucleon for each particle type by:

$$E = \sqrt{M_0^2 + \frac{R^2 Q^2}{A^2}} - M_0 \tag{3.1}$$

where
E = kinetic energy per nucleon
M_0 = rest energy per nucleon
R = magnetic rigidity
Q = charge of the particle
A = atomic mass number of the particle

Figure 3.2b shows the geomagnetic transmission function against the kinetic energy of H nuclei corresponding to the rigidity. The same way rigidity was converted for each particle type into kinetic energy per nucleon. The energy spectra, derived from all GCR models under consideration, of GCR nuclei from 10 MeV/nuc to 100 GeV/nuc outside the magnetosphere were then scaled with the geomagnetic transmission function. For higher energies corresponding to rigidities greater than 20 GV, the GCR energy spectra were linearly extrapolated in log-log scale.

Figure 3.3 shows the energy spectrum of GCR H nuclei calculated for ISS orbit by scaling the energy spectrum outside the magnetosphere with the geomagnetic transmission function. The energy spectrum for outside the magnetosphere was derived from the BON2010 model for January 1998.

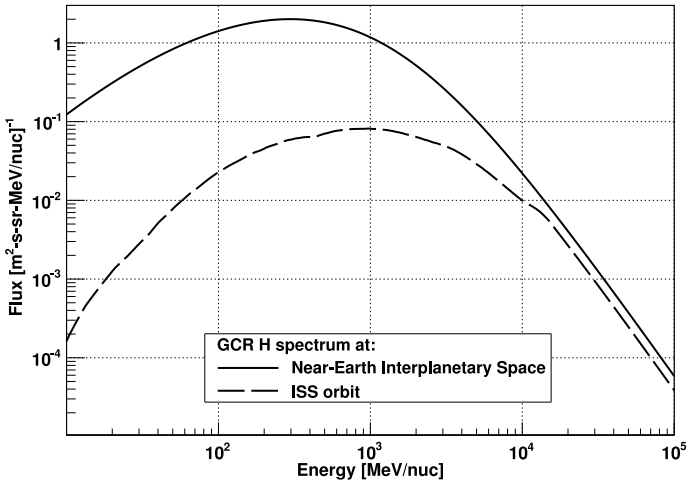

Figure 3.3: GCR H energy spectra outside and inside the magnetosphere calculated using the Badhwar-O'Neill2010 model for January 1998 and the geomagnetic transmission function.

3.3 GEANT4 Simulation

GEANT4 (GEometry ANd Transport)[1] is a software toolkit for the simulation of the passage of particles through matter (Agostinelli et al. 2003, Allison et al. 2006). GEANT4 was initially designed and developed for high-energy physics experiments but due to its functionality and flexibility, it gained popularity in many other research fields such as space and medical physics. It is currently being developed and maintained by a world-wide collaboration including premier scientific institutions and universities[2].

The toolkit is open source written in C++ language and due to its object-oriented programming approach, it allows application developers to use available functions and also customize them for their application. It uses a large set of physics models that are theoretical, parameterised and data-driven, to handle the interactions between incident particles and matter for a wide energy range, from a few keV to above 1 TeV. Each particle trajectory is simulated according to the stochastics of the possible particle interactions between the incident particle and the target material by applying Monte-Carlo (MC) techniques (see James 1980 for details about the MC method) that are used at various steps of the simulation process from particle generation to its final state. Furthermore, the toolkit allows the user to integrate data analysis software such as ROOT (Brun and Rademakers, 1997)[3] which provides histogramming methods and gives a possibility to process and visualize the simulation output data outside the GEANT4 simulation runs. GEANT4 also provides interfaces to various graphics visualization programs such as Virtual Reality Modelling Language (VRML) which are used to visualize the model geometries as well as particle trajectories. Visualization is especially useful as it serves as a method for troubleshooting the simulated experimental setup, e.g., position of the volumes or the properties of the simulated radiation source such as its position and angular distribution.

The GEANT4 website provides the necessary documentation[4] regarding the software, e.g., its design and functionality, the physics models therein, and the tools available for individual applications. It should be noted that the software is continuously evolving and each year there is a new version of GEANT4 released. The older versions and their corresponding manuals are nevertheless available on the website.

[1] http://geant4.cern.ch/

[2] see https://geant4.cern.ch/collaboration/index.shtml

[3] http://root.cern.ch/drupal/

[4] http://geant4.web.cern.ch/geant4/support/userdocuments.shtml

In this work GEANT4 version 4.9.3 patch 02 was used.

3.3.1 GEANT4 Monte-Carlo Method

In contrast to deterministic numerical problem solving techniques Monte-Carlo uses random numbers and probability distributions in order to obtain a close approximation to the exact solution. GEANT4 uses MC techniques to quantify the interactions of accelerated particles with matter.
The basic task of the GEANT4 toolkit is to track randomly generated particles along their path inside a target volume and simulate their interactions with the traversed matter. The particles are generated with a specified energy and spatial distribution by the Generic Particle Source included with the toolkit.
GEANT4 tracks a particle from interaction to interaction until it has lost its entire kinetic energy or it has left the so-called World volume. Each particle is associated with a repertoire of interaction processes, $i = 1, 2, 3...., n$, that may occur during its flight. Each interaction, when it occurs, may lead to loss of momentum, change in direction of movement and creation of secondary particles (which are then tracked separately).
In between the interactions the trajectory of the particle is propagated according to the applicable equation of motion taking into account possibly present EM fields in the case of charged particles.
After every interaction event GEANT4 applies a MC process to determine the type of the next interaction to occur and the distance the particle will travel until it interacts. The decision is influenced by the material properties of the medium through which the particle travels. Such properties are, e.g., the number density of interaction centres, n_i, and interaction cross-section, σ_i, and depend in general on the interaction process and the tracked particle (mass, charge, momentum).
The following simplified description of the GEANT4 interaction selection process is valid under the assumption that no force field is present and the traversed material is homogeneous (e.g. water or air):

- The probability $P_i(L_i)$ that the interaction i occurs after the particle has travelled undisturbed for a distance L_i is given by the distribution function $P_i(L_i) = 1 - exp(-L_i/\lambda_i)$ where the quantity $\lambda_i = \frac{1}{n_i \sigma_i}$ is called the mean free path.

- Inversion of this equation by solving for L_i yields
  $L_i = -\ln(1 - P_i)\lambda_i$

which allows us to determine an L_i for each interaction by drawing n uniformly distributed random numbers between 0..1 for P_i.

- The smallest L_i selects the interaction i to occur and at the same time the distance the particle is transported along its trajectory. The outcome of the interaction itself is simulated as well using MC techniques. The particle state is updated accordingly and the whole process repeats until the particle's energy falls below a threshold or it is transported outside the World volume.

Besides the GEANT4 documentation[5], presentations given by the collaborators during various training sessions, e.g., Liendl (2004) are also recommended for illustration as well as detailed description of the GEANT4 MC methods.

3.3.2 Simulation Setup

Target Geometry

A spherical water phantom with a radius of 25 cm was used as a surrogate for a human body. The sphere was divided into 100 concentric spherical shells with a thickness of 2.5 mm each. Such a construction was used in GEANT4 to discriminate between different regions in the target volume and therefore allowed the numerical estimation of the depth dependent dose distribution. To simulate different amounts of shielding, aluminium shells with an outer radius of 50 cm of 0.3g/cm^2, 10 g/cm^2 and 40 g/cm^2 thickness enveloping the water phantom were added to the target construction.
The rationale for the use of this phantom geometry in this work is discussed in Mrigakshi et. al 2013a, 2013b (Section 4.3 and 4.5).

The construction of the target in GEANT4 is done by specifying an object of type *G4VUserDetectorConstruction* which is a mandatory base class used to define the material and geometry setup, making regions in the setup sensitive (called Sensitive Detectors in GEANT4) to restrict the particle interaction data in certain volumes only.

Figure 3.4 shows a snapshot[6] of the geometry setup. In GEANT4 all volumes must

[5] http://geant4.web.cern.ch/geant4/UserDocumentation/UsersGuides/PhysicsReferenceManual/fo/PhysicsReferenceManual.pdf

[6] The visualization was performed with VRML by using the VRML driver provided in GEANT4 to

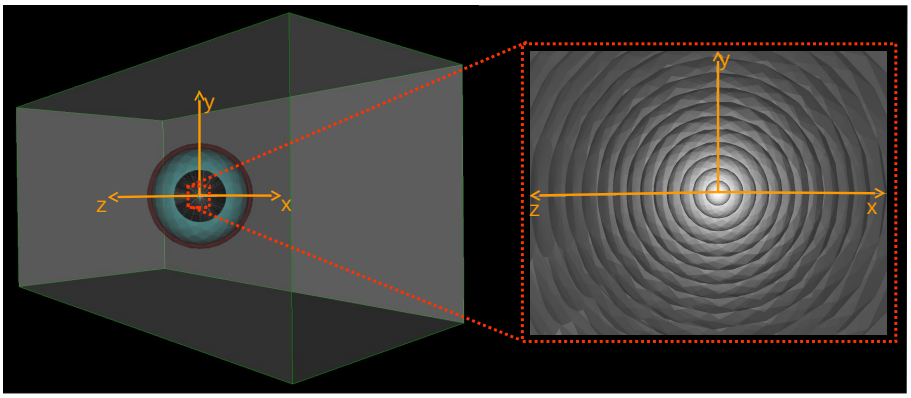

Figure 3.4: Target geometry setup inside the World Volume (Box in gray). The water sphere can be seen in black at the centre surrounded by aluminium shielding shown in brown with air in between coloured in cyan. A zoom-in picture showing concentric shells of the water sphere with the innermost at the origin of the coordinate axes (in orange).

be contained inside the so-called World Volume (the rectangular box in Figure 3.4) and defines the global coordinate system with origin at its centre. In this case the World Volume is constructed as a rectangular box and the spherical water phantom with the spherical shielding (10 g/cm^2 aluminium) and air in between is positioned at its centre. The coordinate axes are also shown in the figure.

Radiation Source

A spherical radiation source radiating from its surface inwards onto the fully-enveloped target was modelled. The target was isotropically irradiated by particles ranging from $1 \leq z \leq 26$ to simulate the GCR distribution in near-Earth space which is nearly isotropic.

The energy spectrum of the isotropic radiation field was set to follow a power law distribution, such that the number of particles simulated were uniformly distributed over logarithmic energy scale E ranging from 10-10^5 MeV/nuc (Figure 3.5a). This means that the same number of particles falls within any energy interval of constant width in a logarithmic energy scale. Therefore, by simulating an appropriate number of particles (see Appendix B), data analysis could be made for particle energies ranging over several orders of magnitude with insignificant statistical biasing of the result over energy. Additionally, a greater computation efficiency is achieved in terms of the number of particles required to be simulated in contrast to the case of a uniform

create text files representing the 3D geometry in VRML format (*.wrl*). These files were then displayed using vrml file viewing software called view3dscene.

particle distribution over a linear energy scale.
The mandatory user base class in GEANT4 for specifying how a primary particle event with specific properties of the radiation source should be generated, is $G4VUserPrimaryGeneratorAction$. For the actual generation of the primary particles the GEANT4 General Particle Source module[7] (GPS) via $G4GeneralParticleSource$ class was utilized.

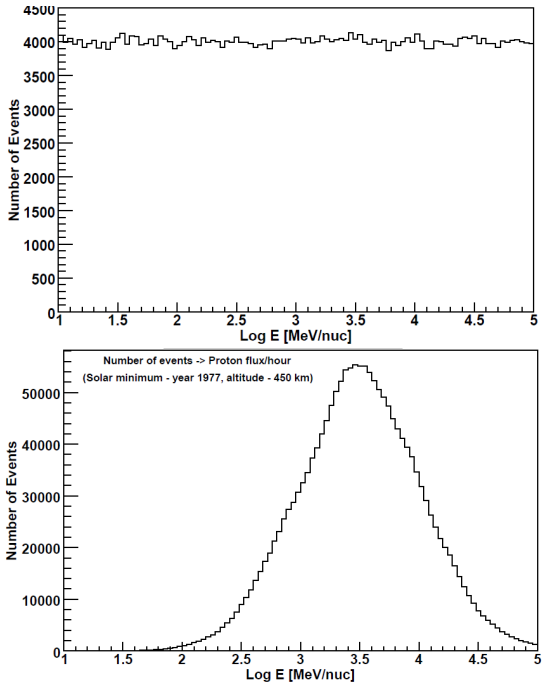

Figure 3.5: Energy histograms of H nuclei simulated from the radiation source distributed over energies following the power-law distribution (Figure 3.5a) and the GCR energy distribution (Figure 3.5b). The GCR H energy spectrum used to calculate the distribution of particle number over energy was calculated using the CREME96 model for January 1977 for an orbit at an altitude of 450 km and an inclination of 51.6°.

As explained in Mrigakshi et al. (2013a) (Section 4.3), the total dose rates from all particle energies was calculated by integrating the dose (absorbed dose or dose equivalent) normalized by the number of particles in every energy interval weighted by the corresponding GCR particle flux. This method of dose estimation instead of simulating particles with GCR particle energy distributions (Figure 3.5b) allowed the calculation of the dose quantities for any given input energy spectrum for a particular geometry setup. This was especially useful in this study wherein the effect of using

[7] http://reat.space.qinetiq.com/gps/

different GCR models and spectra on the dose quantities was studied over several decades and locations outside and inside the Earth's magnetosphere.

Physics Models

In GEANT4, the physics models describing the physical process associated with each particle type involved in the simulation, have to be specified by the user e.g. an electron is assigned with multiple scattering, ionization and bremsstrahlung processes, whereas an ion is assigned with electromagnetic (EM) interaction processes (ionization and energy loss) as well as hadronic interaction processes (elastic and inelastic collisions, capture and fission). These physical processes in Geant4 include decay, transportation, EM and hadronic interactions which are described using theory and data driven models and are collected in the so-called 'Physics Lists'. These lists can be either created by users, or the pre-configured reference physics lists can be used. These reference lists are routinely validated and updated, and are available in GEANT4 for various applications. GEANT4 by default does not provide any physics settings. The mandatory user base class in GEANT4 for specifying the physics settings is $G4VUserPrimaryGeneratorAction$.

One of the reference physics lists recommended[8] for shielding and dosimetric applications is $QGSP\_BERT\_HP$ and it was selected for this work. $QGSP$ refers to the Quark Gluon String Model (for protons, neutrons, pions, kaons and with energies between 10-10^5 GeV), $BERT$ refers to the Bertini cascade model (for protons, neutrons, pions, kaons, hyperons and energies $\leq$ 15 GeV) and HP refers to data-driven High Precision neutron model (<20 MeV). See Ivantchenko et al. (2012) for a summary regarding the hadronic physics models in GEANT4. The selected physics list additionally includes the standard EM model ($emstandard\_opt3$) for the EM interaction processes such as multiple scattering, bremsstrahlung, ionization, pair production, photo and Compton-effect. Additionally, external hadronic interaction models JAM (jet AA microscopic transport model) developed by Niita et al. (1995) and $JQMD$ (Jaeri quantum molecular dynamics) by Nara et al. (2000) were incorporated by applying the interface to these models developed by Koi et al. (2003) for GEANT4. The reason for including these models (also discussed in Mrigakshi et al. 2013b, Section 4.5) was their treatment of inelastic nucleus-nucleus interactions at energies above 10 GeV/nuc and inclusion of heavy ions $\geq$He. The $QGSP\_BERT\_HP$ does not describe these interactions for these particles and energies.

[8] http://geant4.cern.ch/support/proc_mod_catalog/physics_lists/useCases.shtml

It should be noted that in later versions of GEANT4, a native implementation of the JQMD model is provided as the $G4QMD$ model which is able to handle nucleus-nucleus interactions for ions $\geq$He as well. There have been three major releases of GEANT4 versions (4.9.4, 4.9.5 and 4.9.6) since the beginning of this research work but in order to have a consistent simulation setup for the assessment of dose quantities changing with different simulation scenario, the same version of GEANT4 was used throughout the research work.

3.3.3 Simulation Processing and Output

After setting up the target geometry, physics list and the radiation source via the three mandatory base classes $G4VUserDetectorConstruction$, $G4VUserPhysicsList$ and $G4VUserPrimaryGeneratorAction$ respectively, the $G4RunManager$ class must be instantiated in the GEANT4 code's $main()$ method. The run manager controls the flow of the simulation. First it checks for the existence of these mandatory classes then performs their initializations to build the setup and begins the simulation run of events. GEANT4 at this point creates and manages event loops.

All tracks associated with an event are followed (tracking process) and information can be accessed via $Get()$ methods in the $G4Track$ class e.g. the energy, momentum and position of the primary and secondary particles. To get information associated with a step of a particle track (stepping process), e.g., step length or total energy deposited during a step, the $Get()$ methods provided in the $G4Step$ class can be used.

In this work, information for the estimation of the absorbed dose and dose equivalent in every shell in the water phantom was accessed.

1. Absorbed dose: The identification of the traversed shell, n, to determine the shell mass, m_n, and the energy deposited, ϵ, by the particle during each step, s, inside that shell was required. The absorbed dose D_n in each shell n was calculated by:

$$D_n = \sum_s \frac{\epsilon_s}{m_n} \tag{3.2}$$

2. Dose equivalent: The same information as for the calculation of absorbed dose and additionally the step length, l_s, for each step, s, inside a shell was required.

This was done to first calculate the LET ($LET_s = \epsilon_s/l_s$) for each step and then to determine the corresponding quality factor, $Q_s(LET_s)$, using the Q-LET relationship (equation 2.13). The dose equivalent, H_n, in each shell n was calculated by:

$$H_n = \sum_s \frac{\epsilon_s \cdot Q_s(LET_s)}{m_n} \tag{3.3}$$

Note that these calculations were made separately for each particle type from $1 \leq z \leq 26$ and the results were stored in histograms for data processing outside the GEANT4 simulation process. Figure 3.6 shows the flow chart of the simulation process in GEANT4 and all the quantities accessed in this work that were essential for GCR dose assessment.

The ROOT software was integrated with the GEANT4 code to perform histogramming of the data after each event. Three histograms were written into *ROOT* files and were used after the simulation for the estimation of GCR exposure based on the results from the simulation output (see Section 3.4). These histograms contained:

1. Energy histogram: 1-D histogram storing number of particles per primary particle energy bins (100 bins in total selected).
2. Absorbed dose histogram: 2-D histogram storing the absorbed dose per energy bin and in each shell constituting the water phantom.
3. Dose equivalent histogram: 2-D histogram storing the dose equivalent per energy bin and in each shell of the water phantom

The energy histogram was utilized for the normalization of dose values by the number of primary particles for each energy bin to get the dose per primary particle. This was the first step to scale the dose values to GCR energy spectra.
Besides the obvious requirement of the other two histograms, i.e. for storing dose values for GCR dose estimation at a later stage, these allowed the study of the relative contribution of different particle energies to total dose and also for depth-dose analysis.

In this work, separate *ROOT* files were created corresponding to the individual simulation runs for each particle type and for exposure scenarios without and with aluminium shielding of varying thicknesses around the water phantom.

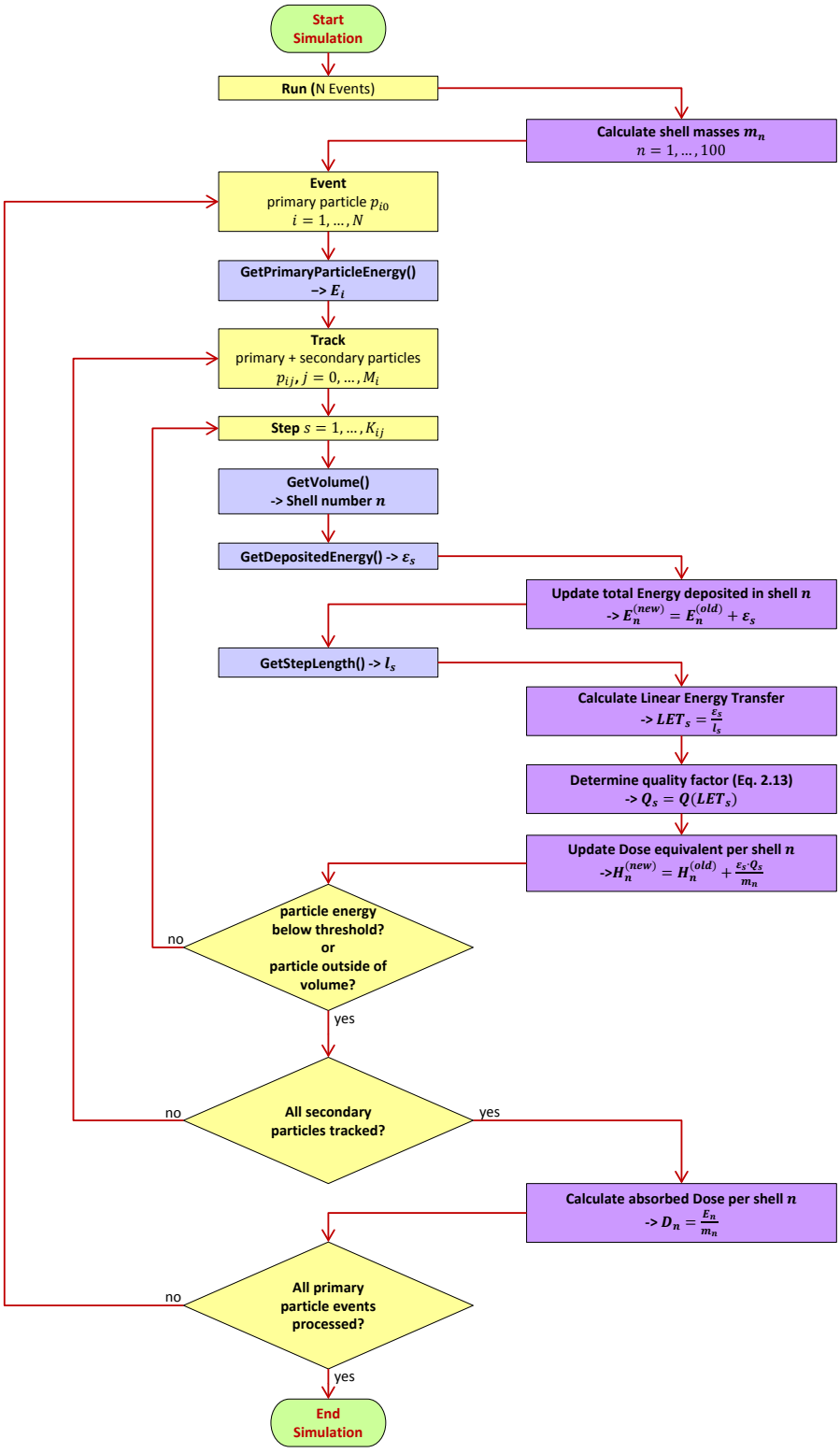

Figure 3.6: Flow chart of the simulation process in GEANT4 and all the quantities accessed in this work to calculate the absorbed dose and dose equivalent inside each shell of the water phantom.

3.4 GCR Dose Estimation

The GCR absorbed dose rate, dD/dt, for each particle type were separately calculated by the scaling procedure explained in Section 2.3 in Mrigakshi et al. (2013a) (Section 4.3). Note that the same procedure is used to estimate the dose equivalent rate and the procedure is only shown for absorbed dose rate as an example. In the procedure, first the dose calculated from the simulations, $d_i = D_i/N_i$, per primary particle number in each energy bin, i, was calculated, where D_i was the absorbed dose from all primary particles, N_i, in that bin. Then d_i was weighted by the number of primary particles in the energy interval i integrated over each energy bin and additionally integrated over the simulated radiation source surface and the solid angle of emission is calculated (f_i in equation 3.4). The dose rate in a volume is thereafter calculated by summing up this scaled quantity over all energy bins.

$$\frac{dD}{dt} = \sum_{i=1}^{n} f_i \cdot d_i \tag{3.4}$$

In the equation the quantity f_i is calculated as follows:

1. Integration over the spherical radiation source surface yields $4\pi R^2$ where R is the radius of the radiation source sphere

2. Integration over the solid emission angle restricted to inward direction and biased with cosine law to generate isotropic distribution of particles: $\int_0^{2\pi} \mathrm{d}\varphi \int_0^{\pi} \mathrm{d}\theta \cos\theta \sin\theta = \pi$

3. If j_i is the energy distribution in energy bin i then $f_i = j_i \cdot 4\pi R^2 \cdot \pi = 4\pi^2 R^2 j_i$

In this work the radius of the radiation source was different for different simulation scenarios. For the case without shielding wherein $R_{noShield} = 0.35m$ was selected, the scaling factor was $f_i = 4.836 j_i$ and for the case with shielding wherein $R_{shield} = 0.55m$ was selected, the factor was $f_i = 11.94 j_i$.

The absorbed dose rate dD_z/dt (equation 3.5) and the dose equivalent rate per day (equation 3.6) induced by each GCR particle species from $1 \leq z \leq 26$ over the whole sphere of mass M was therefore calculated by:

$$\frac{dD_z}{dt} = \frac{1}{M} \sum_{i=1}^{100} \sum_{n=1}^{100} D_n(z) \cdot m_n \cdot 4\pi^2 R^2 j_i(z) \cdot \triangle E_i \tag{3.5}$$

and

$$\frac{dH_z}{dt} = \frac{1}{M} \sum_{i=1}^{100} \sum_{n=1}^{100} H_n(z) \cdot m_n \cdot 4\pi^2 R^2 j_i(z) \cdot \triangle E_i \tag{3.6}$$

M	=	total mass of the water sphere of radius 0.25 m i.e. 65.45 kg
i	=	energy bin number
n	=	shell number
D_n	=	absorbed dose in shell n
H_n	=	dose equivalent in shell n
m_n	=	mass of shell n
$\triangle E_i$	=	bin width of energy bin i
R	=	$R_{noShield}$ or R_{shield}, radius of the radiation source
j_i	=	GCR flux

The total absorbed dose rate dD/dt and the dose equivalent rate dH/dt from all the relevant GCR particles were then calculated by summing up results for individual particle types:

$$\frac{dD}{dt} = \sum_{z=1}^{26} \frac{dD_z}{dt} \qquad \text{and} \qquad \frac{dH}{dt} = \sum_{z=1}^{26} \frac{dH_z}{dt} \tag{3.7}$$

The entire data analysis for the estimation of radiation exposure from GCR described in this section was performed using the ROOT software. In fact ROOT was also used for all the data visualizations presented in this work.

With the methodology explained in this chapter, GCR exposure of humans in space was estimated and the effect of the following parameters on the dose rates was studied as presented in Mrigakshi et al. 2013a, 2013b (see Chapter 4) and in Chapter 5:

1. The influence of using different GCR models by deriving and applying the GCR fluxes, j_i, from all considered GCR models in this work (Section 3.2),

2. The difference in the GCR exposure at locations in space outside and inside the Earth's magnetosphere and at ISS orbit by deriving GCR fluxes from all models for these locations (Section 3.2.1 and 3.2.2)

3. The effect of the changing GCR particle fluxes with solar activity by calculating dose rates for time period ranging from 1970 to 2011

4. The effect of shielding by simulating aluminium shieldings of varying thicknesses of 0.3 g/cm^2 , 10 g/cm^2 and 40 g/cm^2 and calculating the corresponding dose rates

5. The variation of the dose rates with the depth, by storing the doses induced in each shell inside the water phantom

6. The relative contribution of GCR particles with different energies to the total dose rates, by storing the dose rates contributed by different particle energies in each energy bin

4 Publications

The focus of the work throughout the research period has been to contribute towards making better predictions of GCR exposure for humans in space. Several aspects involved in the estimation of the GCR dose were therefore investigated during the course of the research work. In this chapter, the publications containing many of the results from these investigations are presented.

Each publication is put under a different section and are arranged in a manner to logically follow the study as it evolved during the research period. Note that additional results, besides those published in the papers, are also included in the dissertation in the following Chapter 5 and Appendix C.

4.1 An Overview of the papers

This section gives a brief introduction to the papers with an aim to solely aid the reader to understand the contextual connection between the papers. Each of these papers presents various investigations related with numerical dose calculations and therefore individually contain data analysis methods, results and detailed discussions. An overall summary discussing the major findings of the research work is given in Chapter 6.

Paper I: Assessment of galactic cosmic ray models

A mandatory requirement for the GCR dose calculation is the description of the energy spectra of all relevant GCR particles for the time period and the location of interest. As discussed in Section 2.1, the GCR flux in near-Earth space varies with the 11-year sunspot and the 22-year Hale cycle. Therefore, one of the research objectives was to inspect how the change in the particle fluxes over time influences the level of GCR exposure. For this purpose, a model capable of describing the temporal variation in the GCR particle fluxes was required.

There exist several models fullfilling these criteria. For this work, GCR models most frequently used for dosimetry applications were compared with measurements to find the most accurate model in order to reduce uncertainties introduced by the model spectra in the dose calculations. The first paper, Mrigakshi et al. (2012), presents this evaluation of the GCR models. It briefly introduces each model and the

measurements, explains the methods used to investigate the models and of course provides a detailed discussion of the level of accuracy of each model to describe the energy spectra of light (hydrogen and helium) and heavy (oxygen and iron) GCR nuclei.

Paper II: How Galactic Cosmic Ray models affect the estimation of radiation exposure in space

The results presented in Paper I showed several short-comings of each model. Some rather severe discrepancies were found between model and measured spectra for certain epochs in the past decade. The immediate question that occurred naturally was how much do the differences in the model spectra and the large discrepancies observed at certain times impact the dose estimations. Especially as these models have been used in the past and are still being used to make dose estimations for time periods where they have shown disagreement with the measurements.
In the second paper, Mrigakshi et al. (2013a), the question raised above is addressed. The radiation exposure in terms of the absorbed dose rate and dose equivalent rate in an unshielded target was estimated for a time period ranging from 1970 to 2010 using the models investigated in the first paper. The differences arising in the dose values as a result of the differences in the energy spectra derived by the GCR models were also quantified. The investigation was conducted for near-Earth interplanetary space and ISS orbit.
Another objective of the research was to probe the contribution of different particle energies to the total GCR exposure and to study the variation of dose rates with the depth. These studies are also included in the paper as well as the methods applied for the dose calculations and a detailed discussion of the obtained results.

Paper III: A Ready-to-Use Galactic Cosmic Ray Model

The results presented in the Paper II clearly showed that the choice of GCR model influences the dose estimations. The overestimation of the GCR intensity by models especially during certain epochs (solar maximum period, 2000-2003) leads to doses as high as 1.5-2 times those calculated using the most accurate model. The underestimation by the models of particle fluxes observed during the deep solar minimum in 2009-2010, on the other hand, resulted in no unusual increase in the dose rates for this time period in comparison with the previous solar minima.
Since the GCR intensity is the lowest during the solar maximum periods and

vice-versa for solar minimum, the dose estimations are usually made during these two periods in order to assess the expected range of the minimum and maximum GCR exposure. Furthermore, as stated earlier, each component used for the numerical calculations can lead to inaccuracies in the dose estimations. To pinpoint the source of the uncertainties while benchmarking the numerical calculation tools with the dose measurements, it is essential to validate each of the components separately.
It became apparent that due to the findings reported in the first two papers in addition to the reasoning stated above, a better GCR model was required. As a consequence, a new model was developed and is presented in the third paper, Matthiä et al. (2013a). The energy spectra from this model showed the best agreement with the measurements in comparison with the other GCR models for most of the time periods.

Paper IV: Estimation of Galactic Cosmic Ray exposure inside and outside the Earth's magnetosphere during the recent solar minimum between solar cycles 23 and 24

With the new model developed, the dose estimations made earlier (Paper II) were updated and are presented in the fourth paper, Mrigakshi et al. (2013b). Additionally, the paper also includes dose estimations made with the target surrounded by aluminium shielding representing the hull of a spacecraft. This was done in order to approximately simulate the real scenario wherein the astronauts in space are usually stationed inside a spacecraft. Different shielding thicknesses were simulated to examine how the different amounts of shielding influences the level of radiation exposure from GCR. The study with the shielding was performed for a period ranging from 1997 to 2011 to see whether there is any influence of the solar activity on the GCR exposure of the target surrounded with shielding.
Furthermore, the peak GCR exposure during the deep solar minimum between the solar cycles 23 and 24 was estimated and compared with the peak exposure calculated for the previous solar minimum.

4.2 Paper I - Mrigakshi et al. 2012

Assessment of galactic cosmic ray models

Alankrita Isha Mrigakshi, Daniel Matthiä, Thomas Berger, Günther Reitz and Robert F. Wimmer-Schweingruber, ***Journal of Geophysical Research***, Volume 117 , Issue A8 , A08109, 2012, doi:10.1029/2012JA017611

Assessment of galactic cosmic ray models

Alankrita Isha Mrigakshi,[1] Daniel Matthiä,[1] Thomas Berger,[1] Günther Reitz,[1] and Robert F. Wimmer-Schweingruber[2]

Received 15 February 2012; revised 31 May 2012; accepted 29 June 2012; published 18 August 2012.

[1] Among several factors involved in the development of a manned space mission concept, the astronauts' health is a major concern that needs to be considered carefully. Galactic cosmic rays (GCRs), which mainly consist of high-energetic nuclei ranging from hydrogen to iron and beyond, pose a major radiation health risk in long-term space missions. It is therefore required to assess the radiation exposure of astronauts in order to estimate their radiation risks. This can be done either by performing direct measurements or by making computer based simulations from which the dose can be derived. A necessary prerequisite for an accurate estimation of the exposure using simulations is a reliable description of the GCR spectra. The aim of this work is to compare GCR models and to test their applicability for the exposure assessment of astronauts. To achieve this, commonly used models capable of describing both light and heavy GCR particle spectra were evaluated by investigating the model spectra for various particles over several decades. The updated Badhwar-O'Neill model published in the year 2010, CREME2009 which uses the International Standard model for GCR, CREME96 and the Burger-Usoskin model were examined. Hydrogen, helium, oxygen and iron nuclei spectra calculated by the different models are compared with measurements from various high-altitude balloon and space-borne experiments. During certain epochs in the last decade, there are large discrepancies between the GCR energy spectra described by the models and the measurements. All the models exhibit weaknesses in describing the increased GCR flux that was observed in 2009–2010.

Citation: Mrigakshi, A. I., D. Matthiä, T. Berger, G. Reitz, and R. F. Wimmer-Schweingruber (2012), Assessment of galactic cosmic ray models, *J. Geophys. Res.*, *117*, A08109, doi:10.1029/2012JA017611.

1. Introduction

[2] In addition to the considerable engineering challenges associated with unmanned space missions, human spaceflight poses even greater challenges in limiting the negative health effects and hazards to humans. Among other important factors such as microgravity or psycho-social effects due to the confined living space associated with long-term space missions the radiation environment in space poses a substantial risk to the astronauts' health [*Berger*, 2008; *NCRP*, 1989, 2000, 2002; *Cucinotta et al.*, 2003]. Space radiation near Earth includes galactic cosmic rays (GCR), solar particle events, trapped particles in the Van Allen belts and albedo particles, mostly neutrons, produced by scattering of primary radiation from Earth's atmosphere [*NCRP*, 2002]. Therefore, due to the elevated exposure from these radiations, astronauts are considered to be radiation occupational workers [*ICRP*, 1991] for which the assessment of radiation related risks is mandatory.

[3] Radiation exposure of astronauts is studied based on the determination of dose quantities related to the biological effects of ionizing radiation and recommended by the International Commission on Radiological Protection [*ICRP*, 1991]. Two approaches can be taken to estimate these quantities: one is by performing dose measurements and the other is by making numerical simulations utilizing radiation transport codes [*NCRP*, 2002]. The latter approach has the advantage that it is possible to make predictions of the radiation exposure on future missions or for situations where measurements are not feasible or unavailable. The precision of the dose calculations using simulations, however, directly depends on the validity of the physical models in the transport code, on the level of detail of the geometry describing the target and its environment, and last but not least on the models specifying the composition and the spectra of the different components of the external radiation field. Thus it is important to make a careful evaluation of these factors in order to reduce the uncertainty in dose calculations.

[4] This paper presents an evaluation of commonly used models describing the spectrum of GCR nuclei for dosimetry purposes.

[1]Radiation Biology, Institute of Aerospace Medicine, German Aerospace Center, Cologne, Germany.
[2]Extraterrestrische Physik, IEAP, Christian-Albrechts-Universität zu Kiel, Kiel, Germany.

Corresponding author: A. I. Mrigakshi, Radiation Biology, Institute of Aerospace Medicine, German Aerospace Center, Linder Hoehe, D-51147 Cologne, Germany. (alankrita.mrigakshi@dlr.de)

0148-0227/12/2012JA017611

1.1. Galactic Cosmic Rays

[5] The hadronic component of GCR is mainly composed of fully ionized atomic nuclei which consist of hydrogen (~87%), helium (~12%) and heavier nuclei (~1%) [*Simpson*, 1983] with kinetic energies extending beyond 10^{20} eV [*Hörandel*, 2008]. GCR components up to 10^{18} eV are thought to be of galactic origin with sources like supernova explosions of massive stars and above 10^{18} eV of extra-galactic origin [*Biermann and de Souza*, 2011]. Since GCR particles are ions they are modulated by the heliospheric magnetic field which is frozen in and carried along with the solar wind [*Heber*, 2001]. The GCR intensity close to Earth is anti-correlated to the solar activity during the 22-year magnetic cycle of the Sun and the 11-year sunspot cycle [*Heber*, 2001; *Wiedenbeck*, 2011; *Usoskin et al.*, 2001a].

[6] The models discussed in this paper describe the spectra of the nucleonic component of the GCR beyond the heliospheric modulation region, the so-called Local Interstellar Spectrum (LIS), and the modulation inside the heliosphere. They provide the differential energy distribution of GCR particle fluxes. This energy spectrum is calculated for a selected point of time inside the heliosphere at 1 AU. Therefore, these models can be used for the estimation of the radiation exposure in near-Earth interplanetary space.

2. Galactic Cosmic Ray Models

[7] Several models frequently used in space dosimetry - CREME96 [*Tylka et al.*, 1997] (https://creme.isde.vanderbilt.edu/), CREME2009 (https://creme.isde.vanderbilt.edu/) and Badhwar-O'Neill 2010 [*O'Neill*, 2010] were investigated. These models were selected due to their capability of describing spectra of GCR nuclei between $1 \leq Z \leq 26$ over an energy range from 10 to 10^5 MeV/nuc. Another model based on the work of *Usoskin et al.* [2005] and *Burger and Potgieter* [2000] is considered in this work which is confined to describe hydrogen and helium spectra.

2.1. CREME96

[8] CREME96 stands for Cosmic Ray Effects on Micro-Electronics Code updated in the year 1996. This package was primarily designed to make radiation effect calculations on electronic systems and it is easily accessible over the Internet. CREME96 applies the semi-empirical model developed by *Nymmik et al.* [1992] to describe GCR particle fluxes. The particle spectrum in the model is calculated as a product of two functions: one describes the LIS, and the second describes the particle's modulation which is dependent on particle rigidity and solar activity.

[9] The expression for the LIS, j_{lis}, of particle species i in the CREME96 model, is given by,

$$j_{lis}(R) = D_i \left(\frac{R}{GV}\right)^{-\gamma_i} \beta^{\alpha_i}, \quad (1)$$

where R is the rigidity of the particle in GV. D_i, γ_i, α_i are constant parameters for each particle species. D_i and γ_i are determined from high-energy experiments and α_i describes the form of the low energy region (see *Nymmik et al.* [1994] for details). β is the ratio of particle velocity to the speed of light in vacuum.

[10] The modulation function is calculated by using the Wolf number W [*American National Standards Institute*, 2004] which is defined as:

$$W = k(10\ g + f), \quad (2)$$

where, f is the number of individual sunspots, g is the number of sunspot groups, and k is an empirical observational factor depending on site of observation and the individual observer.

[11] The CREME96 model describes GCR particle fluxes over energies from 10 to 10^5 MeV/nuc from Hydrogen (Z = 1) up to Nickel (Z = 28) nuclei for locations both inside the magnetosphere and near-Earth interplanetary space. The model also describes flux spectra of the Anomalous Cosmic Rays (ACR) component of GCR. This component, however, is of no importance for the assessment of radiation exposure in space and spacecraft design due to the low energies and flux levels of the ACR [*Tylka et al.*, 1997; *NCRP*, 2000].

[12] In 2010 an announcement was made on the CREME website stating that the CREME96 package is valid only from the year 1950 to 1997. Additionally, an upgraded version called CREME2009 (https://creme.isde.vanderbilt.edu/) was released. Since no such information was provided earlier on the Website, CREME96 was extensively used for periods after 1997 as well [e.g., *Gustafsson et al.*, 2010; *Sihver et al.*, 2010; *Ryu et al.*, 2007; *Palfalvi et al.*, 2008]. In order to estimate the accuracy of CREME96 and the reliability of published estimations of the radiation exposure in space using this model for time periods after 1997, CREME96 was included in the comparison even for times after the official period of validity.

2.2. CREME2009

[13] CREME2009 (https://creme.isde.vanderbilt.edu/) is the latest version in the CREME package and is based on the GCR standard model described in ISO 15390 [*American National Standards Institute*, 2004] and the model by *Nymmik et al.* [1992]. CREME2009 model uses 12-month averages of the Wolf numbers centered at the requested time instead of using the monthly averaged values as in the case of CREME96.

[14] GCR particle spectra in the energy range from 10 to 10^5 MeV/nuc are described from Hydrogen up to Nickel nuclei from the year 1760 to present. The model, at the time of this work, was not yet able to provide estimates for particles at locations inside the magnetosphere.

2.3. Badhwar-O'Neill 2010

[15] The Badhwar-O'Neill 2010 (BON2010) [*O'Neill*, 2010] model is the latest revision of a model which was first developed in the 1990s by G. D. Badhwar and P. M. O'Neill [*Badhwar and O'Neill*, 1992, 1996; *O'Neill*, 2006]. The data presented in this publication was obtained from a computer program written in FORTRAN implementing the BON2010 model and kindly provided by the author (P. M. O'Neill, private communication, 2010).

[16] Unlike the CREME models which describe the particle flux variation in the heliosphere semi-empirically, the BON2010 model uses the spherically symmetric Fokker-Planck equation that accounts for GCR propagation in the heliosphere due to diffusion, convection and adiabatic

deceleration (described by *Parker* [1965]). *Gleeson and Axford* [1968] suggested a solution of this equation resulting in a single parameter called the deceleration parameter or the potential, Φ, which describes the modulation of the particle spectra. This solution is called the force-field solution. The modulation parameter in the BON2010 model is derived from the International Sunspot Number (ISSN) accounting for the time lag of GCR flux variations relative to the solar activity (see *Nymmik* [2000] for details). It is calibrated with GCR measurements from space missions such as the Advanced Composition Explorer (ACE) and the Interplanetary Monitoring Platform-8 (IMP-8).

[17] The differential energy distribution of GCR particles at 1 AU expressed in $(\text{s-m}^2\text{-sr-MeV/nuc})^{-1}$ for a given LIS, j_{lis}, is described in the model by,

$$j_{lis}(E) = j_0 \beta^{\delta} (E + E_0)^{-\gamma}, \quad (3)$$

where, E is the kinetic energy of the GCR particle in MeV/nuc; E_0 is the particle's rest mass per nucleon (938 MeV/nuc); β is particle speed relative to the speed of light; j_0, γ, and δ are parameters constant for each type of GCR particle and which are determined from various balloon and space measurements.

[18] The BON2010 model describes the spectra of GCR nuclei in the energy range from 1 to 10^6 MeV/nuc and for elements from Hydrogen (Z = 1) to Plutonium (Z = 94) for near-Earth interplanetary space. The model, however, does not provide spectra for locations inside the magnetosphere.

2.4. Burger-Usoskin

[19] The Burger-Usoskin model [*Usoskin et al.*, 2005], as called in this paper, also uses the force-field approximation of the cosmic ray modulation. The LIS, j_{lis}, of GCR hydrogen nuclei used in the model was developed by *Burger and Potgieter* [2000]:

$$j_{lis}(E) = \frac{1.9 \times 10^4 \cdot P(E)^{-2.78}}{1 + 0.4866 P(E)^{-2.51}}, \quad (4)$$

$$P(E) = \sqrt{E(E + 2E_0)}, \quad (5)$$

where, E is the kinetic energy (in MeV/nuc) and E_0 = 938 MeV is the rest mass. The LIS of the helium nuclei is derived by approximating the ratio of helium to hydrogen particle number to 5% and thus scaling equation (4) by 0.05. The local interstellar spectra together with the modulation parameter provided by *Usoskin et al.* [2005] (http://cosmicrays.oulu.fi/phi/phi.html) is applied in the force-field model to derive the energy spectra of the GCR hydrogen and helium particles at 1 AU.

[20] The major differences between the models investigated in this work are:

[21] 1. The Burger-Usoskin model is limited to GCR ions with $Z \leq 2$ and a constant ratio of helium to hydrogen particle number in the LIS is assumed. The other models can be used for the description of GCR spectra for ions ranging from hydrogen to iron and beyond.

[22] 2. The reconstruction of the modulation parameter in the Burger-Usoskin model is based on neutron monitor count rates which are a direct measure of the GCR intensity while the other models rely on sunspot numbers which are not necessarily directly related to the GCR intensity at Earth.

[23] 3. While the CREME models use an empirical description of the modulated GCR, a physical approach is taken in the Burger-Usoskin and BON2010 models by solving the Fokker-Planck equation to describe the GCR transport in the heliosphere.

3. Galactic Cosmic Ray Measurements

[24] The fluxes derived from the models presented above were compared with measurements (see section 4) in order to assess the accuracy of the models in terms of temporal variations and spectral shape. The GCR measurements were obtained from the following space and high altitude balloon experiments.

3.1. Advanced Composition Explorer

[25] The Advance Composition Explorer (ACE) [*Stone et al.*, 1998] is an ongoing NASA Explorer mission which was launched on August 25, 1997 (http://www.srl.caltech.edu/ACE/ace_mission.html). The spacecraft orbits the Sun-Earth L1 Lagrange point.

[26] The data from the Cosmic Ray Isotope Spectrometer (CRIS) and the Solar Isotope Spectrometer (SIS) onboard the ACE spacecraft was used for the purpose of this comparison study. The CRIS instrument measures the isotopic composition of the GCR particle species from Li to Ni (Z = 3 to 28) and provides spectral information over an energy range from about 100 to 500 MeV/nuc. The SIS instrument measures the isotopic composition of energetic nuclei from He to Ni (Z = 2 to 28) and provides spectral information over the energy range from about 10 to 100 MeV/nuc. In this work, 27-Day averages of oxygen and iron nuclei flux are used which can be accessed from the online database (http://www.srl.caltech.edu/ACE/ASC/level2/index.html).
Although ACE measures data for many particles, it doesn't provide data for GCR hydrogen and high energy He nuclei which are the most abundant GCR particles and therefore are highly relevant in radiation protection for humans in space.

3.2. A Payload for Antimatter Matter Exploration and Light-Nuclei Astrophysics

[27] The Payload for Antimatter Matter Exploration and Light-nuclei Astrophysics (PAMELA) experiment [*Mocciutti et al.*, 2009] was launched in June 2006 (http://pamela.roma2.infn.it). It is a satellite-borne experiment orbiting Earth at an altitude ranging from 350 to 610 km with an inclination of 70 degrees.

[28] The energy spectrum of the GCR hydrogen and helium nuclei averaged over a period of July 2006 to March 2008 [*Adriani et al.*, 2011] are employed in this work. The spectrum for hydrogen is provided in the energy range of 0.43 GeV to about 860 GeV and for helium in the range of 0.12 GeV/nuc to about 595 GeV/nuc.

3.3. Electron Proton Helium Instrument

[29] Electron Proton Helium Instrument (EPHIN) [*Müller-Mellin et al.*, 1995] was launched in December 1995 aboard the Solar and Heliospheric Observatory (SOHO) [*Domingo et al.*, 1995]. It measures the energy spectra of hydrogen

and helium nuclei over three energy ranges from 4.3–7.8 MeV/nuc, 7.8–25 MeV/nuc and 25–53 MeV/nuc.

[30] The data collected over the last two energy ranges during the period of June 1998, August 2000 and January 2009 has been used in this work to test the model spectra at the corresponding energies (http://www2.physik.uni-kiel.de/SOHO/phpeph/EPHIN.htm).

3.4. Alpha Magnetic Spectrometer

[31] Alpha Magnetic Spectrometer (AMS) is an experiment built to search for cosmic antimatter and dark matter and to study the composition and energy spectrum of the primary cosmic rays [*Aguilar et al.*, 2002]. It was flown on the space shuttle Discovery during flight STS-91 in June 1998. The orbital inclination was 51.7 degrees and the altitude ranged from 320 to 390 km.

[32] The GCR hydrogen spectrum from 0.2–200 GeV [*Alcaraz et al.*, 2000a] and helium spectrum from 0.1 to 100 GeV/nuc [*Alcaraz et al.*, 2000b] collected by AMS-01 is included in this work.

3.5. Balloon-Borne Experiments

[33] The energy spectrum of hydrogen and helium nuclei measured by the following balloon experiments were taken for this study. All these experiments flew from Lynn Lake, Manitoba, Canada (56.5° N, 101.0° W) at an altitude of ~36–37 km.

3.5.1. Balloon-borne Experiment With a Superconducting Spectrometer

[34] Balloon-borne Experiment with a Superconducting Spectrometer (BESS) is a project to search for antimatter in the cosmic radiation as well as to measure energy and intensity of less exotic components of the cosmic radiation [*Mitchell et al.* 2010].

[35] The results from the flights in 1997 (27th July), 1998 (29th July), 1999 (11th August), 2000 (10th August) and 2002 (7th August) [*Shikaze et al.*, 2007] have been used for this study. The observation time during these flights varied between ~14 h and 33 h. The geomagnetic cut-off rigidity at the location of the experiments is approximately 0.4 GV (corresponding to ~82 MeV/nucleon for H nuclei and ~21 MeV/nucleon for He nuclei). Due to the low geomagnetic cut-off rigidity at the location of the experiments, the GCR particles are not affected by the magnetosphere and can penetrate into the atmosphere. The experiments provide data on GCR proton and helium spectra in the kinetic energy range between 0.215 and 21.5 GeV/nuc.

3.5.2. Isotope Matter-Antimatter Experiment

[36] Isotope Matter-Antimatter Experiment (IMAX) was designed to measure the galactic cosmic ray abundances of protons, antiprotons, deuterium, helium-3 and helium-4 [*Menn et al.*, 2000] (http://ida1.physik.uni-siegen.de/imax.html). The experiment was launched on 16th July 1992 and made observations for ~16 h. The proton and helium spectra were measured from 0.2 GeV/nuc to 200 GeV/nuc.

3.5.3. Cosmic Antiparticle Ring-Imaging Cerenkov Experiment

[37] Cosmic Antiparticle Ring-Imaging Cerenkov Experiment (CAPRICE-1) was flown from 8th to 9th August 1994 and made observations for ~18 h [*Boezio et al.*, 1999] (http://ida1.physik.uni-siegen.de/caprice.html). The proton and helium spectra were measured from 0.2 GeV/nuc to 200 GeV/nuc.

[38] GCR Radiation exposure in space mainly arises from particles with energies between 100 MeV/nuc to 10 GeV/nuc. Therefore, continuous measurements over time covering such a broad range of energies are important in order to develop reliable GCR models. Since these balloon experiments provide measurements of H and He nuclei above 200 MeV/nuc, it is difficult to draw conclusions on the accuracy of GCR models to describe the energy spectra of these particles at lower energies. Furthermore, due to the lack of continuous data for these particles over the critical energy range during the last decade, it is difficult to the judge precision of the models accurately for recent times. The description of heavier particles by the models can be evaluated for the last decade due to the availability of continuous measurements from the ACE mission, though, only for energies from about 100 to 500 MeV/nuc. There is data available for high Z particles with energies above 10 GeV/nuc measured by experiments like HEAO 3 [*Engelmann et al.*, 1990], CREAM 1 [*Wakely et al.*, 2008] and TRACER [*Obermeier et al.*, 2011; *Ave et al.*, 2008] etc. However, they do not exist at regular or frequent intervals in time particularly for the recent times.

4. Comparison of Models With Measurements

[39] For dosimetry purposes the GCR models should be able to describe the temporal variation of the GCR spectra related to their modulation during the solar cycle. The models were accordingly examined by comparing the model-derived spectra at 1 AU with the available measurements. The study was performed for hydrogen, helium, oxygen and iron nuclei. The first two nuclei represent the light GCR component, while O was taken as a representative for the mid-heavy and Fe for the heavy GCR component. Moreover, due to the large abundance of light nuclei and the greater biological effectiveness of the heavier nuclei, these particles contribute significantly to the radiation exposure.

[40] In this section, the variation of energy integrated flux over the last four decades as described by the models is compared with GCR measurements from the different experiments. For several points in time the deviations of energy spectra obtained from the models and measured in the experiments are investigated. As a measure of the level of accuracy of the three models under consideration, the chi-square value calculated from the comparison of models against experimental data over the available energy ranges are presented.

4.1. Temporal Variation of Integral Fluxes

[41] GCR hydrogen, helium, oxygen and iron spectra measurements together with the corresponding spectra described by Burger-Usoskin, CREME96, CREME2009 and BON2010 models were integrated over the energy range of the measurements.

[42] The model-derived flux and measurements of hydrogen and helium nuclei integrated over energy are shown in Figures 1a and 1b respectively. The hydrogen flux was integrated over the common energy range for which the measurements were made by all three balloon experiments (IMAX, CAPRICE-1 and BESS) that is from 210 MeV/nuc

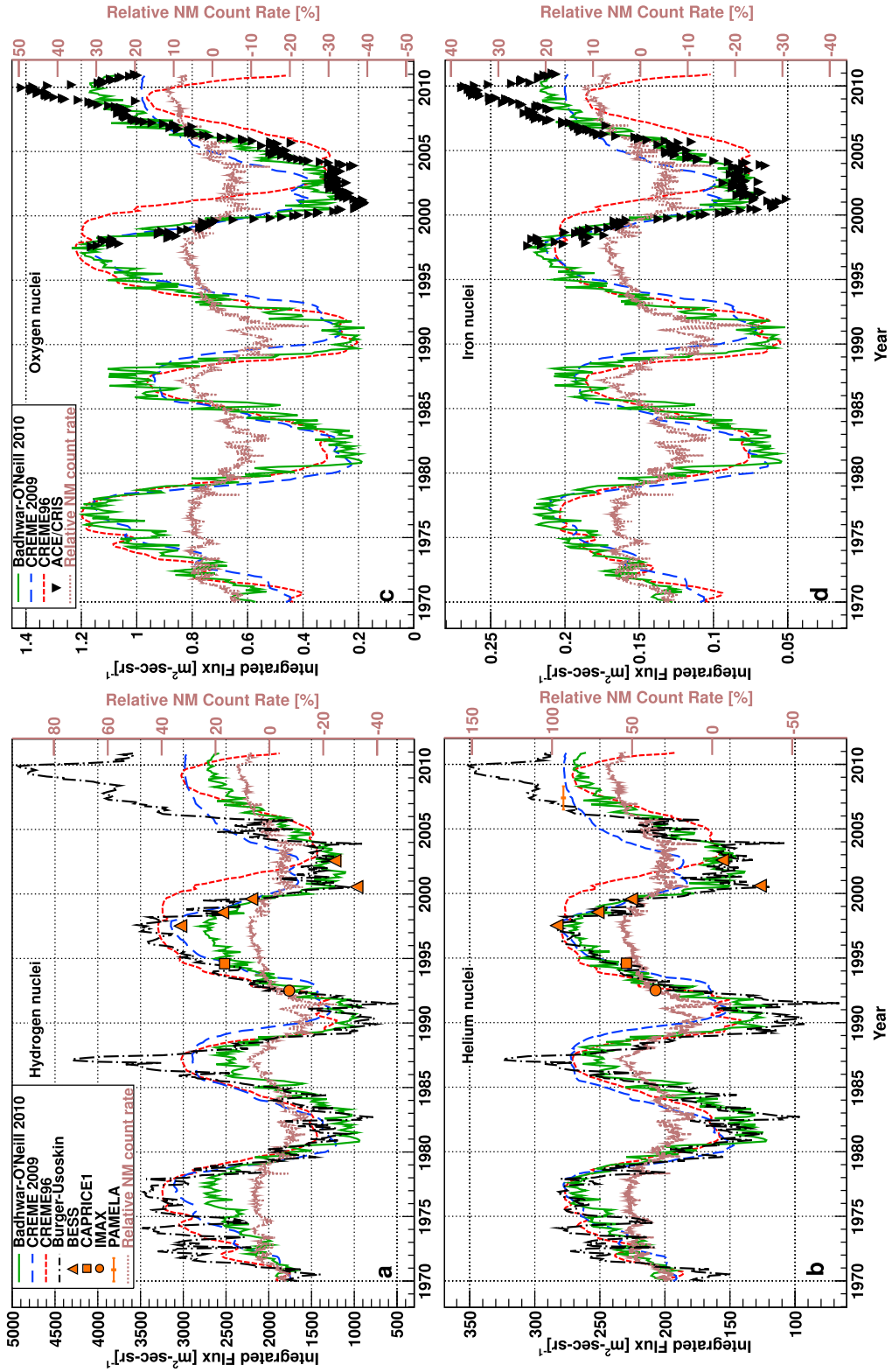

Figure 1. (a) GCR hydrogen, (b) helium, (c) oxygen, and (d) iron flux described by CREME96 (red dotted line), CREME2009 (blue dashed line), BON2010 (green continuous line) integrated over energy. Figures 1a and 1b also show integrated flux from the Burger-Usoskin model (black dashed-dotted lines). Hydrogen model and measured data from IMAX (solid circles), CAPRICE-1 (solid squares) and BESS (solid triangles) are integrated over the energy range 210 MeV/nuc to 24 GeV/nuc. Helium flux data from the same balloon experiments and additionally from PAMELA measured between 2006 and 2008 (orange line) is integrated over 230 MeV/nuc to 24 GeV/nuc. Oxygen and iron model-derived data and measurements from ACE/CRIS instrument (solid triangles) are integrated over the energy range from 80 MeV/nuc to 231 MeV/nuc and 150 MeV/nuc to 460 MeV/nuc respectively. Also shown are variations in the NM count rates (brown line) relative to the mean count rate.

Table 1. Percent Difference in the Integrated Flux Calculated From Models Relative to PAMELA Data

	Hydrogen ($430–24{\cdot}10^3$ MeV)	Helium ($210–24{\cdot}10^3$ MeV/nuc)
Burger-Usoskin	+25	+6
Badhwar-O'Neill 2010	−17	−11
CREME2009	−3	−2
CREME96	−6	−12

to 24 GeV/nuc and helium flux was integrated from 230 MeV/nuc to 24 GeV/nuc. The average helium flux from July 2006 to March 2008 measured by PAMELA was integrated over the same energy range and is shown in Figure 1b. The integrated hydrogen flux from PAMELA is not presented in Figure 1a due to the different energy range over which the data is published. However, a summary of the comparison between the PAMELA hydrogen as well as helium measurements is given in Table 1. The integrated flux of oxygen and iron nuclei from measurements and models are shown in Figures 1c and 1d respectively. The flux was integrated over the CRIS energy range from 80 to 231 MeV/nuc for oxygen nuclei and from 150 MeV/nuc to 460 MeV/nuc for iron. The model-derived fluxes were each produced for 10 equally distributed points in time per year from 1970 until the end of 2010.

[43] It should be noted that due to the properties of the different models, the corresponding GCR fluxes could not be averaged over the same time intervals. The CREME models do not describe time averaged spectra as in the case of the BON2010 model which provides flux averaged over a user defined number of days. For this study an averaging time of one day was selected in the BON2010 model.

[44] The temporal variation of the integrated particle flux over the selected time period (1970–2011) was plotted against the 10-day averaged relative difference between the Neutron Monitor (NM) count rates of the Oulu station [*Usoskin et al.*, 2001b] (http://cosmicrays.oulu.fi/) and its mean count rate (6134.09 counts/min). It was done in order to investigate the general behavior of models over time in comparison to the NM count rates which give an indirect measure of the GCR intensity and are most sensitive to them in the energy range between 0.5 and 20 GeV [*Usoskin et al.* 2001a] (Figure 1).

[45] In Figure 1 the difference observed in the smoothness of the curves from the CREME models in comparison to the BON2010 and the Burger-Usoskin model is due to the fact that the sunspot numbers used to calculate the modulation functions in the models are averaged over several days. For most of the time until the year 2009, the models describe the trend in the variation of the GCR intensity as measured by the neutron monitor and the balloon and spacecraft experiments. CREME96, however, shows large discrepancies during the maximum of solar cycle 23 around the year 2000. This is more evident in Figures 1c and 1d where the O and Fe measurements are plotted at regular intervals over the last decade respectively. A phase shift of about 3 years can be observed as a result of which the end of solar maximum of this solar cycle is delayed in the CREME96 model compared to measurements.

[46] Clearly, all the models exhibit shortcomings in describing the increased GCR intensity observed by ACE/CRIS instrument and the NM during the most recent solar minimum in the years 2009 and 2010. The peak integrated flux of oxygen and iron in 2009–2010 measured from ACE was found to be about 22%–20% greater than the previous solar minimum in 1998. The Burger-Usoskin model does show heightened fluxes during this time however its accuracy cannot be judged correctly due to the limited set of measurements. It overestimates the PAMELA H measurement by ∼25% and He by ∼6% (Table 1).

[47] Owing to the lack of experimental data after the year 2002 no conclusions can be drawn on the accuracy of the models in predicting the GCR hydrogen and helium flux for recent times. Nevertheless, for the times during which measurements are available, the Burger-Usoskin model describes the measurements most accurately. The CREME2009 model reproduces the measurements relatively well except for the 2000–2002 solar maximum. During this period it overestimates the hydrogen measurements by around 70% to 40% and helium by around 45% to 20%. Of the models discussed in this work, the BON2010 model is found to be the best model to describe the measurements of the heavier particles. It also shows good agreement with the helium data. For hydrogen it underestimates the BESS data during the solar minimum in 1998 by ∼7% and the PAMELA data by ∼17% (Table 1).

4.2. Differential Energy Distributions

[48] A direct comparison of model-derived H, He, O and Fe differential energy spectra with measurements can be seen in Figure 2.

[49] The investigation was carried out for the last solar minimum and maximum conditions corresponding to the GCR maximum and minimum. The distributions are shown for two solar minimum periods, 1998 (Figure 2a) and 2009 (Figure 2c) and for the solar maximum in the year 2000 (Figure 2b). Initially, the models were investigated for the most recent solar minimum and solar maximum period only. In order to compare the hydrogen and helium energy spectra predicted by the models with experimental results for low solar activity, however, the solar minimum of the year 1998 was selected in addition to 2009 due to the unavailability of H and He measurements for the year 2009. The data for these two particles were taken from BESS, AMS-01 and EPHIN/SOHO instruments whereas the measurements for O and Fe nuclei were acquired from the SIS and CRIS instruments onboard the ACE spacecraft. Note that the H flux between 7.8 and 25 MeV/nuc from EPHIN which is out of range in Figure 2a and very high in Figure 2b is dominated by solar energetic protons not GCR.

[50] Table 2 shows the date and the period of the selected experiments together with the measured energy ranges for the different particle types. For these periods the distributions from the instruments are compared to the model predictions. The ACE data is averaged over 27 day periods corresponding to one Bartels Rotation (BR) uniquely identified by a number.

[51] It should be noted that the GCR data described by the CREME models were produced for the fractional year closest to the time at which the measurements were taken.

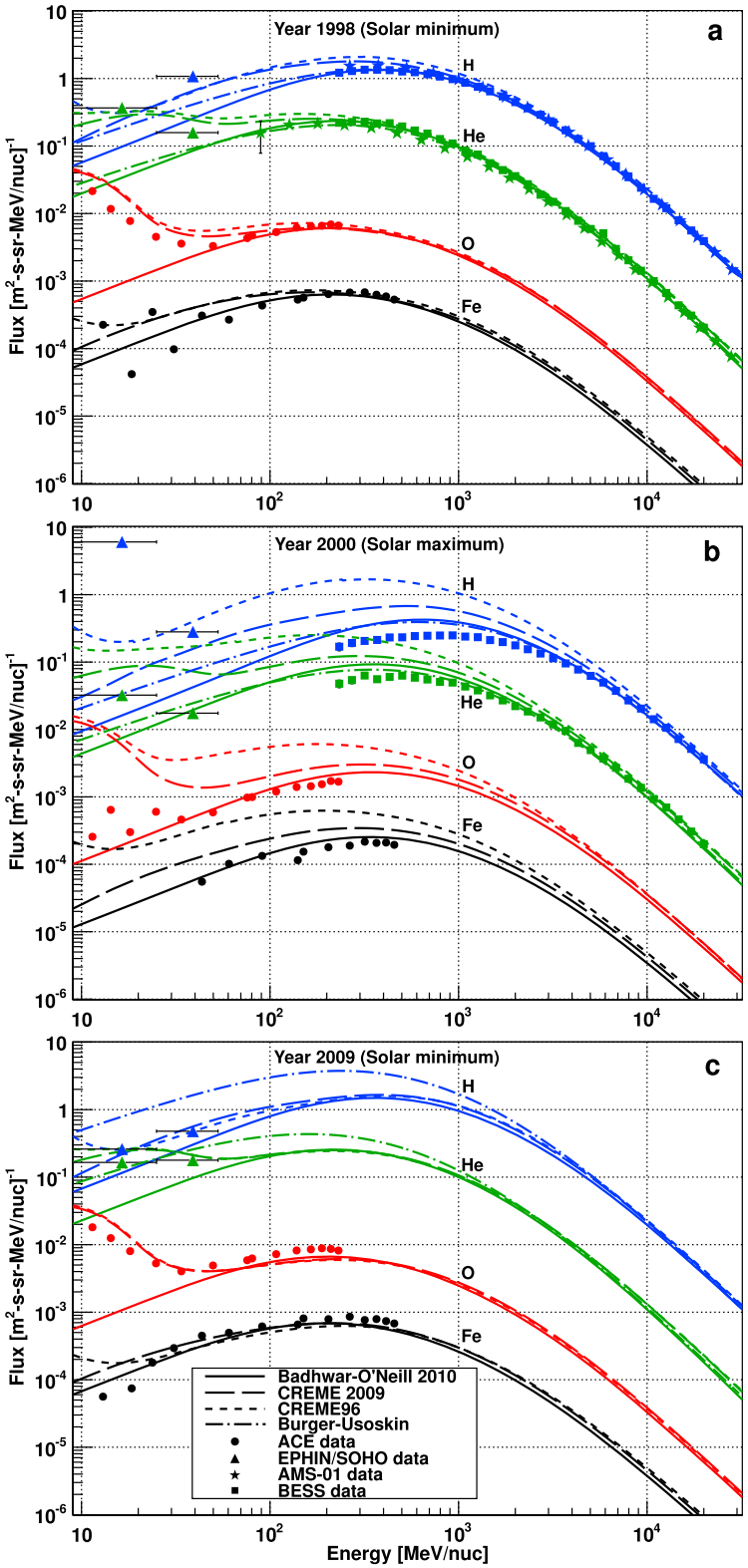

Figure 2. Comparison of H (blue lines), He (green lines), O (red lines) and Fe (black lines) GCR differential energy spectra described by Burger-Usoskin (dotted-dashed lines), CREME96 (dotted lines), CREME2009 (dashed lines) and BON2010 (continuous lines) models with the AMS-01 (solid stars), EPHIN/SOHO (solid triangles), BESS (solid squares) and ACE - SIS and CRIS (solid circles) measurements during different solar activity extremes. (a) The flux distributions for the year 1998 (solar minimum), (b) for the year 2000 (solar maximum), and (c) for the year 2009 (solar minimum).

Table 2. Summary of Data Selection to Plot the Differential Energy Distributions as Shown in Section 4.2

Particle	Experiment	Energy Range (MeV/nuc)	1998 (Solar Minimum)	2000 (Solar Maximum)	2009 (Solar Minimum)
H and He	AMS-01	$90–181 \cdot 10^3$	2–12 Jun	-	-
	BESS	$210–20 \cdot 10^3$	29 Jul	10–11 Aug	-
	EPHIN	7–53	2–12 Jun	6–7 Aug	1–2 Jan
O and Fe	ACE (SIS/CRIS)	7–460	31 Jul–26 Aug BR number = 2253	29 Jul–24 Aug BR number = 2280	1–27 Jan BR number = 2394

For instance for the year 1998, the BESS data was recorded on the 29th July which corresponds to the fractional year 1998.58. But the corresponding particle distributions from the CREME models were reproduced for the fractional year 1998.6 i.e., 8th Aug. This method of data selection was first tested and it was found that the flux described by the CREME models does not change significantly over such small time intervals. With the BON2010 on the other hand it is possible to produce the GCR distributions for exactly the same time as that of the observation. Accordingly, the H and He distributions from this model were averaged over 1 day whereas for O and Fe over 27 days in order to match the experimental conditions stated in the Table 2. The spectra from Burger-Usoskin model was produced by using the monthly averages of the modulation potential for the corresponding periods.

[52] By looking at the distributions for the selected time periods one can deduce that BON2010 model describes the spectrum of all the particles for the energy range above ~40 MeV/nuc more accurately than the CREME models. The H and He spectra from the Burger-Usoskin model also fits the measurements noticeably well. The increase in the particle flux measured from SIS/ACE at lower energies is due to the ACR component. The CREME models include the ACR component but the agreement between the model and measured spectra is limited.

[53] The expected decrease in the intensity from solar minimum (Figure 2a) to solar maximum (Figure 2b) period is clearly visible. For all particles under consideration, the CREME2009 and BON2010 models are capable to reproduce this significant decrease whereas CREME96 cannot. The CREME models overestimate the particle fluxes with respect to the measurements for the year 1998 and 2000. For H and He nuclei with energies above ~1 GeV/nuc, all models perform well. At these energies the particles get less attenuated by the solar modulation and follow a power law distribution.

[54] During the solar maximum of the year 2000 (Figure 2b), all the models have relatively large discrepancies with respect to experimental data for the H and He particle fluxes. CREME96 produces the largest deviation for all particles with the maximum difference lying between 100 MeV/nuc to 250 MeV/nuc with respect to the other models and the experimental data. For instance, the H and He flux at 210 MeV/nuc described by CREME96 differs by about an order of magnitude with respect to the measurements. The discrepancy produced by CREME96 for this time period is no surprise as the investigation of the temporal behavior of the energy integrated particle flux in section 4.1 revealed a large phase shift in the model with respect to the solar cycle at that time.

[55] For the time chosen during solar minimum in 2009 (Figure 2c), only higher Z particle data from ACE are available. The Burger-Usoskin model shows increased flux which corresponds to the increased cosmic ray intensity as observed by the neutron monitor in section 4.1 (Figure 1). However, its accuracy cannot be fairly judged due to the limited H and He measurements. The rest of the models do not reproduce this observation. They slightly underestimate the O and Fe flux, which is also in accordance with the observations of section 4.1 (Figure 1) where the significant increase in the GCR flux during this period was not reproduced by the models.

[56] No final conclusion can be drawn from the investigation of the particle spectra regarding the accuracy of the models over the entire GCR energy range due to the lack of data concerning heavier nuclei at energies above a few hundred MeV/nucleon and also for the lighter particles in the last decade. As mentioned earlier in section 3.5, continuous measurements of particles over time covering the energy range important for the purpose of radiation protection and are essential for better judgment of the models especially for recent times. Additionally, in order to appropriately intercompare the GCR models for the description of higher Z particles, continuous measurements at regular energy intervals from a few hundreds of MeV/nuc to about 10 GeV/nuc are also necessary.

4.3. Chi-Square Analysis

[57] A chi-square test was performed to examine the accuracy of all four models (in comparison with measured data) using Chi-square as defined in equation (6),

$$\chi^2 = \frac{1}{N-1}\sum_{i=1}^{N}\left[f_{meas}(E_i) - f_{\mathrm{model}}(E_i)\right]^2/\sigma_i^2, \qquad (6)$$

where, $f_{meas}(E_i)$ *and* $f_{model}(E_i)$ are the measured and model flux at the measured energy i respectively, σ_i is the error of the measurement and N is the number of points measured in the spectrum. The errors in the measurements from balloon experiments (BESS, IMAX and CAPRICE-1) are provided in the respective papers [*Shikaze et al.*, 2007; *Menn et al.*, 2000; *Boezio et al.*, 1999]. For ACE/CRIS data the error was taken to be 10% as suggested in the CRIS documentation (http://www.srl.caltech.edu/ACE/ASC/level2/cris_l2desc.html).

[58] Figure 3 shows the Chi-square calculated between the models and the available measurements for GCR H, He, O and Fe nuclei. It should be noted that the lines joining every point in the plots have been added in order to track plots for each model clearly and the y axis representing the chi-square

is shown in logarithmic scale to see the features of each plot in detail.

[59] Figures 3a and 3b show the chi-square for the GCR H and He spectra over time respectively. The hydrogen data from the balloon experiments over the energy range of 210 MeV/nuc to 24 GeV/nuc and helium data over the energy range of 230 MeV/nuc to 24 GeV/nuc were used to calculate the chi-square. The GCR spectra described by the CREME models were derived for the fractional year closest to the time at which the measurements were taken. The distributions derived from BON2010 were produced for exactly the same time as that of the observation and were averaged over one day whereas the Burger-Usoskin model was applied by using the monthly averages of the modulation potential for the corresponding month of observation. Due to the lack of hydrogen and helium measurements for recent time periods, chi-square could be calculated only for 7 points in time for which the data was available (section 3.5). Therefore, the accuracy of the models for these two particles cannot be judged reliably on the basis of these few measurement points.

[60] For these 7 points in time, large values of chi-square calculated for CREME96 relative to the other models during most of the times can be observed indicating that it produces the largest deviations in GCR flux spectrum with respect to the measurements. The difference is maximum in the year 2000 (September) which was expected due to the phase shift that was observed around this time in section 4.1. In general, by looking at the high chi-square values, it can be said that all the models describe the measured H data inaccurately around the year 2000–2002. The same is true for the description of He spectra for the time in year 2000 but not for the time in 2002 where the chi-square value was found to be between 1 and 5 for all the models. This shows that the models especially BON2010 and CREME96, are able to describe the He spectra relatively well for this time. On average the chi-square for the H nuclei is the lowest from BON2010 model ($\sim$14.5) whereas for He it is the lowest from Burger-Usoskin model ($\sim$2.5).

[61] The chi-square value for GCR O and Fe spectra over time calculated from the comparison of models against measurements is shown in Figures 3c and 3d respectively. Due to the availability of GCR particle spectra for heavy ions from the ACE mission continuously since August 1997 up to now, the capability of the GCR models to describe O and Fe spectrum over time in the energy range of the CRIS measurements could be analyzed in detail.

[62] Chi-square for iron nuclei was calculated over the energy range from 150 MeV/nuc to 500 MeV/nuc (ACE/CRIS) and from 80 MeV/nuc to 231 MeV/nuc for oxygen nuclei. In this case as well, the GCR spectra described by the CREME models were produced for the fractional year closest to the time at which the measurements were taken whereas the distributions described by BON2010 were produced for exactly the same time and averaged over the same duration (27 days) as that of the observation (same as in section 4.2). The calculated chi-square values are found to be similar for both the particle spectra. The level of accuracy of the models is found to vary over different time periods. The incorrect description of the O and Fe spectra by all the models and the large deviation by CREME96 model with respect to the measurements around the year 2000–2002 is also visible here. The CREME2009 and BON2010 model perform similarly during 1998 to 2000 and 2009 onwards in case of Fe spectra. From mid-2002 to mid-2003, the description of Fe spectra by the CREME96 model is in close agreement with the measurements in contrast to the other times where it shows an overestimation. The O spectra from CREME2009 model is also in good agreement with the measurements for the time period from mid-1997 to 2000 and from 2006 to 2007. Similar to the trend of the CREME96 chi-square values for the Fe spectra, the differences between the measurements and the model fluxes are found to decrease from mid-2002 to mid-2003 for O spectra. The discrepancies by the CREME2009 and BON2010 models are also observed to reduce after 2010 while they remain high for CREME96 model.

[63] The averaged chi-square over the selected time period from August 1997 to September 2010 for oxygen nuclei was found to be 5.29, 17.19 and 108.8 and for iron nuclei to be 4.01, 12.77 and 43.96 for BON2010, CREME2009 and CREME96 models respectively. The smallest value of the averaged chi-square for the BON2010 model with respect to the other models indicates that on average it describes the GCR O and Fe spectra most accurately in comparison to the CREME models over the last 10 years. There are only some periods where the chi-square values of the other models are slightly below BON2010, e.g., iron and oxygen data and CREME96 for 2004; iron data and CREME09 between 2006 and 2008.

5. Conclusion and Outlook

[64] Widely used galactic cosmic ray models – Burger-Usoskin, CREME96, CREME2009 and Badhwar-O'Neill 2010 were investigated concerning their accuracy in the energy range between a few hundreds of MeV per nucleon and several tens of GeV per nucleon by comparing the differential energy spectra of the dosimetrically most relevant particles and derived energy integrated fluxes with measurements. Important outcomes of the work are the following:

[65] 1. Badhwar-O'Neill 2010 was found to be most accurate GCR model in comparison to the CREME models for the description of GCR spectra for heavy ions with the smallest chi-square for most of the periods in the last decade.

[66] 2. The CREME96 model should be used with caution for 1998 onwards and calculations using this model should be interpreted carefully.

[67] 3. All the models display limitations in describing the elevated GCR intensity which was observed around the year 2009. The Burger-Usoskin model shows increase in particle fluxes which overestimate the only available data set from PAMELA. The insufficiency of the hydrogen and helium measurements makes it difficult to accurately judge the models.

[68] The results of this work have shown that a detailed analysis on the accuracy of models for the galactic cosmic radiation applied to radiation protection in space is essential. In this context it is desirable to broaden the knowledge and the description of the energy distribution of galactic cosmic radiation in the energy range between a few hundreds of

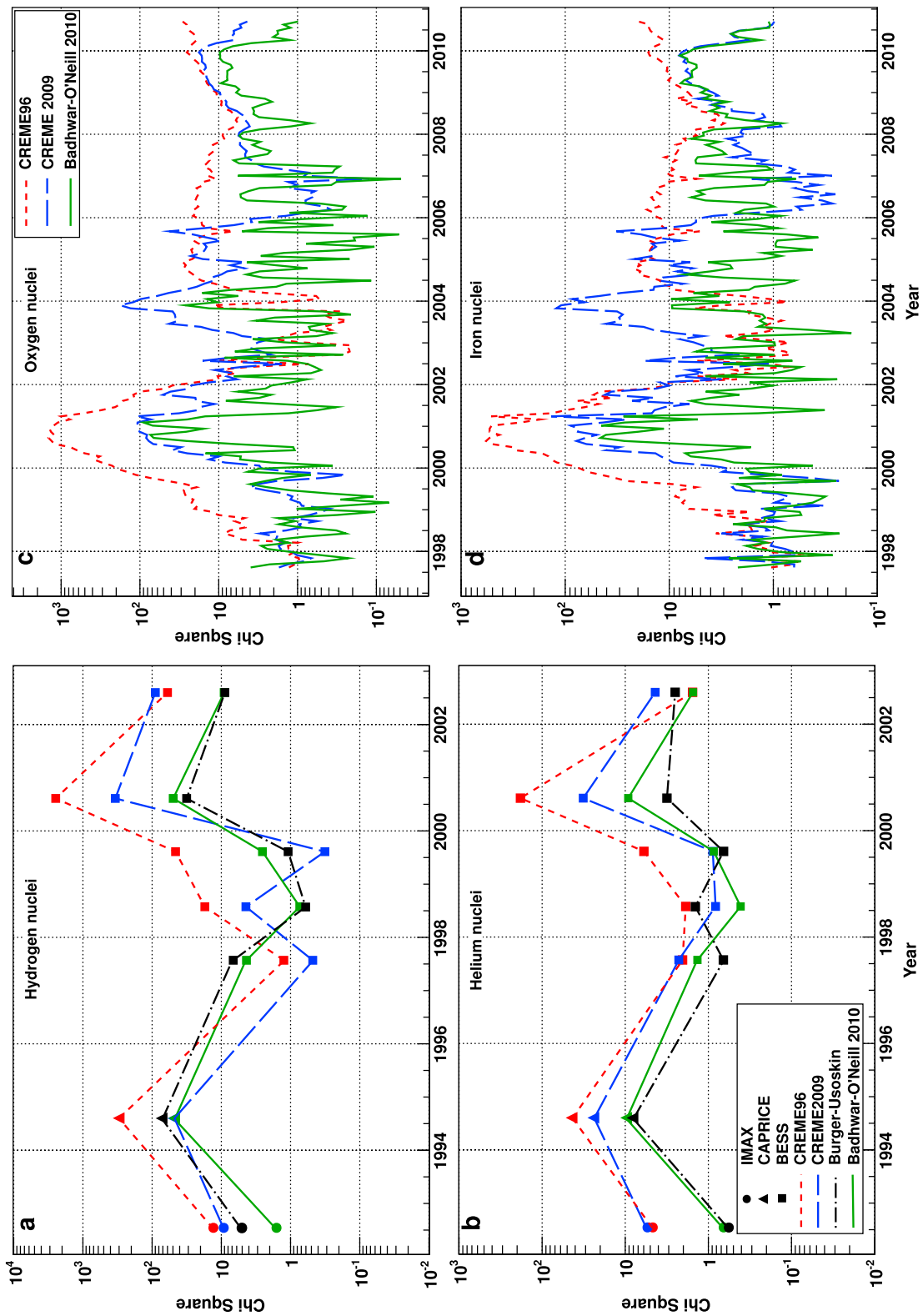

Figure 3. Chi-square to test the capability of Burger-Usoskin (black dashed-dotted lines), CREME96 (red dotted line), CREME2009 (blue dashed line) and BON2010 (green continuous line) models to describe the GCR H, He, O and Fe spectra. It was calculated with respect to the measurements from IMAX (solid circles), CAPRICE-1 (solid triangles) and BESS (solid squares) experiments for GCR H and He particles over an energy range of (a) 210 MeV/nuc to 24 GeV/nuc and (b) 230 MeV/nuc to 24 GeV/nuc. Whereas measurements from ACE/CRIS instrument were used to calculate the chi-square for GCR O and Fe particles over an energy range of (c) 80 MeV/nuc to 231 MeV/nuc and (d) 150 MeV/nuc–500 MeV/nuc.

MeV per nucleon to tens of GeV per nucleon especially for the most relevant hydrogen and helium nuclei and their modulation in the heliosphere and how this modulation changes during the solar cycle.

[69] **Acknowledgments.** We thank the ACE SWEPAM instrument team and the ACE Science Center for providing the ACE data, and Sodankyla Geophysical Observatory and the Oulu NM team for providing the Oulu neutron monitor count rates and the modulation parameters. The SOHO/EPHIN project is supported under grant 50 OC 0105 by the German Bundesminister für Wirtschaft through the Deutsches Zentrum für Luft- und Raumfahrt (DLR). We would also like to acknowledge P.M. O'Neill for the kind provision of the Badhwar-O'Neill 2010 model and the CREME team including the administrators of the CREME website who have been very helpful regarding the questions on both the CREME models and their usage. The first author, Alankrita Isha Mrigakshi, received a SpaceLife scholarship funded by the Initiative and Networking Fund of the Helmholtz Association and the German Aerospace Center as a participant of the Helmholtz Space Life Sciences Research School (SpaceLife) at the German Aerospace Center.

[70] Philippa Browning thanks the reviewers for their assistance in evaluating this paper.

References

Adriani, O., et al. (2011), PAMELA measurements of cosmic-ray and helium spectra, *Science*, *332*, 69–72, doi:10.1126/science.1199172.

Alcaraz, J., et al. (2000a), Cosmic protons, *Phys. Lett. B*, *490*, 27–35, doi:10.1016/S0370-2693(00)00970-9.

Alcaraz, J., et al. (2000b), Helium in near Earth orbit, *Phys. Lett. B*, *494*, 193–202, doi:10.1016/S0370-2693(00)01193-X.

Aguilar, M., et al. (2002), The Alpha Magnetic Spectrometer (AMS) on the International Space Station: Part I—Results from the test flight on the space shuttle, *Phys. Rep.*, *366*, 331–405, doi:10.1016/S0370-1573(02)00013-3.

American National Standards Institute (2004), Space environment (natural and artificial)—Galactic cosmic ray model, *Tech. Rep. ISO 15390*, Washington, D. C.

Ave, M., P. J. Boyle, F. Gahbauer, C. Hoppner, J. R. Horandel, M. Ichimura, D. Muller, and A. Romero-Wolf (2008), Composition of primary cosmic-ray nuclei at high energies, *Astrophys. J.*, *678*(1), 262–273, doi:10.1086/529424.

Badhwar, G. D., and P. M. O'Neill (1992), An improved model of galactic cosmic radiation for space exploration missions, *Nucl. Tracks Radiat. Meas.*, *20*(3), 403–410, doi:10.1016/1359-0189(92)90024-P.

Badhwar, G. D., and P. M. O'Neill (1996), Galactic cosmic radiation model and its applications, *Adv. Space Res.*, *17*(2), 7–17, doi:10.1016/0273-1177(95)00507-B.

Berger, T. (2008), Radiation dosimetry onboard the International Space Station ISS, *Z. Med. Phys.*, *18*, 265–275, doi:10.1016/j.zemedi.2008.06.014.

Biermann, P. L., and V. de Souza (2011), On a common origin of galactic and extragalactic cosmic rays, paper presented at Space and Cosmic Ray Physics Seminar, Univ. of Md, College Park.

Boezio, M., et al. (1999), The cosmic-ray proton and helium spectra between 0.4 and 200 GV, *Astrophys. J.*, *518*, 457–472, doi:10.1086/307251.

Burger, R. A., and M. S. Potgieter (2000), Rigidity dependence of cosmic ray proton latitudinal gradients measured by the Ulysses spacecraft: Implications for the diffusion tensor, *J. Geophys. Res.*, *105*(A12), 27,447–27,455, doi:10.1029/2000JA000153.

Cucinotta, F. A., H. Wu, M. R. Shavers, and K. George (2003), Radiation dosimetry and biophysical models of space radiation effects, *Gravit. Space Biol. Bull.*, *16*, 11–18.

Domingo, V., B. Fleck, and A. I. Poland (1995), The SOHO mission: An overview, *Sol. Phys.*, *162*, 1–37, doi:10.1007/BF00733425.

Engelmann, J. J., P. Ferrando, A. Soutoul, P. Goret, and E. Juliusson (1990), Charge composition and energy spectra of cosmic-ray nuclei for elements from Be to NI. Results from HEAO-3-C2, *Astron. Astrophys.*, *233*, 96–111.

Gleeson, L. J., and W. I. Axford (1968), Solar modulation of galactic cosmic rays, *Astrophys. J.*, *154*, 1011–1026, doi:10.1086/149822.

Gustafsson, K., L. Sihver, D. Mancusi, T. Sato, G. Reitz, and T. Berger (2010), PHITS simulations of the Matroshka experiment, *Adv. Space Res.*, *46*, 1266–1272, doi:10.1016/j.asr.2010.05.028.

Heber, B. (2001), Modulation of galactic and anomalous cosmic rays in the inner heliosphere, *Adv. Space Res.*, *27*, 451–460, doi:10.1016/S0273-1177(01)00083-7.

Hörandel, J. R. (2008), The origin of galactic cosmic rays, *Nucl. Instrum. Methods Phys. Res., Sect. A*, *588*, 181–188, doi:10.1016/j.nima.2008.01.036.

ICRP (1991), 1990 Recommendations of the International Commission on Radiological Protection, *ICRP Publ.*, *60*, 141 pp.

Menn, W., et al. (2000), The absolute flux of protons and helium at the top of the atmosphere using IMAX, *Astrophys. J.*, *533*, 281–297, doi:10.1086/308645.

Mitchell, J., et al. (2010), The balloon-borne experiment with a superconducting spectrometer (BESS) program, paper presented at 38th Scientific Assembly, Comm. on Space Res., Bremen, Germany.

Mocciutti, E., et al. (2009), The PAMELA space experiment, paper presented at 44th Session Devoted to Electroweak Interactions and Unified Theories, Rencontres de Moriond, La Thuile, Italy.

Müller-Mellin, R., et al. (1995), COSTEP—Comprehensive Suprathermal And Energetic Particle Analyser, *Sol. Phys.*, *162*, 483–504, doi:10.1007/BF00733437.

NCRP (1989), Guidance on radiation received in space activities, *Rep. 98*, Bethesda Md.

NCRP (2000), Radiation protection guidance for activities in low-Earth orbit, *Rep. 132*, Bethesda, Md.

NCRP (2002), Operational radiation safety program for astronauts in low-Earth orbit: A basic framework, *Rep. 142*, Bethesda, Md.

Nymmik, R. A. (2000), Time lag of galactic cosmic ray modulation: Conformity to general regularities and influence on particle energy spectra, *Adv. Space Res.*, *26*(11), 1875–1878, doi:10.1016/S0273-1177(99)01242-9.

Nymmik, R. A., M. I. Panasyuk, T. I. Pervaya, and A. A. Suslov (1992), A model of galactic cosmic ray fluxes, *Nucl. Tracks Radiat. Meas.*, *20*(3), 427–429, doi:10.1016/1359-0189(92)90028-T.

Nymmik, R. A., M. I. Panasyuk, T. I. Pervaya, and A. A. Suslov (1994), An analytical model, describing dynamics of galactic cosmic ray heavy particles, *Adv. Space Res.*, *14*, 759–763, doi:10.1016/0273-1177(94)90538-X.

O'Neill, P. M. (2006), Badhwar–O'Neill galactic cosmic ray model update based on Advanced Composition Explorer (ACE) energy spectra from 1997 to present, *Adv. Space Res.*, *37*, 1727–1733, doi:10.1016/j.asr.2005.02.001.

O'Neill, P. M. (2010), Badhwar-O'Neill 2010 galactic cosmic ray flux model—Revised, *IEEE Trans. Nucl. Sci.*, *57*(6), 3148–3153.

Obermeier A., M. Ave, P. Boyle, C. Höppner, J. Hörandel, D. Müller (2011), Energy spectra of primary and secondary cosmic-ray nuclei measured with TRACER, *Astrophys. J.*, *742*(1), 14, doi:10.1088/0004-637X/742/1/14.

Palfalvi, J., J. Szabo, B. Dudas, I. Feher, and I. Eordogh (2008), Cosmic ray detection on the Foton-M2 satellite by a track etch detector stack, *Adv. Space Res.*, *42*, 1030–1036, doi:10.1016/j.asr.2008.05.007.

Parker, E. N. (1965), The passage of energetic charged particles through interplanetary space, *Planet. Space Sci.*, *13*, 9–49, doi:10.1016/0032-0633(65)90131-5.

Ryu, K., G.-H. Shin, H.-M. Kim, S. Kim, D.-H. Ko, H. Kim, and K. Min (2007), Simulation and ground test for the total ionizing dose effects of STSAT-2, *J. Korean Phys. Soc.*, *50*(95), 1552–1556, doi:10.3938/jkps.50.1552.

Shikaze, Y., et al. (2007), Measurements of 0.2–20 GeV/n cosmic-ray proton and helium spectra from 1997 through 2002 with the BESS spectrometer, *Astropart. Phys.*, *28*, 154–167, doi:10.1016/j.astropartphys.2007.05.001.

Sihver, L., T. Sato, M. Puchalska, and G. Reitz (2010), Simulations of the MATROSHKA experiment at the international space station using PHITS, *Radiat. Environ. Biophys.*, *49*, 351–357, doi:10.1007/s00411-010-0288-y.

Simpson, J. A. (1983), Elemental and isotopic composition of the galactic cosmic rays, *Annu. Rev. Nucl. Part. Sci.*, *33*, 323–382, doi:10.1146/annurev.ns.33.120183.001543.

Stone, E. C., A. M. Frandsen, R. A. Mewaldt, E. R. Christian, D. Margolies, J. F. Ormes, and F. Snow (1998), The Advanced Composition Explorer, *Space Sci. Rev.*, *86*, 1–22, doi:10.1023/A:1005082526237.

Tylka, A. J., Jr., J. H. Adams, P. R. Boberg, B. Brownstein, W. F. Dietrich, E. O. Flueckiger, E. L. Petersen, M. A. Shea, D. F. Smart, and E. C. Smith (1997), CREME96: A of the cosmic ray effect on micro-electronics code, *IEEE Trans. Nucl. Sci.*, *44*, 2150–2160, doi:10.1109/23.659030.

Usoskin, I. G., K. Mursula, H. Kananen, and G. A. Kovaltsov (2001a), Dependence of cosmic rays on solar activity for odd and even solar cycles, *Adv. Space Res.*, *27*, 571–576, doi:10.1016/S0273-1177(01)00084-9.

Usoskin, I. G., K. Mursula, and J. Kangas (2001b), On-line database of cosmic ray intensities, paper presented at 27th International Cosmic Ray Conference, Copernicus Gesellschaft, Hamburg, Germany, 7–15 Aug.

Usoskin, I. G., K. Alanka-Huotari, G. A. Kovaltsov, and K. Mursula (2005), Heliospheric modulation of cosmic rays: Monthly reconstruction for 1951–2004, *J. Geophys. Res.*, *110*, A12108, doi:10.1029/2005JA011250.

Wakely, S. P., et al. (2008), First measurements of cosmic-ray nuclei at high energy with CREAM, *Adv. Space Res.*, *42*(3), 403–408, doi:10.1016/j.asr.2007.03.080.

Wiedenbeck, M. E. (2011), Cosmic-ray energy spectra and time variations in the local interstellar medium: Constraints and uncertainties, *Space Sci. Rev.*, doi:10.1007/s11214-011-9778-8, in press.

4.3 Paper II - Mrigakshi et al. 2013a

How galactic cosmic ray models affect the estimation of radiation exposure in space

Alankrita Isha Mrigakshi, Daniel Matthiä, Thomas Berger, Günther Reitz and Robert F. Wimmer-Schweingruber, ***Advances in Space Research***, Volume 51, Issue 5, p. 825-834, 2013, doi:10.1016/j.asr.2012.10.017

Available online at www.sciencedirect.com

SciVerse ScienceDirect

Advances in Space Research 51 (2013) 825–834

ADVANCES IN SPACE RESEARCH (a COSPAR publication)

www.elsevier.com/locate/asr

How Galactic Cosmic Ray models affect the estimation of radiation exposure in space

Alankrita Isha Mrigakshi [a,*], Daniel Matthiä [a], Thomas Berger [a], Günther Reitz [a], Robert F. Wimmer-Schweingruber [b]

[a] DLR – German Aerospace Center, Institute of Aerospace Medicine, Department of Radiation Biology, Linder Hoehe 1, 51147 Cologne, Germany
[b] Christian-Albrechts-University Kiel, Institute of Experimental and Applied Physics, Extraterrestrial Physics, Leibnizstr. 11, 24098 Kiel, Germany

Received 29 June 2012; received in revised form 27 September 2012; accepted 22 October 2012
Available online 2 November 2012

Abstract

The radiation environment in space is a major concern for human spaceflight because of the adverse effects of high levels of radiation on astronauts' health. Therefore, it is essential to perform radiation risk assessments already during the concept studies of a manned mission. Galactic Cosmic Rays (GCR) have been identified to be one of the primary sources of radiation exposure in space.

This work presents an evaluation of the radiation exposure caused by GCR between 1970 and 2011 in near-Earth interplanetary space and at the orbit of the International Space Station (ISS) by making numerical simulations with the Monte–Carlo framework GEANT4. Commonly used GCR models – CREME96, CREME2009 and Badhwar–O'Neill2010 are used to describe the GCR spectra and the differences arising from the application of these different models in terms of absorbed dose and dose equivalent rates are investigated. Additionally, the depth distribution of the dose quantities and the relative contribution of particles with different energies to the total exposure during solar maximum and minimum conditions are studied.

The differences in the spectra, described by the models, result in considerable differences in the estimation of the radiation exposure.

Keywords: Radiation exposure in low-Earth orbit and near-Earth interplanetary space; Galactic Cosmic Ray models; Monte–Carlo simulations

1. Introduction

The presence of high-energy ionizing radiation in space poses substantial risk to astronauts' health. The assessment of the health risks from radiation is therefore of paramount importance (NCRP, 1989, 2000, 2002, 2006; Cucinotta et al., 2001; Cucinotta and Durante, 2006). The radiation exposure varies both spatially and temporally as a result of varying characteristics of the radiation field such as intensity, energy distribution and its composition. This is observed, for instance, at Low-Earth Orbits (LEO) where the exposure is greater than on Earth owing to the thinning and eventually the absence of atmosphere at higher altitudes (Berger, 2008). The exposure by Galactic Cosmic Rays (GCR) at LEO is smaller in comparison to near-Earth interplanetary space due to the reduced intensity of the GCR caused by the shielding effect of the Earth's magnetosphere and the shadowing effect of the Earth (Adams et al., 1983; Cooke et al., 1991). Therefore, with Moon and Mars being potential destinations for manned spaceflight beyond LEO, the evaluation of radiation induced health risks is a necessary prerequisite for human exploration missions.

The quantification of the health risks requires the determination of dose quantities that are related to the biological effects of ionizing radiation. These quantities are recommended by the International Commission on Radiological Protection (ICRP, 1991) and can be estimated by performing computer simulations using radiation transport codes (NCRP, 2002). The resulting quantities from simulations contain uncertainties that arise from various factors

* Corresponding author. Tel.: +49 2203 6013147; fax: +49 2203 61970.
E-mail address: alankrita.mrigakshi@dlr.de (A.I. Mrigakshi).

0273-1177/$36.00
http://dx.doi.org/10.1016/j.asr.2012.10.017

such as the validity of the physical models in the transport code, the level of detail of the geometry describing the target and its environment, and the models specifying the composition and the spectra of the different components of the external radiation field. These uncertainties need to be evaluated in order to assess the accuracy of the dose estimates.

An evaluation of models comparing the predicted GCR spectra at near-Earth interplanetary space with measurements was presented in Mrigakshi et al. (2012). The study showed significant discrepancies in the model spectra with respect to observations for several epochs in the last decade and some of the results relevant for the work presented here are summarized in Section 1.2.

The goal of this work besides estimating the radiation exposure in space is to evaluate the consequence of the differences in the model spectra on the estimated radiation exposure.

This paper investigates the effect of applying different GCR models on the estimated dose quantities inside a simple geometry for locations outside and inside the Earth's magnetosphere over the last four decades. The dependency of the dose on depth in the target and on the particle energy during solar maximum and minimum conditions is studied as well.

1.1. GCR models

Galactic Cosmic Rays have been identified to be one of the primary sources of radiation exposure in space both outside and inside the Earth's magnetosphere (NCRP, 2000, 2006). They consist of about 98% charged nuclei with H constituting ~87%, He ~12% and heavier nuclei ~1% of the entire nuclear component (Simpson, 1983). The contribution of lighter nuclei to the radiation exposure in space is substantial due to their large elemental abundances while the heavy ions gain significance considering the greater biological effect related with the higher specific energy loss within a material which is proportional to the square of charge (Mewaldt, 1994; Cucinotta et al., 2001). Energetic heavy ions like Fe are able to penetrate inside the spacesuits and spacecrafts and by interacting with astronauts' bodies can cause extensive cellular damage due to the large energy deposition along their densely ionizing tracks (Cucinotta and Durante, 2009). Above iron the GCR particle species being much scarcer do not play a vital role.

Therefore, for the purpose of radiation protection in near-Earth interplanetary space and at Low-Earth Orbits it is sufficient to consider GCR nuclei between $1 \leqslant Z \leqslant 26$ (Z = atomic number) with energies ranging from 10 to 10^5 MeV/nuc. Three commonly used GCR models CREME96 (Tylka et al., 1997; https://creme.isde.vanderbilt.edu/), its updated version CREME2009 (https://creme.isde.vanderbilt.edu/) and Badhwar–O'Neill2010 (O'Neill, 2010) which is referred to as BON2010 in this paper were employed. The models are able to provide spectra of the relevant particles over the energy range relevant for radiation protection in space. In the year 2010, CREME96 was announced to be valid only from 1950 until 1997. Due to this late announcement it has been applied for times after its valid period (e.g. in Gustafsson et al. (2010), Sihver et al. (2010), Kwangsun et al. (2007), Palfalvi et al. (2008)) and therefore is included in this work for years 1997–2011 as well.

Each model describes the spectra of the nucleonic component of GCR beyond the heliospheric modulation region, the Local Interstellar Spectrum (LIS), and the modulation inside the heliosphere which is related to the solar activity. They provide the differential energy distribution of the GCR particle flux which is the number of particles per area, time, solid angle and particle energy. This energy spectrum is calculated for a selected point of time and in near-Earth interplanetary space corresponding to a distance of 1 AU from the sun outside the Earth's magnetosphere.

For a specific orbit the CREME package provides the so-called geomagnetic transmission function (Tylka et al., 1997; https://creme.isde.vanderbilt.edu/) which can be used to calculate the GCR spectra inside the Earth's magnetosphere. The geomagnetic transmission function gives the fraction of particles reaching an orbit of interest as a function of the particles' magnetic rigidity which is defined as the ratio of its momentum to charge. It also accounts for the effect of solid Earth's obstruction to the incoming radiation. In this work, the spectra for LEO were determined from the models by scaling the GCR spectra at 1 AU by the orbit-averaged geomagnetic transmission function derived for the International Space Station (ISS) with an inclination of 51.6° and an altitude of 350 km.

1.2. GCR models vs. measurements

As mentioned earlier, the work presented in Mrigakshi et al. (2012) showed a comparison study between models and measured GCR spectra. The investigation was performed for the GCR spectra at near-Earth interplanetary space. Large discrepancies were observed between the measured and model spectra during several periods in the last decades. During August 2000, for instance, the CREME96 model showed the largest differences of about 190% for H and about 100% for He fluxes integrated over the energy range 210 MeV/nuc to 24 GeV/nuc in comparison to the measurements from the BESS instrument (Shikaze et al., 2007). CREME2009 also showed large deviations from the experiment by about 73% for H and 44% for He while BON2010 showed about 27% and 18% respectively. For the seven H and He measurements investigated in Mrigakshi et al. (2012) between July 1992 and August 2002, BON2010 showed the least deviation from the experimental data. The models were also tested for the accuracy of the description of heavy nuclei by comparing GCR O and Fe spectra with continuous measurements taken between August 1997 and September 2010 by the Advanced Composition Explorer (ACE) spacecraft (Stone et al., 1998; http://www.srl.

caltech.edu/ACE/ASC/level2) over an energy range of about 70–470 MeV/nuc. BON2010 for almost all time periods showed the least deviation from the data indicating that among the three models it is the most accurate GCR model for the recent past.

The peak integrated flux of O and Fe spectra measured by ACE during the extended solar minimum between 2008 and 2010 was found to be about 20% greater than the previous solar minimum in 1998. However, all the models failed to describe the elevated particle fluxes for this time period.

2. Dose calculation procedure

To estimate the exposure numerically, the transport of radiation was simulated using the GEANT4 Monte–Carlo framework (**GE**ometry **AN**d **T**racking, Agostinelli et al., 2003; Allison et al., 2006).

2.1. Simulation setup

GEANT4 version 4.9.3 patch 02 was used to implement the geometry, to simulate the particle transport through the target and to calculate the resulting radiation exposure. In this work, the recommended hadronic and electromagnetic physics model lists (*QGSP_BERT* and *emstandard_opt3*) were selected to calculate the transport of primary and secondary particles in the defined target (see GEANT4 Physics Reference Manual in http://geant4.cern.ch/G4UsersDocuments/UsersGuides/PhysicsReferenceManual/html/ PhysicsReferenceManual.html for details). Due to the limitation of the intrinsic models in GEANT4.9.3 describing inelastic nucleus–nucleus interactions to energies below 10 GeV/nuc, an interface (Koi et al., 2003; Sihver et al., 2008) to the external *JQMD/JAM* model (Niita et al., 1995; Nara et al., 1999) was applied to extend the simulations to higher energies. Such interactions are important as they can lead to projectile and target fragmentation thereby affecting the amount of the radiation exposure. During this study it was found that there is a significant contribution of GCR nuclei with energies above 10 GeV/nuc to exposure especially at low-Earth orbit (see Section 3.3).

A first approach to estimate the radiation exposure is to use a spherical water phantom as target. In this work a water sphere of 25 cm in radius consisting of 100 shells with a thickness of 2.5 mm each was adopted as the irradiated target. A spherical radiation source with a radius of 35 cm, enveloping the water sphere was created to simulate particles from $1 \leqslant Z \leqslant 26$ with energies between 10 MeV/nuc and 100 GeV/nuc inwards onto the target with an isotropic angular distribution.

2.2. Radiation protection quantities

The following dose quantities that were calculated are amongst the principal dosimetric quantities in radiation protection as recommended by the ICRP 60 (ICRP, 1991) and are defined in Eqs. (1) and (2)

I. Absorbed dose D in the unit J/kg or gray (Gy):

$$D = \frac{d\bar{\varepsilon}}{dm} \tag{1}$$

where $d\bar{\varepsilon}$ is the mean energy imparted in a volume of mass dm by ionizing radiation.

Different types of radiation have different effects on human tissue. Some produce greater biological damage than others for the same amount of energy they impart. This information regarding the extent of biological damage caused cannot be conceived by absorbed dose alone and consequently the dose equivalent was introduced:

I. Dose equivalent H in the unit J/kg or sievert (Sv):

$$H = D \cdot Q \tag{2}$$

where D is the mean absorbed dose in the target and Q is the mean quality factor related to the biological effectiveness of the radiation and is given as a function of the unrestricted Linear Energy Transfer (LET) in water defined in ICRP 60 as the Q-LET relationship (ICRP, 1991). The unrestricted LET is the energy lost by a charged particle divided by the path length.

In GEANT4, information such as deposited energy is registered in steps along a particle's trajectory inside the target. Therefore, to calculate the absorbed dose in a certain volume the energy deposited for each step in the volume is summed up and divided by the mass of the volume. To calculate the dose equivalent in the volume, the deposited energy for each step is multiplied by the quality factor, which is calculated by applying the Q-LET relationship.

2.3. Method for GCR dose estimation

Simulation of the transport of GCR particles, especially heavy nuclei at high energy, is very time consuming. A simplified procedure was thus applied in order to calculate the radiation exposure for many different input spectra from different models and for different time periods under investigation. An example to illustrate this procedure is shown in Fig. 1. The GCR spectrum for H nuclei in near-Earth interplanetary space was derived using BON2010 model for January 1998 (Fig. 1a).

A number of primary particles N with energies uniformly distributed over logarithmic energy scale were simulated. For each energy bin i the dose per primary particle d_i was calculated (Fig. 1b): $d_i = D_i/N_i$, where D_i is the dose from all primary particles N_i in that bin.

The resulting dose per primary particle d_i for each energy bin was then scaled (Fig. 1c) by f_i, which is the GCR particle energy distribution integrated over the

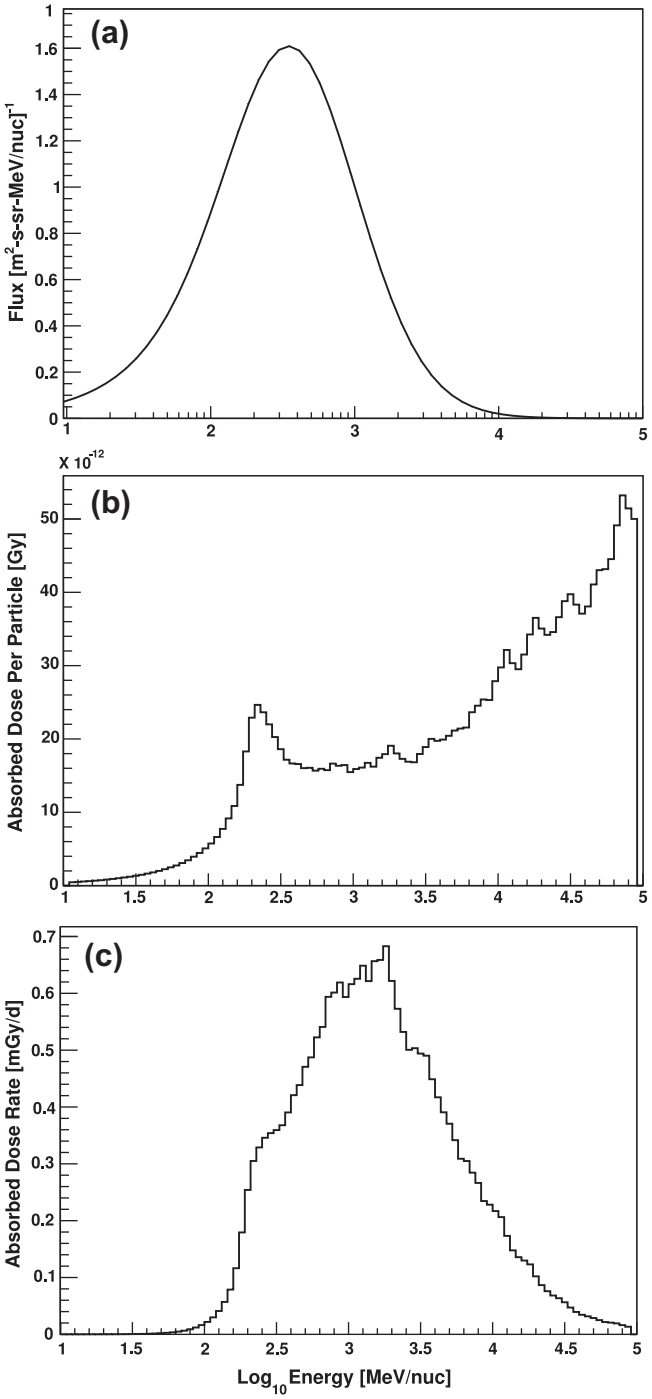

Fig. 1. Graphical representation of the procedure used to calculate the GCR exposure as described in Section 2.3. Fig. 1a: Energy distribution of GCR H nuclei derived from BON2010 model for the January 1998. Fig. 1b: Dose per primary particle (H nuclei) in each energy bin. Fig. 1c: Dose calculated by multiplying absorbed dose per particle with the corresponding GCR flux at each energy bin.

energy bin i, the simulated radiation source surface and the solid angle of emission. The sum over all energy bins n was then calculated to obtain the dose rate dD/dt:

$$\frac{dD}{dt} = \sum_{i=1}^{n} f_i d_i \tag{3}$$

This indirect method was adopted due to its flexibility and practicality which allows an efficient calculation of doses using three models over the last 40 years with a resolution of ten dates per year. The method was validated by comparing the calculated dose quantities with the results of estimations using the GCR flux spectra directly as an input for the transport code. The difference in the mean absorbed dose from hydrogen and iron particles calculated from both the methods was found to be less than 3%.

In Fig. 1b, the peak observed around 300 MeV/nuc can be attributed to protons whose range in water is about 50 cm corresponding to the diameter of the simulated water sphere. All protons above this threshold keep a fraction of their initial energy regardless of their incident angle on the target and deposit less energy to the sphere due to the decreasing LET at higher energies.

3. GCR exposure analysis

The work presented in Mrigakshi et al. (2012) regarding the evaluation of the GCR models showed discrepancies between the model spectra and measurements. Accordingly, the differences arising in the dose quantities on applying these models were investigated for the last four decades and are discussed in this section.

3.1. Radiation exposure using different GCR models

The absorbed dose and the dose equivalent rate in the water sphere induced by the GCR particles were calculated for ten dates per year starting from 1970 until the end of the year 2010. The spectra were derived from CREME96, CREME2009 and BON2010 models. The dose rate variation over time in near-Earth interplanetary space and at the ISS orbit is shown in Fig. 2a and b respectively.

The GCR intensity close to Earth is modulated by the solar activity and is the highest during the solar minimum periods and vice versa. For example, the GCR O and Fe flux integrated over the measured energy range (~70–470 MeV/nuc) by the ACE spacecraft was about 4–6 times greater during the solar minimum in 1997–1998 than during the solar maximum in 2000–2001 (Mrigakshi et al., 2012). In Fig.2 the temporal variation in the dose rates as a result of the variation in GCR intensity is clearly visible.

Although the work in Mrigakshi et al. (2012) showed several weaknesses in all the models, BON2010 model exhibited the best agreement with measurements for most of the times in the last decade (see Section 1.2). Based on the BON2010 model, the absorbed dose and dose equivalent rates for near-Earth interplanetary space (Fig. 2a) are estimated to range from ~0.14 to ~0.38 mGy/d and from ~0.45 to ~1.18 mSv/d from solar maximum to solar minimum periods respectively. Fig. 2a shows that the dose rates increased by over a 100% from solar maximum e.g. in 1990–1992 to minimum period in 1997–1998.

The GCR intensity inside the magnetosphere is reduced by the Earth's magnetic field which has a shielding effect on

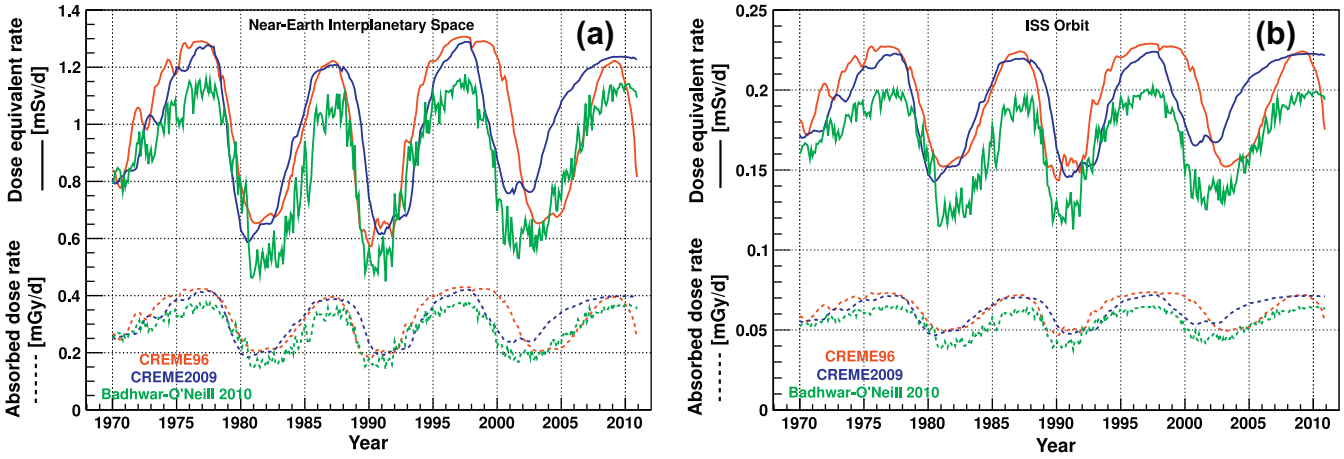

Fig. 2. Absorbed dose (dashed lines) and dose equivalent rates (solid lines) in the water sphere calculated from the spectra described by CREME96 (red), CREME2009 (blue) and BON2010 (green) for near-Earth interplanetary space (Fig. 2a) and for ISS orbit (Fig. 2b). (For interpretation of the references to color in this figure legend, the reader is referred to the web version of this article.)

the charged particles and only those with sufficient rigidity are able to penetrate inside the magnetosphere. Nuclei with low rigidities are thus affected the most and are unable to penetrate deep into the magnetosphere. Due to this reduction in the GCR intensity the exposure at the ISS orbit is reduced as well. For ISS orbit (Fig. 2b) the absorbed dose and dose equivalent rates range from 0.038 to 0.066 mGy/d and from 0.11 to 0.20 mSv/d from solar maximum to solar minimum periods. The variation in the dose rates from solar minimum periods to solar maximum is not as large as observed in near-Earth interplanetary space due to the reduced GCR particles with energies below a few GeV/nuc where the modulation is the highest.

The predicted dose rates based on the CREME models exceed the values obtained with BON2010 at several epochs. For instance in January 1998 the absorbed dose rates calculated for near-Earth interplanetary space using CREME96, CREME2009 and BON2010 are found to be ~0.42, ~0.41 and ~0.37 mGy/d respectively. The dose equivalent rates for the same time and location are ~1.27 mSv/d from CREME96, ~1.26 mSv/d from CREME2009 and ~1.14 mSv/d from BON2010. The high dose rate using CREME96 during the solar maximum of 2000–2002 is due to the overestimation of the GCR intensity by the model which was observed in Mrigakshi et al. (2012) and the values estimated with the BON2010 model are expected to be much closer to the real values at that time.

As mentioned in Section 1.2, during the last solar minimum in 2008–2010, a significant increase in the GCR intensity in comparison to the previous solar minimum in 1998 was observed by ACE. The resulting exposure during this time should therefore be greater than during solar minimum periods in the recent past. However this is not reflected in the results of this work because the GCR models do not describe the enhanced particle fluxes (Mrigakshi et al., 2012). It can therefore be assumed that the estimated radiation exposure for this epoch is underestimated by all three models under investigation. Since only a limited part of the entire energy spectra is measured by ACE, it is difficult to draw conclusions regarding the accuracy of models at higher energies and subsequently to account for the differences in the dose calculations. For example, at the time when GCR intensity reached maximum in late 2009, the energy-integrated O flux measured between ~80 and 230 MeV/nuc by the ACE spacecraft is underestimated by BON2010 by about 30% and the Fe flux integrated between ~150 and 460 MeV/nuc by about 26% (Mrigakshi et al., 2012). The underestimation in the dose is however expected to be less than 26–30% as the contribution to the total dose from particles at these energies (see Fig. 6 and Table 1) is relatively small especially at ISS orbit (Fig. 6b).

The quality factor Q over time for the GCR spectra was calculated by dividing the dose equivalent rate by the absorbed dose rate estimated for the water sphere. The average Q over the last 40 years is about 3.1 from all the models for both locations in space. The increase in Q from ISS orbit to near-Earth interplanetary space is about 2% from BON2010 and 1% from the CREME models.

To quantify the difference in the estimated radiation exposure, the ratio of the dose rates based on the CREME models to the BON2010 model were calculated. The resulting relative absorbed dose rates and dose equivalent rates are presented in Fig. 3 for near-Earth interplanetary space (Fig. 3a) and for the ISS orbit (Fig. 3b).

The differences between the models are more or less the same for absorbed dose and dose equivalent rates. The average difference in the dose rates over the last 40 years for both locations in space is about 16%. At certain points in time, however, the differences are significantly larger. The dose quantities estimated with the CREME96 model between the years 1999–2002, for instance, differ from the results using the BON2010 on average by approximately 60% for near-Earth interplanetary space and for the ISS orbit by approximately 40%. The average differences in

Table 1
Contribution of GCR particles with energies lying in different energy ranges to the total absorbed dose rate dD/dt and dose equivalent rate dH/dt estimated by applying the BON2010 model in an unshielded water sphere of radius 25 cm during solar minimum (January 1998) and solar maximum (August 2002) periods.

Near-earth interplanetary space								
Solar activity	Total dose		0.1–1 GeV/nuc		1–10 Gev/nuc		10–100 Gev/nuc	
	dD/dt (μGy/d)	*dH/dt* (μSv/d)	*dD/dt* (μGy/d)	*dH/dt* (μSv/d)	*dD/dt* (μGy/d)	*dH/dt* (μSv/d)	*dD/dt* (μGy/d)	*dH/dt* (μSv/d)
Minimum	368.0	1136.9	167.8	594.8	174.4	478.9	22.0	45.8
Relative contribution	100%		45.6%	52.3%	47.4%	42.1%	6.0%	4.0%
Maximum	180.6	570.9	54.8	222.7	105.5	303.8	19.6	41.2
Relative contribution	100%		30.3%	39.0%	58.4%	53.2%	10.9%	7.2%
ISS orbit (Altitude – 350 km and inclination – 51.6°)								
Minimum	64.3	198.3	10.8	47.4	39.6	121.5	13.8	29.0
Relative contribution	100%		16.9%	23.9%	61.6%	61.3%	21.5%	14.9%
Maximum	43.3	131.1	4.2	20.1	26.8	84.7	12.3	26.2
Relative contribution	100%		9.7%	15.3%	61.8%	64.7%	28.5%	20.0%

the dose rates calculated from CREME2009 model for time periods between 2002 and 2006 are ~35% for near-Earth interplanetary space and about 30% for the ISS orbit. The maximum differences observed in the estimation of radiation exposure at near-Earth interplanetary space using the CREME96 model is more than a factor of two whereas for the ISS orbit is about 1.6.

GCR models are a necessary prerequisite for making predictions of the radiation exposure for future manned missions to space. The choice of GCR model can affect the level of accuracy in the projected dose estimations leading to uncertainties in the duration planned for a mission. It also influences the selection of astronauts especially as the amount of doses accumulated during previous spaceflights is strictly taken into consideration (NCRP, 2000) as well.

3.2. Variation of dose rate with depth

The radiation risk assessment for astronauts involves the determination of the radiation load received in all relevant organs of the human body (NCRP, 2002). These organs are of course positioned at different sites and depths inside the body. For this reason, the simulated water sphere was built up of shells such that a depth-dose analysis could be performed by estimating the exposure at the shell corresponding to the mean shielding of an organ.

The dose rates plotted against depth in the water sphere during solar minimum in January 1998 and solar maximum in August 2002 are shown in Fig. 4a for near-Earth interplanetary space and in Fig. 4b for ISS orbit. The dose quantities presented here were calculated using the GCR spectra described by BON2010 model.

The dose rates are higher during solar minimum with respect to solar maximum as was also observed in Fig. 2 which is due to the fact that the radiation exposure which is directly related with the GCR intensity varies with solar activity (Section 3.1). In Fig. 4a and b it is visible that while the dose equivalent rate decreases with depth, the absorbed dose increases slightly at LEO and remains fairly constant in near-Earth interplanetary space. The highest dose equivalent is induced in the outer shells of the sphere where the shielding is lower and the dose equivalent reduces with depth owing to the shielding by the outer water shells.

In order to see how the depth-dose rates behave over time, the absorbed dose and dose equivalent rates in different shells located at certain depths inside the water sphere between 1970 and 2011 are shown in Fig. 5a for near-Earth interplanetary space and in Fig. 5b for ISS orbit. The two quantities were calculated for shells starting from the outermost (0–0.25 cm) and for three inner shells (1–1.25 cm, 5–5.25 cm and 10–10.25 cm). The outermost shell corresponds to an average shielding of 12.9 g/cm^2 and the dose can be used as an estimate of the skin dose whereas the dose in the shell that lies between 1 and 1.25 cm (average shielding 14.7 g/cm^2) can be considered as the dose in an inner organ or the skin dose beneath a shielding of 1 cm of water, etc.

As seen in Fig. 4, the opposite behavior of the dose equivalent and the absorbed dose rates with depth is clearly visible for all periods in time in Fig. 5b as well. The increase in the absorbed dose rates with depth for outside the magnetosphere is not visible in comparison to ISS orbit. The dose rates are similar for all depths and the curves are difficult to distinguish in Fig. 5a. The dose equivalent rates for outside the magnetosphere also decreases with depth.

3.3. Variation of dose rate with particle energy

Radiation exposure varies with the energy, flux and the type of the incoming particles. To investigate the contribution of different particle energies to the total exposure, the integrated absorbed dose and dose equivalent rates were calculated as a function of energy. The dose quantities were estimated by applying the BON2010 model.

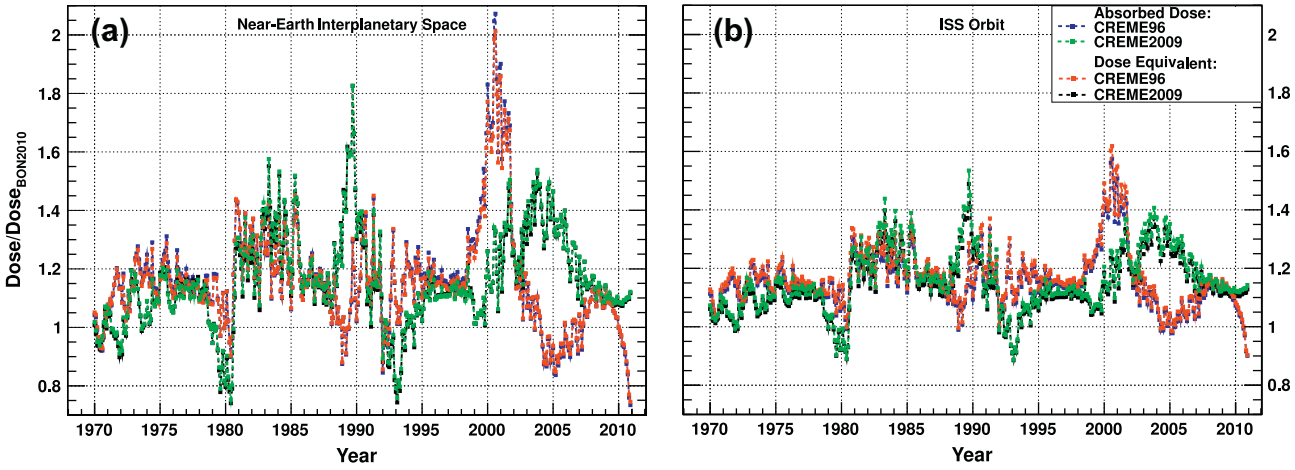

Fig. 3. Ratio of the dose rates based on the CREME models to the BON2010 model. Relative absorbed dose (blue) and dose equivalent rates (red) from CREME96 and relative absorbed dose (green) and dose equivalent rates (black) from CREME2009 for near-Earth interplanetary (Fig. 3a) space and for the ISS orbit (Fig. 3b). (For interpretation of the references to color in this figure legend, the reader is referred to the web version of this article.)

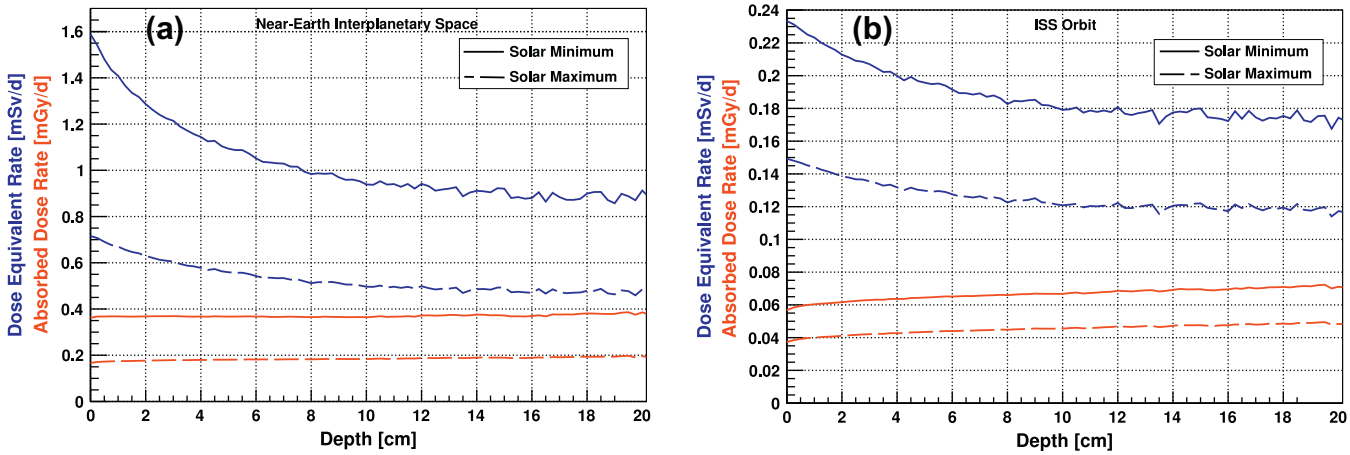

Fig. 4. Variation of absorbed dose (red) and dose equivalent rates (blue), estimated by applying the BON2010 model, with depth during solar minimum (January 1998) and solar maximum (August 2002) conditions for near-Earth Interplanetary space (Fig. 4a) and ISS orbit (Fig. 4b). (For interpretation of the references to color in this figure legend, the reader is referred to the web version of this article.)

Fig. 6 shows the absorbed dose and dose equivalent rates integrated from 10 MeV/nuc to 100 GeV/nuc for solar minimum (January 1998) and solar maximum (August 2002) conditions for near-Earth interplanetary space (Fig. 6a) and ISS orbit (Fig. 6b). The figures provide information about the significance of different particle energies on the radiation exposure. The relative contribution of GCR particles with energies lying in different energy ranges to the total dose rates have been quantified in Table 1.

As mentioned in Section 3.1 and observed in Fig. 2, the radiation exposure which is directly related to the GCR intensity varies with the solar activity. It is the highest during solar minimum and the least during solar maximum. This can be also seen in Fig 6 and Table 1 for both the locations in space. The ratio of the doses in August 2000 to January 1998 in near-Earth interplanetary space is about two and at ISS orbit about 1.5. The lower ratio for the ISS orbit can be attributed to the fact that the low energetic particles that are strongly modulated by the solar activity also experience the strongest shielding effect of the geomagnetic field and are unable to penetrate into low orbits as discussed earlier in Section 3.1. As a result of this, the effect of particle energies on the radiation exposure at ISS orbit in comparison with outside the magnetosphere is dominated by particles with energies above 1 GeV/nuc as shown in Fig. 6b and Table 1. While about 90% of total dose for near-Earth interplanetary space comes from particles with energies between 100 MeV/nuc and 10 GeV/nuc (Fig. 6a), about 80–90% of the total dose at ISS orbit is caused by particles with higher energies between 1 and 100 GeV/nuc Fig. 6b).

In addition to this result, the contribution of GCR particles with energies above 100 GeV/nuc was also estimated in order to investigate the importance of such high particle energies on the radiation exposure. The dose contribution

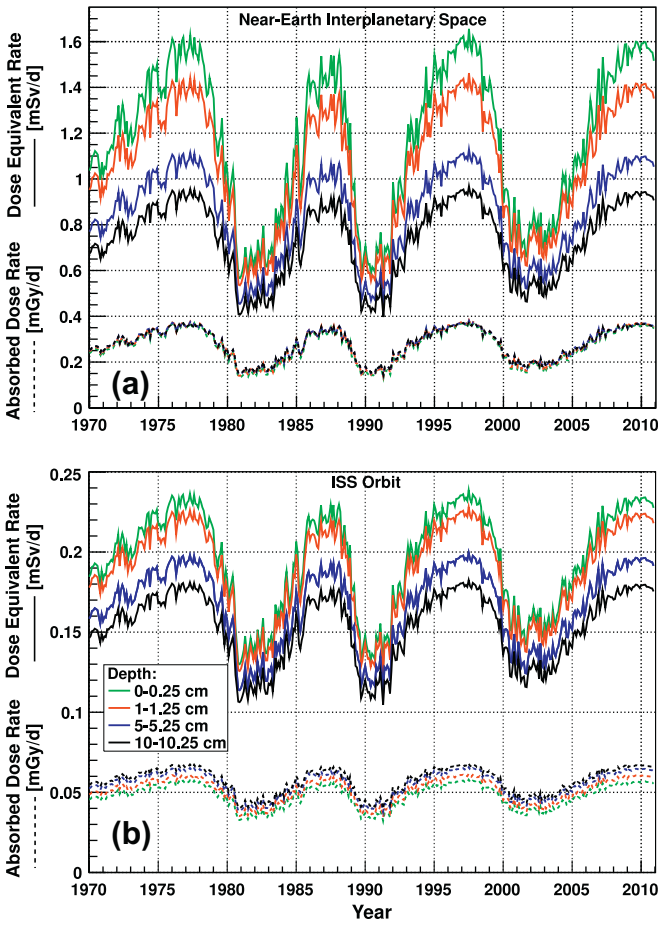

Fig. 5. Absorbed dose and dose equivalent rates, estimated by applying the BON2010 model, at selected depths in the water sphere based on the GCR intensities given by the BON2010 model for near-Earth interplanetary space (Fig. 5a) and for the ISS orbit (Fig. 5b). (For interpretation of the references to color in this figure, the reader is referred to the web version of this article.)

from selected nuclei, most relevant for dosimetery (H, He, C, O, Ne, Mg, Si, S, Ca, Fe), with energies between 100 and 175 GeV/nuc was found to be less than 1% relative to the total dose from particle energies ranging from 10 to 175 MeV/nuc for both solar maximum and minimum periods at ISS orbit as well as in near-Earth interplanetary space.

4. Conclusion and outlook

Calculations of the absorbed dose and dose equivalent rate in an unshielded water sphere exposed to GCR intensities predicted by CREME96, CREME2009 and Badhwar–O'Neill2010 models for a location outside the Earth's magnetosphere and for the ISS orbit were performed. The goal was to estimate the differences in the derived dose quantities resulting from the different descriptions of the GCR spectra from the models. Additionally, dose rate as a function of depth and primary particle energy were studied. Important outcomes of the work are the following:

- The GCR induced absorbed dose rate in an unshielded water sphere in near-Earth interplanetary space was estimated to range from about 0.14–0.4 mGy/d and the dose equivalent rate from about 0.45–1.18 mSv/d during solar maximum to minimum periods whereas at ISS orbit the absorbed dose range from about 0.038–0.066 mGy/d and the dose equivalent from about 0.11–0.20 mSv/d on applying the Badhwar–O'Neill2010 model. Mrigakshi et al. (2012) concluded that, based on measurements, the Badhwar–O'Neill2010 model is more accurate than the CREME models for most of the last 10–15 years. However, all models fail to describe the increase in GCR intensity in 2009 and 2010 and the accuracy of all models for the description of H and He nuclei cannot be judged thoroughly. It can be assumed that the results presented in this work obtained with the BON2010 model are the best estimate of the real

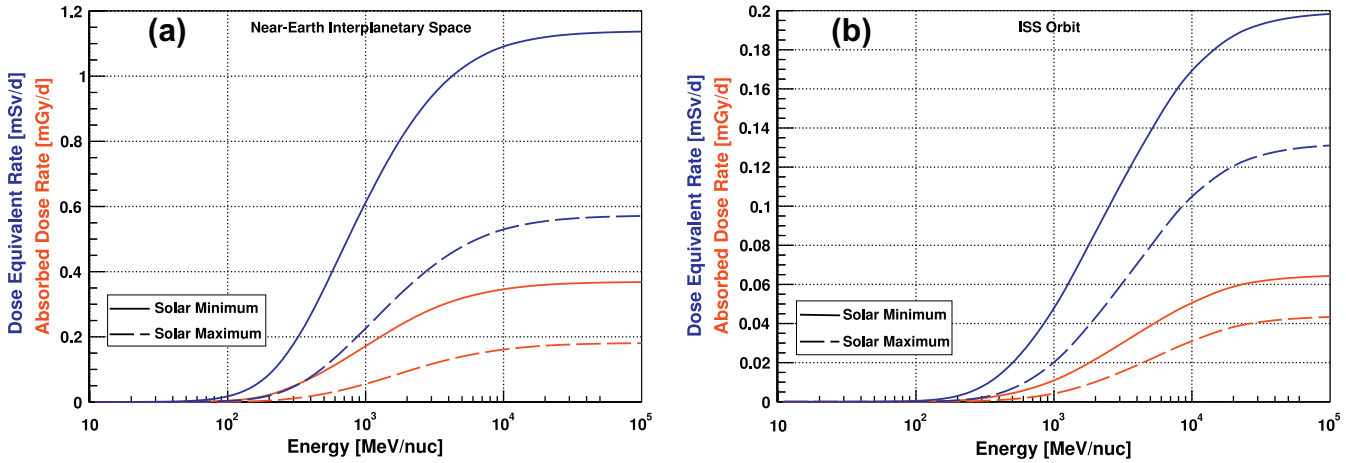

Fig. 6. Integrated absorbed dose and dose equivalent rates calculated by applying the BON2010 model, plotted in red and blue respectively, over energy during solar minimum (January 1998) and solar maximum (August 2002) conditions for near-Earth interplanetary space (Fig. 6a) and ISS orbit (Fig. 6b). (For interpretation of the references to color in this figure legend, the reader is referred to the web version of this article.)

values. However the presented dose rates for the recent deep solar minimum are assumed to underestimate the true radiation exposure.

- There are significant variations in the calculated radiation exposure as a result of the differences in the description of GCR spectra by using the three models. The average differences in the dose rates over the last 40 years for both the locations in space are about 16%. However, large differences were observed during several periods particularly between 1999 and 2006 the highest of which was found to be greater than 100% for the end of the year 2000 for near-Earth interplanetary space. The estimations made for the epoch from 1999 to 2002 differ by about 40% and 60% for ISS orbit and near-Earth interplanetary space respectively (CREME96 vs. BON2010); and the estimations for 2002–2006 differ by about 30% and 35% for ISS orbit and near-Earth interplanetary space respectively (CREME2009 vs. BON2010).
- Around 90% of the GCR exposure in near-Earth interplanetary space is caused by particles with energies between 100 MeV/nuc and 10 GeV/nuc whereas at the ISS orbit about 85–90% of the exposure is caused by particles with energies between 1 and 100 GeV/nuc. It was estimated that particles above 100 GeV/nuc contribute with less than 1% to the total dose and can be neglected.

The estimation of the dose quantities for the unusually deep solar minimum in 2009–2010, when the largest increase in the GCR intensity in the past decades was observed, could serve as a worst case scenario for GCR exposure assessments. However, the models investigated in this work are unable to describe this increased GCR flux and thus lead to an underestimation of the dose quantities. A comparison of the dose estimations with measurements performed at the International Space Station and data collected by the Radiation Assessment Dectector (RAD) (Hassler et al., 2012) onboard the Mars Science Laboratory (MSL) will be subject of future work and will add important information on the applicability of the GCR models in radiation exposure assessments for space outside and inside the Earth's magnetosphere. Additionally, the application of a simple water sphere as target and neglecting the shielding of any spacecraft can only serve as an approximation for realistic irradiation conditions for humans in space. The accuracy of this approach will also be investigated in the future.

Acknowledgment

We would like to acknowledge P.M. O'Neill for the kind provision of the Badhwar–O'Neill 2010 model and the CREME team including the administrators of the CREME website who have been very helpful regarding the questions on both the CREME models and their usage.

The first author, Alankrita Isha Mrigakshi, receives a SpaceLife scholarship funded by the Initiative and Networking Fund of the Helmholtz Association and the German Aerospace Center as a participant of the Helmholtz Space Life Sciences Research School (SpaceLife) at the German Aerospace Center.

References

Adams, J.H., Letaw, J.R., Smart, D.F. Cosmic ray effects on microelectronics, Part 2: the geomagnetic cutoff effects. NRL Memorandum, Report 5099, May 1983.

Agostinelli, S., Allison, J., Amako, K., et al. Geant4 – a simulation toolkit. Nucl. Instrum. Methods Phys. Res. Sec. A 506, 250–303, 2003.

Allison, J., Amako, K., Apostolakis, J., et al. Geant4 developments and applications. IEEE Trans. Nucl. Sci. 53, 270–278, 2006.

Berger, T. Radiation dosimetry onboard the international space station ISS. Z. Med. Phys. 18, 265–275, 2008.

Cooke, D.J., Humble, J.E., Shea, M.A., et al. On cosmic ray cut-off terminology. Nuovo Cimento 14C, 213–234, 1991.

Cucinotta, F.A., Schimmerling, W., Wilson, J.W. et al. Space radiation cancer risk projections for exploration missions: uncertainty reduction and mitigation. NASA JSC Document (JSC-29295), NASA Washington DC, 2001.

Cucinotta, F.A., Durante, M. Cancer risk from exposure to galactic cosmic rays: implications for space exploration by human beings. Lancet Oncol. 7, 431–435, 2006.

Cucinotta, F.A., Durante M. Risk of radiation carcinogenesis, in: NASA Human Health and Performance Risks of Space Exploration Missions, NASA Johnson Space Centre, Houston, TX, 2009

Gustafsson, K., Sihver, L., Mancusi, D., Sato, T., Reitz, G., Berger, T. PHITS simulations of the Matroshka experiment. Adv. Space Res. 46, 1266–1272, 2010.

Hassler, D.M., Zeitlin, C., Wimmer-Schweingruber, R.F., et al. The radiation assessment detector (RAD) investigation. Space Sci. Rev., http://dx.doi.org/10.1007/s11214-012-9913-1, 2012.

ICRP, 1991. Recommendations of the international commission on radiological protection. In: Annals of ICRP, vol. 21, ICRP Publication 60.

Koi, T., Asai, M., Wright, D.H. et al. Interfacing the JQMD and JAM nuclear reaction codes to Geant4, in: Computing in High Energy and, Nuclear Physics, SLAC-PUB-9978, 2003.

Kwangsun, R., Goo-Hwan, S., Hyung-Myung, K., et al. Simulation and ground test for the total ionizing dose effects of STSAT-2. J. Korean Phys. Soc. 50, 1552–1556, 2007.

Mewaldt, R.A. Galactic cosmic ray composition and energy spectra. Adv. Space Res. 14, 737–747, 1994.

Mrigakshi, A., Matthiä, D., Berger, T., Reitz, G., Wimmer-Schweingruber, R.F. Assessment of galactic cosmic ray models. J. Geophys. Res. 117, 12, http://dx.doi.org/10.1029/2012JA017611, 2012.

Nara, Y., Otuka, N., Ohnishi, A., et al. Relativistic nuclear collisions at 10A GeV energies from p+Be to Au+Au with the hadronic cascade model. Phys. Rev. C 61, 2, 1999.

NCRP, National council on radiation protection and measurements, operational radiation safety program for astronauts in low-earth orbit: a basic framework, NCRP Report No. 142, 2002.

NCRP, National council on radiation protection and measurements, guidance on radiation received in space activities, NCRP Report No. 98, 1989.

NCRP, National council on radiation protection and measurements, radiation protection guidance for activities in low-Earth orbit, NCRP Report No. 132, 2000.

NCRP, National council on radiation protection and measurements, radiation information needed to make radiation protection recommendations for space missions beyond low-earth orbit, NCRP Report No. 153, 2006.

Niita, K., Chiba, S., Maruyama, T., et al. Analysis of the (N, xN') reaction by quantum molecular dynamics plus statistical decay model. Phys. Rev. C 52, 2620–2635, 1995.

O'Neill, P.M. Badhwar–O'Neill 2010 galactic cosmic ray flux model—Revised. IEEE Trans. Nucl. Sci. 57, 3148–3153, 2010.

Palfalvi, J., Szabo, J., Dudas, B., et al. Cosmic ray detection on the Foton-M2 satellite by a track etch detector stack. Adv. Space Res. 42, 1030–1036, 2008.

Shikaze, Y., Haino, S., Abe, K., et al. Measurements of 0.2–20 GeV/n cosmic-ray proton and helium spectra from 1997 through 2002 with the BESS spectrometer. Astropart. Phys. 28, 154–167, 2007.

Sihver, L., Matthiä, D., Koi, T., Mancusi, D. Dose calculations at high altitudes and in deep space with GEANT4 using BIC and JQMD models for nucleus–nucleus reactions. New J. Phys. 10, 105019, 2008.

Sihver, L., Sato, T., Puchalska, M., Reitz, G. Simulations of the MATROSHKA experiment at the international space station using PHITS. Radiat. Environ. Biophys. 49, 351–357, 2010.

Simpson, J.A. Elemental and isotopic composition of the galactic cosmic rays. Ann. Rev. Nucl. Part. Sci. 33, 323–381, 1983.

Stone, E.C., Frandsen, A.M., Mewaldt, R.A., et al. The advanced composition explorer. Space Sci. Rev. 86, 1–22, 1998.

Tylka, A.J., Adams Jr., J.H., Boberg, P.R. CREME96: a of the cosmic ray effect on micro-electronics code. IEEE Trans. Nucl. Sci. 44, 2150–2160, 1997.

4.4 Paper III - Matthiä et al. 2013

A ready-to-use galactic cosmic ray model

Daniel Matthiä, Thomas Berger, **Alankrita Isha Mrigakshi** and Günther Reitz, ***Advances in Space Research***, Volume 51, Issue 3, p. 329-338, 2013, doi:10.1016/j.asr.2012.09.022

Available online at www.sciencedirect.com

SciVerse ScienceDirect

Advances in Space Research 51 (2013) 329–338

ADVANCES IN SPACE RESEARCH (a COSPAR publication)

www.elsevier.com/locate/asr

A ready-to-use galactic cosmic ray model

Daniel Matthiä *, Thomas Berger, Alankrita I. Mrigakshi, Günther Reitz

German Aerospace Center, Institute of Aerospace Medicine, Linder Höhe, 51147 Cologne, Germany

Received 15 May 2012; received in revised form 14 September 2012; accepted 16 September 2012
Available online 25 September 2012

Abstract

Galactic cosmic ray nuclei close to Earth are of great importance in different fields of research. By studying their intensity in near-Earth interplanetary space and modeling their modulation in the heliosphere it is possible to gain knowledge both about the structure of the heliosphere and the transport processes within. Additionally, secondary phenomena like cloud formation, ionization processes in the atmosphere, cosmogenic nuclide production and radiation exposure in space and at aviation altitudes are related to the intensity of the galactic cosmic rays and their modulation in the heliosphere. In order to improve the knowledge about these processes and underlying mechanisms it is often beneficial to perform numerical simulations. A necessary prerequisite for such simulations is a model describing the galactic cosmic ray intensities for all particle types and energies of importance. Several of these models exist in the literature. However, many of these do not provide essential characteristics like the description of heavier nuclei or it is difficult to associate them to recent or actual solar modulation conditions. In this work a model is presented which describes the galactic cosmic ray spectra of nuclei based on a single parameter. The values of this parameter for different solar modulation conditions are derived from measurements of the Advanced Composition Explorer (ACE) spacecraft and Oulu neutron monitor count rates. Comparing the galactic cosmic ray spectra predicted by the model to a comprehensive set of experimental data from literature shows very good agreement.

Keywords: Galactic Cosmic Rays; Solar modulation; Neutron monitors; Solar activity; Sun spot number

1. Introduction

Galactic Cosmic Rays (GCRs) are of importance in many geophysical phenomena and are a major source of the radiation exposure in interplanetary space, low Earth orbit and at aviation altitudes. The nuclear component of the Galactic Cosmic Rays accounting for about 98% of the particles consists mainly of hydrogen (≈87%), helium (≈12%) and to a lesser extent of heavier nuclei (≈1%) (Simpson, 1983). Regardless of their low numbers, nuclei heavier than helium play an important role in some phenomena due to their large number of nucleons, the corresponding masses and their high energies. The enhanced biological effectiveness of the heavier nuclei are of particular relevance concerning the radiation exposure in space (Cucinotta et al., 2003, 2008; McKenna-Lawlor et al., 2011).

Galactic Cosmic Rays are not only the major source of radiation exposure in space, but they are also the cause for a number of atmospheric phenomena such as elevated exposure at aviation altitudes (Reitz, 1993; EURADOS, 2004; Beck et al., 2009), the formation of cosmogenic nuclei (Matthiä et al., 2011; Beer et al., 1988, 1990; Steinhilber et al., 2008), and they are possibly linked to low-level cloud formation and climate change (Svensmark and Friis-Christensen, 1997; Kirkby, 2007).

In order to study such processes in detail and to relate their magnitude to the galactic cosmic ray intensity, an accurate and applicable model of the Galactic Cosmic Rays, their temporal modulation and respective energy distribution is essential. Many of the existing models lack a description of nuclei heavier than hydrogen or helium, e.g. Garcia-Munoz et al. (1975) and Usoskin et al.

* Corresponding author. Tel.: +49 2203 6013151; fax: +49 2203 61970.
E-mail address: Daniel.Matthiae@dlr.de (D. Matthiä).

0273-1177/$36.00 © 2012 COSPAR. Published by Elsevier Ltd. All rights reserved.
http://dx.doi.org/10.1016/j.asr.2012.09.022

(2005), or are difficult to handle due to an extensive formalism (e.g. the GALPROP model, http://galprop.stanford.edu Strong and Moskalenko (1998), Strong et al. (2007), Shibata et al. (2004, 2006), Nymmik et al. (1992, 1996). Some of these models focus on energies above hundreds of GeV per nucleon which are of great interest in astrophysical questions but do not contribute significantly to most atmospheric processes or radiation exposure due to the low intensities at these energies.

The CHIME model (Chenette et al., 1994) provides spectra of GCR ions in near Earth interplanetary space and inside the geomagnetic field based on estimates of the solar modulation of GCR from IMP-8 helium measurements in the energy range between 70 and 95 MeV/n and Climax neutron monitor count rates for the epoch from 1973 to 1993.

Other models (CREME96/CREME2009, https://creme.isde.vanderbilt.edu/, and O'Neill (2010) are not capable to describe accurately the changes in GCR intensities due to solar modulation. It was found that especially during the recent very deep and extended solar minimum in the years 2008–2010 widely used models could not to describe the prolonged increase in GCR intensity (Mrigakshi et al., 2012).

This work presents a simplified version of the GCR ISO-model (ISO, 2004) modified in order to reduce the number of free parameters to one. This single free parameter is then derived from measurements of galactic cosmic ray carbon fluxes by the Cosmic **R**ay **I**sotope **S**pectrometer (CRIS) on-board the **A**dvanced **C**omposition **E**xplorer (ACE) spacecraft (Stone et al., 1998) for the time period between August 1997 and April 2012. By establishing a linear relationship between the model parameter derived from ACE data and the count rate of the Oulu neutron monitor, http://cosmicrays.oulu.fi/, the backward estimate of the parameter can be extended until the year 1964. Based on these data, an extensive comparison of the model predictions of other galactic cosmic ray nuclei with experimental data is presented and very good agreement is found.

2. The Galactic Cosmic Ray model

The galactic cosmic ray model presented in this work was derived from the GCR-ISO model (ISO, 2004). The ISO model itself is based on publications by Nymmik et al. (1992, 1996), Nymmik and Suslov (1995) and relates the particle intensities to 12 month averages of the sun spot number. In practice, the maximum and minimum average sun spot number during the solar cycle of interest are used together with the average sun spot number at the time of interest taking into account a certain time lag between sun spot numbers and GCR intensities. Additionally, the time of the polar magnetic field reversal of the sun in the solar cycle has to be put in the model. Due to the fact that these quantities are not easily derived and sometimes not even well defined, for instance in the time period close to the end of a solar cycle and the beginning of the subsequent or in the ongoing cycle prior to the magnetic field reversal, the goal of this work was to eliminate the manifold dependence on the sun spot number and on the time of the field reversal and replace it by a single dependence on a well observed parameter.

The starting point of the GCR-ISO model is a description of the rigidity spectrum of the different nuclei:

$$\Phi_i(R,t) \equiv \frac{dN}{dAdt'd\Omega dR}(R,t) = \frac{C_i\beta^{\alpha_i}}{R^{\gamma_i}}\left[\frac{R}{R+R_0(R,t)}\right]^{\Delta_i(R,t)} \quad (1)$$

- Φ_i is the differential fluence rate or flux density of GCR particle type i with respect to particle rigidity R in GV at time t, i.e., number of particles N per area A, time t', solid angle Ω, and rigidity R.
- β is the ratio of particle speed to the speed of light.
- C_i, α_i, γ_i are parameters given by the ISO model and listed in Table 1. C_i is in the unit $(\mathrm{s\ sr\ m^2\ GV})^{-1}$.
- $\Delta_i(R,t)$ and $R_0(R,t)$ describe the modulation of the GCR in the heliosphere.

At very large rigidities the right part of Eq. (1) and β approach unity and the spectrum is described by a pure power law: $\Phi_i = C_i R^{-\gamma i}$. The right part of the equation describes the modulation of the spectrum at lower rigidities.

R_0 is a function of the mean sun spot or Wolf number W:

Table 1
Parameters of the galactic cosmic ray ISO-Model.

Nucleus	Z_i	A_i	C_i [$(\mathrm{s\ sr\ m^2\ GV})^{-1}$]	γ_i	α_i
H	1	1.0	1.85×10^4	2.74	2.85
He	2	4.0	3.69×10^3	2.77	3.12
Li	3	6.9	19.50	2.82	3.41
Be	4	9.0	17.70	3.05	4.30
B	5	10.8	49.20	2.96	3.93
C	6	12.0	103.00	2.76	3.18
N	7	14.0	36.70	2.89	3.77
O	8	16.0	87.40	2.70	3.11
F	9	19.0	3.19	2.82	4.05
Ne	10	20.2	16.40	2.76	3.11
Na	11	23.0	4.43	2.84	3.14
Mg	12	24.3	19.30	2.70	3.65
Al	13	27.0	4.17	2.77	3.46
Si	14	28.1	13.40	2.66	3.00
P	15	31.0	1.15	2.89	4.04
S	16	32.1	3.06	2.71	3.30
Cl	17	35.4	1.30	3.00	4.40
Ar	18	39.9	2.33	2.93	4.33
K	19	39.1	1.87	3.05	4.49
Ca	20	40.1	2.17	2.77	2.93
Sc	21	44.9	0.74	2.97	3.78
Ti	22	47.9	2.63	2.99	3.79
V	23	50.9	1.23	2.94	3.50
Cr	24	52.0	2.12	2.89	3.28
Mn	25	54.9	1.14	2.74	3.29
Fe	26	55.8	9.32	2.63	3.01
Co	27	58.9	0.10	2.63	4.25
Ni	28	58.7	0.48	2.63	3.52

$$R_0(R,t) = 0.37 + 3 \cdot 10^{-4} \cdot (W(t, \Delta t(R,t)))^{1.45} \quad (2)$$

In the ISO model the mean sun spot number $W(t,\Delta t(R,t))$ is calculated considering a rigidity dependent time lag Δt between the sun spot number and the intensity of the galactic cosmic rays at Earth. In this work, however, W will be treated as a rigidity independent, free parameter which will later be derived by fitting cosmic ray measurements and neutron monitor count rates.

The exponent Δ_i in the modulation term of Eq. (1) in the ISO model is described as a function of the rigidity, the time and the mean sun spot number (for details see ISO (2004)). It will be shown later that Δ_i can be approximated by a linear function of W. During periods of very small time lag between the sun spot number and the GCR intensity, the numerical value of W is expected to be similar to the sun spot number.

By inserting Eq. (2) in 1, by replacing Δ_i with the assumed linear relationship $\Delta = b \cdot W + c$, and by assuming a rigidity independent W, the following description of the rigidity spectrum is obtained:

$$\Phi_i(R,t) = \frac{C_i \beta^{\alpha_i}}{R^{\gamma_i}} \left[\frac{R}{R + (0.37 + 3 \cdot 10^{-4} \cdot W(t)^{1.45})} \right]^{b \cdot W(t) + c} \quad (3)$$

This leaves the description of the rigidity spectrum by the model with the single, time- or modulation-dependent parameter W, and two constant parameters b and c which will be derived below.

The differential fluence rate with respect to energy or flux density F_i can then be calculated from Eq. (3) as follows:

$$\begin{aligned} F_i(E,t) &\equiv \frac{dN}{dA dt d\Omega dE}(E,t) = \Phi_i(R(E),t) \frac{A_i}{|Z_i|} \frac{1}{\beta} \\ &= \frac{C_i \beta^{\alpha_i}}{R(E)^{\gamma_i}} \left[\frac{R(E)}{R(E) + (0.37 + 3 \cdot 10^{-4} \cdot W(t)^{1.45})} \right]^{b \cdot W(t) + c} \frac{A_i}{|Z_i|} \frac{1}{\beta} \end{aligned} \quad (4)$$

Here,

- F_i is the differential fluence rate or flux density of particle i with respect to energy E at time t.
- A_i and Z_i are the mass number and atomic number of GCR nucleus i.

The fundamental difference between the GCR-ISO model and its modified version presented in this work and given in Eq. (4) is the description of the solar modulation effect by a single parameter under the assumption that b and c are modulation independent, constant parameters.

3. Determination of the model parameters

In order to make the model applicable and to estimate the modulated GCR spectra at Earth W has to be determined. For this purpose, the particle flux density F_i described by Eq. (4) was fitted to experimental data provided by the **C**osmic **R**ay **I**sotope **S**pectrometer (CRIS) on-board the **A**dvanced **C**omposition **E**xplorer (ACE) spacecraft (Stone et al., 1998; http://www.srl.caltech.edu/ACE/ASC/level2). Galactic cosmic ray carbon data was found to be appropriate for the determination of the model parameters due to the relatively large abundance of carbon. Additionally, the energy range of carbon measured by CRIS, 68.3 MeV/n $< E <$ 194.4 MeV/n, is very well suited for an investigation of the solar modulation as the particles at these energies are heavily affected on their way through the heliosphere. The data used for the analysis are averages of the carbon flux over one Bartels rotation (27 days) and cover the period between August 14th 1997 (day of the year, DOY = 226) and April 2nd 2012 (DOY = 93), which is a total number of 198 Bartels rotations. The parameters b and c of the model are derived by performing a minimization procedure and it was found that the minimization of the average absolute deviation yielded good results. The average absolute deviation s between the model predictions and the ACE carbon data for all Bartels rotations was calculated as:

$$s = \sum_{i=1}^{N=198} \frac{1}{N} \sum_{j=1}^{M=7} \frac{\left| F(E_j, t_i) - y_j(t_i) \right|}{M} \quad (5)$$

N is the number of Bartels rotations in the data set, and M is the number of data points from the ACE carbon data with energies E_j and particle flux density y_j during Bartels rotation i. $F(E_j, t_i)$ is the model predicted particle flux density dependent on the model parameters b, c and W. The latter differs between the time intervals i and is a measure of the heliospheric modulation of the GCR.

By minimizing s the relationship between W and $\Delta = b \cdot W + c$ can be obtained. This minimization procedure was conducted with the MINUIT package (James and Roos, 1975) implemented in the ROOT v5.28 analysis software (http://root.cern.ch). The minimization was performed in a way that for a single calculation of s the set of b and c was kept constant and W was fitted for each set of ACE data between the year 1997 and 2012. Then, a new set of b and c is selected in the minimization process and W is again fitted for all time intervals. These steps are repeated until a stable minimum of s is identified.

On performing this procedure it was found that $b = 0.02$ and $c = 4.7$ minimize s and the exponent Δ in Eq. (1) can be expressed in terms of W:

$$\Delta = 0.02 \cdot W + 4.7 \quad (6)$$

However, it has to be noted that this solution is not necessarily unique. The minimization procedure might converge to other results of b and c depending on the starting values and limits of the parameters and other preconditions. Nevertheless, it was found that using the results given in Eq. (6) leads to very good agreement to experimental data.

The application of Eq. (6) to Eq. (4) results in a description of the GCR fluxes dependent only on the single

Table 2
Model parameter W derived from ACE carbon data between August 1997 and April 2012.

Year	$W_{(ACE)}$	Year	$W_{(ACE)}$	Year	$W_{(ACE)}$	Year	$W_{(ACE)}$
1997.65	15.6	2001.35	109.9	2005.05	73.9	2008.74	18.5
1997.73	17.1	2001.42	107.3	2005.12	74.2	2008.82	16.5
1997.80	19.3	2001.50	102.4	2005.19	72.5	2008.89	13.7
1997.88	22.5	2001.57	100.1	2005.27	70.0	2008.96	14.6
1997.95	22.5	2001.65	103.5	2005.34	70.0	2009.04	14.4
1998.02	21.0	2001.72	100.7	2005.42	69.2	2009.11	10.2
1998.10	19.7	2001.79	107.5	2005.49	66.4	2009.18	8.7
1998.17	18.6	2001.87	104.4	2005.56	68.7	2009.26	6.5
1998.25	20.6	2001.94	99.1	2005.64	71.4	2009.33	4.4
1998.32	34.6	2002.02	97.7	2005.71	77.4	2009.41	3.1
1998.39	36.3	2002.09	99.5	2005.78	68.1	2009.48	4.5
1998.47	37.3	2002.16	94.6	2005.86	62.8	2009.55	1.9
1998.54	35.8	2002.24	95.7	2005.93	60.5	2009.63	3.1
1998.62	34.0	2002.31	96.8	2006.01	57.9	2009.70	0.7
1998.69	32.5	2002.38	97.9	2006.08	55.5	2009.78	0.0
1998.76	35.0	2002.46	95.9	2006.15	53.2	2009.85	1.4
1998.84	33.9	2002.53	92.6	2006.23	48.7	2009.92	0.0
1998.91	38.4	2002.61	104.2	2006.30	47.4	2010.00	0.2
1998.98	39.0	2002.68	99.8	2006.38	45.5	2010.07	0.0
1999.06	44.2	2002.75	96.7	2006.45	43.4	2010.15	4.0
1999.13	44.1	2002.83	97.7	2006.52	42.5	2010.22	11.0
1999.21	47.1	2002.90	96.8	2006.60	41.1	2010.29	18.7
1999.28	45.4	2002.98	97.9	2006.67	43.2	2010.37	17.8
1999.35	46.7	2003.05	95.0	2006.75	39.5	2010.44	18.5
1999.43	46.7	2003.12	94.3	2006.82	38.7	2010.52	18.9
1999.50	47.7	2003.20	92.6	2006.89	37.6	2010.59	21.9
1999.58	44.2	2003.27	95.9	2006.97	43.0	2010.66	20.9
1999.65	47.7	2003.35	96.9	2007.04	37.3	2010.74	22.8
1999.72	53.5	2003.42	98.7	2007.12	37.5	2010.81	23.1
1999.80	61.6	2003.49	99.7	2007.19	35.5	2010.89	25.1
1999.87	66.2	2003.57	97.8	2007.26	31.4	2010.96	27.2
1999.95	70.0	2003.64	96.5	2007.34	30.6	2011.03	26.6
2000.02	74.8	2003.72	97.2	2007.41	30.6	2011.11	26.2
2000.09	78.7	2003.79	96.4	2007.49	28.5	2011.18	30.8
2000.17	83.0	2003.86	107.3	2007.56	27.1	2011.26	37.3
2000.24	86.5	2003.94	108.8	2007.63	26.4	2011.33	38.7
2000.32	86.7	2004.01	102.3	2007.71	25.6	2011.40	39.8
2000.39	93.3	2004.09	100.0	2007.78	25.0	2011.48	47.0
2000.46	99.4	2004.16	93.9	2007.86	23.9	2011.55	45.9
2000.54	99.8	2004.23	89.0	2007.93	24.8	2011.63	46.8
2000.61	110.9	2004.31	84.1	2008.00	24.2	2011.70	44.3
2000.68	112.2	2004.38	81.0	2008.08	23.8	2011.77	51.7
2000.76	111.2	2004.46	79.8	2008.15	23.9	2011.85	46.9
2000.83	109.6	2004.53	76.8	2008.23	25.1	2011.92	45.3
2000.91	114.4	2004.60	77.7	2008.30	26.3	2012.00	43.9
2000.98	115.5	2004.68	74.5	2008.37	25.1	2012.07	44.5
2001.05	118.5	2004.75	72.5	2008.45	23.9	2012.14	46.9
2001.13	115.9	2004.82	69.5	2008.52	22.0	2012.22	57.7
2001.20	111.2	2004.90	69.9	2008.59	21.5		
2001.28	116.6	2004.97	67.2	2008.67	17.3		

parameter W. Using the same data set of ACE/CRIS carbon data it is possible to derive W for the time period between August 1997 and present. The values of W obtained from a fit of the model to the experimental data for all Bartels rotations between August 1997 and April 2012 are presented in Table 2 and in the lower panel of Fig. 1. The fractional years in Table 2 mark the center of a Bartels rotation.

In order to extend the temporal validity of the model the Oulu neutron monitor (NM) count rates (Fig. 1, top panel, from http://cosmicrays.oulu.fi/) were selected as a second source of information on the intensity of galactic cosmic rays. As the NM count rates are a measure of the GCR intensity a strong correlation between the parameter W and the count rates can be assumed. Fig. 2 illustrates this relation between W derived from the ACE carbon data (W_{ACE}) and the Oulu count rates averaged over the same Bartels rotation. Fitting the data with a polynomial of the first degree gives a description of W as a function of the NM count rate cr (cr in counts/min):

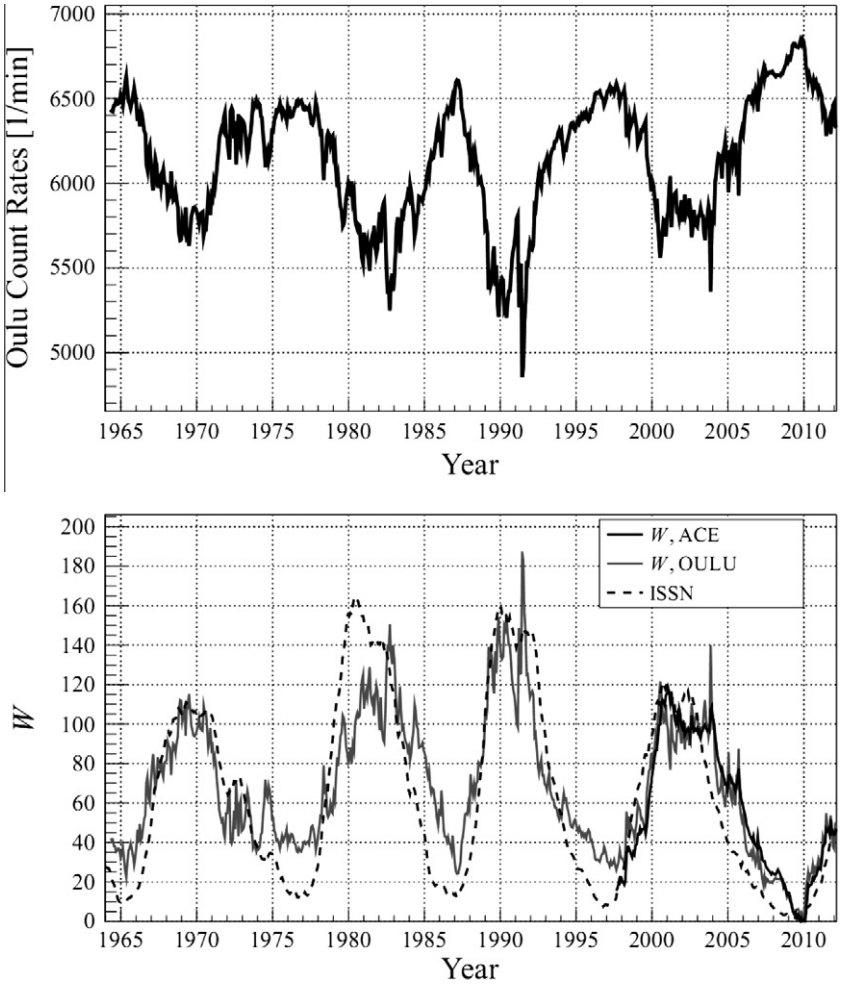

Fig. 1. Oulu neutron monitor count rate between January 1964 and April 2012 in the upper panel. Model parameter W derived from the direct fit to the ACE/CRIS carbon data (black line) and from Oulu count rates (grey line) compared to the 12 month averaged International Sun Spot Number (ISSN, dashed line) in the lower panel.

$$W_{\mathrm{Oulu}} = -0.093 \cdot cr + 638.7 \tag{7}$$

Certainly, a similar correlation could as well be performed with other neutron monitor stations or other parameters monitoring the galactic cosmic ray intensity.

The sun spot number (SIDC-team, 2012) is compared to the parameter of the model derived from the Oulu neutron monitor and the ACE data in the lower panel of Fig. 1. It is obvious that the values taken by the different variables are very similar, especially during some of the solar maximum periods. However, there are several noteworthy features. The time lag between the sun spot number and the model parameters, occurring during different periods in the time interval under investigation, is a manifestation of the corresponding time lag between the solar activity and the GCR intensity at Earth.

The different levels of solar activity reached during the solar maxima and expressed by the sun spot number are, with some exceptions around 1980–1983, well described by W. At the solar minima preceding the most recent, however, the model parameter derived from the neutron

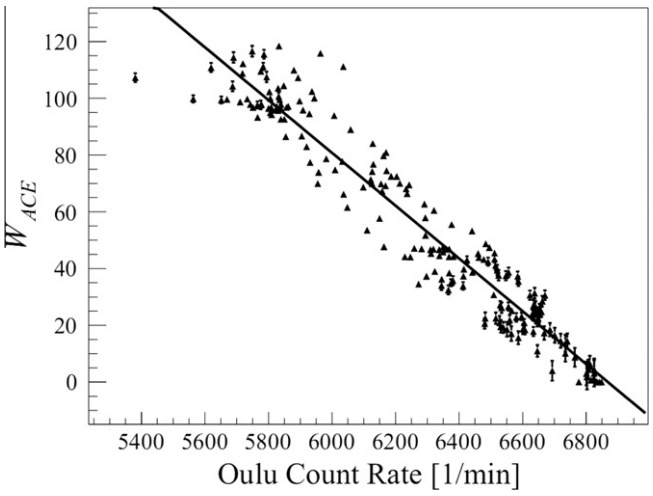

Fig. 2. Scatter plot of the Oulu neutron monitor count rates vs. the model parameter W derived from ACE carbon data. The data was fitted with a linear function.

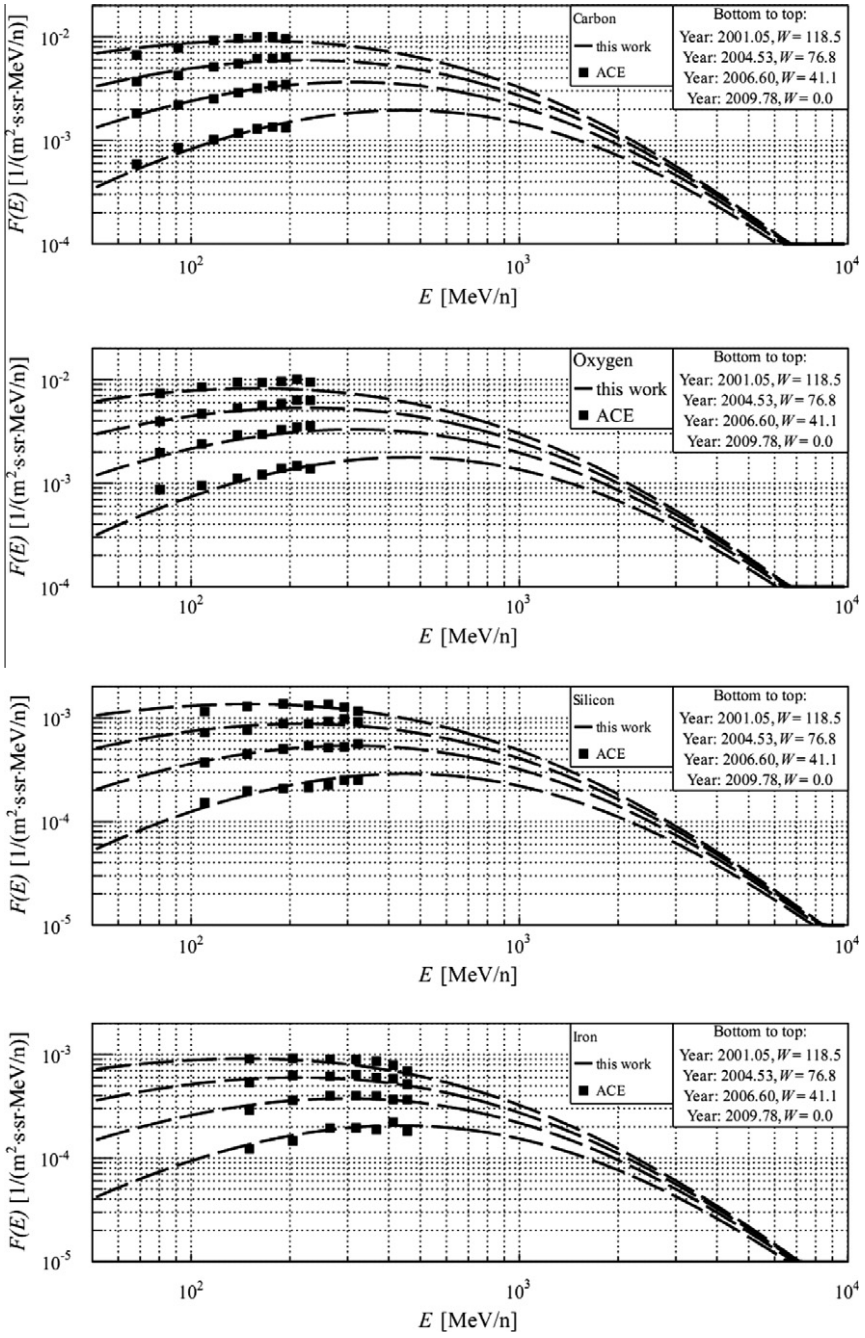

Fig. 3. GCR spectra described by the model (dashed lines) compared to ACE data (squares). From top to bottom panel: Carbon, Oxygen, Silicon, and Iron. The selected dates between 2001 and 2010 represent different modulation expressed by model parameters between very low modulation $W_{ACE} = 0.0$ (uppermost set of data and line in each panel) and very high modulation $W_{ACE} = 118.5$ (lowest set of data and line in each panel).

monitor does not reach the lowest values of the sun spot number. During the most recent solar minimum around the year 2009, on the other hand, all parameters are close to zero. The fact that the parameter derived from the neutron monitor data deviates from the sun spot number during extreme solar activity periods is most probably due to the low sensitivity of the ground based neutron monitor to lower energies being most affected by the modulation.

4. Comparison of the galactic cosmic ray model with experimental data

A comparison to a large set of experimental data including a wide range of energies for several GCR nuclei was performed to validate the model presented above.

In Fig. 3, the data of the ACE/CRIS detector for GCR carbon, oxygen, silicon and iron is compared to the predictions of the model using W_{ACE}. It is important to remem-

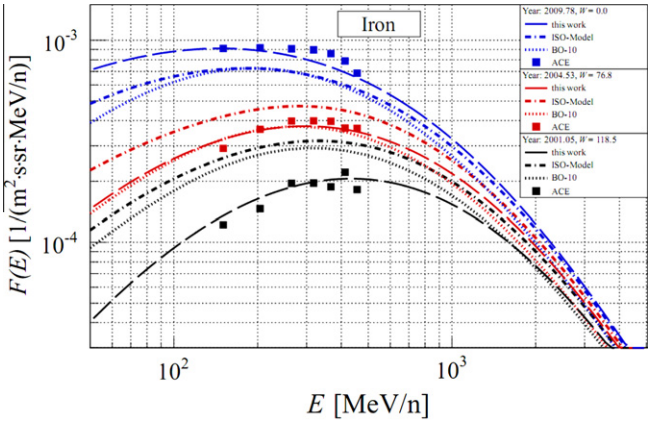

Fig. 4. Comparison of the model presented in this work with the ISO model, the BO-10 model and ACE data for GCR iron. The selected dates between 2001 and 2010 represent low modulation ($W_{ACE} = 0$, solar minimum), moderate modulation ($W_{ACE} = 76.8$), and strong modulation ($W_{ACE} = 118.5$, solar maximum).

ber that the carbon data was used in the fitting procedure to obtain W. All other spectra, on the other hand, are derived from this single parameter. Four different points from the measurement period of ACE between 2001 and present were selected to cover the whole range of solar modulation in this period. The maximum modulation during that time with the lowest GCR intensity was in the beginning of the year 2001 ($W_{ACE} = 118.5$). The lowest modulation leading to the maximum GCR flux was reached at the end of the year 2009 ($W_{ACE} = 0.0$). These values are very similar to the International Sun Spot Number (ISSN, cf. Fig. 1). In between the two dates during the period of decreasing activity, however, the downward slope of the sun spot number is steeper compared to the model parameter W which expresses the time delay of the GCR intensity at Earth with respect to the solar activity.

The ACE data is illustrated as squares and the model predictions as dashed lines in Fig. 3. The lowest set of data represents the largest solar modulation (2001), and the data lying above illustrate the increasing GCR intensity with decreasing solar modulation. The agreement between the model predictions and the ACE measurements is very good for all solar modulation conditions and for all ions. The mean absolute deviation between the model predictions and the ACE data averaged over the period between 1997 and 2012 is: 5% for carbon, 7% for silicon and iron, and 9% for oxygen.

A comparison of the model predictions, which is not shown here, using W derived from the Oulu data from Eq. (7) revealed similar good agreement for the three lower modulations in 2009, 2006 and 2004. For the solar maximum conditions in the year 2001, however, an overestimation of the experimental data by the model was observed. Fig. 1 exhibits partial discrepancies between the two sets of W around 2001 which is the cause of this disagreement. Neutron monitor count-rates are always to a certain degree dependent on environmental conditions which may be a reason for this disagreement. On the other hand, the comparison relies on data of the same instrument which was used for the parameter determination and, as a consequence, it can not necessarily be concluded that W_{ACE} gives the better estimate of the GCR intensity.

To investigate the agreement of the ISO-model, the O'Neill (2010) model (BO-10) and the model from this work with experimental results, a comparison of the models to the ACE iron data is illustrated in Fig. 4. The data for the GCR-ISO model were retrieved from its implementation in SPENVIS ("The Space Environment Information System", http://www.spenvis.oma.be/spenvis/). The ACE data as well as the data from the different models are retrieved as averages over one Bartels rotation the center of which is indicated by the fractional date given in the legends.

There is an obvious disagreement between the ACE data and both the GCR ISO and BO-10 model, especially for very strong modulation corresponding to low GCR intensity. The same behavior was observed for the other nuclei (C, O, and Si). The mean absolute deviations between the models and the ACE data for the three selected times given in Table 3 are below 10% for the model presented in this work and significantly larger for the ISO and BO-10 models. As the data provided by ACE/CRIS is restricted to heavier elements and energies below a few 100 MeV, an additional comparison to balloon data from the BESS experiment (Shikaze et al., 2007) was performed for hydrogen, helium

Table 3
Relative deviation of the model presented in this work from experimental data compared to the ISO model and the BO-10 model. For the ACE data, the fractional year indicates the center of the Bartels rotation over which the averaging was performed.

Experiment	Ion	Energy range [MeV/n]	Year	W	Relative deviation from experimental data		
					This work	ISO	BO-10
ACE/CRIS	Fe	129.1–470.9	2001.05	118.5	8%	73%	58%
ACE/CRIS	Fe	129.1–470.9	2004.53	76.8	5%	23%	7%
ACE/CRIS	Fe	129.1–470.9	2009.78	0.0	8%	23%	24%
BESS1998	H	215–21.5 × 10^3	29th July 1998	47.1	4%	17%	5%
BESS2000	H	215–21.5 × 10^3	10th August 2000	116.1	16%	120%	34%
BESS1998	He	215–21.5 × 10^3	29th July 1998	47.1	9%	9%	5%
BESS2000	He	215–21.5 × 10^3	10th August 2000	116.1	12%	59%	24%
HEAO-3-C2	C	620–3.5 × 10^3	October 1979–June 1980	88.4	6%	7%	7%
HEAO-3-C2	Fe	800–3.5 × 10^3	October 1979–June 1980	88.4	11%	19%	9%

and to data from the HEAO-3-C2 (Engelmann et al., 1990) experiment for carbon and iron (Fig. 5).

The experimental data from the BESS and HEAO-3-C2 experiments comprise of GCR intensities at energies between a few 100 MeV/n and 20 GeV/n and above. The data from the BESS experiment were recorded on 29th of July 1998 corresponding to a $W_{\mathrm{Oulu}} = 47.1$ and on 10th/11th of August 2000 ($W_{\mathrm{Oulu}} = 116.1$). The results from HEAO-3-C2 were obtained between October 1979 and June 1980 ($W_{\mathrm{Oulu}} = 88.4$). Note, that although the HEAO-3-C2 measurements lasted for eight months the GCR intensity changed only moderately in this period. Oulu neutron monitor count rates varied by less than 4% during that time and the results for the models were derived for a solar modulation averaged over the time between October 1979 and June 1980.

While the comparison at higher energies in Fig. 5 shows the accuracy of the models compared to relatively weak

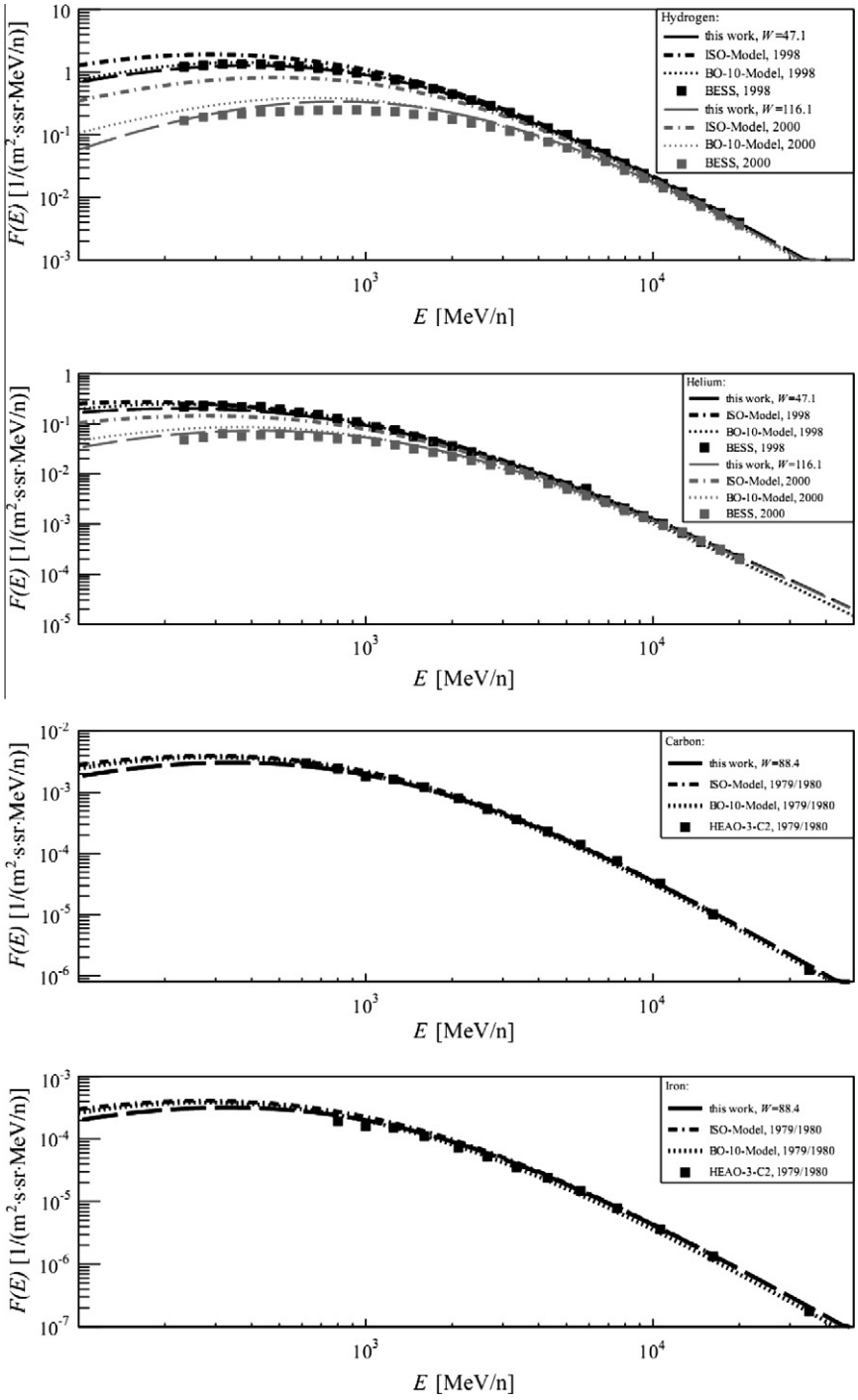

Fig. 5. Comparison of GCR spectra described by the model presented in this work with the ISO model, the BO-10 model and selected experimental data for Hydrogen, Helium, Carbon and Iron (from top to bottom panel).

modulated spectra, the impact of the passage of the heliosphere on the GCR intensity is evident at lower energies. The observations confirm the result of the above comparison: Good agreement between experimental data and the model presented in this work for both weak (BESS, 1998) and strong modulation conditions (BESS, 2000) and deviations between the ISO model, the BO-10 model and experimental data.

For intermediate modulation (HEAO-3-C2) all three models describe the experimental data accurately. It is noteworthy that the parameters used to describe the model spectra in Fig. 5 were retrieved from the Oulu data and the good agreement confirms the applicability of the Oulu derived parameters to the model.

The relative deviations of the models compared to the experimental data averaged over the measured energy ranges are given in Table 3. The model presented in this work shows significantly smaller deviations from the experimental data compared to the ISO model and the BO-10 model.

5. Summary

In this work, a promising galactic cosmic ray model derived from the ISO standard model is presented. By simplifying the description of the solar modulation to a single parameter the galactic cosmic ray intensity could be quantified by fitting the experimental ACE carbon data. The values of the derived parameter W are similar but not equal to the International Sun Spot Number. It was found that using the average sun spot number, as described in the ISO standard, is difficult and the resulting GCR intensities do not agree very well with experimental data. Especially during times of solar activity extremes the model presented here exhibits much better agreement with ACE and balloon data than the ISO and BO-10 model. Additionally, the model does not show similar disagreement to experimental data during the recent solar minimum as observed for other models by Mrigakshi et al. (2012). While the model presented here deviates for most of the experimental conditions on average by around 10% or less, the ISO model in many cases shows discrepancies to the measurements of several tens of percent and more. This result supports the conclusion that the model presented in this work offers a significant improvement in the description of the intensity of the modulated galactic cosmic rays close to Earth.

By assuming a linear relationship between the model parameter derived from ACE data with the Oulu neutron monitor count rates, the characterization of the solar modulation and the corresponding GCR intensities and energy spectra could be determined for times prior to the ACE mission back to the year 1964. The comparison of the model to balloon data from earlier times proved that deriving the model parameter from the Oulu neutron monitor count rates provides reliable results. The procedure of coupling the ACE derived model parameter to neutron monitor data can certainly be performed for other parameters as well which may further increase the period of applicability of the model.

Acknowledgments

The authors thank the Sodankyla Geophysical Observatory and the website team (http://cosmicrays.oulu.fi) for providing the Oulu neutron monitor data and the ACE CRIS instrument team and the ACE Science Center for providing the ACE data. We would like to acknowledge P.M. O'Neill for providing the Badhwar–O'Neill 2010 model.

Alankrita Mrigakshi receives a SpaceLife scholarship funded by the Initiative and Networking Fund of the Helmholtz Association and the German Aerospace Center as a participant of the Helmholtz Space Life Sciences Research School (SpaceLife) at the German Aerospace Center.

References

Beck, P., Bartlett, D., Lindborg, L., McAulay, I., Schnuer, K., Schraube, H., Spurny, F. Aircraft crew radiation workplaces: comparison of measured and calculated ambient dose equivalent rate data using the EURADOS in-flight radiation data base. Radiat. Protect. Dosimet. 118 (2), 182–189, 2009.

Beer, J., Siegenthaler, U., Bonani, G., Finkel, R.C., Oeschger, H., Suter, M., Wölfli, W. Information on past solar activity and geomagnetism from ^{10}Be in the Camp Century ice core. Nature 331, 675–679, 1988.

Beer, J., Blinov, A., Bonani, G., Finkel, R.C., Hofmann, H.J., Lehmann, B., Oeschger, H., Sigg, A., Schwandner, J., Staffelbach, Stauffer, B., Suter, M., Wölfli, W. Use of ^{10}Be in polar ice to trace the 11-year cycle of solar activity. Nature 137, 164–166, 1990.

Chenette, D.L., Chen, J., Clayton, E., Guzik, T.G., Wefel, J.P., Garcia-Muñoz, M., Lopate, C., Pyle, K.R., Ray, K.P., Mullen, E.G., Hardy, D.A. The CRRES/SPACERAD heavy ion model of the environment (CHIME) for cosmic ray and solar particle effects on electronic and biological systems in space. IEEE Trans. Nucl. Sci. 41 (6), 2332–2339, 1994.

Cucinotta, F.A., Wu, H., Shavers, M.R., George, K. Radiation dosimetry and biophysical models of space radiation effects. Gravitat. Space Bull. 16 (2), 11–22, 2003.

Cucinotta, F.A., Kim, M.Y., Willingham, V., George, K. Physical and biological organ dosimetry analysis for international space station astronauts. Radiat. Res. 170, 127–138, 2008.

Engelmann, J.J., Ferrando, P., Soutoul, A., Goret, P., Juliusson, E., Koch-Miramond, L., Lund, N., Masse, P., Peters, B., Petrou, N., Rassmussen, I.L. Charge composition and energy spectra of cosmic-ray nuclei for elements from Be to Ni. Results from HEAO-3-C2. Astron. Astrophys. 233, 96–111, 1990.

EURADOS. Final Report of EURADOS WG 5, Cosmic radiation exposure of aircraft crew – compilation of measured and calculated data, ISBN 92-894-8448-9, 2004.

Garcia-Munoz, M., Mason, G.M., Simpson, J.A. The anomalous 4He component in the cosmic-ray spectrum at <50 MeV per nucleon during 1972–1974. Astrophys. J. 202, 265–275, 1975.

ISO 15390. Space environment (natural and artificial) – galactic cosmic ray model, 2004.

James, F., Roos, M. MINUIT: a system for function minimization and analysis of the parameter errors and corrections. Comp. Phys. Commun. 10, 343–367, 1975.

Kirkby, J. Cosmic rays and climate. Surveys Geophys. 28 (5–6), 333–375, 2007.

Matthiä, D., Herbst, K., Heber, B., Berger, T., Reitz, G. ^{10}Be production in the atmosphere by galactic cosmic rays. Space Sci. Rev. doi 10.1007/s11214-011-9817-5, 2011.

McKenna-Lawlor, S., Goncalves, P., Keating, A., Reitz, G., Matthiä, D. Overview of energetic particle hazards during prospective manned missions to Mars. Planet. Space Sci. doi: 10.1016/j.pss.2011.06.017, 2011.

Mrigakshi, A., Matthiä, D., Berger, T., Reitz, G., Wimmer-Schweingruber, R.F. Assessment of galactic cosmic ray models. J. Geophys. Res. 117, A08109, doi:10.1029/2012JA017611, 2012.

Nymmik, R.A., Panasyuk, M.I., Pervala, T.I., Suslov, A.A. A model of galactic cosmic ray fluxes. Nucl. Tracks Radiat. Meas. 20 (3), 427–429, 1992.

Nymmik, R.A., Suslov, A.A. Characteristics of galactic cosmic ray flux lag times in the course of the solar modulation. Adv. Space Res. 16 (9), 9217–9220, 1995.

Nymmik, R.A., Panasyuk, M.I., Suslov, A.A. Galactic cosmic ray flux simulation and prediction. Adv. Space Res. 17 (2), 219–230, 1996.

O'Neill, P.M. Badhwar–O'Neill 2010 galactic cosmic ray flux model—Revised. IEEE Transactions on Nuclear Science 57 (6), 3148–3153, 2010.

Reitz, G. Radiation environment in the stratosphere. Radiat. Protect. Dosimet. 48 (1), 5–20, 1993.

Shibata, T., Hareyama, M., Nakazawa, M., Saito, C. A possible approach to three-dimensional cosmic-ray propagation in the galaxy. I. Stable nuclei without energy change. Astrophys. J. 612, 238–261, 2004.

Shibata, T., Hareyama, M., Nakazawa, M., Saito, C. A possible approach to three-dimensional cosmic-ray propagation in the galaxy. II. Stable nuclei with energy change. Astrophys. J. 642, 882–901, 2006.

Shikaze, Y., Haino, S., Abe, K., Fuke, H., Hams, T., Kim, K.C., Makida, Y., Matsuda, S., Mitchell, J.W., Moiseev, A.A., Nishimura, J., Nozaki, M., Orito, S., Ormes, J.F., Sanuki, T., Sasaki, M., Seo, E.S., Streitmatter, R.E., Suzuki, J., Tanaka, K., Yamagami, T., Yamamoto, A., Yoshida, T., Yoshimura, K. Measurements of 0.2-20 GeV/n cosmic-ray proton and helium spectra from 1997 through 2002 with the BESS spectrometer. Astroparticle Phys. 28, 154–167, 2007.

SIDC-team. World data center for the sunspot index, royal observatory of belgium, monthly report on the international sunspot number, online catalogue of the sunspot index: <http://www.sidc.be/sunspot-data>, 2012.

Simpson, J.A. Elemental and isotopic composition of the galactic cosmic rays. Ann. Rev. Nucl. Particle Sci. 33, 323–381, 1983.

Steinhilber, F., Abreu, J.A., Beer, J. Solar modulation during the Holocene. Astrophys. Space Sci. Trans. 4, 1–6, 2008.

Stone, E.C., Frandsen, A.M., Mewaldt, R.A., Christian, E.R., Margolies, D., Ormes, J.F., Snow, F. The advanced composition explorer. Space Sci. Rev. 86, 1–22, 1998.

Strong, A.W., Moskalenko, I.V. Propagation of cosmic-ray nucleons in the galaxy. Astrophys. J. 509 (1), 212–228, 1998.

Strong, A.W., Moskalenko, I.V., Ptuskin, V.S. Cosmic-ray propagation and interactions in the galaxy. Ann. Rev. Nucl. Particle Sci. 57, 285–327, 2007.

Svensmark, H., Friis-Christensen, E. Variation of cosmic ray flux and global cloud coverage – a missing link in solar-climate relationships. J. Atmos. Solar-Terres. Phys. 59 (11), 1225–1232, 1997.

Usoskin, I.G., Alanko-Huotari, K., Kovaltsov, G.A., Mursula, K. Heliospheric modulation of cosmic rays: Monthly reconstruction for 1951–2004. J. Geophys. Res. 110, A12108, doi:10.1029-2005JA011250, 2005.

4.5 Paper IV - Mrigakshi et al. 2013b

Estimation of galactic cosmic ray exposure inside and outside the Earth's magnetosphere during the recent solar minimum between solar cycles 23 and 24

Alankrita Isha Mrigakshi, Daniel Matthiä, Thomas Berger, Günther Reitz and Robert F. Wimmer-Schweingruber, ***Advances in Space Research***, Volume 52, Issue 5, p. 979-987, 2013, doi:10.1016/j.asr.2013.05.007

Available online at www.sciencedirect.com

SciVerse ScienceDirect

Advances in Space Research 52 (2013) 979–987

ADVANCES IN SPACE RESEARCH (a COSPAR publication)

www.elsevier.com/locate/asr

Estimation of Galactic Cosmic Ray exposure inside and outside the Earth's magnetosphere during the recent solar minimum between solar cycles 23 and 24

Alankrita Isha Mrigakshi [a,b,*], Daniel Matthiä [a], Thomas Berger [a], Günther Reitz [a], Robert F. Wimmer-Schweingruber [b]

[a] DLR – German Aerospace Center, Institute of Aerospace Medicine, Radiation Biology Department, Linder Höhe, 51147 Cologne, Germany
[b] Christian-Albrechts-University Kiel, Institute of Experimental and Applied Physics, Extraterrestrial Physics, Leibnizstr. 11, 24098 Kiel, Germany

Received 21 December 2012; received in revised form 2 April 2013; accepted 6 May 2013
Available online 15 May 2013

Abstract

The evidently low solar activity observed between solar cycles 23 and 24 during the years 2008–2010 led to a substantial increase in the Galactic Cosmic Ray (GCR) intensity in comparison with preceding solar minima. As the GCRs consist of highly-ionizing charged particles having the potential to cause biological damage, they are a subject of concern for manned missions to space. With the enhanced particle fluxes observed between 2008 and 2010, it is reasonable to assume that the radiation exposure from GCR must have also increased to unusually high levels. In this paper, the GCR exposure outside and inside the Earth's magnetosphere is numerically calculated for time periods starting from 1970 to the end of 2011 in order to investigate the increase in dose levels during the years 2008–2010 in comparison with the last three solar minima. The dose rates were calculated in a water sphere, used as a surrogate for the human body, either unshielded or surrounded by aluminium shielding of 0.3, 10 or 40 g/cm^2.

By performing such a long-term analysis, it was estimated that the GCR exposure during the recent solar minimum was indeed the largest in comparison with previous minima and that the increase was more pronounced for locations outside the magnetosphere.

Keywords: Radiation exposure in Low Earth Orbit and near-Earth interplanetary space; Variation of dose rates with shielding over time; Galactic Cosmic Rays; Solar minimum; Monte-Carlo simulations

1. Introduction

The expansion of human space exploration to destinations like the Moon and Mars is likely to occur within the first half of this century. Additionally, the opportunities for the general public travelling into space with commercial spaceflights are becoming reality. With the rising number of people visiting and likely to visit space, the studies improving the knowledge on health risks related to the exotic environment encountered in space are of great importance as they can help to reduce these risks.

One of the primary concerns for manned missions to space is the elevated level of radiation exposure especially due to Solar Particle Events (SPE) and Galactic Cosmic Rays (GCRs) (NCRP, 1989, 2000, 2002, 2006; Cucinotta et al., 2001; Cucinotta and Durante, 2006). High-energy GCR nuclei, ranging from hydrogen to iron and beyond, contribute to the significant amount of dose to which astronauts are exposed to both outside and inside the Earth's magnetosphere (NCRP, 2000, 2006). The dose levels are directly related to the GCR particle intensities which vary with the 11-year sunspot cycle and the 22-year solar magnetic cycle (Belov, 2000; Heber, 2011; Usoskin et al.,

* Corresponding author at: DLR – German Aerospace Center, Institute of Aerospace Medicine, Radiation Biology, Linder Höhe, 51147 Cologne, Germany. Tel.: +49 2203 6013147; fax: +49 2203 61970.
E-mail address: alankrita.mrigakshi@dlr.de (A.I. Mrigakshi).

0273-1177/$36.00 © 2013 COSPAR. Published by Elsevier Ltd. All rights reserved.
http://dx.doi.org/10.1016/j.asr.2013.05.007

2001). Since the GCR intensity is anti-correlated with the solar activity, the GCR exposure peaks at solar minimum and is lowest at solar maximum conditions.

During the last solar minimum between the solar cycles 23 and 24 an unusual rise in the GCR intensity in comparison with several minima in the past decades was observed. This phenomenon was related to the unusually low solar activity during the extended solar minimum conditions in the heliosphere (Mewaldt et al., 2010). In this work, the increase in the GCR exposure during the last solar minimum is investigated for the orbit of the International Space Station (ISS) and for near-Earth interplanetary space at a distance of one Astronomical Unit (AU) from the Sun outside the Earth's magnetosphere. The exposure was estimated in terms of absorbed dose and dose equivalent rates for a period ranging from January 1970 to October 2011 in order to examine the relative change in the dose quantities at different solar minima. The GCR model recently developed by Matthiä et al. (2013a) was employed in the work since other models used for dosimetric purposes like CREME96 (Tylka et al., 1997; https://creme.isde.vanderbilt.edu/), CREME2009 (https://creme.isde.vanderbilt.edu/) and the Badhwar-O'Neill 2010 model (O'Neill, 2010), were found not to be able to describe the increased GCR intensity and the respective increase in dose during 2008–2010 as presented in Mrigakshi et al. (2012) and Mrigakshi et al. (2013).

A similar study numerically determining the GCR exposure over the time period between the years 1975 and the end of 2009 was performed by Schwadron et al. (2010) who did not predict a significant increase in dose rates between the years 2008 and 2010. One of the reasons for this is likely due to the application of the Badhwar-O'Neill 2006 GCR model (O'Neill, 2006) by Schwadron et al. (2010) to estimate the radiation exposure. The authors mention in the paper that the value of the solar modulation parameter Φ, frequently used for the description of the modulation of GCR in the heliosphere in the force field model (Gleeson and Axford, 1968), ranged between 400 MV and 1800 MV in the model from solar minimum to maximum during the inspected time period. This parameter gives an indication about the strength of the solar modulation in the Heliosphere. A smaller Φ implies weaker modulation allowing more GCR particles to penetrate inside the heliosphere. In Section 1.1 the value of Φ based on GCR measurements during the solar minimum in late 2009 is shown to have been much lower than the value used by the GCR model from O'Neill (2006) to describe the GCR spectra during that time period.

1.1. GCR during the solar minimum between solar cycles 23 and 24

Since the discovery of GCR by Victor Franz Hess (Hess, 1912) a century ago, a large number of GCR measurements by various ground-based, high-altitude balloon-borne and space-borne instruments have been performed (Grieder, 2001 and the references therein). Continuous data especially from Neutron Monitors (NM) (Simpson, 2000) since 1951 complemented by recent space missions like the Advanced Composition Explorer (ACE) (Stone et al, 1998) which has been operating since 1997 are of special importance as they reveal the long-term variation of the GCR intensity. Among others, ACE measures nuclei from Li to Ni over an energy range from about 40 to 500 MeV/nuc while the Neutron Monitor count rates provide an indirect measure of the GCR intensity (Usoskin et al. 2001).

Fig. 1a shows the temporal variation of the monthly sunspot numbers (http://sidc.oma.be/DATA/monthssn.dat) with the solar cycle number indicated and Fig. 1b shows the NM count rates measured by the Oulu station (http://cosmicrays.oulu.fi/) from January 1970 to October 2011. The Oulu station is located at 65.05°N, 25.47°E where the geomagnetic shielding quantified by the effective vertical cut-off rigidity is about 0.8 GV. The rigidity R of a charged particle is defined as its momentum p per charge q, $R = p/q$. The effective vertical cut-off rigidity lies in the rigidity interval between the value below which no particle arrives in vertical direction at the location of interest and the highest rigidity value above which

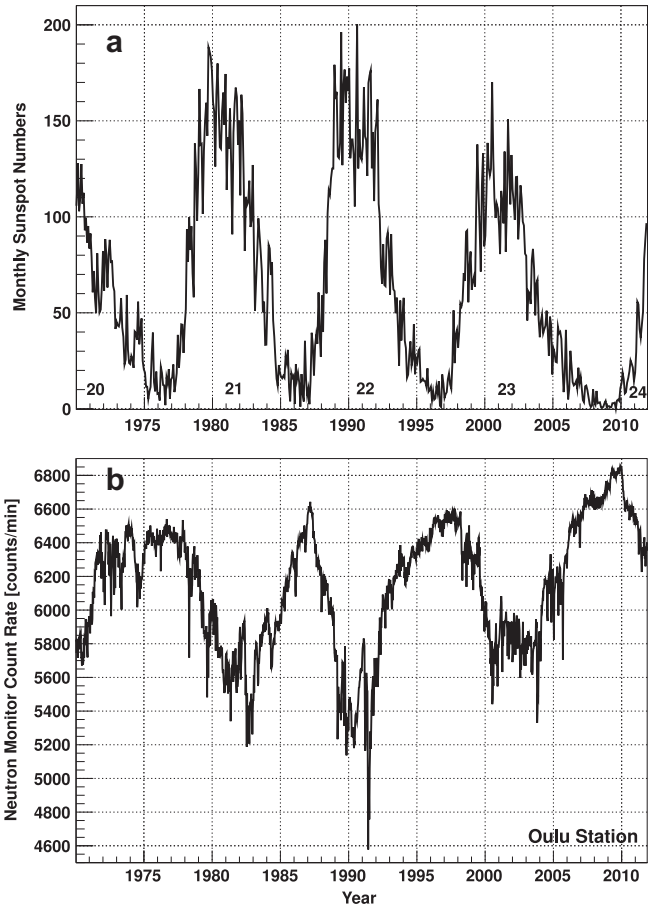

Fig. 1. Monthly sunspot numbers and solar cycle numbers from 20 to 24 (Fig. 1a). 10-day averaged neutron monitor count rates from the Oulu station starting from 1970 to the end of 2011 (Fig. 1b).

all particles arrive in vertical direction (see Cooke et al., 1991 for a detailed discussion on the cut-off terminology). The effective vertical cut-off rigidity is often used to calculate the lowest energy for a charged particle to penetrate the magnetosphere and reach the top of the atmosphere.

By comparing Fig. 1a and b, the negative correlation between the monthly sunspot numbers, which are an index for the level of solar activity, and the 10-day averaged NM count rates can be seen. The elevated GCR intensity during the last solar minimum relative to the minima in the past decades is clearly visible. In 2009 the peak neutron count rate of 6850 min^{-1} was about 3–5% greater than the peak count rates measured during preceding minima.

Fig. 2 shows the GCR particle fluxes integrated over energy measured by the Cosmic Ray Isotope Spectrometer (CRIS) instrument aboard the ACE spacecraft between August 1997 and October 2011 relative to the maximum integrated flux observed in the 1997/1998 solar minimum. The data is presented for C, O, Ne, Mg, Si and Fe nuclei as these are highly abundant GCR ions measured by the instrument over different energy ranges from approximately 59 MeV/nuc to 471 MeV/nuc. The fluxes are averaged over 27 days and were obtained from the ACE website (http://www.srl.caltech.edu/ACE/ASC/level2/lvl2DATA_CRIS.html). The elevated particle fluxes in 2009/2010 in comparison with the previous minimum can also be seen. The peak values were observed in late 2009 where the fluxes are showing an increase of about 16–21% in comparison with the peak intensity during the previous solar minimum.

The solar modulation parameter Φ reconstructed from data collected by various neutron monitors since 1936 is provided at http://cosmicrays.oulu.fi/phi/Phi_mon.txt according to Usoskin et al., 2011. The lowest of these monthly averaged values of Φ during the last solar minimum was 255 MV during December 2009 whereas for the solar minimum between cycle 22 and 23 it was 394 MV (August 1997). In fact the modulation levels in late 2009 were the lowest in the last half century. The value Φ derived from the measured intensities of the particle species mentioned above at ~200 MeV/nuc by the ACE/CRIS instrument and averaged from late October 2009 to about mid-January 2010 was found to be ~235 MV (Mewaldt et al., 2010). For the solar minimum between cycles 22 and 23, the averaged Φ between late August and early November 1997 was ~320 MV (Mewaldt et al., 2010).

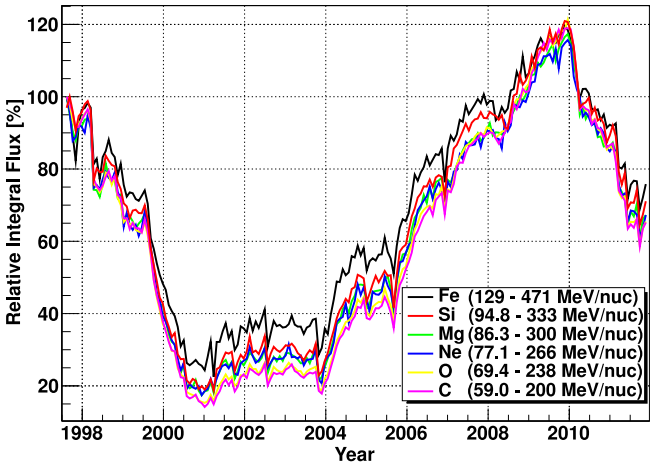

Fig. 2. 27-Day averages of the GCR flux integrated over energy ranges measured by ACE/CRIS instrument between August 1997 and October 2011 relative to the maximum integrated flux observed in the 1997/1998 solar minimum.

2. Method – numerical dose estimation

GCR arriving at Earth, as measured via various balloon and satellite experiments, consist of about 98% charged nuclei out of which H constitutes ~87%, He ~12% and heavier nuclei up to iron and beyond ~1% (Simpson, 1983). Although the heavy nuclei are less abundant, they are critical for the purpose of radiation exposure assessments for astronauts. The extent of biological damage is related to a particle's energy loss, which in turn is proportional to the square of charge of the particle within a material and therefore is greater for heavy nuclei (Mewaldt, 1994; Cucinotta et al., 2001). Since the intensity of elements above Fe falls down dramatically in GCR, it is sufficient to consider nuclei between $1 \leqslant Z \leqslant 26$ (Z = atomic number). It was shown in Mrigakshi et al. (2013) that the selected energy range between 10 MeV/nuc and 100 GeV/nuc is adequate for the simulation setup used in this work which is described in Section 2.1. For a detailed explanation of the dose calculation method refer to Mrigakshi et al. 2013.

The radiation exposure was numerically estimated in terms of absorbed dose rate (dD/dt) and dose equivalent rate (dH/dt) as defined in Eq. (1) and Eq. (2):

I. Absorbed Dose D in the unit J/kg or gray (Gy):

$$D = \frac{d\bar{\varepsilon}}{dm} \tag{1}$$

where $d\bar{\varepsilon}$ is the mean energy imparted in a volume of mass dm by ionizing radiation

II. Dose Equivalent in the unit J/kg or sievert (Sv):

$$H = D \cdot Q \tag{2}$$

where D is the mean absorbed dose in the target and Q is the mean quality factor related to the biological effectiveness of the radiation. Q is defined as a function of the unrestricted linear energy transfer (LET) in water in ICRP 60 (ICRP, 1991). The unrestricted LET is the energy lost by a charged particle divided by the path length.

The absorbed dose and the dose equivalent are among the principal dosimetric quantities recommended by the International Commission on Radiological Protection in ICRP 60 (ICRP, 1991). While the absorbed dose gives

the amount of energy per mass imparted in a material the dose equivalent includes information regarding the extent of biological damage.

2.1. Simulation setup

Radiation transport codes are required to simulate the passage of radiation through matter. Such codes utilize different methods to describe the physics of particle interactions and the transport the primary and secondary radiation through simulated media e.g. spacecraft shielding and human body. Several studies (e.g. Lin et al. 2012 and Sihver et al. 2008a) have been performed to inter-compare and validate these transport codes for their application in radiation protection in space.

In this work, the Monte-Carlo transport code GEANT4 (**GE**ometry **AN**d **T**racking, Agostinelli et al., 2003; Allison et al., 2006) version 9.3 patch 02 was employed to describe the shield and target geometries, simulate and transport radiation and estimate the dose quantities.

2.1.1. Target

Spherical phantoms (e.g. Berger et al., 2004; Jadrníčková et al., 2010), and the anthropomorphic phantoms (e.g. Reitz et al., 2009; Yasuda, 2009), are often used to measure the dose distribution inside the human body in space. For numerical dose calculations, spherical phantoms are easier to model and require less computational time in comparison with human voxel phantoms. The organ doses from spherical phantoms can be derived from the computed values at points inside the sphere where the mean shielding equals the mean shielding of the organs inside the human body (NCRP, 1989; Kireeva et al. 2007; Matthiä et al. 2013b). Matthiä et al. (2013b) investigated the applicability of a water sphere of radius 20 cm as a surrogate for anthropomorphic phantoms and estimated organ doses for isotropic irradiation from GCR in Low Earth Orbit. The mean organ shielding ρ in the ICRP male phantom was calculated to range from 10.5 g/cm^2 to 19.1 g/cm^2 and in the water sphere from 10 g/cm^2 to 20 g/cm^2. By comparing the calculated organ absorbed dose and dose equivalent rates in the spherical and the ICRP voxel phantoms, it was found that these quantities differed by less than 5% and 11%, respectively.

In this work, a spherical water phantom with a radius of 25 cm, consisting of 100 shells with a thickness of 2.5 mm each, was used as a surrogate for the human body to estimate the radiation exposure. The mean shielding for isotropic irradiation for the sphere lies between 12.5 g/cm^2 at the surface to 25 g/cm^2 at the centre of the sphere. This implies that while the mean shielding for many organs e.g. red bone marrow ($\rho = 17.1$ g/cm^2, see Matthiä et al. 2013b) is covered by the sphere used in this work and the dose rates can be estimated, but for some organs like the brain ($\rho = 11.6$ g/cm^2, see Matthiä et al. 2013b this is not the case due to the heavier self-shielding of the water sphere.

The dose quantities presented in this paper are calculated over the entire water sphere. To calculate the absorbed dose, the summation of the energy deposited at each step along a particle's trajectory in the sphere was divided by its mass (Eq. (1)) and to calculate the dose equivalent, the summation of the energy deposited weighted by the quality factor (dependent on the LET) for each step was divided by the mass of the sphere (Eq. (2)).

2.1.2. Shielding and radiation source

Ions ranging from hydrogen to iron were simulated from a spherical radiation source inwards onto the water sphere with and without shielding made of aluminium. The shielding geometry is also spherically surrounding the target sphere with an outer radius of 50 cm with varying thicknesses corresponding to areal densities 0.3 g/cm^2 ($\sim$0.11 cm), 10 g/cm^2 ($\sim$3.70 cm), and 40 g/cm^2 ($\sim$14.8 cm). The space between the shielding and the target consists of air.

2.1.3. Physics models

The relevant hadronic and electromagnetic physics model lists (*QGSP_BERT_HP* and *emstandard_opt3*) were selected to calculate the transport of primary and secondary particles in the water sphere (see GEANT4 Physics Reference Manual in http://geant4.cern.ch/G4UsersDocuments/UsersGuides/PhysicsReferenceManual/html/PhysicsReferenceManual.html for details). Additionally, the JQMD/JAM model (Niita et al., 1995; Nara et al., 1999) interface for GEANT4 (Koi et al., 2003) was used due to the limitation of the intrinsic models in GEANT4.9.3 describing inelastic nucleus–nucleus interactions to energies below 10 GeV/nuc. Furthermore, the hadron model (*QGSP_BERT_HP*) used for the simulations in this work is applicable for protons, neutrons, pions, kaons and hyperons only and not for heavy ions from helium onwards (see Ivantchenko et al., 2012 and the references therein for details regarding the available Geant4 models for inelastic nucleus–nucleus interactions). With the inclusion of the JQMD/JAM model, the contribution of heavy ions ($Z \geqslant 2$) and the contribution of particle energies ranging from 10 MeV/nuc to 100 GeV/nuc to the GCR exposure could be calculated (Sihver et al., 2008b).

2.2. GCR model

The GCR model developed by Matthiä et al., 2013a was used to describe the spectra of the relevant particles. This model is based on the GCR-ISO model (ISO, 2004) and is capable of describing energy spectra of nuclei ranging from H to Ni for a selected point of time at 1 AU distance from the Sun outside the Earth's magnetosphere. The only free parameter required to calculate the particle spectra is derived from either the GCR carbon measurements from the ACE spacecraft for periods since August 1997 (referred to as Matthiä/ACE in this paper) or from the Oulu NM

count rates to extend the validity period of the model back to 1964 (referred to as Matthiä/OULU). In this work both methods were used to derive the GCR spectra for the estimation of the dose quantities.

To calculate the GCR spectra inside the Earth's magnetosphere, the so-called geomagnetic transmission function provided by the CREME package (Tylka et al., 1997; https://creme.isde.vanderbilt.edu/) was used. The geomagnetic transmission function gives the fraction of particles reaching an orbit of interest as a function of the particles' magnetic rigidity. It also accounts for the effect of solid Earth's obstruction to the incoming radiation. For this work, the spectra at Low Earth Orbit (LEO) were calculated by scaling the GCR spectra at 1 AU by the orbit-averaged geomagnetic transmission function derived for the ISS orbit with an inclination of 51.6° and an altitude of 350 km.

3. Results – GCR exposure

For the identification of any unusual changes in the level of GCR exposure, the dose estimations were performed for an extended period of time. A detailed explanation of the method applied to estimate the dose rates over several decades using different models can be found in Mrigakshi et al., 2013.

Fig. 3 shows the calculated absorbed dose and dose equivalent rates in the water sphere without shielding from January 1970 to October 2011 at near-Earth interplanetary space (Fig. 3a) and at the ISS orbit (Fig. 3b). The dose quantities were estimated by applying the Matthiä/ACE and Matthiä/OULU model. As expected, the dose rate correlates with the GCR intensity and is anti-correlated to the solar activity. The exposure is largest during the solar minimum periods (around years 1977, 1986, 1997, 2009) when the GCR flux reaches its peak values. The estimated dose values using the ACE and OULU data in the GCR model are very similar. However, during certain epochs e.g. 1997–1998 and 2001–2002 small differences can be seen which occur as a result of the differences in the GCR spectra derived using the two sets of data. The Neutron Monitor is mainly sensitive to the flux of secondary neutrons and protons produced by the interaction of primary GCR within the atmosphere. Due to their large abundance, primary hydrogen and helium are the main sources of these secondary particle fluxes. The ACE data on the other hand are direct measurements of GCR carbon nuclei. Additionally, the carbon spectra provided by ACE is measured over energies ranging from 59 MeV/nuc to 200 MeV/nuc whereas the NM is sensitive to higher energies as the low-energetic particles do not affect the count rate of a sea-level Neutron Monitor due to the shielding provided by the Earth's atmosphere.

The absorbed dose rate between January 1970 and October 2011 ranged from 88.5 μGy/d to 472 μGy/d and the dose equivalent rate from 280 μSv/d to 1.43×10^3 μSv/d from solar maximum to minimum in near-Earth interplanetary space. For ISS orbit the

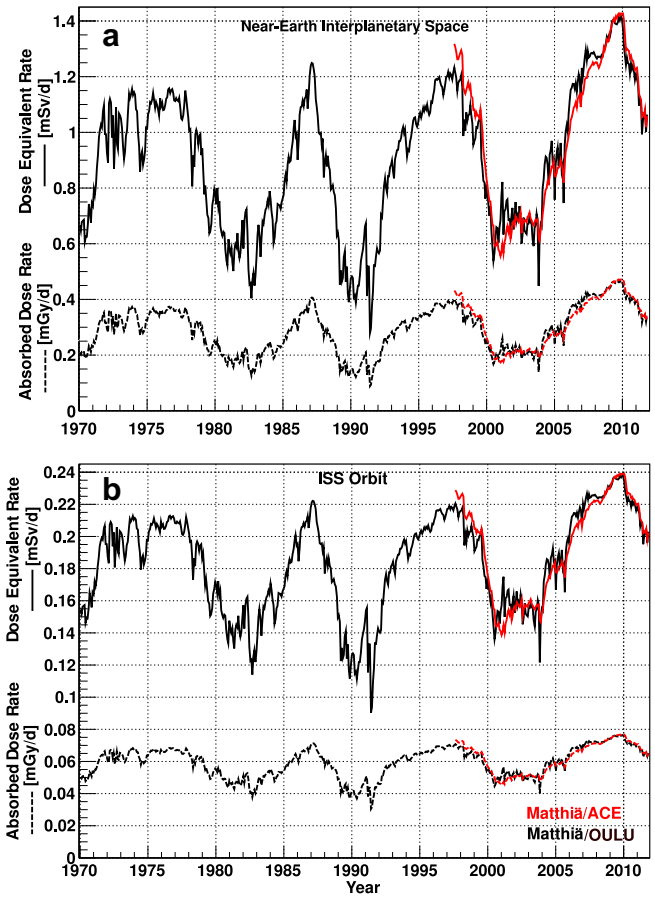

Fig. 3. Absorbed dose rates (dashed lines) and dose equivalent rates (solid lines) in a water sphere for near-Earth interplanetary space (Fig. 3a) and ISS orbit (Fig. 3b) estimated by applying the GCR model by Matthiä et al (2013a) using either ACE measurements (Matthiä/ACE, red lines) or Oulu Neutron Monitor count rates (Matthiä/OULU, black lines). (For interpretation of the references to colour in this figure legend, the reader is referred to the web version of this article.)

absorbed dose rate ranged from 30.5 μGy/d to 76.7 μGy/d and the dose equivalent rate from 90.3 μSv/d to 239 μSv/d which is about 15% (30%) of the dose rates outside the magnetosphere during solar minimum (solar maximum). The variation of dose rates during a solar cycle between solar maximum and minimum is about a factor of 2–2.5 inside the magnetosphere (Fig. 3b) in comparison to about a factor of 3–4.5 outside the magnetosphere (Fig. 3a). The lower variation at LEO is due to the fact that low energetic particles which experience the strongest modulation by the solar activity get also strongly modulated by the geomagnetic field leading to a reduced solar cycle related variation in the exposure. For the same simulation scenario in Mrigakshi et al. (2013), it was shown that the GCR exposure from particles with energies ranging from 100 MeV/nuc to 1 GeV/nuc contribute to about 30–52% of the total exposure in near-Earth interplanetary space while this contribution is reduced to about 10–24% at ISS orbit. The mean quality factor averaged over the inspected time period was found to be about 3.1 for both the locations in space.

To investigate the influence of shielding on the exposure from GCR, calculations of the dose rates in the water sphere surrounded by aluminium with thicknesses corresponding to areal densities of 0.3 g/cm^2, 10 g/cm^2 and 40 g/cm^2 were made and are shown in Fig. 4. The dose quantities were estimated by applying the Matthiä/ACE GCR model for a time period ranging from August 1997 to October 2011 for near-Earth interplanetary space and ISS orbit.

The dose rates calculated for a shielding of 0.3 g/cm^2 differ by less than 1% from those calculated in the target without shielding for both locations in space. The absorbed dose rates are found to increase for 10 g/cm^2 and 40 g/cm^2 shielding for both locations in space, although the increase is higher at ISS orbit (Fig. 4b). Compared to the unshielded target the relative increase in the absorbed dose rate calculated for ISS orbit (near-Earth interplanetary space) with 10 g/cm^2 shielding is 16–22% (2–12%) and 70–96% (13–50%) for 40 g/cm^2. The increase in absorbed dose rates can be attributed to the increase in secondary radiation like neutrons with increasing shield thickness that is created by nuclear interactions of high-energy GCR particles with atoms constituting the shielding. The variation of dose equivalent rates with shielding show different behaviors with location and time indicating that the influence of the shielding on the dose rates is also dependant on the energy spectra of the GCR particles which changes with the solar activity.

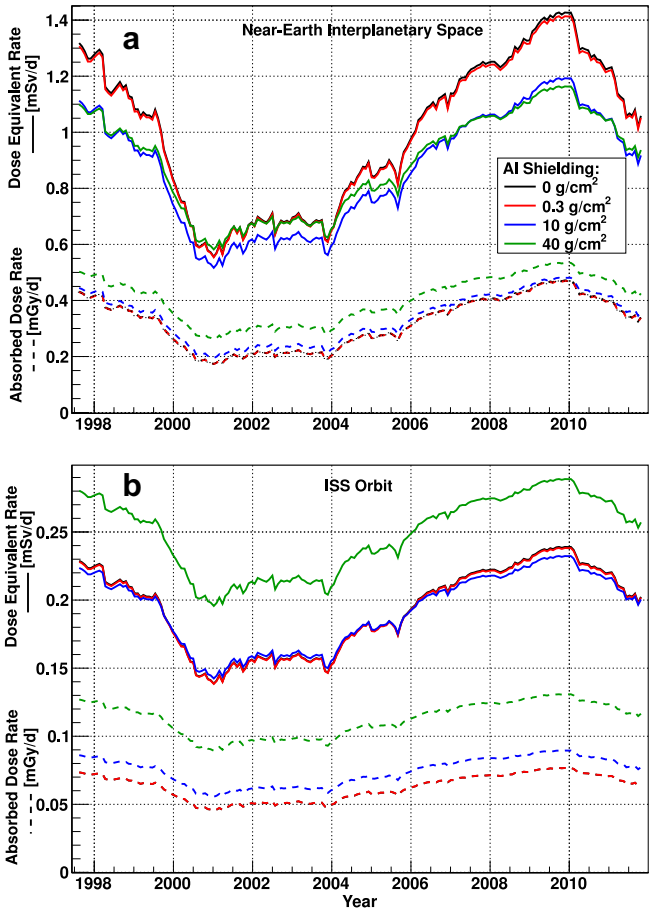

Fig. 4. Absorbed dose rates (dashed lines) and dose equivalent rates (solid lines) in a water sphere with varying shield thicknesses (0 g/cm^2 in black, 0.3 g/cm^2 in red, 10 g/cm^2 in blue and 40 g/cm^2 in green) for near-Earth interplanetary space (Fig. 4a) and ISS orbit (Fig. 4b). The dose rates are calculated by applying the GCR model by Matthiä et al (2013a) (Matthiä/ACE). (For interpretation of the references to colour in this figure legend, the reader is referred to the web version of this article.)

In near-Earth interplanetary space (Fig. 4a) the reduction in the dose equivalent rate by adding 10 g/cm^2 Al shielding is stronger during solar minimum periods (−16%) than during solar maximum (−7%). By increasing the shielding from 10 g/cm^2 to 40 g/cm^2, the change in the dose equivalent rate is, on average, about 4% over time. It increases during solar maximum (up to +12%) and decreases during solar minimum (less than −2%). At ISS orbit the change in dose equivalent rate by increasing the shielding to 10 g/cm^2 is small. It increases during solar maximum and decreases during solar minimum by up to ±3%. If the shielding is changed from 10 g/cm^2 to 40 g/cm^2 then the dose equivalent rate increases by about 25–35%. The trend of the dose equivalent rates showing a reduction from 0–0.3 g/cm^2 to 10 g/cm^2 shielding and then increasing again from 10 g/cm^2 to 40 g/cm^2 for solar minimum e.g. during November 2009 was also found by Matthiä et al. (2013b). In fact the non-monotonic behaviour in the dose equivalent rates with increasing shielding was also observed in the dose measurements taken during the STS-89 flight in the solar minimum period of Jan 1998 (Badhwar and Cucinotta, 2000).

The quality factors, calculated as the ratio of the dose equivalent rate to the absorbed dose rate, are found to reduce with increasing shielding and the averages over the whole time period are about 3.1 (no shielding, 0.3 g/cm^2), 2.6 (10 g/cm^2) and 2.2 (40 g/cm^2) for different shielding configurations. The decreasing quality factors suggest that the fraction of the dose contribution from low-LET particles increases with increasing shielding.

Clearly, Fig. 3 indicates that the GCR exposure was the largest during the solar minimum cycle 23/24 with respect to the three solar minima in the past and peaked in November 2009. For the case without shielding, both dose quantities, taken as the average values from Matthiä/ACE and Matthiä/OULU (Fig. 3), are expected to have risen by about 13% in near-Earth interplanetary space and about 6% at ISS orbit relative to the highest exposure during the previous solar minimum in August 1997. The level of increase in the dose rates from the peak exposure in 1997 to 2009 is found to reduce with shielding (Fig. 4) and has been quantified in Table 1.

Mrigakshi et al. (2013) showed that for an unshielded water sphere the application of commonly used GCR models for the purpose of radiation protection in space – CREME96, CREME2009 and Badhwar-O'Neill2010 (BON2010), did not result in elevated exposure estimates during the recent solar minimum in 2009. The peak dose values in 2009 estimated for an unshielded water sphere

Table 1
Peak absorbed dose rate dD/dt and dose equivalent rate dH/dt estimated by using Matthiä/ACE GCR model for a water sphere shielded by aluminum shells of varying thicknesses during the recent solar minimum in 2009.

Shielding (g/cm^2)	Near-Earth interplanetary space		Change in dose relative to peak dose in 1997 (%)	ISS Orbit		Change in dose relative to peak dose in 1997 (%)
	dD/dt (μGy/d)	dH/dt (μSv/d)		dD/dt (μGy/d)	dH/dt (μSv/d)	
0	472	1.43×10^3	+9	76.7	239	+4
0.3	469	1.41×10^3	+9	76.7	238	+4
10	481	1.19×10^3	+8	89.5	232	+4
40	534	1.16×10^3	+6	131	289	+3

Table 2
Estimation of the maximum radiation exposure in an unshielded water sphere during the recent solar minimum in 2009 in terms of the absorbed dose rate dD/dt and dose equivalent rate dH/dt applying various GCR models.

GCR models	Month/2009	Near-Earth interplanetary space		Change in dose relative to peak dose in 1997 (%)	ISS Orbit		Change in dose relative to peak dose in 1997 (%)
		dD/dt (μGy/d)	dH/dt (μSv/d)		dD/dt (μGy/d)	dH/dt (μSv/d)	
Matthiä/ACE	November	472	1.43×10^3	+9	76.7	239	+4
Matthiä/OULU	November	469	1.42×10^3	+16	76.4	238	+8
BON2010	August	370	1.14×10^3	−3	64.5	199	−2
CREME96	March	395	1.22×10^3	−8	71.9	224	−2
CREME2009	August	398	1.24×10^3	−5	71.3	223	−1

by applying these models (Mrigakshi et al., 2013) are presented in Table 2 together with the dose estimates based on the GCR model by Matthiä et al. (2013a) using both methods to derive the GCR spectra. The table also shows the relative difference in the peak dose calculated for 2009 relative to the peak dose estimated for the previous solar minimum in 1997. The highest exposure during these years was calculated to occur at different times using all GCR models as indicated in the table. Note that the result is not indicated separately for absorbed dose rate and dose equivalent rate as it was found to be similar for both these quantities with less than 1.5% difference. The exposure calculated using Matthiä/OULU differed by less than 1% for 2009 and less than 7% for 1997 relative to the exposure calculated using Matthiä/ACE model. The application of the Badhwar-O'Neill2010 model produced the largest difference in the dose values in comparison with the doses estimated by applying the models by Matthiä et al. (2013a). For near-Earth interplanetary space the dose equivalent and absorbed dose rates from BON2010 are ~21%, from CREME96 ~16% and from CREME2009 ~14% lower than the values calculated using Matthiä/ACE. For ISS orbit the dose values based on BON2010, CREME96 and CREME2009 are lower by ~16%, ~6% and ~7%, respectively relative to the values calculated using Matthiä/ACE.

The peak skin absorbed dose during the year 2009 was calculated by Schwadron et al. (2010) behind aluminium shielding of 0.3 g/cm^2, 10 g/cm^2 and 40 g/cm^2 for near-Earth interplanetary space and was about 330 μGy/d, 325 μGy/d and 274 μGy/d. The reducing trend in the absorbed dose rates is contradictory to the results presented in this paper (Fig. 4) and the work presented in Matthiä et al. (2013b). Furthermore, in this work an increase in the peak dose rates during the recent solar minimum in November 2009 relative to the previous minimum in August 1997 for all shielding configurations is visible (Table 1) while in the results by Schwadron et al. (2010) it is not. The differences in the absorbed dose rates calculated with the various GCR models in this work for the recent solar minimum (Table 2) show that the selection of the GCR model plays an important role in the estimation of the radiation exposure. It was shown above that the Badhwar-O'Neill model does not predict the increased intensity in 2009 which indicates that the lower exposure estimates by Schwadron et al. (2010) could indeed be due to their selection of the GCR model.

However, the large differences in the dose rates calculated for the year 2009 in general e.g. behind a shielding of 0.3 g/cm^2 which is about 30% lower than the estimates made in this work using Matthiä/ACE is likely due to the transport models in the HZETRN code. The transport code HZETRN used by Schwadron et al. (2010) in their calculations was recently extended to include the production, the transport and the decay of pions in matter (Norman et al., 2012; Slaba et al., 2012). Recent studies showed that the lack of a description of these physical interactions lead to an underestimate in the absorbed dose from GCR in the order of tens of percent (Aghara et al., 2009; Slaba et al., 2012). Additional factors causing the differences in the dose rates as shown in the two studies could be due to the differences in the setup of the shield and/or target geometries which, however, were not described explicitly by Schwardon et al. (2010).

4. Conclusion and outlook

The goal of this work was to quantify the rise in the GCR exposure during the solar minimum between cycles 23 and 24 as a result of elevated GCR intensities observed at the time compared to the preceding solar minima. A

numerical estimation of the absorbed dose rate and dose equivalent rate was thus performed for time periods starting from 1970 to the end of 2011 in a water sphere either unshielded or behind aluminium shielding of 0.3, 10 and 40 g/cm^2. The calculations were made for a location outside the Earth's magnetosphere at a distance of about 1 AU from the Sun and at the ISS orbit. A GCR model recently developed by Matthiä et al. (2013a) was employed to estimate the GCR exposure to overcome the finding of the recent work presented in Mrigakshi et al. (2012) showing that other commonly used GCR models CREME96, CREME2009 and the Badhwar-O'Neill2010 do not describe an elevated GCR intensity in the years 2008–2010 and therefore their application does not result in an increased estimate of the GCR exposure (Mrigakshi et al., 2013).

The study showed that the GCR exposure between the years 2008 and 2010 is expected to have been the highest since the beginning of the space age. The peak absorbed dose rate and the dose equivalent rate in an unshielded water sphere during to the peak GCR intensity in November 2009 were estimated to be 472 μGy/d and 1.43×10^3 μSv/d for near-Earth interplanetary space and for ISS orbit 76.7 μGy/d and 239 μSv/d. The absorbed dose and dose equivalent rates exceeded the previous maximum levels by about 10% for near-Earth interplanetary space and about 6% at the ISS orbit if no shielding is used. The relative increase in the peak dose rates from 1997 to 2009 was found to reduce with shielding ranging to about 6% (40 g/cm^2 shielding) for near-Earth interplanetary space and to about 3% at the ISS orbit. The results were compared with the dose estimates presented in Mrigakshi et al. (2013) wherein the calculations were made using Badhwar-O'Neill2010, CREME96 and CREME2009 models for the same simulation setup without shielding. It was found that the application of these models results in lower dose rates with respect to the values calculated using the model by Matthiä et al. (2013a).

The dose estimations made for this period could serve as a reference for the worst case GCR exposure scenario for manned spaceflight to destinations close to Earth.

Acknowledgement

We thank the ACE SWEPAM instrument team and the ACE Science Center for providing the ACE data, and Sodankyla Geophysical Observatory and the Oulu neutron Monitor team for providing the Neutron Monitor count rates.

The first author, Alankrita Isha Mrigakshi, receives a SpaceLife scholarship funded by the Initiative and Networking Fund of the Helmholtz Association and the German Aerospace Center as a participant of the Helmholtz Space Life Sciences Research School (SpaceLife) at the German Aerospace Center.

References

Aghara, S., Blattnig, S., Norbury, J., Singleterry, R. Monte Carlo analysis of pion contribution to absorbed dose from Galactic cosmic rays. Nucl. Instrum. Methods B 267 (7), 1115–1124, 2009.

Agostinelli, S., Allison, J., Amako, K., et al. Agostinelli, S. Geant4 – a simulation toolkit. Nucl. Instrum. Methods Phys. Res. Sec. A 506, 250–303, 2003.

Allison, J., Amako, K., Apostolakis, J., et al. Geant4 developments and applications. IEEE Trans. Nucl. Sci. 53, 270–278, 2006.

Badhwar, G.D., Cucinotta, F.A. A comparison of depth dependence of dose and linear energy transfer spectra in aluminum and polyethylene. Radiat. Res. 153, 1–8, 2000.

Belov, A.V. Large scale modulation: view from the Earth. Space Sci. Rev. 93, 79–105, 2000.

Berger, T., Hajek, M., Summerer, L., Vana, N., Akatov, Y., Shurshakov, V., Arkhangelsky, V. Austrian dose measurements onboard space station MIR and the International Space Station – overview and comparison. Adv. Space Res. 34 (6), 1414–1419, http://dx.doi.org/10.1016/j.asr.2003.08.063, 2004.

Cooke, D.J., Humble, J.E., Shea, M.A., Smart, D.F., Lund, N., Rasmussen, I.L., Byrnak, B., Goret, P., Petrou, N. On cosmic-ray cut-off terminology. Il Nuovo Cimento 14 (C), 213–234, 1991.

Cucinotta, F.A., Schimmerling, W., Wilson, J.W. et al., Space radiation cancer risk projections for exploration missions: uncertainty reduction and mitigation, NASA JSC Document (JSC-29295), NASA Washington DC, 2001.

Cucinotta, F.A., Durante, M. Cancer risk from exposure to galactic cosmic rays: implications for space exploration by human beings. Lancet Oncol. 7, 431–435, 2006.

Gleeson, L.J., Axford, W.I. Solar modulation of galactic cosmic rays. Astrophys. J. 154, 1011, 1968.

Grieder, P.K.F. Cosmic Rays at Earth: Researcher's Reference Manual and Data Book. Elsevier Science B. V, Amsterdam, The Netherlands, 2001.

Heber, B. Cosmic rays through the solar hale cycle. Space Sci. Rev. 1-14, 2011, doi:10.1007/s11214-011-9784-x.

Hess, V.F. Űber Beobachtungen der durchdringenden Strahlung bei sieben Freiballonfahrten. Physikalische Zeitschrift 13, 1084–1091, 1912.

ICRP, 1990 Recommendations of the International Commission on Radiological Protection, ICRP Publication 60. Ann. ICRP 21, 1991

International Standard ISO 15390, Space environment (natural and artificial)-Galactic cosmic ray model, 2004.

Jadrnícková, I., Brabcová, K., Mrázová, Z., Spurný, F., Shurshakov, V.A., Kartsev, I.S., Tolochek, R.V. Dose characteristics and LET spectra on and inside the spherical phantom onboard of ISS. Radiat. Meas., http://dx.doi.org/10.1016/j.radmeas.2010.07.002, 2010.

Ivantchenko, A.V., Ivanchenko, V.N., Molina, J.M., Incerti, S.L. Geant4 hadronic physics for space radiation environment. Int. J. Radiat. Biol. 88 (1–2), 171–175, 10.3109/09553002.2011.610865, 2012.

Kireeva, S.A., Benghin, V, Kolomensky, A.V., Petrov, V. Phantom–dosimeter for Estimating Effective Dose Onboard International Space Station. 2007 Feb-Apr; 60(4–7): 547–553. DOI: 10.1016/j.actaastro.2006.09.019.

Koi, T., Asai, M., Wright, D.H. Interfacing the JQMD and JAM Nuclear Reaction Codes to Geant4. Comput. High Energ. Nucl. Phys., SLAC-PUB-9978, 2003.

Lin, Z.W., Adams Jr., J.H., Barghouty, A.F., Randeniya, S.D., Tripathi, R.K., Watts, J.W., Yepes, P.P. Comparisons of several transport models in their predictions in typical space radiation environments. Adv. Space Res. 49, 797–806, http://dx.doi.org/10.1016/j.asr.2011.11.025, 2012.

Matthiä, D., Berger, T., Mrigakshi, A.I., Reitz, G. A ready-to-use Galactic Cosmic Ray model. Adv. Space Res. 51, 329–338, 10.1016/j.bbr.2011.03.031, 2013a.

Matthiä, D., Berger, T., Reitz, G. Organ shielding and doses in low earth orbit calculated for spherical and anthropomorphic phantoms. Adv. Space Res., 10.1016/j.asr.2013.03.025, 2013b.

Mewaldt, R.A. Galactic cosmic ray composition and energy spectra. Adv. Space Res. 14, 737–747, 1994.

Mewaldt, R.A., Davis, A.J., Lave, K.A. Record-setting cosmic-ray intensities in 2009 and 2010. Astrophys. J. Lett. 723, L1–L6, 10.1088/2041-8205/723/1/L1, 2010, 2010.

Mrigakshi, A.I., Matthiä, D., Berger, T., Reitz, G., Wimmer-Schweingruber, R.F. Assessment of Galactic Cosmic Ray models. J. Geophys. Res. 117, A08109, 10.1029/2012JA017611, 2012.

Mrigakshi, A.I., Matthiä, D., Berger, T., Reitz, G., Wimmer-Schweingruber, R.F. How Galactic Cosmic Ray models affect the estimation of radiation exposure in space. Adv. Space Res. 51, 825–834, 2013.

Nara, Y., Otuka, N., Ohnishi, A., et al. Relativistic nuclear collisions at 10A GeV energies from p + Be to Au + Au with the hadronic cascade model. Phys. Rev. C 61, 2, 1999.

NCRP, National Council on Radiation Protection and Measurements, Operational Radiation Safety Program for Astronauts in Low-Earth Orbit: A Basic Framework, NCRP Report No. 142, 2002.

NCRP, National Council on Radiation Protection and Measurements, Guidance on Radiation Received in Space Activities, NCRP Report No. 98, 1989.

NCRP, National Council on Radiation Protection and Measurements, Radiation Protection Guidance for Activities in Low-Earth Orbit, NCRP Report No. 132, 2000.

NCRP, National Council on Radiation Protection and Measurements, Radiation Information Needed to Make Radiation Protection Recommendations for Space Missions Beyond Low-Earth Orbit, NCRP Report No. 153, 2006.

Niita, K., Chiba, S., Maruyama, T., et al. Analysis of the (N, xN') reaction by quantum molecular dynamics plus statistical decay model. Phys. Rev. C 52, 2620–2635, 1995.

Norman, R.B., Blattnig, S.R., De Angelis, G., Badavi, F.F., Norbury, J.W. Deterministic pion and muon transport in Earth's atmosphere. Adv. Space Res. 50 (1), 146–155, 2012.

O'Neill, P.M. Badhwar–O'Neill galactic cosmic ray model update based on advanced composition explorer (ACE) energy spectra from 1997 to present. Adv. Space Res. 37 (9), 1727–1733, 10.1016/j.asr.2005.02.001, 2006.

O'Neill, P.M. Badhwar–O'Neill 2010 Galactic Cosmic Ray flux model—revised. IEEE Trans. Nucl. Sci. 57 (6), 3148–3153, 2010.

Reitz, G., Berger, T., Bilski, P. Astronaut's organ doses inferred from measurements in a human phantom outside the International Space Station. Radiat. Res. 171, 225–235, http://dx.doi.org/10.1667/RR1559.1, 2009.

Schwadron, N.A., Boyd, A.J., Kozarev, K. Galactic cosmic ray radiation hazard in the unusual extended solar minimum between solar cycles 23 and 24. Space Weather 8, S00E04, http://dx.doi.org/10.1029/2010SW000567, 2010.

Sihver, L., Mancusi, D., Niita, K., Sato, T., Townsend, L., Farmer, C., Pinsky, L., Ferrari, A., Cerutti, F., Gomes, I. Benchmarking of calculated projectile fragmentation cross-sections using the 3-D, MC codes PHITS, FLUKA, HETC-HEDS, MCNPX_HI, and NUCFRG2. Acta Astronaut. 63, 865–877, 10.1016/j.actaastro.2008.02.012, 2008a.

Sihver, L., Matthiä, D., Koi, T., Mancusi, D. Dose calculations at high altitudes and in deep space with GEANT4 using BIC and JQMD models for nucleus–nucleus reactions. New J. Phys. 10 (10), 105019, 2008b.

Simpson, J.A. The cosmic ray nucleonic component: the invention and scientific uses of the neutron monitor. Space Sci. Rev. 93 (1), 11–32, 2000.

Simpson, J.A. Elemental and isotopic composition of the Galactic Cosmic Rays. Annu. Rev. Nucl. Part. Sci. 33, 323–382, http://dx.doi.org/10.1146/annurev.ns.33.120183.001543, 1983.

Slaba, T.C., Blattnig, S.R., Reddell, B., Norman, R.B., Badavi, F.F., ISS dose estimates due to pions and electromagnetic cascade, 17th Workshop on Radiation Monitoring onboard the ISS, 2012.

Stone, E.C., Frandsen, A.M., Mewaldt, R.A., Christian, E.R., Margolies, D., Ormes, J.F., Snow, F. The advanced composition explorer. Space Sci. Rev. 86, 1998.

Tylka, A.J., Adams Jr., J.H., Boberg, P.R. CREME96: a of the cosmic ray effect on micro-electronics code. IEEE Trans. Nucl. Sci. 44, 2150–2160, 1997.

Usoskin, I.G., Mursula, K., Kananen, H., Kovaltsov, G.A. Dependence of cosmic rays on solar activity for odd and even solar cycles. Adv. Space Res. 27, 571–576, 2001.

Usoskin, I.G., Bazilevskaya, G.A., Kovaltsov, G.A. Solar modulation parameter for cosmic rays since, reconstructed from ground-based neutron monitors and ionization chambers. J. Geophys. Res. 116, A02104, 10.1029/2010JA016105, 2011, 2011.

Yasuda, H. Effective dose measured with a life size human phantom in a low Earth orbit mission. J. Radiat. Res. 50 (2), 89–96, http://dx.doi.org/10.1269/jrr.08105, 2009.

5 Additional Results

Besides the published findings and results, which were presented in the previous chapter, additional investigations were performed during the course of the research work and are presented in this chapter. These include an assessment of the latest Badhwar-O'Neill2011 model in terms of accuracy of the GCR flux description and the influence on dose calculations. Additionally, the variation of dose with primary particle energy calculated for a shielded water sphere, and furthermore, estimations of the effective dose and comparison of calculated dose with measurements are presented as well.

Note that Appendix C contains an evaluation of the SPENVIS/ISO15390 model for solar maximum (year 2000) and minimum (year 2009) periods. The results are not presented in this chapter as the study was performed for only two time periods in the recent past and from the results presented in Chapter 4 and in this chapter, it is clear that the accuracies of the models change over time. Nevertheless, the study shown in the appendix indicates that the SPENVIS/ISO15390 model as well must be carefully examined before using it for dose calculations.

5.1 Badhwar-O'Neill2011 model

The Badhwar-O'Neill model published in 2010 (O'Neill, 2010) was updated and released in 2012 as the Badhwar-O'Neill2011 (BON2011) model. Similar to the previous model, the updated model can be accessed by contacting the author of O'Neill (2010). The model is delivered as a DOS binary along with its source code written in FORTRAN. Currently, there is no article published explaining this latest model and describing the difference with respect to the older Badhwar-O'Neill2010 model.

5.1.1 Model vs measured energy spectra

To investigate the BON2011 for its accuracy, the model spectra of selected light and heavy nuclei were compared with measurements. The spectra from BON2010 and Matthiä/ACE (Matthiä et al., 2013a) models are also presented to study the differences between these models.

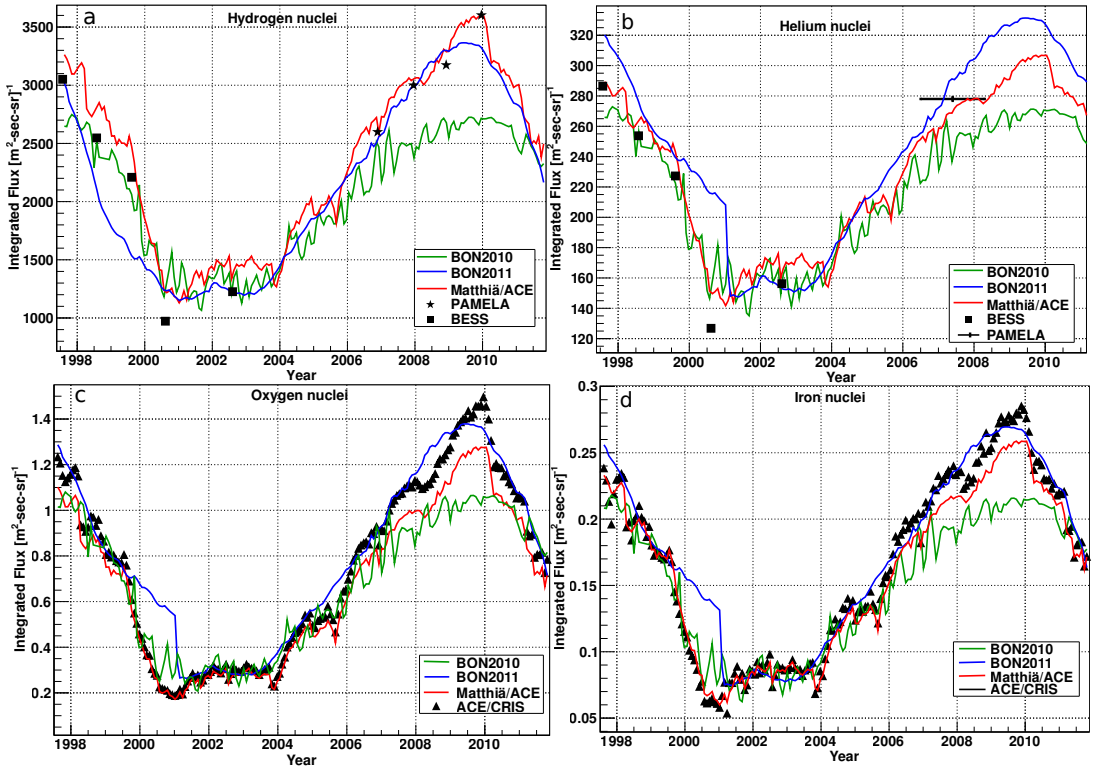

Figure 5.1: Model and measured fluxes of hydrogen (a), helium (b), oxygen (c) and iron (d) nuclei integrated over energy. The hydrogen and helium data, both model and measured, is integrated between the common energy ranges starting from 215 MeV/nuc to 21.5 GeV/nuc as measured by the BESS (solid square symbols) and PAMELA (solid star symbols) experiments. The oxygen spectrum is integrated between 69 MeV/nuc and 240 MeV/nuc and the iron spectrum between 129 MeV/nuc and 471 MeV/nuc as measured by ACE/CRIS (solid triangle symbols) experiment. The solid lines show model data using BON2011 (blue line), BON2010 (green line) and Matthiä/ACE (red line).

A similar assessment of the BON2010, Burger-Usoskin and the CREME models was presented in Mrigakshi et al. 2012 (see Section 4.2).

Figure 5.1 shows the model and measured fluxes[1] of hydrogen, helium, oxygen and iron nuclei integrated over the energy ranges of the available measurements from the year 1997 onwards.

The hydrogen (Figure 5.1a) and helium data (Figure 5.1b) are integrated over an energy range starting from 215 MeV/nuc to 21.5 GeV/nuc as measured by the

[1]Refer to Mrigakshi et al. (2012) presented in Section 4.2 and the references therein for a short description of the space and balloon experiments from which the GCR data was taken for this work.

BESS and PAMELA experiments. As can be seen in the figure, there are only few measurements available for these particles especially for helium. There is just one data set of the helium fluxes measured by the PAMELA experiment which has been published so far and in fact it is an average over a period of July 2006 to March 2008 (Adriani et al., 2011). Note that the energy spectrum of hydrogen and helium nuclei published by the PAMELA team is given over a broader energy range (H: 82 MeV - 49 GeV and He: 120 MeV/nuc - 595 GeV/nuc) in comparison with the BESS experiments but in this figure the flux has been integrated over the common energy ranges covered by both these experiments.
The oxygen data (Figure 5.1c) has been integrated between 69 MeV/nuc and 240 MeV/nuc and the iron data (Figure 5.1d) between 129 MeV/nuc and 471 MeV/nuc as measured by ACE/CRIS experiment. The ACE/CRIS data provided in 27-day averages were used here.
The energy spectra are derived for the starting time of each measurement point as the model spectra showed negligible differences over the entire observation period.

From the figures, it can be seen that the updated Badhwar-O'Neill model BON2011 gives a more accurate description of the particle fluxes than BON2010 for most of the time periods after the year 2001. Unlike the BON2010 model it describes the elevated GCR fluxes observed during the deep solar minimum between the solar cycles 23 and 24. However, the differences between the measurements (hydrogen and helium fluxes) by the BESS experiment and the model integrated fluxes calculated using the BON2011 are larger than those calculated using BON2010 model for most of the datasets. There seems to be a systematic overestimation between the years 2000 and about 2001 wherein the integrated flux from the model differ significantly with respect to the measurements and falls sharply for heavy nuclei. For most of the investigated time periods, the BON2011 model calculates higher particle fluxes in comparison to the BON2010 model. In comparison with BON2011, the spectra derived from Matthiä/ACE model show better agreement with the measurements of hydrogen and helium nuclei and of heavy nuclei for most of the the investigated time periods up to the year 2006. The Matthiä/ACE model is able to describe the peak hydrogen fluxes observed in 2009, however, it shows an underestimation for oxygen and iron nuclei which are described better by the BON2011 model in the investigated energy range.

Figure 5.2 shows a comparison of the measured differential energy spectra of hydrogen, helium, oxygen and iron nuclei from various instruments (BESS, AMS-01, PAMELA,

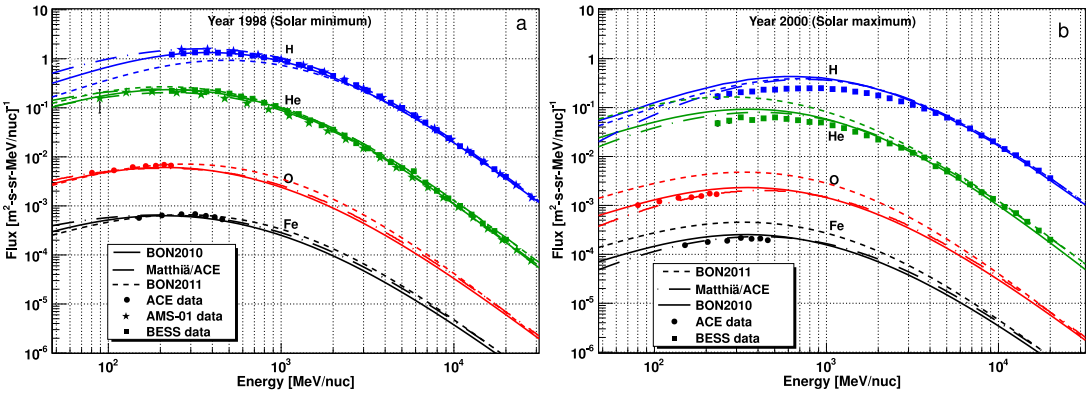

Figure 5.2: Comparison of GCR hydrogen (blue lines), helium (green lines), oxygen (red lines) and iron (black lines) energy spectra described by BON2011 (dashed lines), BON2010 (continuous lines) and Matthiä/ACE (dashed-dotted lines) models with measurements from various measurements: BESS (solid square symbols), AMS-01 (solid star symbols) and ACE/CRIS (solid circle symbols) for solar minimum (June-July 1998) and solar maximum periods (August 2000).

ACE/CRIS) and model spectra from BON2011, BON2010 and Matthiä/ACE models for solar maximum (August 2000) and minimum (June-July 1998) periods. See Table 2 in Mrigakshi et al. 2012 (see Section 4.2) for details regarding the data selection from AMS-01, BESS, ACE and PAMELA (helium data) experiments for this figure. The hydrogen data presented here were measured by the PAMELA experiment between the dates 06.12.2009 and 01.01.2010.

The drop in the measured fluxes and the shift in the peak to higher energies from solar minimum (Figure 5.2a) to maximum (Figure 5.2b) period is clearly visible in the figure. The differences between the measured and model fluxes found in the previous Figure 5.1 are also seen in this figure. For these two epochs the differences between model and measured fluxes are smaller using the BON2010 model in comparison with the new BON2011 model. The overestimation of the fluxes of heavy nuclei using the BON2011 model for the year 2000 can also be seen here. The Matthiä/ACE model shows the least difference with respect to the measurements for this time period of all the selected nuclei. For the year 1998, BON2011 shows better agreement with measurements of oxygen and iron nuclei whereas BON2010 does better for the lighter nuclei.

Figure 5.3 shows the model spectra using the BON2011 and Matthiä/ACE in comparison with the GCR H nuclei measurements taken by the PAMELA mission between July 2006 and December 2009 (Adriani et al., 2013).

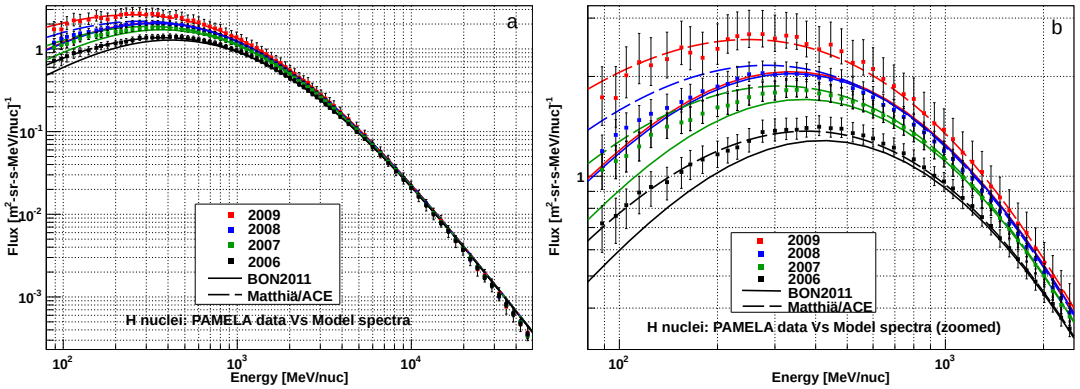

Figure 5.3: Comparison of the differential energy spectra of H nuclei described by BON2011 (continuous lines) and Matthiä/ACE models (dashed lines) with the measured data from the PAMELA mission (solid square symbols). The measurements taken during 2006 are shown in black (13th November to 4th December), 2007 in green (30th November to 27th December), 2008 in blue (19th November to 15th December) and 2009 in red (6th December 2009 to 1st January 2010).

The observation periods are indicated in the figure caption. The effect of solar modulation on hydrogen nuclei can be seen below 10 GeV (Figure 5.3a). The continuous increase in the GCR hydrogen fluxes measured from a period of intermediate solar activity at the end of the year 2006 to the solar minimum at the end of the year 2009 is clearly visible.

The model spectra from both BON2011 and Matthiä/ACE above 700 MeV are in agreement with the measured spectra within the uncertainties. At higher energies above 40 GeV, the model spectra seem to diverge from the data points and furthermore the slopes of the measured spectra seem to be greater than those of the model spectra (Figure 5.3a). Certainly, GCR measurements at higher energies of all particle types will be useful to benchmark the models for these high energies. Figure 5.3b shows a clearer picture of the discrepancies in the model spectra at lower energies. The hydrogen fluxes described by the Matthiä/ACE model are in agreement with the measurements for all time periods except for the year 2008 wherein BON2011 shows a better agreement with the measurements. These observations are consistent with the results shown in Figure 5.1. It should be noted that the differences in the integrated model flux using BON2011 and measurements as seen in Figure 5.3 are larger in comparison to the differences seen in Figure 5.1. This occurs due to the smaller energy range over which the fluxes were integrated (from 215 MeV upwards). The discrepancies are larger at lower energies.

5.1.2 Influence on the dose calculations

Hydrogen, helium, oxygen and iron nuclei are the most important GCR particles that contribute to the total GCR exposure in space. Thus the differences observed in the energy spectra described by different models must result in different dose values as was shown in Mrigakshi et al. 2013a (see Section 4.3) wherein dose rates calculated using CREME96, CREME2009 and BON2010 were inter-compared. In this section, the exposure from GCR is estimated using the new BON2011 model and compared with the results calculated using the BON2010 and Matthiä/ACE model.

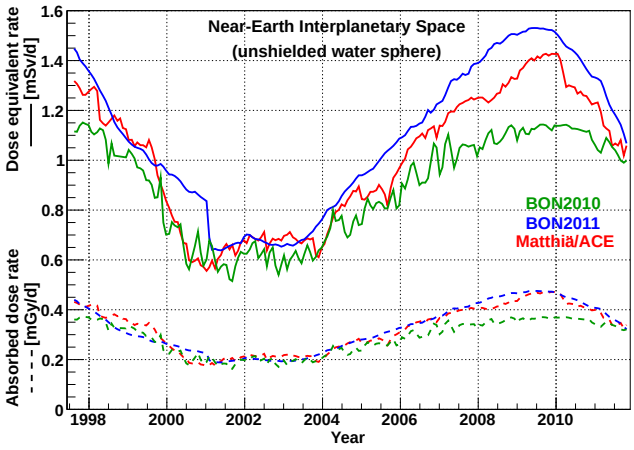

Figure 5.4: Absorbed dose rate (dashed lines) and dose equivalent rate (continuous lines) calculated for an unshielded water sphere located outside the magnetosphere close to the Earth using BON2011 (blue lines), BON2010 (green lines) and Matthiä/ACE model (red lines).

Figure 5.4 shows the absorbed dose rate and dose equivalent rate calculated using BON2011, BON2010 and Matthiä/ACE models for a time period ranging from July 1997 up to October 2011. The dose values are shown for an unshielded water sphere located outside the magnetosphere close to Earth.

The differences in the dose rates using these models are in accordance with the model flux inter-comparison results. For most of the time periods BON2011 calculated higher GCR fluxes in comparison with the BON2010 model and thus the dose rates predicted using the BON2011 model yield higher dose values as well. The dose rates calculated using this model are also higher in comparison with the values calculated using the Matthiä/ACE model for most of the time periods. The peak dose values for the GCR maximum period during 2009 are estimated to occur at different time periods using BON2011 (around mid of 2009) and Matthiä/ACE model (end of 2009).

The GCR measurements as presented in the section above and the neutron monitor count rates presented in Mrigakshi et al. 2013b (see Section 4.5) and Chapter 2 also show the peak GCR fluxes at the end of the year 2009. In general the differences in the dose values calculated using different models are higher during the solar minimum periods and converge to nearly the same values at the end of the year 2011.

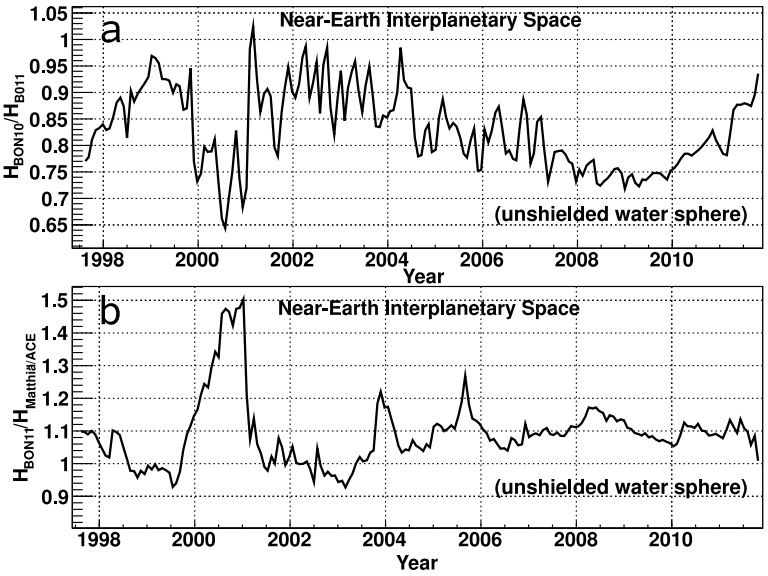

Figure 5.5: Figure a shows the ratio of the dose equivalent rates using the BON2010 and BON2011 models respectively and Figure b shows the ratio of the dose equivalent rates using the BON2011 and Matthiä/ACE models respectively.

In Figure 5.5 the differences in the dose rates using these models are quantified. Figure 5.5a shows the ratio of the dose rate calculated using the BON2010 and the values calculated using the BON2011 model. Around the mid of 2000 and between 2008 and 2010, the use of the BON2010 model leads to dose rates about 35% and 30% lower than those calculated using the BON2011 model.

Figure 5.5b shows the ratio of the dose rate calculated using the BON2011 and the values calculated using the Matthiä/ACE model. The difference lies within 10% for most of the time periods. However, around the end of the year 2000 the BON2011 model produces dose values about 50% higher than that using the Matthiä/ACE model. At this time the discrepancies in the model spectra using the BON2011 were observed as shown in the section above.

5.2 Variation of dose with particle energy

In this section, the contribution of different particle energies to the total exposure is investigated for either an unshielded and shielded water sphere surrounded by aluminium shielding of 0.3 g/cm^2, 10 g/cm^2 and 40 g/cm^2. The aluminium shielding of 0.3 g/cm^2 corresponds to the shielding of a nominal spacesuit and is often used for dose assessments (e.g. in Schwadron et al. 2010, Ballarini et al. 2005, Kim et al. 1999). The other two shielding configurations represent typical shieldings encountered in the lower shielding parts of the ISS, e.g., in the Pirs modules the shielding is estimated to range from 2 g/cm^2 to 40 g/cm^2 (Semkova et al., 2012).

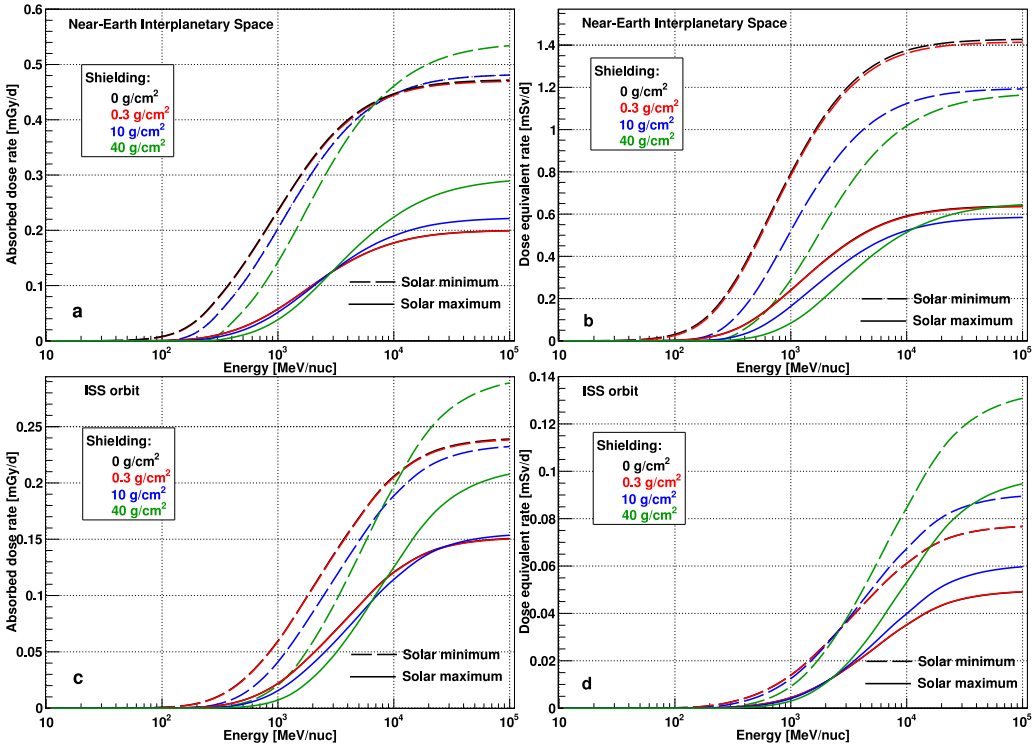

Figure 5.6: Cumulative dose rates over primary particle energy estimated for unshielded (0 g/cm^2 in black) and shielded (0.3 g/cm^2 in red, 10 g/cm^2 in blue, 40 g/cm^2 in green) water sphere at different locations in space during solar maximum and minimum periods. Figure a and b show the absorbed dose rate and dose equivalent rate respectively estimated for near-Earth interplanetary space. Figure c and d show the same dose quantities for ISS orbit. The solar maximum period corresponds to August 2002 (solid squares) and the solar minimum to November 2009 (solid triangles). Note that due to the similar dose values estimated in the water sphere with no shielding (0 g/cm^2) and with a shielding of 0.3 g/cm^2, the corresponding energy vs dose curves shown in red and black mostly overlap.

The variation of dose with primary particle energy was studied by calculating the dose rates integrated over primary particle energy from 10 MeV/nuc to 100 GeV/nuc for all investigated shielding configurations as shown in Figure 5.6. The calculations are made for time periods corresponding to the GCR intensity minimum (August 2002) and maximum (November 2009) using the Matthiä/ACE model. Figure 5.6a and b show the estimated absorbed dose rate and dose equivalent rate respectively for near-Earth interplanetary space, and Figure 5.6c and d show the same for ISS orbit.

Note that Mrigakshi et al. 2013a (see Section 4.3) presented similar study for the case of an unshielded water sphere using the BON2010 model. The total absorbed dose and dose equivalent rates calculated for the water sphere with sheilding using Matthiä/ACE model over a time period ranging from the year 1997 to 2011 can be found in Mrigakshi et al. 2013b (see Section 4.5). Figure 5.7 shows the total dose rates plotted against shielding for August 2002 and November 2009.

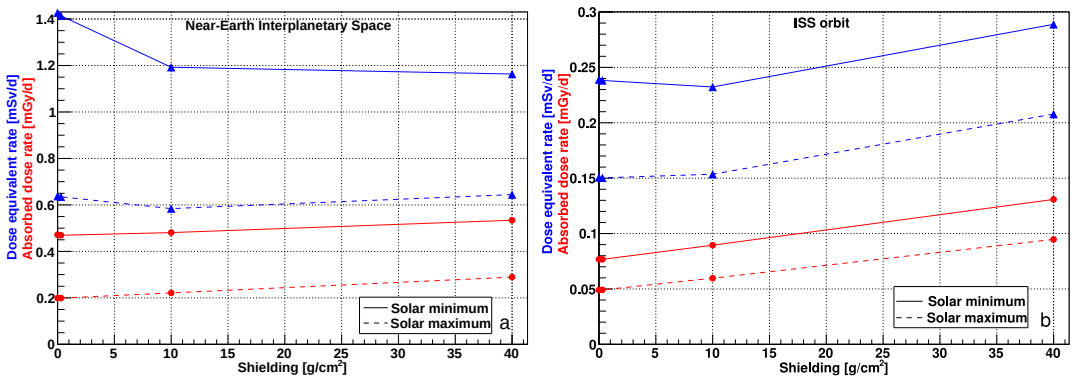

Figure 5.7: Absorbed dose (red lines with solid circle symbols) and dose equivalent rate (blue lines with solid triangle symbols) calculated using the Matthiä/ACE model for aluminium shielding of 0 g/cm^2, 0.3 g/cm^2, 10 g/cm^2 and 40 g/cm^2 during solar maximum in August 2002 (dashed lines) and solar minimum period in November 2009 (continuous lines).

Results for both the investigated locations in space presented in the figures show that:

1. The contribution to total GCR exposure from particles with energies between 10 and 100 MeV/nuc is insignificant for all cases. It is estimated to be either null or less than 0.5% except for the near-Earth interplanetary space where it can be up to 2% for the case of 0-0.3 g/cm^2 shielding.

2. The particle energies ranging from 100 MeV/nuc to 1 GeV/nuc can contribute

from 3% for 40 g/cm^2 up to 55% for 0-0.3 g/cm^2 shielding.

3. The largest contribution to dose of about 40%-70% for most of the cases comes from particle energies ranging from 1 GeV/nuc to 10 GeV/nuc.

4. The contribution of particle energies from 10 GeV/nuc to 100 GeV/nuc ranges from about 4% for 0-0.3 g/cm^2 to about 44% for 40 g/cm^2.

Continuing the discussion of Figure 5.6, it can be observed that with increasing aluminium thickness, the contribution from high energy particles to total dose increases. This can be explained by the greater shielding effect on low-energy particles due to larger shield thickness.
In these graphs, the point of steepest slope in each curve indicates a peak in the dose values. A shift in these points or peak towards higher energies from solar minimum to maximum period can be observed in all the graphs for all shielding configurations. E.g., in Figure 5.6a, the peak in the dose values for 10 g/cm^2 is at about 1 GeV/nuc during solar minimum period in comparison to solar maximum at about 3 GeV/nuc. This is due to the fact that the low energy component of the GCR is strongly attenuated by the increased solar activity and therefore the contribution to dose from these particles reduces as well.

For calculation of the GCR exposure at ISS orbit, particles with energies below 100 MeV/nuc can be ignored due to the negligible contribution to dose. While for the same location the upper limit of the particle energy of 100 GeV/nuc should be sufficient for 0 g/cm^2 to 10 g/cm^2, the contribution of higher energies to total dose for 40 g/cm^2 shielding should be investigated as the integrated dose curves seem to still rise at these energies. For near-Earth interplanetary space the simulated energy range seems to be sufficient for all the investigated shielding configurations.

5.3 Estimation of effective dose rate

In this section, the effective dose rate is estimated. The effective dose can be calculated from the equation 2.15. It requires the calculation of dose equivalent in various organs, also known as organ dose equivalent (NCRP, 2000 and NCRP, 2002), which is weighted by the tissue weighting factor w_T (Table 5.1) for the corresponding organs and summed up over all organs to deduce the effective dose (Chapter 2).

Table 5.1: Tissue weighting factors w_T recommended by ICRP (ICRP, 2007).

Tissue	w_T
Red bone marrow, Colon, Lung, Stomach, Breast, Remainder tissues*	0.12
Gonads	0.08
Bladder, Oesophagus, Liver, Thyroid	0.04
Bone surface, Brain, Salivary glands, Skin	0.01

* Remainder tissues: Adrenals, Extrathoracic region, Gall bladder, Heart, Kidneys, Lymphatic nodes, Muscle, Oral mucosa, Pancreas, Prostate (male), Small intestine, Spleen, Thymus, Uterus/cervix (female)

To estimate the dose in different organs by using a spherical phantom, the mean shielding of each organ in the human body has to be correlated to a location inside the spherical phantom. Matthiä et al. (2013b) calculated the mean shielding of all the organs required for the estimation of the effective dose (Table 5.1) in the ICRP male phantom. The ICRP male phantom is a reference computational voxel phantom[2] based on tomographic imaging data set of an adult male (see ICRP 2009 for details). The result of the study showed that the mean organ shielding in the ICRP male phantom ranges from 10.5 g/cm^2 (skin) to 19.1 g/cm^2 (bladder) for isotropic irradiation. Note that in the same paper, Matthiä et al. (2013b) also showed that a spherical water phantom of 20 cm radius is less thana good approximation to estimate the radiation exposure from GCR at ISS orbit. The absorbed dose rate and dose equivalent rate calculated using the spherical phantom and the ICRP phantoms (for both male and female) differed by less than than 5% and 11% respectively.

[2]Computational anthropomorphic phantom based on medical tomographic images in which the anatomy is described by small three-dimensional volume elements (voxels) specifying the organ or tissue to which they belong (ICRP, 2009)

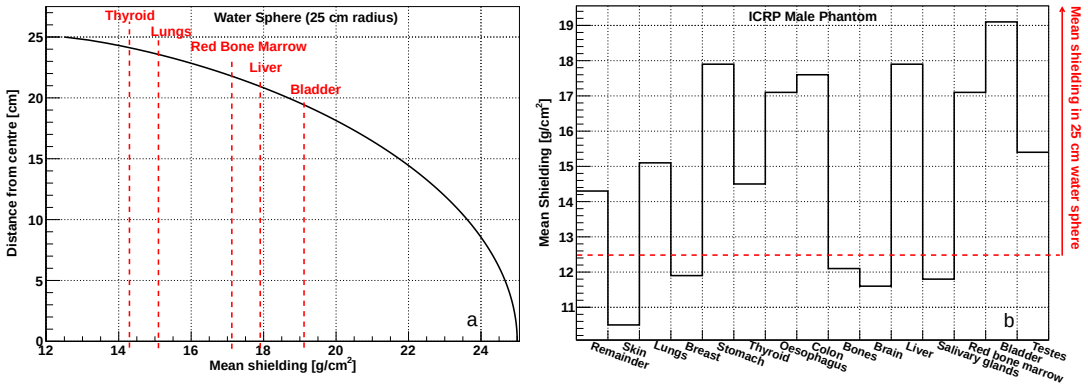

Figure 5.8: Figure a shows the mean shielding in the simulated water sphere of 25 cm radius from its centre to the surface (black line). Also shown are mean shielding of some organs in the ICRP male phantom (red dashed lines). For reference, the mean shielding of all organs (black lines) in the ICRP male phantom, that are required for the estimation of the effective, is shown in Figure b. The red dashed line indicates the mean shielding level at the surface of the simulated water sphere. Locations with mean shielding below this threshold lie outside the sphere.

Note that the mean shielding at a given point inside the water sphere is defined as the product of density ρ with the mean distance $\bar{x}$ from that point to the surface of the sphere. For the isotropic GCR radiation field the mean distance $\bar{x}$ is obtained by integrating the distance to the surface $x(\theta)$ as a function of incident direction over the entire sphere (see Matthiä et al. 2013b for a detailed description). The mean shielding profile for the simulated water sphere used in this work was calculated by applying this method. The shielding values estimated for the simulated water sphere ranges from 12.5 g/cm^2 at the surface to 25 g/cm^2 at the centre. Figure 5.8 shows the mean shielding inside the simulated water sphere of 25 cm in radius (Figure 5.8a) together with the mean shielding of all relevant organs inside the ICRP male phantom (Figure 5.8b).

Clearly, the water sphere is heavily self-shielded (12.5 g/cm^2 - 25 g/cm^2) and thus does not cover the entire range of mean organ shieldings of the ICRP male phantom (10.5 g/cm^2 - 19.1 g/cm^2). However, the mean shielding of ten out of the required fifteen organs, to estimate the effective dose (Table 5.1), is covered by the sphere and with some assumptions the effective dose can be calculated.

Figure 5.9 shows the variation of absorbed dose and dose equivalent rates with depth in the water sphere estimated for near-Earth interplanetary space and ISS orbit using the Matthiä/ACE model.

The data is presented for all the shielding configurations simulated in this work from no shielding to aluminium shielding of 0.3 g/cm^2, 10 g/cm^2 and 40 g/cm^2.

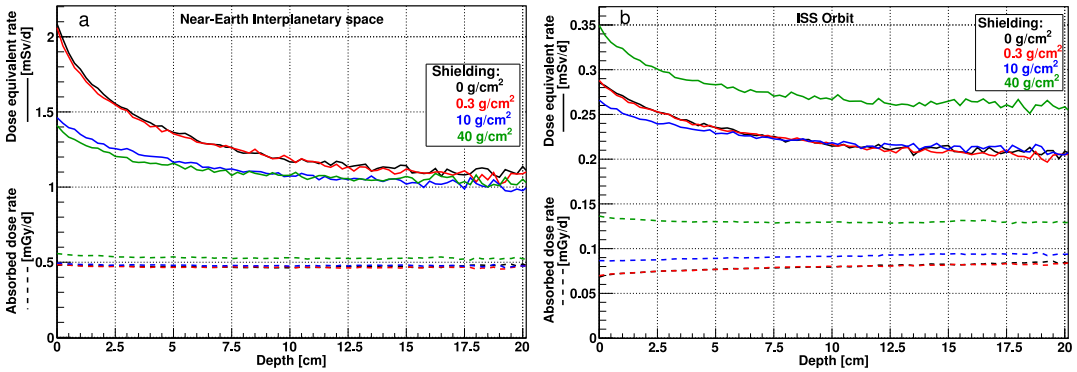

Figure 5.9: Variation of absorbed dose rate (dashed lines) and dose equivalent rate (continuous lines) with depth, estimated by applying the Matthiä/ACE model during the peak exposure period in the last solar minimum (November 2009) for near-Earth interplanetary space (Figure a) and ISS orbit (Figure b). The dose rates are shown for an unshielded (black) and shielded water sphere with aluminium of 0.3 g/cm^2 (red), 10 g/cm^2 (blue) and 40 g/cm^2 (green).

The mean shielding required for the calculation of effective dose ranges from 10.5 g/cm^2, which is outside the range of shieldings covered by the simulated sphere, up to 19.1 g/cm^2 i.e. about 6 cm inside from the surface. The absorbed dose rate from the surface up to 6 cm in depth varies by less than 5% in near-Earth interplanetary space for all shielding configurations whereas for ISS orbit by less than 15%. Therefore, assuming the same absorbed dose values calculated for the surface of the sphere for the organs that have lower mean shielding (skin, breast, bones, brain and salivary glands) should give a reasonable value of the organ absorbed dose rates.

The dose equivalent rate on the other hand shows a stronger variation of dose with depth which is due to the fragmentation of primary heavy nuclei at outer shells of the water sphere which lead to the production of secondary particles which have lower quality factor and yield lower dose equivalent rates with increasing depth. The dose equivalent rate from the surface to 6 cm in depth varies by up to 55 % for near-Earth interplanetary space and up to 25% for ISS orbit. Nevertheless, since the tissue weighting factors w_T (Table 5.1) of four out of the five organs not covered by the sphere is 0.01, their influence on effective dose is low. For the breast which has a weighting of 0.12, the dose equivalent rate at the outer most shell of the water sphere could be a fair assumption as the mean shielding at this shell is 12.5 g/cm^2 not very different from 11.9 g/cm^2 which corresponds to that of the breast in a male ICRP phantom. It is also important to note that these are only five organs are out of fifteen organs, required for the calculation of effective dose, and thus their total

contribution to effective dose should not be dramatic. Matthiä et al. (2013b) estimate a contribution of 20% by these organs to the effective dose.

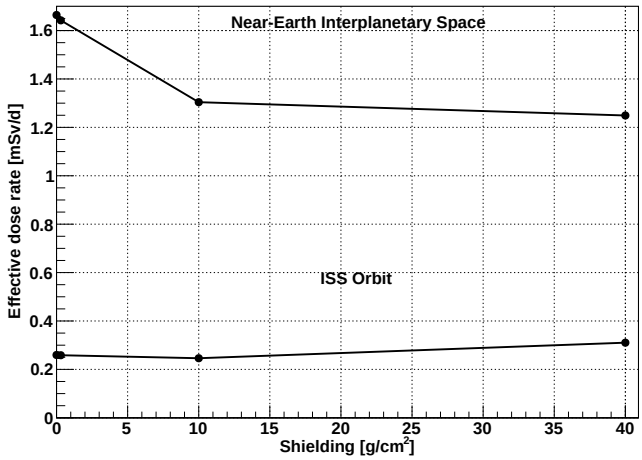

Figure 5.10: Effective dose rate calculated for a male astronaut either unshielded or surrounded by aluminium shielding of 0.3 g/cm^2, 10 g/cm^2 and 40 g/cm^2 during the peak exposure period in the last solar minimum (November 2009) calculated using the Matthiä/ACE model for near-Earth interplanetary space and ISS orbit.

Figure 5.10 shows the effective dose rate in water sphere with and without shielding estimated for November 2009 using the Matthiä/ACE model for near-Earth Interplanetary space and ISS orbit. The values calculated for near-Earth interplanetary space are 1660 μSv/d, 1640 μSv/d, 1300 μSv/d and 1250 mSv/d for 0 g/cm^2, 0.3 g/cm^2, 10 g/cm^2 and 40 g/cm^2 and for ISS orbit are 260 μSv/d (0-0.3 g/cm^2), 250 μSv/d and 310 μSv/d.

The NASA space flight human system standard (NASA, 2007), provides career effective dose limits for missions of 1-year duration or less and are shown in Table 5.2 for males and females. These limits are based on 3% risk of exposure-induced death from cancer. The decrease in risk with age is due to the reduced susceptibility for radiation-induced cancer. The results shown here indicate that the annual effective dose in a male astronaut are expected to be above 456 mSv, 476 mSv, 600 mSv and 607 mSv behind shielding of 40 g/cm^2, 10 g/cm^2, 0.3 g/cm^2 and 0 g/cm^2 in near-Earth interplanetary space. These values are either above or approach the career limit for 25 and 30 year old males as recommended by NASA for all of their human space flight programs (NASA, 2007). Note that these results have been calculated for the time period (November 2009) when the GCR intensity and the GCR exposure reached highest levels observed since 1970.

Table 5.2: Career effective dose limits (in units mSv) for 1-year missions as recommended by the NASA space flight human system standard for all of their human space flight programs (NASA, 2007).

Age, yr	Males	Females
25	520	370
30	620	470
35	720	550
40	800	620
45	950	750
50	1150	920
55	1470	1120

Using the same method for the estimation of effective dose for a male astronaut, the dose quantity can also be estimated for a female astronaut. The mean organ shielding calculated by Matthiä et al. (2013b) for the ICRP female phantom is different than the male phantom and it ranges from 8.8 g/cm^2 to 16.9 g/cm^2. The organs of which the mean shielding are not covered by the simulated water sphere are skin (8.8 g/cm^2), breast (11.5 g/cm^2), brain (10.8 g/cm^2) and salivary glands (11.6 g/cm^2). For these organs, the dose equivalent estimated for the outermost shell corresponding to a mean shielding of 12.5 g/cm^2 is taken to calculate the effective dose. This assumption follows the same reasoning as explained for the calculation of the effective dose for a male astronaut. Therefore, with these assumptions the effective dose in a female astronaut can be estimated. For a female astronaut the annual effective dose for November 2009 are expected to be 456 mSv, 476 mSv, 633 mSv and 643 mSv behind shielding of 40 g/cm^2, 10 g/cm^2, 0.3 g/cm^2 and 0 g/cm^2 in near-Earth interplanetary space. The values indicate the 1-yr career dose limits to have been either reached or beyond those allowed for 25 to 40 year old females as recommended by NASA for all of their human space flight programs (NASA, 2007).

A round trip to Mars is usually assumed to take up to a year or more and with GCR exposure alone (no consideration of radiation from the Sun) contributing by such high amounts to dose, the shielding to be used for future missions to deep space must be appropriately optimized.

5.4 Comparison with experimental data

The accuracy of the methods applied to estimate the dose values must be tested by comparing the calculated dose with measurements. Often however, it is not trivial to make reasonable comparisons because of numerous reasons. Such reasons are for instance, the lack of detailed information about the shielding around the radiation dose detectors, the energy deposition range or the particles measured by the detector and also the kind of approximations made in the models during the simulation process.
There are several experiments dedicated to measure radiation dose at various locations inside the ISS. As mentioned in Chapter 2, the dose measurements made onboard the ISS show large variation from location to location. To compare the experimental data with the calculated data from this work, only measurements at locations where the shielding is similar to those simulated in this work have to be considered.

Semkova et al. (2013) measured absorbed dose rates from July 2007 to February 2009 inside the Pirs module wherein the detectors are estimated to be surrounded by shielding ranging from 2 g/cm^2 to 40 g/cm^2 (Semkova et al., 2012). In another experiment, Lishnevskii et al. (2012) measured absorbed dose rates from 2005 - 2009 inside the Zvezda module where the average shielding around the detectors are estimated to range from 32 g/cm^2 - 47 g/cm^2 (Jadrníčková et al., 2009). In the same module, Zvezda, Semones (2009) also measured absorbed dose rate between May 2009 - August 2009. The calculated absorbed dose rates for a shielding of 10 g/cm^2 and 40 g/cm^2 could therefore be compared with the data available from these modules. Table 5.3 shows a summary of the measured and calculated absorbed dose rates.

Note that the calculations were made for the observation period as provided in the publications and the range of the dose rates over these periods are provided here as shown in the table. Since the information about the shielding distribution is unavailable, it is difficult to weight the calculated dose per the shielding amount. If the average of the absorbed dose rates calculated with a shielding of 10 g/cm^2 and 40 g/cm^2 is considered then the relative difference of the calculations with the measured data on the Pirs module ranges from less than 1% to 10% for July 2007 to February 2009.

The difference between the measured absorbed dose rates by Lishnevskii et al. (2012) inside the Zvezda module and the calculated values are 7% to 33% for 2005-2006 and about 20% for 2007-2009. However, the calculated dose rates are in good agree-

ment with the measurements made by Semones (2009) for the same module where the difference between the measurements and the calculated dose is about 4%.

Table 5.3: Comparison of the measured dose from GCR onboard the ISS with the calculated dose over the whole sphere.

Module	Dates	Measured dD/dt (μGy/d)	Calculated dD/dt (μGy/d)	
Pirs	July 2007 - Feb. 2009[a]	104 - 119	83 - 87	(10 g/cm^2)
			123 - 128	(40 g/cm^2)
Zvezda	2005 - 2006[b]	80 - 100	106 - 118	(40 g/cm^2)
	2007 - 2009[b]	100 - 110	120 - 131	(40 g/cm^2)
	May 2009 - Aug. 2009[c]	125	130	(40 g/cm^2)

[a]Semkova et al. (2013); [b]Lishnevskii et al. (2012); [c]Semones (2009)

In addition measurements from inside the Columbus module are available where the median shielding has been estimated to be 100 g/cm^2 (Stoffle et al., 2012). Unfortunately, the largest shielding simulated in this work equals 40 g/cm^2, thus calculated and the measured dose rates cannot be compared.

Since manned missions to locations beyond LEO such as Mars are being planned, it is also important to investigate the radiation exposure during such long-duration and long-distant flights.
The first ever measurements of the dose rate outside the terrestrial environment were recently performed by the MSL/RAD instrument during its transit flight to Mars (Zeitlin et al., 2013). In comparison with the data in LEO, this data is also very important for benchmarking the modelling process. This is because of the lesser number of parameters that could have influenced the GCR fluxes and thus the resulting dose measured by the instrument. The dose measurements were made in the near-Earth interplanetary space wherein the GCR are not attenuated by the Earth's magnetosphere and by the solid-obstruction caused by the planet. If simulating this scenario, the question of uncertainties arising in the calculated dose from the application of geomagnetic transmission function (transporting GCR fluxes from outside to inside the Earth's magnetosphere) therefore does not exist. This should aid the scientists to pinpoint other sources of errors in the calculated dose better and

help to further improve the reliability of numerical dose estimation.
The shielding distribution around the MSL/RAD instrument is complex. During the transit to Mars the shielding around the instrument ranged from 1 g/cm^2 to 80 g/cm^2. Zeitlin et al. (2013) have provided the cumulative probability distribution as a function of shielding depth which should be useful to appropriately model the shielding distribution around the instrument. In this work, limited set of shieldings were modelled which certainly does not cover the range of shielding that surrounded the instrument. Nevertheless, by making use of the cumulative probability distribution of the shielding and by making some assumptions, the calculated dose can be roughly compared with the MSL/RAD measurements.
Due to the large size of the water sphere the dose in the outermost shell is considered for this comparison study wherein the mean shielding inside the sphere is the least. It should be noted that for a more realistic benchmarking of the dose calculations for this MSL/RAD in-transit scenario, a smaller geometry of the detector should be simulated.
The cumulative probability distribution vs shielding depth indicates that about 30% of the shielding amounted to 3 g/cm^2, 50% to 10 g/cm^2, 10% to 40 g/cm^2 and 70 g/cm^2 each. The calculated dose therefore can be weighted with these factors in order to compare the dose values. In this work, not all of these shielding amounts were simulated and hence after weighting the dose with the factors shown above, a certain fraction of the dose (from 3 g/cm^2 and 70 g/cm^2) will still be unaccounted for. However, the dose rates in the common shielding used for the measurement and calculation can be compared.

Table 5.4 shows the measured and calculated dose rates averaged over the observation period, i.e., between December 2011 to July 2012. The dose rates were calculated using the Matthiä/ACE GCR model. The table also indicates the amount of shielding used.
The sum of the calculated absorbed dose rate for a shielding of 10 g/cm^2 weighted by 50% and for 40 g/cm^2 weighted by 10% equals to 220 μGy/d. For the remaining shielding some assumptions must be made. If the dose rates for 3 g/cm^2 is considered to be the same as that for 0-0.3 g/cm^2 and the dose rates for 70 g/cm^2 is taken the same as that of 40 g/cm^2 then the total absorbed dose rate sums up to 360 μGy/d. This is about 22% lower than the measured value. The variation in the absorbed dose rate has been estimated in this work to increase with increasing aluminium shielding and the dose for 3 g/cm^2 and 70 g/cm^2 are expected to be greater than for 0-0.3 g/cm^2 and 40 g/cm^2 respectively. These assumptions are likely to therefore

Table 5.4: Absorbed dose measurements by MSL/RAD instrument during the transit flight to Mars between December 2011 to July 2012 (Zeitlin et al., 2013) and the calculated dose for the same time period.

	Measured	Calculated		
Shielding	1-80 g/cm^2	0-0.3 g/cm^2	10 g/cm^2	40 g/cm^2
dD/dt (μGy/d)	461 ± 92 to 481 ± 80	319	353	435

cause an underestimation in the calculated absorbed dose rate and the difference in comparison with the measurements can be reasoned.
MSL/RAD also measured dose equivalent rate (1840 ± 330 μGy/d) but due to the fact that the dose equivalent rate shows a stronger variation with increasing shielding (see Figure 5.7), the same assumptions made for the comparison of the measured and absorbed dose rate are difficult to make. Therefore, the dose equivalent rates are not compared here.

Considering all the simplified approximations made during the simulations and the assumptions applied to compare the calculated and measured dose rates, the results of this work show reasonable agreement with the experimental data.
It is stressed that this comparison study was only intended to check whether the methods applied in this work to make dose estimates were rational. However, in order to perform rigorous benchmarking of the numerical calculation methods, the experimental setups have to be modelled as accurately as possible.

6 Summary and Conclusions

Radiation is one of the primary concerns for manned missions to space. An important source of radiation exposure are the galactic cosmic rays (GCR). They continuously bombard the heliosphere with high-energy and high-z particles, and have been found to contribute up to 60% to total absorbed dose rate and up to 80% to the total dose equivalent rate in low Earth orbits. At these altitudes, the GCR intensity and the resulting exposure is attenuated to a certain extent by the Earth's magnetosphere. Beyond the magnetosphere the GCR exposure increases to levels which, if not properly anticipated and protected against, will be health-threatening for humans traveling on long-duration space missions. Therefore, to counteract the radiation exposure in space, standards, e.g., the dose limits concerning the safety of astronauts from radiation are established. These standards are followed by monitoring the radiation exposure of the crew through dose measurements and by numerically estimating the radiation exposure for every mission scenario. Additionally, methods to mitigate the exposure levels, e.g. shielding optimisation, are investigated as well.

Several studies in the past have shown disagreement between the measured and numerically estimated GCR dose values indicating the shortcomings of the methods used for numerical calculations of dose. Initiatives have thus been taken by the space dosimetry community to improve the GCR dose predictions especially because of the growing interest of not only the national space agencies but also the private commercial industry for space travel beyond the low Earth orbit such as to the Moon and Mars. Thus, all elements involved in the modeling process to make reliable estimation of radiation exposure are continuously studied, optimised and updated with the growing knowledge of these domains. These elements are, e.g., GCR models, the underlying physics models in the radiation transport codes, phantom geometries and materials that simulate the human body and the spacecraft.

This PhD work contributes towards making more reliable calculations of the exposure from GCR in space and to understand how the dose is affected by various parameters. During the course of the research, the influence of the following environmental parameters on the GCR exposure, as well as modeling parameters used for the numerical dose estimation were studied:

- GCR models
- Influence of different GCR models on the dose estimations

- GCR dose estimation and influence of shielding
- Implications on space travel to near-Earth interplanetary space

1. **GCR models:**
   To reduce uncertainties arising in the dose values from discrepancies in the GCR model spectra at 1 AU, several GCR models (CREME96, CREME2009, Badhwar-O'Neill2010, Badhwar-O'Neill2011, Matthiä-ACE/OULU, Burger-Usoskin and SPENVIS/15390 models) used for the purpose of radiation protection in space were tested. This was done by comparing the model spectra with the GCR measurements from the year 1994 onwards. The model spectra were also inter-compared for periods before 1994 starting from the year 1970.

   - During the initial phase of the research work in the year 2010-2011, the widely used CREME96, CREME2009, Badhwar-O'Neill2010 and the Burger-Usoskin models were evaluated by comparing model spectra with the GCR measurements. Several discrepancies were found in the spectra described by all models at various points in time in the last decade. The largest difference between the measured and the modeled GCR fluxes was found for the hydrogen fluxes for the year 2000 using the CREME96 model (>150%). The updated CREME2009 model also showed differences as high as 70% for hydrogen nuclei for the same time period indicating further room for improvement in the new model. The Burger-Usoskin model shows good agreement for hydrogen and helium nuclei, however, the model is limited to only these two particles. The Badhwar-O'Neill2010 model shows the least discrepancies with measurements of both light and heavy nuclei for most of the time periods. However, along with the rest of the models it also shows deficiency in describing the unusual increase in the GCR intensity observed in the recent deep solar minimum period between the 23^{rd} and the 24^{th} solar cycle.
   - As a consequence of the findings of this work, a new GCR model for a better prediction of the GCR intensity was developed within the work-group based on either the GCR carbon measurements by the CRIS instrument on-board the ACE spacecraft (Matthiä/ACE model) or the neutron monitor count rates from the OULU station (Matthiä/OULU). The GCR spectra using the

new model show better agreement with the measurements for most of the investigated time periods. The model is also able to describe the increase in the GCR fluxes for the last solar minimum period, however with a slight underestimation for heavy nuclei fluxes.

- Later in 2012, an update of the Badhwar-O'Neill2010 model was released. The model was also examined. It works much better than the older model and shows good agreement with the measurements. It is also able to describe the increase in the GCR fluxes during the last solar minimum showing better agreement with the measurement of heavy nuclei in comparison to the Matthiä/ACE model.
- Another GCR model SPENVIS/ISO15390 was evaluated but only for two epochs that is for the last solar minimum and maximum period. It was found to perform similar to the CREME2009 model which is also based on the ISO15390 model and showed severe discrepancies especially for the solar maximum period.

To summarize, the spectra derived from all investigated models were found to disagree among each other and also with measurements for various time periods. The differences are found to vary over time. The widely used CREME96 model was found to produce the largest discrepancies with respect to the measurements and the newly developed Matthiä/ACE model and the Badhwar-O'Neill2011 model show the best agreement with the measured data.

2. **Influence of different GCR models on the dose estimations**

The impact on the dose estimations of using various GCR models was studied by calculating the absorbed dose and dose equivalent rates using all GCR models and by quantifying the differences arising in the dose rates. The Monte-Carlo transport code GEANT4 was used to simulate the transport of radiation in a water sphere used as a surrogate for the human body. The investigation was performed for the time period from 1970 to 2011.

- Differences in the dose values were estimated corresponding to the periods where differences between GCR fluxes using different GCR models were found. E.g., the ratio of the dose values calculated using CREME96 model to the Matthiä/ACE model showed a large difference of over 100% between

the model for near-Earth interplanetary space and about 45% for ISS orbit for the solar maximum period in the year 2000-2002. The CREME2009 model showed differences as high as about 30%-50% during 2004-2006 for both locations in space compared to Matthiä/ACE model.

- Dose values using the Badhwar-O'Neill2010 model were lower with respect to the Matthiä/ACE model for most of the time periods and for both locations in space with differences up to 20%. The Badhwar-O'Neill2011 model was used to estimate the GCR dose for near-Earth interplanetary space only and produced higher dose values in comparison with its older version. With respect to the Matthiä/ACE model the differences lie within 10-20% for most of the time periods except in 2000 where the dose is estimated 50% higher. During this period the Badhwar-O'Neill2011 model also showed large disagreement with the measurements.
- The ratio of the dose values using SPENVIS/ISO15390 with respect to the values calculated using the Matthiä/ACE model were estimated to be 1.45 and 0.87 during the last solar maximum and minimum period for near-Earth interplanetary space.

To conclude, the differences among the GCR model spectra and the discrepancies with respect to the measurements can considerably influence the dose estimates. It is worth mentioning that no previous studies were found that investigate the effect of the GCR model spectra on the dose quantities for an extended time range. However, some studies comparing the GCR fluxes from different models with measurements usually only for one solar maximum and minimum period can be found in literature. But as the above results indicate that the accuracies of the GCR models vary with time, the GCR models must be tested first against the measurements.
These results are also important to interpret published GCR dose estimations made in the past using the GCR models considered in this work for epochs when discrepancies between measured data and calculated dose results or results using other models were found.

3. **GCR dose estimation and influence of shielding**
It is known that the distribution and the amount of shielding inside the ISS differs from one location to another. In this work, aluminium shieldings of 0.3 g/cm^2, 10

g/cm^2 and 40 g/cm^2 were therefore modeled as a spherical shell surrounding the water sphere for the simulations. By calculating the GCR exposure for different shielding amounts, the influence on the dose rates from 1970 to 2011 and thus the importance of the application of correct shielding for numerical estimation of dose was studied. This investigation was performed using the Matthiä/ACE model.

- The dose calculation over a period of over 40 years reveals the variation of GCR dose rates with the changing solar activity. The absorbed dose and dose equivalent rates in the unshielded water sphere are estimated to range from 0.14 mGy/d to 0.47 mGy/d and from 0.28 to 1.43 mSv/d respectively for near-Earth interplanetary space from solar maximum to minimum periods (increase by a factor of up to 5). For ISS orbit the absorbed dose and dose equivalent rates are lower and are estimated to range from 0.03 mGy/d to 0.08 mGy/d and from 0.09 to 0.24 mSv/d respectively from solar maximum to minimum periods (increase by a factor of about 2.7).
- The highest GCR exposure was estimated for November 2009 and in comparison with the peak exposure during the previous solar minimum was found to be elevated by 6%-10% for near-Earth interplanetary space and up to 3%-4% for ISS orbit depending on the shielding.
- The effect of shielding on dose is found to vary with location and time. While the absorbed dose rate for both the investigated locations increases with increase in shielding, the dose equivalent rate shows variable behaviour depending on solar activity and location. For instance, the dose equivalent rate calculated for near-Earth interplanetary space decreases during solar minimum period in November 2009 for 0 g/cm^2 to 40 g/cm^2 shielding. But during the solar maximum period in August 2002, the dose equivalent first decreases with increasing shielding from 0 g/cm^2 to 10 g/cm^2 and then increases with increasing shielding from 10 g/cm^2 to 40 g/cm^2. For the ISS orbit, the trend in the dose equivalent rate with increasing shielding is opposite for these solar activity periods.
- The effect of primary particle energy on dose was also investigated for all the shielding configurations. Over 98% of the dose, calculated for an energy range of 10 MeV/nuc to 100 GeV/nuc, is estimated to come from particle energies ranging from 100 MeV/nuc to 100 GeV/nuc. A large part of the total dose (about 40% -67%) comes from particles with energies between

1 GeV/nuc and 10 GeV/nuc for all shielding thicknesses. With increasing aluminium thickness, the bulk contribution to dose comes from higher energies. For 0-0.3 g/cm^2 the contribution from particle energies to total dose from 100 MeV/nuc to 1 GeV/nuc is up to 55% whereas for 40 g/cm^2 it is only about 4% and from 10 GeV/nuc to 100 GeV/nuc it is only about 4% for 0-0.3 g/cm^2 and about 44% for 40 g/cm^2. The results show, as expected, the stronger influence of shielding on low-energy particles.

To conclude, there is a strong dependence of GCR exposure on solar activity, location in space and the amount of shielding. Proper information regarding these parameters is vital for a reasonable prediction of dose. Lastly, the GCR exposure during the last solar minimum is expected to be the largest since the dawn of human space flight era and could serve as reference for worst-case GCR exposure studies.

4. **Implications on space travel to near-Earth interplanetary space**
The estimate of the peak annual effective dose (a quantity required for individual monitoring of a person) calculated for the deep solar minimum period in 2009 was found to range from 456 mSv to 607 mSv for male astronauts and from 456 mSv to 643 mSv for female astronauts from no shielding to a shielding of 40 g/cm^2 for near-Earth interplanetary space. The study suggests that if a fast round-trip mission to Mars (365 days) was to happen during a period of such high GCR intensity, then a 25-30 year old male or a 25-40 year old female would either surpass or approach the 1 year career effective dose limits as recommended by NASA for all of their human space flight programs (NASA, 2007). Not only would the astronauts immediately reach the end of their career by receiving such high exposures but, more importantly, they would also have significantly increased their risk of developing fatal cancer later in life.

To go for such long-duration space travels into the near-Earth interplanetary space, ways to reduce the radiation exposure have to be found. Shielding studies are of particular interest as the often used material in spacecraft that is aluminium (large amount of shielding), in some cases, seems to be counter-efficient in shielding the GCR appropriately. There are other materials with low mean atomic mass that are being investigated for use in spacecraft for long-duration flights.

Another way to reduce the health-risks to individuals is by selecting older astronauts who have a smaller probability of developing fatal cancer.
Traveling during the GCR intensity-minimum periods will help reduce the exposure in comparison with the maximum periods as well.

7 Outlook

The results of this work show that the investigated parameters invloved in the numerical estimation of the radiation exposure from GCR, strongly influence the calculated dose values. Therefore, these parameters have to be evaluated and carefully selected for applications in radiation protection in space.
In addition to the investigations presented here, there are other parameters involved in GCR modelling that should be inspected to further increase the confidence in the dose calculations. Some of them are listed below:

1. **GCR model spectra**

   - In this work, the GCR models evaluated are able to describe the GCR energy spectrum of particles outside the Earth's magnetosphere at about 1 AU from the sun. To calculate the GCR fluxes at ISS orbit, the model spectra for near-Earth interplanetary space had to be scaled with the geomagnetic transmission function. This function gives the fraction of the GCR particles as a function of energy that are able to penetrate to a location inside the Earth's magnetosphere and was derived using the tool available on the CREME website. The accuracy of this model and therefore the GCR fluxes in low Earth orbits should be tested to check whether or not there is any influence on the dose rates calculated for these orbits.
   - Since many of the GCR models (CREME96, CREME2009, SPENVIS/15390, Badhwar-O'Neill2010 models) use sunspot numbers as inputs and since there are predictions of the sunspots available for the coming years, the models could be used to calculate the GCR fluxes for future missions. The models could therefore be tested for their prediction capabilities. It is however likely that there will be discrepancies in the GCR fluxes as while testing these models, large discrepancies for several time periods in the past were found which perhaps suggests that sunspots are not the optimum index to give a measure of the level of solar modulation of GCR.
   - Measurements of GCR particles from pioneering mission like Voyager-1, once it is beyond the heliosphere, could add knowledge to improve the models used to describe the local interstellar spectrum (LIS) of the GCR particles. Each of the investigated GCR models require the description

of the LIS as it is this spectrum which is then modulated using different techniques to derive the GCR spectra near-Earth. Therefore, improved LIS models would lead to more accurate calculation of GCR fluxes at locations near-Earth.

- Additionally, the in-transit from Earth to Mars data measured by the MSL/RAD instrument (Zeitlin et al., 2013) can be useful to examine whether the GCR spectra described by the model for location outside the magnetosphere (1 AU distance), is appropriate or not and how much the particle intensity changes with distance. In fact, measurements quantifying the spatial variation of GCR particles from other space missions like Ulysses (Heber et al., 1996) should also be useful for this study.

It should be mentioned here that the GCR models included in this work use either an empirical or semi-empirical approach (Force-field approximation) to describe the modulation of GCR. Due to these modelling techniques, these models have limitations to describe the GCR energy spectrum, e.g., models using the Force-field approximation show discrepancies at energies below about 100 MeV/nuc. Inspite of these shortcomings, these models must be considered reasonable attempts at implementing radiation protection in space because particles below these energies contribute only an insignificant amount to the total dose. However, the spectra described by these models still show inaccuracies for energies above 100 MeV/nuc for some time periods as shown in this thesis. Therefore, in order to get reliable description of the GCR energy spectrum, models must be based on the complete GCR transport theory that include all the important physical processes invloved in the modulation of GCR inside the heliosphere as described by the transport equation.

2. **Simulation of the GCR exposure**

- The dose measured by the MSL/RAD instrument (Zeitlin et al., 2013) in-transit to and on the surface of Mars will be useful for validating the transport codes and the methods used to estimate the GCR dose.
  Additionally, the data from the surface should also be useful for validating codes that calculate the particle fluxes for the surface and the atmosphere of Mars. Therefore, thorough simulations for these two scenarios of the MSL/RAD instrument are extremely important for developing reliable

models which will in return give confidence in the GCR dose prediction at least for travel to Mars.

- From the results presented in this work, it is clear that the use of heavy aluminium shielding is counter-productive in terms of reducing the exposure from GCR. Therefore, other materials that can provide optimum shielding against GCR while maintaining the structural integrity of the spacecraft will have to be used for long-duration spaceflights in interplanetary space. Simulations to predict the exposure from GCR of humans to destinations like Moon and Mars must therefore be made with realistic shielding that is likely to be used in the spacecrafts to understand the health-risks associated with the corresponding space travel.
- Dose calculations estimating the peak exposure during the last solar minimum periods must be performed using detailed models of the human body (anthropomorphic voxel phantoms) and shielding, e.g., of the planned spacecraft for long-duration spaceflight, to estimate the worst-case GCR exposures. This could be extremely important since many sunspot number predictions indicate lower level of solar activity in the future, suggesting that elevated intensity of the GCR can be expected.

In this work, the radiation exposure only from GCRs was estimated. However, for the complete assessment of the radiation-related health risks requires the calculation of the dose rates from other sources of radiation as well. E.g., high-energy (up to several GeV) particles that are emitted in large numbers during the Solar Particle Events (SPE). Such events can last for days to weeks and large events can lead to deterministic effects of acute nature like nausea or skin injury. Additionally for locations inside the Earth's magnetosphere exposure from the trapped particles should also be investigated.

Besides these few points mentioned above there are many more fields falling under the realm of radiation protection in space that need attention for better prediction and quantification of the health-risks associated with radiation in space. For instance, a greater understanding of the interaction of body systems with radiation needs to be developed to predict the biological effects that can occur after irradiation.

Bibliography

Ackermann, M., Jackson, M. S., Zimmer, S., et al., 2013. Detection of the characteristic pion-decay signature in supernova remnants. Science 339 (6121).

Adriani, O., Barbarino, G. C., Bazilevskaya, G. A., Bellotti, R., Boezio, M., et al., Jan 2013. Time dependence of the proton flux measured by pamela during the july 2006 - december 2009 solar minimum (arXiv:1301.4108).

Adriani, O., et al., 2011. PAMELA Measurements of Cosmic-ray Proton and Helium Spectra. Science 332, 69–72.

Aghara, S., Blattnig, S., Norbury, J., Singleterry, R., 2009. Monte Carlo analysis of pion contribution to absorbed dose from galactic cosmic rays. Nuclear Instruments and Methods in Physics Research Section B: Beam Interactions with Materials and Atoms 267 (7), 1115 – 1124.

Agostinelli, S., Allison, J., Amako, K., Apostolakis, J., Araujo, H., et al., 2003. Geant4 - a simulation toolkit. Nuclear Instruments and Methods in Physics Research Section A: Accelerators, Spectrometers, Detectors and Associated Equipment 506 (3), 250 – 303.

Aguilar, M., Alcaraz, J., Alpat, B., Ambrosi, G., Anderhub, H., Ao, L., Arefiev, A., Azzarello, P., Babucci, E., et al., L. B., 2002. The Alpha Magnetic Spectrometer (AMS) on the International Space Station: Part I - results from the test flight on the space shuttle. Physics Reports-review Section of Physics Letters 366, 331 – 405.

Allison, J., Amako, K., Apostolakis, J., Araujo, H., Dubois, P., et al., 2006. Geant4 developments and applications. Nuclear Science, IEEE Transactions on 53 (1), 270–278.

Badhwar, G., Cucinotta, F., 2000. A comparison of depth dependence of dose and linear energy transfer spectra in aluminum and polyethylene. Radiation Research 153 (1), 1–8.

Ballarini, F., Battistoni, G., Cerutti, F., Ferrari, A., Gadioli, E., Garzelli, M. V., Ottolenghi, A., Parini, V., Pelliccioni, M., Pinsky, L., Sala, P., Scannicchio, D. A., 2005. Modeling the action of protons and heavier ions in biological targets: Nuclear interactions in hadrontherapy and space radiation protection. AIP Conf. Proc. 769, 1606–1611.

Bazilevskaya, G., Krainev, M., Svirzhevskaya, A., Svirzhevsky, N., 2013. Galactic cosmic rays and parameters of the interplanetary medium near solar activity minima. Cosmic Research 51, 29–36.

Beaujean, R., Kopp, J., Reitz, G., 1999. Active dosimetry on recent space flights. Radiat Prot Dosimetry 85 (1-4), 223–6.

Berger, T., 2008. Radiation dosimetry onboard the International Space Station ISS. Zeitschrift für medizinische Physik 18, 265–275.

Bethe, H., May 1932. Bremsformel für Elektronen relativistischer Geschwindigkeit. Zeitschrift für Physik 76, 293–299.

Bloch, F., 1933. Bremsvermögen von Atomen mit mehreren Elektronen. Zeitschrift für Physik 81 (5-6), 363–376.

Bohr, N., 1913. On the Constitution of Atoms and Molecules. Philosophical Magazine 26 (6), 1–25.

Bohr, N., 1915. LX. on the decrease of velocity of swiftly moving electrified particles in passing through matter. Philosophical Magazine Series 6 30 (178), 581–612.

Brun, R., Rademakers, F., Feb. 1997. ROOT - An object oriented data analysis framework. Nuclear Instruments and Methods in Physics Research A 389, 81–86.

Burmeister, S., Labrenz, J., Beaujean, R., Kortmann, O., Berger, T., Boehme, M., Haumann, L., Reitz, G., Sep. 2012. The DOSIS and DOSIS 3D Experiments onboard the International Space Station - Results From the Active DOSTEL Instruments. 17th WRMISS, Austin, Texas.

Caballero-Lopez, R. A., Moraal, H., 2004a. Limitations of the force field equation to describe cosmic ray modulation. Journal of Geophysical Research: Space Physics 109 (A1).

Caballero-Lopez, R. A., Moraal, H., McCracken, K. G., McDonald, F. B., 2004b. The heliospheric magnetic field from 850 to 2000 ad inferred from 10be records. Journal of Geophysical Research: Space Physics 109 (A12).

Caffrey, J. A., Hamby, D., 2011. A review of instruments and methods for dosimetry in space. Advances in Space Research 47 (4), 563 – 574.

Casolino, M., Simone, N. D., Bongue, D., Pascale, M. P. D., Felice, V. D., et al., 2009. Two years of flight of the pamela experiment: Results and perspectives. Journal of the Physical Society of Japan 78SA (Supplement A), 35–40.

Clem, J., Dorman, L., 2000. Neutron monitor response functions. Space Science Reviews 93, 335–359.

Cooke, D., Humble, J., Shea, M., Smart, D., Lund, N., Rasmussen, I., Byrnak, B., Goret, P., Petrou, N., 1991. On cosmic-ray cut-off terminology. Il Nuovo Cimento C 14 (3), 213–234.
URL http://dx.doi.org/10.1007/BF02509357

Cucinotta, F., Wilson, J., Shinn, J., Badavi, F., Badhwar, G., 1996. Effects of target fragmentation on evaluation of let spectra from space radiations: Implications for space radiation protection studies. Radiation Measurements 26 (6), 923 – 934.

Cucinotta, F. A., Durante, M., 2006. Cancer risk from exposure to galactic cosmic rays - implications for human space exploration. Lancet Oncol. 33, 323–382.

Cucinotta, F. A., Durante, M., 2009. Risk of radiation carcinogenesis, in: NASA Human Health and Performance Risks of Space Exploration Missions. Human Research Program Requirements Document, HRP-47052.

Desorgher, L., Flückiger, E. O., Gurtner, M., Moser, M. R., Bütikofer, R., 2005. Atmocosmics:. a Geant 4 Code for Computing the Interaction of Cosmic Rays with the Earth's Atmosphere. International Journal of Modern Physics A 20, 6802–6804.

Engelmann, J. J., Ferrando, P., Soutoul, A., Goret, P., Juliusson, E., Jul. 1990. Charge composition and energy spectra of cosmic-ray nuclei for elements from Be to Ni - Results from HEAO-3-C2. A&A233, 96–111.

European Communities Commission, 1996. 96/29 Euratom: Council Directive of 13 May 1996 Laying Down Basic Safety Standards for the Protection of the Health of Workers and the General Public Against the Dangers Arising from Ionizing Radiation. Official Journal of the European Communites. Office for Official Publications of the European Communities.

Forbush, S. E., 1954. World-wide cosmic ray variations, 1937-1952. Journal of Geophysical Research 59 (4), 525–542.

Gleeson, L. J., Axford, W. I., Dec. 1968. Solar Modulation of Galactic Cosmic Rays. The Astrophysical Journal 154, 1011.

Goodhead, D. T., 1994. Initial events in the cellular effects of ionizing radiations: clustered damage in DNA. International Journal of Radiation Biology 65 (1), 7–17.

Grieder, P. K. F., 2001. Cosmic Rays at Earth: Researcher's Reference Manual and Data Book. North-Holland, Amsterdam.

Hale, G. E., Ellerman, F., Nicholson, S. B., Joy, A. H., Apr. 1919. The Magnetic Polarity of Sun-Spots. The Astrophysical Journal 49, 153.

Heber, B., 2011. Cosmic rays through the solar hale cycle. Space Science Reviews, 1–14.

Heber, B., Dröge, W., Kunow, H., Müller-Mellin, R., Wibberenz, G., Ferrando, P., Raviart, A., Paizis, C., 1996. Spatial variation of >106 mev proton fluxes observed during the ulysses rapid latitude scan: Ulysses cospin/ket results. Geophysical Research Letters 23 (12), 1513–1516.
URL http://dx.doi.org/10.1029/96GL01042

Heber, B., Kopp, A., Gieseler, J., Müller-Mellin, R., Fichtner, H., Scherer, K., Potgieter, M. S., Ferreira, S. E. S., 2009. Modulation of galactic cosmic ray protons and electrons during an unusual solar minimum. The Astrophysical Journal 699 (2), 1956.

Herbst, K., Heber, B., Kopp, A., Sternal, O., Steinhilber, F., Dec. 2012. The Local Interstellar Spectrum beyond the Heliopause: What can be Learned from Voyager in the Inner Heliosheath? The Astrophysical Journal 761, 17.

Herbst, K., Kopp, A., Heber, B., Steinhilber, F., Fichtner, H., Scherer, K., Matthiä, D., 2010. On the importance of the local interstellar spectrum for the solar modulation parameter. Journal of Geophysical Research: Atmospheres 115 (D1), D00I20.

Hess, V., 1912. Über Beobachtungen der durchdringenden Strahlung bei sieben Freiballonfahrten. Phys. Z. 13, 1084–1091.

Horneck, G., Facius, R., Reichert, M., Rettberg, P., Seboldt, W., Manzey, D., Comet, B., Maillet, A., Preiss, H., Schauer, L., Dussap, C., Poughon, L., Belyavin, A., Reitz, G., Baumstark-Khan, C., Gerzer, R., 2003. HUMEX, a study on the survivability and adaptation of humans to long-duration exploratory missions, Part I: lunar missions. Advances in Space Research 31 (11), 2389–401.

Hüfner, J., 1985. Heavy fragments produced in proton-nucleus and nucleus-nucleus collisions at relativistic energies. Physics Reports 125 (4), 129 – 185.

ICRP, 1991. 1990 Recommendations of the International Commission Radiological Protection. International Commission on Radiological Protection Series. Pergamon Press.

ICRP, 2007. The 2007 Recommendations of the International Commission on Radiological Protection. ICRP Publication 103. Ann. ICRP 37 (2-4).

ICRP, 2009. Adult Reference Computational Phantoms. ICRP Publication 110. Ann. ICRP 39.

ICRU, 2010. Reference data for the validation of doses from Cosmic: radiation exposure of aircraft crew. Vol. 10. ICRU, Bethesda, MD.

ISO-15390, 2004. Space environment (natural and artificial) - galactic cosmic ray model. ISO 15390.

Ivantchenko, A. V., Ivanchenko, V. N., Molina, J.-M. Q., Incerti, S. L., 2012. Geant4 hadronic physics for space radiation environment. International Journal of Radiation Biology 88 (1-2), 171–175, pMID: 21830895.

Jadrníčková, I., Tateyama, R., Yasuda, N., Kawashima, H., Kurano, M., Uchihori, Y., Kitamura, H., Akatov, Y., Shurshakov, V., Kobayashi, I., Ohguchi, H., Koguchi, Y., Spurný, F., 2009. Variation of absorbed doses onboard of ISS Russian Service Module as measured with passive detectors. Radiation Measurements 44 (9-10), 901–904.

James, F., 1980. Monte Carlo theory and practice. Rept.Prog.Phys. 43, 1145.

Kallenrode, M., 2004. Space Physics: An Introduction to Plasmas and Particles in the Heliosphere and Magnetospheres. Advanced Texts in Physics. Springer.

Kim, M. Y., Shinn, J. L., Singleterry, Jr, R. C., Atwell, W., Wilson, J. W., 1999. Solar particle event exposures and local tissue environments in free space and on martian surface. Tech. rep.

Kobetich, E. J., Katz, R., Jun 1968. Energy deposition by electron beams and δ rays. Phys. Rev. 170, 391–396.

Koch, K., 2013. The role of Nuclear Factor kB in the cellular response to different radiation qualities. Dissertation, University of Cologne.

Koi, T., Asai, M., Wright, D. H., Niita, K., Nara, Y., Amako, K., Sasaki, T., Jun. 2003. Interfacing the JQMD and JAM Nuclear Reaction Codes to Geant4. ArXiv Physics e-prints.

Labrenz, J., 2013. University of Kiel. Private Communication.

Leo, W. R., 1994. Techniques for Nuclear and Particle Physics Experiments. Springer Verlag Second Revised Edition.

Liendl, M., 2004. Basics of Physical Interaction & Monte Carlo in Action, Tracking with Physics in Geant4 and The Geant4 Physics Model. "Experiment Simulation" Lectures, The CERN School of Computing 2004, 28 August- 11 September 2004, Vico Equense, Italy.
URL https://csc.web.cern.ch/CSC/2004/This_year_school/Programme/Handouts_PDF_Files/simulation_3_updt.pdf

Lindell, B., 1996. A history of radiation protection. Radiation Protection Dosimetry 68 (1-2), 83–95.

Lishnevskii, A., Panasyuk, M., Benghin, V., Petrov, V., Volkov, A., Nechaev, O., 2012. Variations of radiation environment on the international space station in 2005-2009. Cosmic Research 50 (4), 319–323.

Matthiä, D., 2009. The Radiation Environment in the Lower Atmosphere: A Numerical Approach. Dissertation, University of Kiel.

Matthiä, D., Berger, T., Mrigakshi, A. I., Reitz, G., 2013a. A ready-to-use galactic cosmic ray model. Advances in Space Research 51 (3), 329 – 338.

Matthiä, D., Berger, T., Reitz, G., 2013b. Organ shielding and doses in low-Earth orbit calculated for spherical and anthropomorphic phantoms. Advances in Space Research 52 (3), 528 – 535.

Mewaldt, R. A., Davis, A. J., Lave, K. A., Leske, R. A., Stone, E. C., Wiedenbeck, M. E., Binns, W. R., Christian, E. R., Cummings, A. C., de Nolfo, G. A., Israel, M. H., Labrador, A. W., von Rosenvinge, T. T., 2010. Record-setting cosmic-ray intensities in 2009 and 2010. The Astrophysical Journal Letters 723 (1), L1.

Mrigakshi, A., Matthiä, D., Berger, T., Reitz, G., Wimmer-Schweingruber, R. F., 2012. Assessment of galactic cosmic ray models. J. Geophys. Res. 117, A08109.

Mrigakshi, A. I., Matthiä, D., Berger, T., Reitz, G., Wimmer-Schweingruber, R. F., 2013a. How galactic cosmic ray models affect the estimation of radiation exposure in space. Advances in Space Research 51, 825–834.

Mrigakshi, A. I., Matthiä, D., Berger, T., Reitz, G., Wimmer-Schweingruber, R. F., 2013b. Estimation of Galactic Comic Ray exposure inside and outside the Earth's magnetosphere during the recent solar minimum between solar cycles 23 and 24. Advances in Space Research 52, 979–987.

Mueller, D., Swordy, S. P., Meyer, P., L'Heureux, J., Grunsfeld, J. M., 1991. Energy spectra and composition of primary cosmic rays. The Astrophysical Journal 374, 356–365.

Nara, Y., Otuka, N., Ohnishi, A., Niita, K., Chiba, S., Feb. 2000. Relativistic nuclear collisions at 10A GeV energies from p+Be to Au+Au with the hadronic cascade model. Phys. Rev. C61 (2), 024901.

NASA, 2007. Nasa space flight human system standards, volume 1: Crew health. NASA technical Standard, NASA-STD-3001.

NCRP, 1989. Guidance on Radiation Received in Space Activities. NCRP report 98. NCRP.

NCRP, 2000. Radiation protection guidance for activities in low-Earth orbit. NCRP report 132. National Council on Radiation Protection and Measurements.

NCRP, 2002. Operational Radiation Safety Program for Astronauts in Low-Earth Orbit: a Basic Framework. NCRP report 142. NCRPM.

NCRP, 2006. Information Needed to Make Radiation Protection Recommendations for Space Missions Beyond Low-Earth Orbit: Recommendations of the National Council on Radiation Protection and Measurements. NCRP report 153. National Council on Radiation Protection and Measurements.

Niita, K., Chiba, S., Maruyama, T., Maruyama, T., Takada, H., Fukahori, T., Nakahara, Y., Iwamoto, A., Aug 1995. Analysis of the (n,xn') reactions by quantum molecular dynamics plus statistical decay model (nucl-th/9508004).

Nymmik, R., Panasyuk, M., Pervaja, T., Suslov, A., 1992. A model of galactic cosmic ray fluxes. International Journal of Radiation Applications and Instrumentation. Part D. Nuclear Tracks and Radiation Measurements 20 (3), 427 – 429.

Nymmik, R., Panasyuk, M., Suslov, A., 1996. Galactic cosmic ray flux simulation and prediction. Advances in Space Research 17 (2), 19 – 30.

O'Neill, P., 2010. Badhwar-o'neill 2010 galactic cosmic ray flux model-revised. Nuclear Science, IEEE Transactions on 57 (6), 3148–3153.

Parker, E. N., Jan. 1965. The passage of energetic charged particles through interplanetary space. Planet. Space Sci.13, 9.

Potgieter, M. S., 2011. Cosmic Rays in the Inner Heliosphere: Insights fromÂ Observations Theory and Models. Space Science Reviews, 1–12.

Reitz, G., 2008. Characteristic of the radiation field in low-Earth orbit and in deep space. Zeitschrift für Medizinische Physik 18 (4), 233 – 243.

Ritter, B., 2013. The Mobile Dosimetric Telescope - A small active dosimeter for the application in space. Dissertation, University of Kiel.

Sandoval, L., Shea, C., Otto, C., Leventon, L., 2010. Different Perspectives on Asthenia in Astronauts and Cosmonauts: International Research Literature. NASA Johnson Space Center: NASA JSC Document (JSC-CN-21318).

Schiavi, A., 2003. Study of Laser Produced Plasmas by X-Ray and Proton Radiography. Imperial College of Science, University of London.

Schwabe, M., Feb. 1844. Sonnenbeobachtungen im Jahre 1843. Von Herrn Hofrath Schwabe in Dessau. Astronomische Nachrichten 21, 233.

Schwadron, N. A., Boyd, A. J., Kozarev, K., Golightly, M., Spence, H., Townsend, L. W., Owens, M., 2010. Galactic cosmic ray radiation hazard in the unusual extended solar minimum between solar cycles 23 and 24. Space Weather 8 (5), n/a–n/a.
URL http://dx.doi.org/10.1029/2010SW000567

Semkova, J., Koleva, R., Bankov, N., St. Malchev, Petrov, V. M., Shurshakov, V. A., Chernykh, I. V., Benghin, V. V., Drobyshev, S. G., Yarmanova, E. N., Nikolaev, I. V., Mar. 2013. Study of radiation conditions onboard the International space station by means of the Liulin-5 dosimeter. Cosmic Research 51, 124–132.

Semkova, J., Koleva, R., Maltchev, S., Bankov, N., Benghin, V., Chernykh, I., Shurshakov, V., Petrov, V., Drobyshev, S., Nikolaev, I., 2012. Depth dose measurements with the liulin-5 experiment inside the spherical phantom of the matroshka-r project onboard the international space station. Advances in Space Research 49 (3), 471 – 478.

Semones, E., 2009. Update on NASA TEPC Activities September 08-September 09. Fourteenth Workshop on Radiation Monitoring for the International Space Station (WRMISS), Dublin, www.wrmiss.org.

Setlow, R., 2003. The hazards of space travel. EMBO Rep 4 (11), 1013–6.

Shikaze, Y., Haino, S., Abe, K., Fuke, H., Hams, T., et al., 2007. Measurements of 0.2 to 20-GeV/n cosmic-ray proton and helium spectra from 1997 through 2002 with the BESS spectrometer. Astropart.Phys. 28, 154–167.

Sihver, L., 2008. Transport calculations and accelerator experiments needed for radiation risk assessment in space. Zeitschrift für Medizinische Physik 18 (4), 253–64.

Simpson, J., 2000. The cosmic ray nucleonic component: The invention and scientific uses of the neutron monitor. Space Science Reviews 93, 11–32.

Simpson, J. A., 1983. Elemental and Isotopic Composition of the Galactic Cosmic Rays. Annual Review of Nuclear and Particle Science 33, 323–382.

Stoffle, N., Welton, A., Barzilla, J., Gaza, R., Lee, K., Zapp, N., 2012. CAD Shielding analysis of the international space station. Seventeenth Workshop on Radiation Monitoring for the International Space Station (WRMISS),Austin, www.wrmiss.org.

Stone, E., Cohen, C., Cook, W., Cummings, A., Gauld, B., Kecman, B., Leske, R., Mewaldt, R., et al., T., 1998. The Cosmic-Ray Isotope Spectrometer for the Advanced Composition Explorer. Space Science Reviews 86, 285–356.

Störmer, C., 1930. Periodische Elektronenbahnen im Felde eines Elementarmagneten und ihre Anwendung auf Brüches Modellversuche und auf Eschenhagens Elementarwellen des Erdmagnetismus. Mit 32 Abbildungen. Zeitschrift für Astrophysik 1, 237.

Straube, U., Berger, T., Reitz, G., Facius, R., Fuglesang, C., Reiter, T., Damann, V., Tognini, M., Apr. 2010. Operational radiation protection for astronauts and cosmonauts and correlated activities of ESA Medical Operations. Acta Astronautica 66, 963–973.

Turner, J. E., 2007. Atoms, Radiation, and Radiation Protection; 3rd ed. Wiley, Weinheim.

Tylka, A. J., Boberg, P. R., Brownstein, B., Dietrich, W. F., Flueckiger, E. O., Petersen, E. L., Shea, M. A., Smart, D. F., Smith, E. C., 1997. CREME96: A Revision of the Cosmic Ray Effects on MicroElectronics Code. IEEE Transactions on Nuclear Science 44, 2150–2160.

Usoskin, I. G., Alanko-Huotari, K., Kovaltsov, G. A., Mursula, K., 2005. Heliospheric modulation of cosmic rays: Monthly reconstruction for 1951-2004. Journal of Geophysical Research: Space Physics 110 (A12), A12108.

Vallarta, M. S., Dec 1948. On the energy of cosmic radiation allowed by the Earth's magnetic field. Phys. Rev. 74, 1837–1840.

van Allen, J. A., McIlwain, C. E., Ludwig, G. H., Mar. 1959. Radiation Observations with Satellite 1958ϵ. Journal of Geophysical Research 64, 271–286.

White, R., Averner, M., 2001. Humans in space. Nature 409 (6823), 1115–8.

Wimmer-Schweingruber, R., 2005. Interplanetary disturbances. In: Scherer, K., Fichtner, H., Heber, B., Mall, U. (Eds.), Space Weather. Vol. 656 of Lecture Notes in Physics. Springer Berlin Heidelberg, pp. 71–129.

Zeitlin, C., 2012. Physical interactions of charged particles for radiotherapy and space applications. Health Phys 103 (5), 540–6.

Zeitlin, C., Guetersloh, S. B., Heilbronn, L. H., Miller, J., Nov. 2006. Measurements of materials shielding properties with 1 GeV/nuc ^{56}Fe. Nuclear Instruments and Methods in Physics Research B 252, 308–318.

Zeitlin, C., Hassler, D. M., Cucinotta, F. A., Ehresmann, B., Wimmer-Schweingruber, R. F., Brinza, D. E., Kang, S., Weigle, G., Böttcher, S., Böhm, E., Burmeister, S., Guo, J., Köhler, J., Martin, C., Posner, A., Rafkin, S., Reitz, G., 2013. Measurements of energetic particle radiation in transit to mars on the mars science laboratory. Science 340 (6136), 1080–1084.
URL http://www.sciencemag.org/content/340/6136/1080.abstract

Appendices

A GCR Model Data Retrieval

The assessment of GCR models was performed by comparing model spectra from all models (CREME96, CREME2009, Badhwar-O'Neill2010, Burger-Usoskin and Matthiä-ACE/OULU) under consideration with the available GCR measurements taken over different time periods starting from the year 1992 and at regular intervals (e.g. 27-day averaged data by ACE/CRIS from July 1997 onwards). Additionally, dose rates were calculated using all GCR models for time periods ranging from 1970 to 2011 with a time-resolution of 10 dates per year e.g. 1970.0, 1970.1,....,1970.9. As stated in Chapter 3, Section 3.2.1, the models as available in their original state are able to generate GCR data for only one time period for each run of the programs. Therefore, batch retrieval scripts were written for the models to produce the data for the required time periods and to properly store them with a consistent format for an efficient and automated data processing. These scripts are briefly described in this chapter.

A.1 CREME96 and CREME2009

Accessing the Models

The CREME models can be accessed through the CREME website[1]. The GCR flux of particles ranging from hydrogen to nickel can be produced on running the *Flux* routine provided in the CREME package. The routine requires several inputs such as the particle type (in atomic number), the GCR model (CREME96 or CREME 2009), time period in fractional year, location (outside or inside the Earth's magnetosphere) and the output file name. After running the routine, a TSV (tab-seperated values) data file with energies in the first colum followed by the fluxes of all particles in individual columns is generated e.g.:

Energy (MeV/nuc)	Flux ($m^{-2}s^{-1}sr^{-1}(MeV/nuc)^{-1}$)			
	Z=1	Z=2	Z=3	- - -
1.05919	2.604e-06 November 2009 and	5.3196e-07	1.1611e-09	- - -
1.07391	2.6817e-06	6.813e-07	8.5495e-09	- - -
1.08884	2.7621e-06	8.3764e-07	1.6401e-08	- - -
- - - - -	- - - - -	- - - - -	- - - - -	- - - - -

[1] https://creme.isde.vanderbilt.edu/

Automatic Data Retrieval

The *Wget* utility, a commonly used package for data retrieval, was chosen for downloading data from the CREME website. This utility basically makes HTTP requests as if a user's browser is sending them to the target website, in this case the CREME website. Then, by knowing how the URL has to be formatted and which parameters the CREME website accepts, the data retrieval can be automated by a shell script using *Wget*. Additionally by using the *Gawk* utility the retrieved data files were filtered for individual particle fluxes, and stored in separate files and directories. The script was originally written by Thomas Urlings[2].

The end product of this procedure resulted in sorted out files with a consistent naming format that were stored under directories for every considered year:

Code Snippet:

```
#!/bin/bash -eu

#Setup: Initilize variables and send login request to the CREME website
year = 19700 #Denoting 1970.0
model = 1996 #CREME model either 1996 or 2009
....

#Iterate the loop by 0.1 year steps (data sampling rate)
for (( i=0; i<$numberOfTimeValues; i++))
{
  # Navigate to the Flux routine webpage
  ....

  # Update time value
  y=$(( year + $i )) #e.g. 19700 + 1 = 19701, denoting 1970.1
  ....

  # Create the filename in the format such as 1970.1_Z1_Z28_creme96_outside_EMF.
      tsv
  fname = ...

  # Execute request on server to run the Flux routine
  wget -O- --no-check-certificate --load-cookies "CREMECOOKIE.txt" --save-
      cookies "CREMECOOKIE.txt" --keep-session-cookies --post-data "z1=1&z2=28&
      version=$model&model=Year&year=${y:0:4}.${y:4}&location=Interplanetary%20
      Space&rootname=$fname&form.button.submit=Submit&form.submitted=1&tzoffset=
      None" "https://creme.isde.vanderbilt.edu/CREME-MC/Members/aimsphere/
      FluxTemplate" 2>&1 1>/dev/null || ( echo "wget failed in request!" & exit
```

[2]Thomas Urlings is the IT Manager of the Radiation Biology Department, Institute of Aerospace Medicine, German Aerospace Centre, Germany

```
    $E_WGET )

  #Download datafile
  wget -O "$TARG_DIR/$fname.tsv" --no-check-certificate --load-cookies "$COOKIE"
       "https://creme.isde.vanderbilt.edu/CREME-MC/Members/$username/
      DisplaySessionData?tag=File.tsv&download=1" 2>&1 1>/dev/null || ( echo "
      wget failed in datafile download!" & exit $E_WGET )

  #Load datafile and store Z columns into separate files
  for j in 2 3 ... 27 #j represents the column numbers with first containing the
       energies and the following containing the particle fluxes for Z = j-1
  do
    # generate output filenames
    outfname=${y:0:4}.${y:4}_Z
    [ $j -le 10 ] && outfname=${outfname}0
    outfname=${outfname}$(( $j - 1 ))
    [ $model = 1996 ] && outfname=${outfname}_creme96 || outfname=${outfname}
        _creme2009
    outfname=${outfname}_outside_EMF

    # write header
    echo -e "\"Energy (MeV/nuc)\"\t\"Flux (particles/m2-s-sr-MeV/nuc)\"">"
        $TARG_DIR/$outfname.tsv"
    echo -e "\"\"\tZ=$(( $j - 1 ))">>"$TARG_DIR/$outfname.tsv"

    #filter the columns and print columns 1 and j to the output file
    gawk -v x=$j 'BEGIN { FS = "\t" };NR>2 {print $1 "\t" $x }' "$TARG_DIR/
        $fname.tsv">>"$TARG_DIR/$outfname.tsv"
  done
}
```

A.2 Badhwar-O'Neill 2010 and 2011 models

Accessing the Model

The models are provided in MS-DOS binary format by the author of O'Neill (2010) upon request. The executable file is sent together with the source-code written in Fortran language. Upon execution, the program runs from the command line interface and asks for various inputs to calculate and generate the required GCR spectrum. These inputs include the drive used for the output directory, particle type and either the time (option a) or the level of solar modulation (option b) for which the flux is required. For the option 'a', the program derives the solar modulation parameter based on the International Sunspot Numbers (ISSN) and thus requires the user to keep the file with the ISSN updated by downloading the latest data file from the National Geophysical Data Centre [3]. In this work, the GCR flux was derived using the option 'a' wherein the time period of choice has to be provided. The period over which the flux has to be averaged has to be given as well. The output of the program produces a file containing the energy spectrum of the selected particle for the selected time period.

Automatic Data Retrieval

The data files containing the energy spectrum of all particles ranging from hydrogen to iron for multiple time periods were produced using a set of batch scripts. To allow automatic passing of the input parameters through the standard input stream in DOS by the batch script, it was necessary to recompile the Fortran source code with the g95 Fortran compiler[4]. The batch scripts contain commands to

- Set required inputs like the time in fraction year, particle type in atomic number and the averaging duration in days
- Call the recompiled executable file and pass the input parameters
- Copy and save the created files with a consistent naming format

Code Snippet:

[3] ftp://ftp.ngdc.noaa.gov/STP/SOLAR_DATA/SUNSPOT_NUMBERS/INTERNATIONAL/monthly/MONTHLY

[4] http://www.g95.org/

```
File 1: gcrdr_loop.bat

REM call the gcrdr_loop_year script and pass the Z numbers as input parameters
@echo off
CALL gcrdr_loop_year 1
CALL gcrdr_loop_year 2
CALL gcrdr_loop_year ..
....
....

File 2: gcrdr_loop_year.bat

REM call the gcrdr_param script and pass the Z number, duration and the time
    period read from a text file years.txt as input parameters
@echo off
SET PARTICLE=%1
SET DURATION=1
FOR /F %%i IN (years.txt) DO (CALL gcrdr_param %%i %PARTICLE% %DURATION%)

File 3: gcrdr_param.bat

REM set the input parameters directory (C), Z number (PARTICLE), the time period
     (YEAR) and duration (DURATION) everytime the variables are called by the
    executable file MY_GCRDR.EXE containing the GCR model, and copy and save the
     created file flx.dat to the format %YEAR%_Z%PARTICLE%_1DayAvg_badhwar-o-
    neill.txt
@echo off
SET YEAR=
SET PARTICLE=
SET DURATION=
SET YEAR=%1
SET PARTICLE=%2
SET DURATION=%3
echo batchfile started with parameters: %YEAR% %PARTICLE% %DURATION%
(echo C
echo %PARTICLE%
echo.
echo.
echo %YEAR%
echo.
echo %DURATION%)|MY_GCRDR.EXE
echo %YEAR%
echo %PARTICLE%
echo %DURATION%
SET OUTFILENAME=%YEAR%_Z%PARTICLE%_1DayAvg_badhwar-o-neill.txt
echo.
echo Outputfile: %OUTFILENAME%
copy /Y flx.dat %OUTFILENAME%
```

A.3 Burger-Usoskin and Matthiä et al. 2013a

Accessing the Models

Both the models implemented in the ROOT script/C++ language were provided by Dr. Daniel Matthiä. It should be noted that the Matthiä model (containing both Matthiä/ACE and Matthiä/OULU) can also be provided in an executable JAVA binary file upon request.

The function implementing the GCR models required a set of parameters or arguments that were passed to the function when called on execution. These parameters included the particle type and the parameter indicating the level of solar modulation (Model parameter W in the case of Matthiä and solar modulation parameter Φ in case of Burger-Usoskin model). The program would generate the energy spectrum of the selected particle and the time period for which the parameter indicating the level of solar modulation was selected.

Automatic Data Retrieval

To produce and store the energy spectra into files with consistent format, additional functions were added to the program to iterate over all the particle types and time periods. This was achieved by simply applying the For-loop iteration structure.

Code Snippet:

```
#include "TGraph.h"
#include "TF1.h"
#include ...
...


TGraph* W_ACE = new TGraph ("P0_ACE.txt");
TF1* GetGCRFunction(Int_t Z);
TGraph* makeDanModGraph(double years, int z);

void CalculateOutside(){
  // Create graph object with the text file containing the modulation parameter
      W values (in this case based on ACE measurements) calculated by Matthi{\"a
      } et al. 2013a over time
  TGraph* W_ACE = new TGraph ("P0_ACE.txt");
  Double_t* years;
  Int_t nOfYears;
  years=W_ACE->GetX();
  nOfYears = W_ACE->GetN();
  int nOfParticles = 28;
  int Z[] = {1,2,3, 4, 5,6, 7,8, 9,10, 11,12, 13,14, 15,16, 17, 18, 19, 20, 21,
```

```
      22, 23, 24, 25, 26,27, 28};

  //loop over all Z values (particle types) and time to eventually create txt
      files to have energy spectrum of each particle and time, by creating graph
       objects by the makeDanModGraph function
  for (int zNum = 0; zNum<nOfParticles; zNum++){
    for (int yearIndex = 0; yearIndex<nOfYears ; yearIndex++) {
      char yearExact[20];
      sprintf(yearExact,"%f",years[yearIndex]);
      TString* fractionalYear = new TString(yearExact);
      TGraph* DanModGraph = makeDanModGraph(years[yearIndex],Z[zNum]);
    }
  }
}

TGraph* makeDanModGraph(double year,int z) {

  //Evaluate the values of the modulation parameter W at the desired year by
      linearly interpolating
  between the W provided over various tine periods
  double W_ACE_at = W_ACE->Eval(year);

  //Calculate the energy spectrum of particle z by calling the function
      GetGCRFunction and passing the value of z and for W values evaluated for
      the desired time
  TF1* DanielModel = GetGCRFunction(z);
  DanielModel->SetParameter(0,W_ACE_atYear);

  ...
  ...
  ...
  //Create graph from any text file containing the differential energy spectra
      from CREME model in order to get the energies for which the particle
      fluxes must be derived from model Matthi{\"a}/OULU
  TGraph* for_EnergyColumn = new TGraph("1970.0_Z1_creme96_outside_EMF.tsv");

  // Get number of energy points
  int numPoints = for_EnergyColumn->GetN();
  // Get energy values
  Double_t* energies = for_EnergyColumn->GetX();
  double flux[numPoints];

  //Evaluate the fluxes for the common energy intervals as that produced by the
      CREME model
  for (int i =0; i<=numPoints; i++){
    flux[i] = DanielModel->Eval(energies[i]);
  }

  \\Create file with a particular format
  char dname2[100];
  sprintf(dname2,"%s/%f_Z%d_DLR_OULUyears.txt",path,year,z);
```

```
  ofstream outfile2;
  outfile2.open(dname2);
  ...
  ...
  ...

  //Save the energy spectra of particle z for a desired particle, time and
      energies
  for (int numValues = 0; numValues<numPoints; numValues++){
    outfile2 <<energies[numValues]<<" "<< flux[numValues]<<endl;
  }
        outfile2.close();

}

//The function contains the implementation of the model by Matthi{\"a} et al.
    2013a or by Burger-Usoskin with all the necessary model parameters as
    mentioned in the respective papers
TF1* GetGCRFunction(Int_t Z){ // function return
  // model implementation
  ....
  ....
}
```

B Primary Particle Generation

B.1 Input spectra: particle number over energy

The General Particle Source (GPS) was used to generate the input spectrum of particles in this work. The energy distribution of the primary particles selected for this work was set to follow a power law distribution as described in Chapter 3, Section 3.3.2. This method of particle generation is called indirect method in this section. The other way of generating particles, called as the direct method henceforth, is to use a user-defined histogram which includes the GCR energy distribution and for particle generator is interpreted as the probability distribution to generate particles of certain energies. E.g. the following commands in the GCR macro file shows the GCR H energy spectrum using the CREME96 model used for event generation:

#gps command	Energy	Flux
/gps/hist/point	5.3244	9.4506e-06
/gps/hist/point	5.3984	2.0993e-05
/gps/hist/point	5.4735	3.1674e-05
/gps/hist/point	5.5495	4.1553e-05
/gps/hist/point	5.6266	5.0687e-05
/gps/hist/point	5.7048	5.9125e-05
.....		

In the direct method the number of events generated are distributed with the GCR energy distribution and therefore to have enough statistics at the lower energy range below 100 MeV/nuc and above several tens of GeV/nuc large number of particles have to be simulated in comparison with the indirect method (See Figure 3.5 for a visual illustration). After running the simulations the results have to be normalized by the number of events simulated in order to calculate the absorbed dose rates in units of Gy/d and dose equivalent rates in units Sv/d.

To see if the results by using the two methods yield same results, the doses induced by GCR H and Fe nuclei were calculated for an unshielded water sphere irradiated isotropically. The GCR particle fluxes were derived using CREME96 model for an orbit with an inclination of 51.6° and altitude of 450 km for January 1977 in case of H nuclei and for an altitude of 350 km with the same inclination for January 2004 for Fe nuclei.

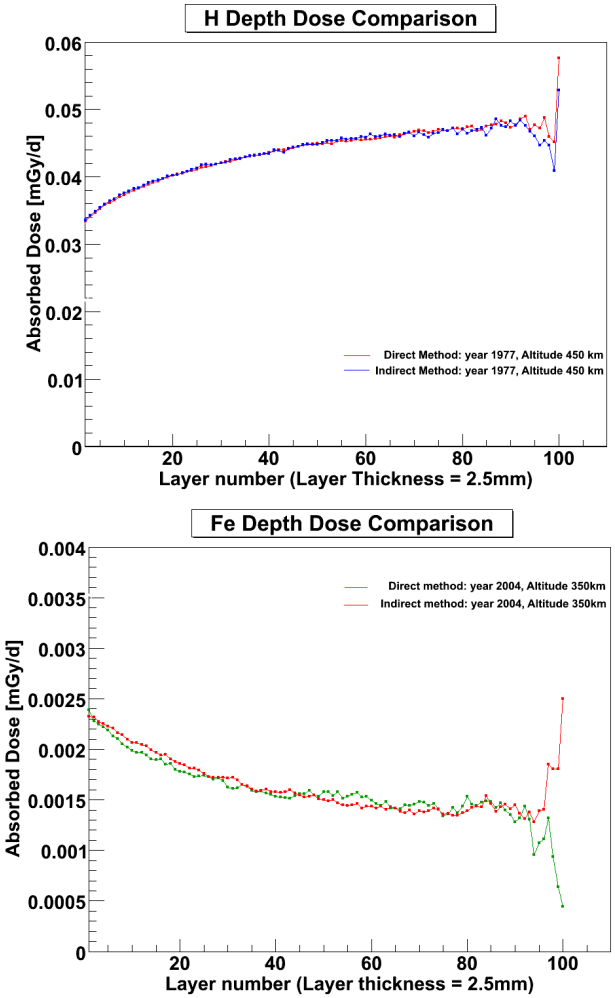

Figure B.1: Comparison of the dose rates calculated using the indirect and the direct method. Layer number 0 corresponds to the outermost shell and the layer number 100 corresponds to the innermost.

Clearly, the dose values calculated using both the methods show good agreement. Severe fluctuations in the dose calculated in the innermost layers (90th layer onwards) can be observed wherein the difference between the dose values calculated using the different methods increases too. This behaviour can be explained by the fact that the volumes of inner layers (or shells) are so small that the probability of particles (primary of secondary) passing through them to deposit significant amount of energies is very low. By increasing the number of particles simulated, lesser fluctuations in the dose rates are observed at the inner layers as shown in the following Section B.2.

B.2 Quality of statistics

For selecting the number of particles to be simulated using the indirect method for the GCR dose assessment, a depth-dose analysis for different numbers of primary particles (or events) was performed. The numbers of particles leading to a reasonably smooth depth-dose distribution were used for further calculations.

The graph below shows an example dose deposited by GCR Fe ion in the unshielded water sphere for different number of primary particles, 10,000, 100,000 and 700,000. The extent of fluctuations is seen to have reduced considerably from 10,000 to 100,000 events atleast for layers up to about 80. At inner layers the fluctuations remain large but on simulating a larger number of particles (700000), the quality of the result improves.

A completely smooth depth-dose profile would require the simulation of a larger number of particles which would lead to an increase in the computational time, as would simulations with increasing shielding. Therefore, the particle number has to be carefully selected.

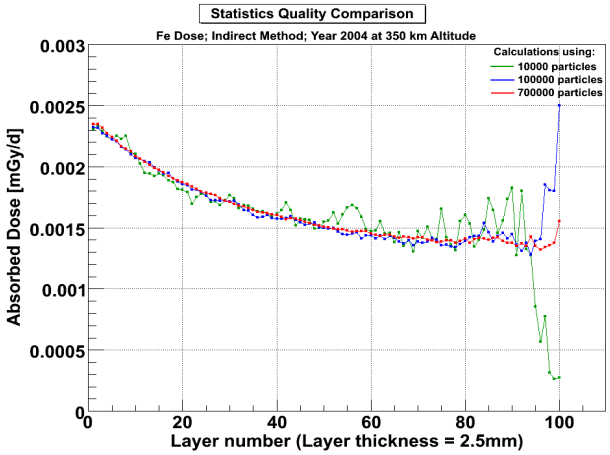

Figure B.2: Influence of the number of simulated particles on the fluctuations in the depth-dose distribution. Layer number 0 corresponds to the outermost shell and the layer number 100 corresponds to the innermost.

In this work, 500,000 particles were simulated for the experimental scenario without shielding, and over 800,000 particles for the case with shielding. Figure 5.9 shows that the selection of this many particles for the respective shielding configurations was acceptable as the criterion of having minimal fluctuations in the depth-dose profile was achieved. In Figure 5.9, the increase in the statistical fluctuations in the dose at deeper locations can also be observed.

B.3 Example GPS macro file

The code below shows an example of a GCR macro file use to setup radiation source to generate primary particles with required properties.

```
#Initialize GEANT4 kernel
/run/initialize

#Sets the source distribution type to Surface and shape to Sphere
/gps/pos/type Surface
/gps/pos/shape Sphere

#Sets the centre coordinates of the source
/gps/pos/centre 0 0 0 cm

#Sets the radius of the source sphere for the scenario without shielding
/gps/pos/radius 0.35 m

#Sets the angular distribution of particle emission to cosine-law with solid
    angle theta from 0 to 90 degrees
/gps/ang/type cos
/gps/ang/mintheta    0. deg
/gps/ang/maxtheta   90. deg

#Sets the energy distribution type to power law with spectral index -1
/gps/ene/type Pow
/gps/ene/alpha -1.0

#Sets atomic number 26 and atomic mass 56 to simulate iron ion
/gps/ion 26 56

#Sets minimum of the energy range of iron ion to 10 MeV/nuc and maximum to 100
    GeV/nuc
/gps/ene/min 560. MeV
/gps/ene/max 5600. GeV

#Switch on tracking with verbosity 2 to get information of each particle step
    and secondary particles
/tracking/verbose 2

#Start a run to simulate 10000 events or primary particles
/run/beamOn 10000
```

C SPENVIS GCR Model

C.1 The ISO15390 GCR model in SPENVIS

The Space Environment Information System (SPENVIS) is a web-based tool[1] which allows users to use models describing the space environment, e.g., radiation, meteoroids and debris, and its effect on spacecraft systems. There are implementations of the ISO model (ISO-15390, 2004) and model by Nymmik et al. (1996) available to derive GCR spectra of particles ranging from hydrogen upto uranium at user-specified mission epochs. The model energy spectra covers particle fluxes from 1 MeV/nuc to 20 GeV/nuc. However, this energy range is not sufficient for the calculation of radiation exposure from GCR which requires particle fluxes for energies up to 100 GeV/nuc (see Figure 5.6). To use SPENVIS/ISO15390 model for dose calculations, the particle fluxes have to be thus extrapolated in log-log scale to cover higher energies.

C.2 Model assessment

Figure C.1 shows model and measured energy spectra of GCR H, He, O and Fe nuclei for August 2000 (solar maximum) and November 2009 (solar minimum). The graph is similar to the Figure 2 in Mrigakshi et al. (2013a) but shows the PAMELA measurements and the model spectra from SPENVIS/ISO15390 (dotted lines) and Matthiä/ACE in addition to CREME2009 and BON2010 only.

The differential energy spectra described by the SPENVIS/ISO15390 model is close to the model spectra using the CREME2009 model. This is most likely due to the fact that the CREME2009 model is also based on the ISO15390. The model results in considerable overestimation of all investigated particle fluxes, e.g., over 70% for hydrogen nuclei in comparison with the measurements for this solar maximum period. For the solar minimum period the model produces similar particle fluxes for helium, oxygen and iron nuclei from 100 MeV/nuc onwards as the Badhwar-O'Neill2010 model. It derives lower GCR hydrogen fluxes in comparison with the data measured by the PAMELA mission.

[1] http://www.spenvis.oma.be/

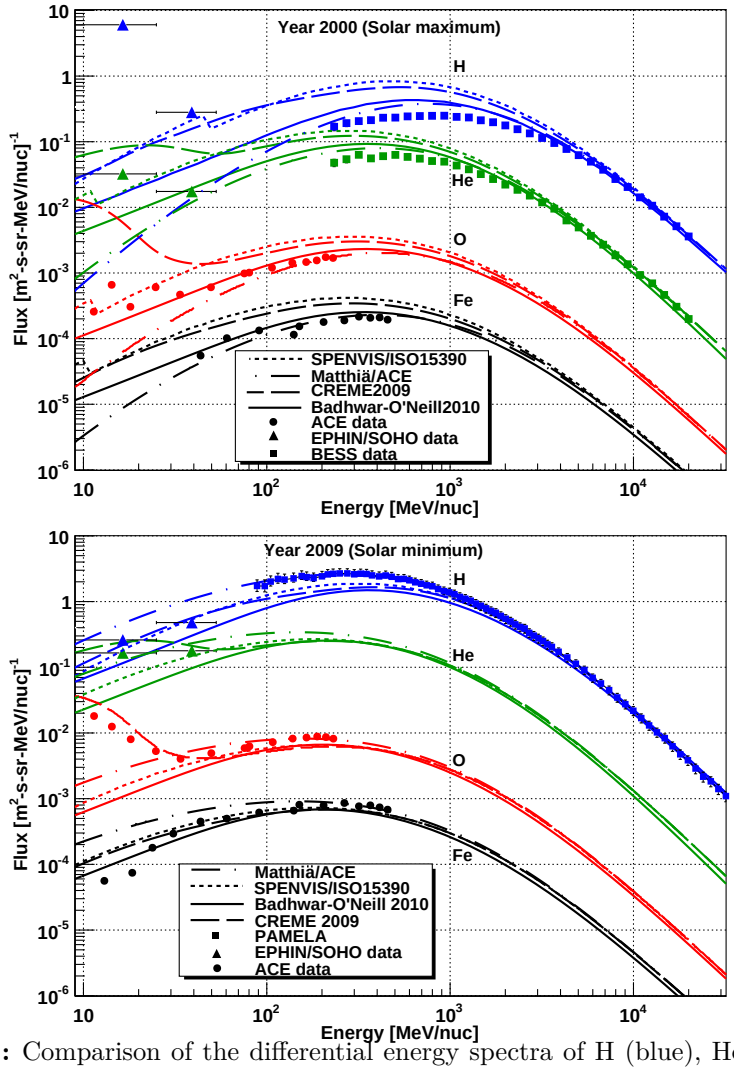

Figure C.1: Comparison of the differential energy spectra of H (blue), He (green), O (red) and Fe (black) nuclei described by SPENVIS/ISO15390 (dotted lines), Matthiä/ACE (dashed-dotted lines), CREME2009 (dashed lines) and BON2010 (continuous lines) with data from EPHIN/SOHO (solid triangles), BESS (solid squares - Figure 5.3a), PAMELA (solid squares - Figure 5.3b) and ACE - SIS and CRIS (solid circles) measured during different solar activity extreme periods. Figure 5.3a shows the assessment for August 2000 (solar maximum) and Figure 5.3b for November 2009 (solar minimum).

C.3 Dose Assessment

The GCR exposure estimated for near-Earth interplanetary space for the solar maximum period in terms of absorbed dose rate is 273 μGy/d and the dose equivalent rate 861 μSv/d. and for solar minimum period 405 μGy/d and 1247 μSv/d respectively. In comparison with the Matthiä/ACE model, the dose values for the solar maximum period are higher and for solar maximum are lower. The ratio of the dose using the SPENVIS/ISO15390 model to the Matthiä/ACE model for the former is 1.45 and for the latter is 0.87.

Although the the SPENVIS/ISO15390 model has been evaluated for only 2 points in time, the results indicate that this model as well must be evaluated against measurements for its accuracy for any required time period before its application.

List of Abbreviations

ACE	Advance Composition Explorer
ACR	Anomalous Cosmic Rays
AMS	Alpha Magnetic Spectrometer
BESS	Balloon-borne Experiment with a Superconducting Spectrometer
BERT	Bertini
BO and BON	Badhwar-O'Neill
BR	Bartels Rotation
CAPRICE	Cosmic Antiparticle Ring-Imaging Cerenkov Experiment
CHIME	CRRES/SPACERAD Heavy Ion Model
CMD	command
CR	Cosmic Rays
CREME	Cosmic Ray Effects on Micro-Electronics
CRIS	Cosmic Ray Isotope Spectrometer
CRN	Cosmic Ray Nuclei
DOY	Day of Year
DNA	Deoxyribonucleic Acid
DOSIS	Dose Distribution Inside the ISS
DOSTEL	Dosimetry Telescope
EM	Electromagnetic
EPHIN	Electron Proton Helium Instrument
EuCPD	European Crew Personal Dosimeter
GALROP	Galactic cosmic-ray propagation code
GCR	Galactic Cosmic Rays
GEANT	Geometry And Tracking
GPS	General Particle Source
GTRN	Geomagnetic Transmission
HEAO	High-Energy Astronomy Observatory
HMF	Heliospheric Magnetic Field
HP	High-Precision
HZETRN	High charge(Z) and Energy TRaNsport
ISS	International Space Station
ICRU	International Commission on Radiation Units
ICRP	International Commission on Radiological Protection
IMAX	Isotope Matter-Antimatter Experiment
IMP	Interplanetary Monitoring Platform
ISO	International Organization for Standardization
ISSN	International Sunspot Numbers
JAM	jet AA microscopic transport model
JQMD	Jaeri quantum molecular dynamics

LEO	Low Earth Orbit
LET	Linear Energy Transfer
LIS	Local Interstellar Spectrum
MC	Monte-Carlo
MDT	Mobile Dosimetric Telescope
MSL	Mars Science Laboratory
NASA	National Aeronautics and Space Administration
NCRP	National Council on Radiation Protection and Measurements
NM	Neutron Monitor
NMDB	Neutron Monitor Database
PAMELA	Payload for Antimatter Matter Exploration and Light-nuclei
PNTD	Plastic Nuclear Etch Track Detectors
RAD	Radiation Assessment Detector
SIDC	Solar Influences Data Center
SIS	Solar Isotope Spectrometer
SOHO	Solar and Heliospheric Observatory
SPE	Solar Particle Event
SPENVIS	Space Environment Information System
STS	Space Transportation System
TLD	Thermoluminescence Detectors
UV	UltraViolet
VRML	Virtual Reality Modeling Language
QGSP	Quark Gluon String Model

List of Figures

2.1 Measured GCR spectra of different ions 7
2.2 GCR spectra: Solar minimum vs Solar maximum 9
2.3 Sunspot numbers vs Neutron Monitor count rates over time 11
2.4 World map of the vertical cut-off rigidities 15
2.5 GCR H spectra at different geomagnetic latitudes 16
2.6 Relative contribution of GCR nuclei to total dose 27

3.1 Schematic diagram showing the dose calculation procedure 32
3.2 Geomagnetic Transmission Function from CREME96 36
3.3 Example model GCR energy spectra for outside and inside the magnetosphere 37
3.4 Simulation setup 41
3.5 Energy histograms following power-law and GCR energy distributions 42
3.6 Simulation processing and output 46

5.1 Integral flux using BON2011, BON2010 and Matthiä/ACE models vs measurements . 106
5.2 Differential energy spectra using BON2011, BON2010, Matthiä/ACE models vs measurements 108
5.3 Differential energy spectra of GCR H nuclei: PAMELA data vs BON2011 vs Matthiä/ACE model 109
5.4 Dose rates using BON2011, BON2010 and Matthiä/ACE model 110
5.5 Quantification of the differences in the dose equivalent rates using BON2011, Matthiä/ACE and BON2010 model 111
5.6 Dose Rates vs Primary particle energy 112
5.7 Variation of dose rates with shielding during solar maximum and minimum periods . . 113
5.8 Mean shielding in the water sphere and ICRP male phantom 116
5.9 Variation of dose with depth for unshielded and shielded water sphere 117
5.10 Effective dose equivalent rates in near-Earth interplanetary space and ISS orbit 118

B.1 Calculation of dose rates: Indirect Vs Direct Method 156
B.2 Quality of statistics 157

C.1 Differential energy spectra: SPENVIS vs Matthiä/ACE vs CREME2009 vs BON2010 vs measurements 160

List of Tables

2.1 Details of the GCR data shown in Figure 2.1. 7

3.1 An overview of the models describing GCR spectra outside the Earth's magnetosphere at a distance of 1 AU from the sun. 35

5.1 Tissue weighting factors w_T recommended by ICRP (ICRP, 2007). 115

5.2 Career effective dose limits (in units mSv) for 1-year missions as recommended by the NASA space flight human system standard for all of their human space flight programs (NASA, 2007). 119

5.3 Comparison of the measured dose from GCR onboard the ISS with the calculated dose over the whole sphere. 121

5.4 Absorbed dose measurements by MSL/RAD instrument during the transit flight to Mars between December 2011 to July 2012 (Zeitlin et al., 2013) and the calculated dose for the same time period. 123

Acknowledgment

First and foremost, I would like to acknowledge Dr. Günther Reitz, Prof. Dr. Robert Wimmer-Schweingruber, Dr. Thomas Berger and Dr. Daniel Matthiä for selecting me as a doctoral candidate for the Space Life Science Research School. Thank you all for believing in me and giving me the opportunity to work on this research project. Without your continuous guidance and support this work would not have been possible. During our discussions I have learnt a great deal from the enormous knowledge and experience that each one of you have.

Dr. Berger and Dr. Matthiä in particular were instrumental in making this research work a success. I believe, our frequent meetings, your ideas, critical reviews and supervision were the key. Thank you for helping me out on various occasions both with administration and work, for sharing your expertise with me, for the scientific training and for making me trust in my work when I didn't quite myself.

I would like to take this opportunity to also thank Prof. Dr. Lembit Sihver who has been always very encouraging and enthusiastic about my work. Thank you for taking out time for my dissertation and defense.

I would like to express my sincerest appreciation of Dr. Christine Hellweg who has made the SpaceLife Program a success. Thank you for providing continuous updates and information regarding the conferences and training courses, for arranging the summer schools and excursions, and for answering to all my endless questions related with administration. The organization of the program is commendable and all of us, the SpaceLife students, recognise and appreciate that.

I am also extremely grateful to Mrs. Anna-Maria Trautmann for helping me out with housing at the beginning of my PhD work and with issues concerning paper work especially related with administration and visa. I thank you for counselling, understanding and encouraging me.

At this point I would like to express my gratitude to Prof. Dr. Rupert Gerzer together with all of you mentioned above for providing me necessary documents and support concerning the Residence Permit to stay in Germany beyond the expected time. I also thank all of you for supporting me on numerous other occasions and for giving me the possibility to attend conferences, training courses and summer schools. I have benefitted a lot from them.

I would like to acknowledge Dr. Cary Zeitlin for the fruitful discussions concerning the issues with shielding and the data from MSL/RAD.

I deeply appreciate Dr. Nicole Santen and Dr. Konstantin Herbst for their review of my Dissertation. Thank you for your time and also for the encouragement. You guys are great!

I am grateful to Thomas Urlings for setting up my work station and for the IT-support whenever I

needed. Thank you for spending time to write the script which was extremely useful for me.

I also thank Britta Rowehl for helping me out with travel applications and for office related matters.

In these last four years I have made some close friends who kept me motivated and understood every bit of my mind. Dr. Birgit Ritter - my dearest friend, office mate and the best counsellor. I could not have asked for a better person to share my office with. I cherish each and every discussion we've had, be it scientific or personal. Thanks for giving me the space and ears whenever I wanted...actually you always sensed it. I sincerely appreciate all your suggestions regarding my work and also the time you spent for me during various occasions. You are simply the best!
My gang of girls including Birgit, Dr. Anja Bauermeister, Ramona Schrage, Rebecca Ruland, Dr. Nevena Stojicic and Silvana Hassel - We have gone through similar experiences and I think these have basically made us understand each other enormously. Thanks for encouraging me and supporting me during my stay in Germany. I have had the most exciting times with you all and I know there are many more to come.

I would like to thank my colleagues and friends at the Kiel university including Robert, Prof. Dr. Bernd Heber, Dr. Sönke Burmeister, Johannes Labrenz, Dr. Jan Köhler, Esther Dönsdorf, Dr. Konstantin Herbst and Ursula Nebendahl who have always been helpful with matters related with work, conferences, administration and have always been welcoming during my visits to Kiel.

My greatest thanks and appreciation goes to my family especially to my grandfather - Sri Kripa Shankar Srivastava for being extremely progressive and paving the way for his daughters and grandchildren such that we are able to live as we wanted, my mother - Dr. Kumkum Srivastava for being my ultimate support system throughout my life and my father - Dr. Arun Kumar Verma for always trusting and believing in me and my work. I am also thankful to my brother Aseem Kumar, his wife and my extended family in Jaipur and Delhi for taking me back to my childhood time and again during our conversations which was rather therapeutic during these last years. Thank you all for being there for me.

I have the utmost respect and admiration for my partner - Johannes Bauer who has been my best friend, my favourite teacher and the most positive person around. While applying for the PhD position, I was concerned about my programming skills but you made me believe that if I set my mind and work towards it step by step I could achieve anything. And I think I did. With your patient training starting from the SpaceMaster time I can now proudly say that I am an independent programmer. Thank you for believing in me, for keeping me motivated, for helping me out at numerous occasions and for being patient with me throughout my doctoral studies. I also want to thank your family for their understanding and support.

Statutory Declaration

I herewith declare that:

- Apart from the supervisor's guidance, the content and the design of the thesis is my own work.
- The thesis has not been submitted either partially or wholly as part of a doctoral degree to another examining body.
- The thesis has been prepared subject to the Rules of Good Scientific practice of the German Research Foundation.

As mentioned in the Preface and referenced in the text, the thesis contains work that has already been published in scientific journals. These publications are:

Mrigakshi, A. I., D. Matthiä, T. Berger, G. Reitz and R. F. Wimmer-Schweingruber, Assessment of galactic cosmic ray models, J. Geophys. Res., 117, A08109, 2012. doi:10.1029/2012JA017611

Mrigakshi, A. I., D. Matthiä, T. Berger, G. Reitz and R. F. Wimmer-Schweingruber, How Galactic Cosmic Ray models affect the estimation of radiation exposure in space, Adv. Space Res., 51, p. 825-834, 2013a. doi:10.1016/j.asr.2012.10.017

Matthiä, D., T. Berger, A. I. Mrigakshi and G. Reitz, A Ready - to - Use Galactic Cosmic Ray Model, Adv. Space Res., 51, p. 329-338, 2013. doi:10.1016/j.asr.2012.09.022

Mrigakshi, A. I., D. Matthiä, T. Berger, G. Reitz and R. F. Wimmer-Schweingruber, Estimation of Galactic Comic Ray exposure inside and outside the Earth's magnetosphere during the recent solar minimum between solar cycles 23 and 24, Adv. Space Res., 52, p. 979-987, 2013b. doi:10.1016/j.asr.2013.05.007

Kiel, _____ _____

(Date) (Signature of the candidate)